NOνA

NuMI Off-Axis ν_e Appearance Experiment

Conceptual Design Report

Contact:
John Cooper, Project Manager, jcooper@fnal.gov
Ron Ray, Deputy Project Manager, rray@fnal.gov

March 31, 2006

Preface

This Conceptual Design Report describes the design of the NOνA detector. A conceptual design is by definition a snapshot of the current work. As the design effort and R&D continues, we expect the design details to evolve and eventually lead to a comprehensive Technical Design Report describing a baseline NOνA detector and project.

Chapter 1 is an Executive Summary with a short description of the NOνA project.

Chapter 2 describes the Scientific Performance Requirements which this detector project must satisfy. This chapter contains an overview of the $\nu_\mu \rightarrow \nu_e$ neutrino oscillation physics which NOνA will study and derives the detector performance requirements from the intended physics measurements. The chapter also describes the Off-Axis NuMI (Neutrinos at the Main Injector) beam which provides the neutrino beam used by NOνA. The NuMI beam was commissioned in 2005 and is now operating at Fermilab. NOνA builds on this investment by using the beam for a new physics study beyond that originally intended for the facility.

Chapter 3 is an overview of the recommended alternative NOνA design, including the site, detector hall, and the detector itself. The performance of the detector is described and the chapter concludes with a summary of the recommended alternative NOνA design performance versus the scientific performance requirements set out in Chapter 2.

Chapter 4 discusses alternative designs considered for NOνA. Alternative sites, alternative detector technologies, and alternative detector structures are discussed. The reasons these alternatives were not chosen are presented.

Chapter 5 describes the optimization process the selected NOνA design has undergone. This chapter discusses in some detail a performance-to-cost optimization of the NOνA basic cellular unit with particular attention to how various parts of the selected design interact with one another. A risk optimization study of the basic cell design is discussed as well. Indications for additional value management studies are presented.

Chapter 6 presents the Work Breakdown Structure dictionary at Level 3.

Chapters 7 through 16 then take each Level 2 WBS element of the NOνA project and discuss the design in more detail than was presented in the overview of Chapter 3. The selected designs within each Level 2 WBS are discussed, alternatives to those designs are presented, and design optimizations are described. Quality Assurance plans are presented. Environment, Safety and Health issues, Risks, and Value Management studies particular to each Level 2 WBS element are presented.

Chapter 17 is a cross-cut chapter summarizing the major ES&H issues across the entire NOνA design. An overview of the preliminary Hazard Assessment is presented here. The NEPA process for NOνA is described in this chapter.

Chapter 18 is a cross-cut chapter summarizing Quality Assurance issues across the entire NOνA design.

Chapter 19 is a cross-cut chapter summarizing the major risks in the design. The NOνA Risk Management Plan is described here.

Chapter 20 discusses Safeguards and Security issues for the NOνA project.

Chapter 21 is a discussion of Public and Stakeholder input.

Chapter 22 is an overview of Life Cycle costs for the NOνA detector. Operating costs are summarized. A Decontamination and Decommissioning plan with estimated costs is presented. The impact of these life cycle costs on the alternatives analysis of Chapter 4 is discussed.

Chapter 23 presents the Cost Range, Scope Range, and Schedule Range for the NOνA Project. R&D, and Project Engineering Design budgets are presented, and the specific goals of these project phases are discussed.

Table of Contents

PREFACE **2**

TABLE OF CONTENTS **3**

1. EXECUTIVE SUMMARY **9**

1.1 INTRODUCTION 9
1.2 PROJECT COMPONENTS 9
1.3 USE OF EXISTING FACILITIES 9
1.4 CAPABILITIES 9
1.5 COST & SCHEDULE 9

2. SCIENTIFIC PERFORMANCE REQUIREMENTS **10**

2.1 NOνA GOALS 10
2.1.1 Table of Scientific Performance Requirements *10*
2.2 OVERVIEW OF NEUTRINO OSCILLATIONS 10
2.3 DETAILS OF NEUTRINO OSCILLATIONS 11
2.2.1 Neutrino Mixing *11*
2.2.2 Matter Effects *12*
2.2.3 CP Violation *13*
2.2.4 Ambiguities *13*
2.2.5. Measurement of the Dominant Mode Oscillation Parameters *15*
2.3 THE OFF-AXIS NEUTRINO BEAM 16
2.3.1 The NuMI Beam *16*
2.3.2 Off-Axis Concept *17*
2.4 SITING REQUIREMENTS 19
2.4.1 Transverse Siting *19*
2.4.2 Longitudinal Siting *20*
2.5 FAR DETECTOR REQUIREMENTS 21
2.5.1 Figure of Merit *21*
2.5.2 Energy Resolution *22*
2.6 FAR DETECTOR HALL OVERBURDEN REQUIREMENT 22
2.7 NEAR DETECTOR REQUIREMENTS 23
CHAPTER 2 REFERENCES 24

3. OVERVIEW OF THE NOνA DESIGN **25**

3.1 INTRODUCTION 25
3.2 FAR DETECTOR SITE: ASH RIVER 25
3.3 NEAR DETECTOR SITE: FERMILAB NUMI ACCESS TUNNEL 28
3.4 DESCRIPTION OF THE NOνA DETECTOR 30
3.4.1 The Basic NOvA Detector Element *30*
3.4.2 Liquid Scintillator *32*
3.4.3 Wavelength-shifting Fiber *32*
3.4.4 Rigid PVC Extrusions *32*
3.4.5 Extrusion Modules *34*
3.4.6 Photodetector and Electronics *35*
3.4.7 Data Acquisition System *35*
3.4.8 Assembly and Structure of the Far Detector. *35*
3.4.9 Assembly and Structure of the Near Detector *39*
3.5 PERFORMANCE OF THE SELECTED NOνA DESIGN 41
3.5.1 Measured Performance of a Single Cell *41*
3.5.2 Simulated Performance of the NOvA Detector: A Visual Overview *42*
3.5.3 Simulated Performance of the NOvA Detector: Quantitative Analysis *49*
3.5.3 Summary: Selected NOvA Design Performance vs. Scientific Requirements *52*

CHAPTER 3 REFERENCES 53

4. ALTERNATIVE NOνA DESIGNS CONSIDERED 54

4.1 INTRODUCTION 54
4.2 ALTERNATIVE FAR DETECTOR SITES 54
4.2.1 Lake Superior Sites 56
4.2.2 Cliffs-Erie Site 56
4.2.3 Peyla Site 56
4.2.4 Orr-Buyck Site 56
4.2.5 Alternatives at the Ash River Site 57
4.2.6 Fort Frances – Mine Center Site 58
4.2.7 Vermilion Bay Site 58
4.3 ALTERNATIVE NEAR DETECTOR SITES 58
4.4 ALTERNATIVE DETECTOR TECHNOLOGIES 59
4.4.1 Water Cherenkov Detectors 59
4.4.2 Liquid Argon TPC 60
4.4.3 Low Z Sampling Calorimeters 60
4.4.4 Performance of Alternative Low Z Sampling Calorimeters vs. the Selected NOνA Design 61
4.4.5 Risk Analysis of Low Z Sampling Calorimeter Alternatives 63
4.4.6 Conclusions on Low Z Sampling Calorimeter Alternatives 63
4.5 ALTERNATIVE STRUCTURES FOR THE SELECTED TOTALLY ACTIVE NOνA DESIGN 63
4.5.1 Less Vertically Challenging Alternative Detectors 63
4.5.2 A "Vee" Design Alternative 64
4.5.3 A Bathtub Design Alternative 65
4.5.4 A Design Alternative based on International Shipping Containers 66
CHAPTER 4 REFERENCES 68

5. OPTIMIZATION OF THE SELECTED NOνA DESIGN 69

5.1 INTRODUCTION 69
5.2 OPTIMIZATION OF THE NOνA DETECTOR SEGMENTATION 69
5.3 OPTIMIZATION OF THE NOνA CELL LIGHT THRESHOLD LEVEL 71
5.4 OPTIMIZATION OF THE HORIZONTAL CELL READOUT ORIENTATIONS 73
5.5 FURTHER PERFORMANCE / COST OPTIMIZATION OF THE NOνA CELL DESIGN 76
5.5.1 Performance Optimization for PVC Extrusions. 76
5.5.2 Performance Optimization for the Liquid Scintillator. 77
5.5.3 Performance Optimization for the Fiber. 78
5.5.4 Performance Optimization for the Photodetector and Electronics. 79
5.5.5 Performance Optimization and Cost Summary. 79
5.6 RISK OPTIMIZATION OF THE NOνA CELL DESIGN 80
5.6.1 Risk Optimization of the PVC Extrusions. 81
5.6.2 Risk Optimization of the Liquid Scintillator. 82
5.6.3 Risk Optimization of the Fiber. 83
5.6.4 Risk Optimization of the Photodetector and Electronics. 84
5.6.5 Risk Optimization Summary. 85
5.7 INDICATIONS FOR ADDITIONAL VALUE MANAGEMENT STUDIES 85
5.8 OPTIMIZATION AND POSSIBLE FURTHER IMPROVEMENTS IN THE ANALYSIS ALGORITHM 86
CHAPTER 5 REFERENCES 86

6. WORK BREAKDOWN STRUCTURE 87

6.1 INTRODUCTION 87
6.2 WBS DICTIONARY AT LEVELS 2 AND 3 87
CHAPTER 6 REFERENCES 94

7. SITE DESCRIPTION 95

7.1 INTRODUCTION 95

7.2 DETAILS OF THE RECOMMENDED ASH RIVER SITE 95
7.2.1 Site Maps and Features *95*
7.2.2 Roads, Power, Data Communications *100*
7.2.3 Proximity to Voyageurs National Park *102*
7.3 ALTERNATIVES: COMPARISONS WITH THE ORR-BUYCK SITE 104
7.3.1 Construction Cost Comparison between Ash River and Orr-Buyck *104*
7.3.1 Scientific Comparison between Ash River and Orr-Buyck *105*
7.4 SITE DESIGN OPTIMIZATION 106
7.5 QUALITY ASSURANCE 106
7.6 ES&H 106
7.7 RISKS 107
7.8 VALUE MANAGEMENT 107
CHAPTER 7 REFERENCES 107

8. CONVENTIONAL FACILITIES 108

8.1 INTRODUCTION 108
8.2 THE RECOMMENDED BUILDING DESIGN 108
8.2.1 Access Road and Site Work *108*
8.2.2 Below Grade Areas *109*
8.2.3 Above Grade Areas *113*
8.3 ALTERNATIVE DESIGNS CONSIDERED 115
8.3.1 Building on the Surface with No Excavation *115*
8.3.2 Building Partially in the Ground for Containment *116*
8.3.3 Building with a 10 meter Overburden *117*
8.3.4 Alternative Construction Techniques *118*
8.4 OPTIMIZATION OF THE SELECTED BUILDING DESIGN 118
8.5 QUALITY ASSURANCE 118
8.6 ES&H 118
8.7 RISKS 119
8.8 SAFEGUARDS AND SECURITY 119
8.9 VALUE MANAGEMENT 119
CHAPTER 8 REFERENCES 120

9. LIQUID SCINTILLATOR 121

9.1 INTRODUCTION 121
9.2 THE RECOMMENDED DESIGN 121
9.2.1 Scintillator Composition *121*
9.2.2 Scintillator Blending at Fermilab *123*
9.2.3 Shipping Components and Scintillator *124*
9.3 ALTERNATIVES CONSIDERED 125
9.4 SCINTILLATOR DESIGN OPTIMIZATION 126
9.4.1 Mineral Oil *126*
9.4.2 Pseudocumene *127*
9.5 QUALITY ASSURANCE AND QUALITY CONTROL 127
9.5.1 Comparison with QA / QC in Other Experiments *128*
9.5.2 NOvA QA / QC plans *129*
9.6 ES&H 130
9.7 RISKS 130
9.8 VALUE MANAGEMENT 131
CHAPTER 9 REFERENCES 132

10. WAVELENGTH SHIFTING FIBER 133

10.1 INTRODUCTION 133
10.2 THE RECOMMENDED DESIGN 133
10.3 ALTERNATIVES CONSIDERED 135
10.4 FIBER OPTIMIZATION 135

10.5 QUALITY ASSURANCE 137
10.6 RISKS 137
10.7 ES&H 138
10.8 VALUE MANAGEMENT 138
CHAPTER 10 REFERENCES 138

11. PVC EXTRUSIONS 139

11.1 INTRODUCTION 139
11.2 THE RECOMMENDED DESIGN 139
11.2.1 NOvA rigid PVC Composition 139
11.2.2 PVC Reflectivity 140
11.2.3 PVC & Strength of Material 141
11.2.4 PVC Exterior Surface Quality 142
11.2.5 PVC Extrusion Shipping 142
11.2.4 PVC Edge Stiffeners 143
11.3 ALTERNATIVES CONSIDERED 144
11.4 PVC DESIGN OPTIMIZATION 145
11.5 QUALITY ASSURANCE 147
11.6 ES&H 147
11.7 RISKS 147
11.8 VALUE MANAGEMENT 147
CHAPTER 11 REFERENCES 148

12. PVC MODULES 149

12.1 OVERVIEW 149
12.2 THE RECOMMENDED DESIGN 149
12.2.1 Bottom Closure Plate and Fiber Manifold 149
12.2.2 PVC Module Factories 152
12.3 ALTERNATIVES CONSIDERED 152
12.4 MODULE AND FACTORY DESIGN OPTIMIZATION 153
12.5 QUALITY ASSURANCE AND QUALITY CONTROL 153
12.6 ES&H 154
12.7 RISKS 154
12.8 VALUE MANAGEMENT 155
CHAPTER 12 REFERENCES 155

13. PHOTODETECTOR AND ELECTRONICS 156

13.1 INTRODUCTION 156
13.2 AVALANCHE PHOTODIODES (APDS) 156
13.3 FRONT END ELECTRONICS 160
13.4 ALTERNATIVES CONSIDERED 163
13.5 OPTIMIZATION OF THE DESIGN 164
13.6 QUALITY ASSURANCE 164
13.7 ES&H 164
13.8 RISKS 165
13.9 VALUE MANAGEMENT 165

14. DATA ACQUISITION SYSTEM 166

14.1 SYSTEM DESCRIPTION 166
14.2 SYSTEM ARCHITECTURE 166
14.3 ALTERNATIVES CONSIDERED 169
14.4 DESIGN OPTIMIZATION 169
14.4.1 Supernova Detection 169
14.5 QUALITY ASSURANCE 169
14.6 ES&H 169
14.7 RISKS 169

14.8 Safeguards and Security 170
14.9 Value Management 170

15. NEAR DETECTOR 171

15.1 Introduction 171
15.2 Near Detector Design 171
15.3 Near Detector Event Rates 171
15.4 Alternatives Considered 172
15.5 Optimization 173
15.6 Quality Assurance 174
15.7 ES&H 174
15.8 Risks 174
15.9 Value Management 174
Chapter 15 References 174

16. FAR DETECTOR ASSEMBLY 175

16.1 Assembly of planes and blocks 175
16.2 Filling the Detector With Liquid Scintillator 177
16.3 Structural Issues 177
16.4 Structural Analysis 179
16.5 Alternatives Considered 182
16.6 Design Optimization 183
16.7 Quality Assurance 183
16.8 ES&H 184
16.9 Risks 184
16.10 Value Management 184
Chapter 16 References 185

17. ES&H OVERVIEW 186

17.1 Introduction 186
17.2 Preliminary Hazard Assessment Documentation 186
17.3 Strategy for NEPA documentation 186
17.3.1 Environmental Assessment 186
17.3.2 Environmental Assessment at Fermilab 187
17.3.3 Environmental Assessment Worksheets for the State of Minnesota 187
Chapter 17 References 187

18. QUALITY ASSURANCE OVERVIEW 188

18.1 Introduction 188
18.2 Quality Management Program 188
Chapter 18 References 188

19. RISK ANALYSIS 189

19.1 Introduction 189
19.2 NOvA Risk Management Plan 189
19.2.1 Application of the Risk Management Plan to an Actual Problem 189
Chapter 19 References 189

20. SAFEGUARDS AND SECURITY 191

20.1 Introduction 191
Chapter 20 References 192

21. STAKEHOLDER INPUT 193

21.1 Introduction 193
21.2 Local Clubs and Groups 193

21.3 Local Communities 193
21.4 Local Economic Development Groups in Northern Minnesota 193
21.5 St. Louis County, Minnesota 194
21.6 The University of Minnesota 194
21.7 Minnesota State Government and Agencies 194
21.8 Voyageurs National Park 194
21.9 Fermi National Accelerator Laboratory 194
21.10 The High Energy Physics Community 195
21.11 The Department of Energy 195
21.9 Individual Briefings to State and Federal Government Officials 196
Chapter 21 References 196

22. LIFE CYCLE COSTS 197

22.1 Operating Costs 197
22.1.1 Operating Costs for NOvA at Ash River 197
22.1.2 Analysis of Operating Costs for Alternative Designs 198
22.2 Decontamination and Decommissioning Plan and Costs 198
22.2.1 Decommissioning of a Previous Experiment 198
22.2.2 Decontamination and Decommissioning of NOvA 198
22.2.3 Analysis of Decommissioning Costs for Alternative Designs 199
Chapter 22 References 200

23. COST, SCHEDULE, AND SCOPE RANGE 201

23.1 Project Deliverables, Test and Acceptance Criteria ..... **Error! Bookmark not defined.**
*23.1.1 The Far Detector Building at Ash River ..... **Error! Bookmark not defined.***
*23.1.2 The NOvA Far Detector ..... **Error! Bookmark not defined.***
*23.1.3 The NOvA Near Detector ..... **Error! Bookmark not defined.***
23.2 Cost Range ..... **Error! Bookmark not defined.**
*23.2.1 R&D Funding Requirements ..... **Error! Bookmark not defined.***
*23.2.2 Cooperative Agreement Requirements ..... **Error! Bookmark not defined.***
*23.2.3 PED Funding Requirements ..... **Error! Bookmark not defined.***
23.3 Scope Range ..... **Error! Bookmark not defined.**
23.4 Schedule Range ..... **Error! Bookmark not defined.**

APPENDIX A. WBS DICTIONARY FOR R&D 203

A.1 R&D WBS Dictionary at Levels 2 and 3 203

APPENDIX B. MINNESOTA POLLUTION CONTROL AGENCY STATEMENT ON NOvA SCINTILLATOR 210

1. Executive Summary

1.1 Introduction

Fermi National Accelerator Laboratory and the NOνA Collaboration composed of 142 scientists and engineers from 28 Universities and Laboratories around the world have collaborated to create this conceptual design for a new detector to study neutrino oscillations using the existing Department of Energy investment in the NuMI neutrino beam at Fermilab.

1.2 Project Components

The NOνA Project consists of three main elements:

1. A new building on a site near the US-Canadian border in Ash River, Minnesota to house the NOνA detector. This site is 810 kilometers from Fermilab. The building is 22.5 meters wide by 196 meters long and is sunk 14 meters below the existing grade into granite rock at the site. The excavated granite is used to cover the detector with a 3 meter thick overburden as a cosmic ray shield.
2. A 25 kiloton neutrino detector composed of ~ 643,000 cells of extruded PVC plastic in a cellular structure. Each cell is 3.9 centimeters wide by 6.0 centimeters deep and is 15.7 meters long. The cells are filled with a total of 5.7 million gallons of liquid scintillator. The liquid scintillator comprises 73% of the total mass, making this a totally active tracking calorimeter detector designed for identification of electron neutrino (ν_e) interactions. The detector is read out via 22,000 kilometers of 0.8 millimeter diameter optical wave-shifting fiber into approximately 20,000 avalanche photodiodes with associated electronics.
3. A small 200 ton detector on the Fermilab site to measure the inherent beam backgrounds.

1.3 Use of Existing Facilities

The existing Fermilab NuMI beam transport, target, focusing horns, vacuum decay pipe, and absorber will be used to provide the neutrino beam for NOνA. The NuMI beam is used in a new way by placing the NOνA detector at an angle ~ 15 milliradians off the beam axis to obtain a muon neutrino (ν_μ) beam sharply peaked at 2 GeV in energy. The small 200 ton detector will be placed in the existing NuMI underground tunnel at a depth 105 meters below grade.

1.4 Capabilities

In a six year run with 6.5 x 10^{20} protons per year delivered by the Fermilab Main Injector to the NuMI target, NOνA would measure the probability for muon neutrino to electron neutrino oscillations ($\nu_\mu \rightarrow \nu_e$) down to a value ten times smaller than the existing experimental limit.

The existence of neutrino oscillations means that neutrinos have mass. In a six year run equally split between neutrino and anti-neutrino beams, NOνA can resolve the neutrino mass ordering for a significant portion of the available parameter space for these oscillations. This capability is a unique aspect of NOνA not duplicated by any other formally proposed experiment.

1.5 Cost & Schedule

The Total Estimated Cost of the NOνA Project is in the range $ 185 M - $ 244 M. The Total Project Cost is in the range $ 197 M - $ 256 M. The Scope Range of the NOνA Project includes a Far Detector of mass in the range 25 - 34 kilotons. A Schedule Range of 45 to 58 months is proposed for the construction project.

2. Scientific Performance Requirements

2.1 NOνA Goals

The primary goal of the NOνA experiment is to use the existing Fermilab NuMI muon neutrino (ν_μ) beam [1] to measure electron neutrino (ν_e) appearance due to $\nu_\mu \rightarrow \nu_e$ oscillations. A secondary goal is a greatly improved measurement of the ν_μ disappearance parameters.

2.1.1 Table of Scientific Performance Requirements

These NOνA goals translate into the scientific performance requirements summarized in Table 2.1. The requirements are developed in this chapter in the sections indicated in the table.

Design Parameter	Scientific Performance Requirement	Section
Distance off-axis	11.5 to 12.0 km	2.4.1
Distance from Fermilab	As far from Fermilab as practically possible.	2.4.2
Experimental Sensitivity	Figure of merit greater than or equal to 30 (The Figure of Merit is defined as the number of ν_e signal events divided by the square root of the background for 32.5 x 10^{20} protons on the NuMI target at the oscillation values $\sin^2(2\theta_{13}) = 0.1$ and $\Delta m^2_{32} = 0.0025$ eV^2 without regard to matter and atmospheric-solar interference effects.)	2.5.1
Energy resolution for ν_e Charged Current events	Less than 8% at 2 GeV	2.5.2
Energy resolution for Quasi-Elastic ν_μ Charged Current events	Less than 4% at 2 GeV	2.5.2
Far Detector overburden	2 meters of rock with density 2.5 g/cm^3	2.6
Near Detector	At least a 20 ton fiducial volume located about 1 kilometer from the NuMI target with sufficient transverse and longitudinal size for neutrino event containment. At least 62 tons if located at 2.5 km from the NuMI target.	2.7

Table 2.1: Summary of the scientific requirements and the chapter sections in which they are established.

2.2 Overview of Neutrino Oscillations

The standard picture of neutrinos consists of three different types: ν_e, ν_μ, and ν_τ, each of which is a partner to a charged lepton: e (electron), μ (muon), and τ (tau lepton). We know that the neutrinos have mass and as a result, one type of neutrino can transform (oscillate) into another type. Oscillations of ν_e into $\nu_\mu + \nu_\tau$ have been observed in solar neutrino experiments [2] and by a long baseline reactor neutrino experiments [3]. Oscillations of ν_μ into ν_τ have been observed in atmospheric neutrino experiments [4], from a Japanese accelerator experiment [5], and soon from the MINOS experiment now running in the Fermilab NuMI beam. The oscillation of ν_μ into ν_e has yet to be observed. There is an upper limit on the rate of this oscillation from a reactor

neutrino experiment [6]. The primary goal of the NOνA experiment is to observe $\nu_\mu \rightarrow \nu_e$ oscillations.

The amplitude of the $\nu_\mu \rightarrow \nu_e$ oscillations is expressed mathematically in terms of an angle, θ_{13}, and the number of signal events observed in the oscillations is proportional $\sin^2(2\theta_{13})$. For neutrino beams which pass through the Earth, the amplitude of the $\nu_\mu \rightarrow \nu_e$ oscillation also depends on the relative masses of two of the neutrinos, parameterized by the quantity Δm_{32}^2. Oscillations are in general enhanced if this parameter is larger than zero and suppressed if this parameter is less than zero. Currently the sign of this parameter is not known, and this is commonly referred to as the mass hierarchy problem. Additionally, the rate of the $\nu_\mu \rightarrow \nu_e$ oscillations depends on a phase angle which violates charge-parity (CP) symmetry. A non-zero value of this phase angle, δ, leads to CP violation in the lepton sector and possibly gives information on the matter – antimatter asymmetry of the universe.

The goal of the NOνA experiment is to extend the search for $\nu_\mu \rightarrow \nu_e$ oscillations a factor of 14 below the current best limit and a factor of 10 beyond the sensitivity of the MINOS experiment which is now running. Additionally, NOνA can begin to study the mass hierarchy problem and search for the effects of the CP violating phase angle δ. NOνA is particularly well suited to the study of the mass hierarchy problem due to the large amount of earth between the neutrino source and the detector. No other planned experiment can attack this problem.

The remainder of this chapter outlines the neutrino oscillation formalism in more mathematical detail and develops the scientific performance requirement for NOνA from first principles.

2.3 Details of Neutrino Oscillations

2.2.1 Neutrino Mixing

Neutrino oscillations come about because the weak eigenstates are rotated from the mass eigenstates. The unitary matrix that rotates the mass eigenstates into flavor eigenstates is

$$U = \begin{pmatrix} c_{13}c_{12} & c_{13}s_{12} & s_{13}e^{-i\delta} \\ -c_{23}s_{12} - s_{13}s_{23}c_{12}e^{i\delta} & c_{23}c_{12} - s_{13}s_{23}s_{12}e^{i\delta} & c_{13}s_{23} \\ s_{23}s_{12} - s_{13}c_{23}c_{12}e^{i\delta} & -s_{23}c_{12} - s_{13}c_{23}s_{12}e^{i\delta} & c_{13}c_{23} \end{pmatrix}, \quad (2.1)$$

where $c_{jk} \equiv \cos\theta_{jk}$ and $s_{jk} \equiv \sin\theta_{jk}$. With this labeling, the atmospheric neutrino oscillations are primarily determined by the θ_{23} and Δm_{32}^2 parameters, whereas the solar neutrino oscillations depend on θ_{12} and Δm_{12}^2, where $\Delta m_{ij}^2 = m_i^2 - m_j^2$. If the phase δ is neither 0 nor π, then neutrinos exhibit CP violation.

From SuperKamiokande[7] we already have some knowledge of $\left|\Delta m_{32}^2\right| = (1.5 - 3.4) \times 10^{-3}$ eV^2 and $\sin^2 2\theta_{23} > 0.92$ at the 90% confidence level. The combined analysis of the SNO[2], SuperKamiokande[4] and KamLAND[3] experiments gives $\Delta m_{21}^2 = +7.9 \pm 0.6 \times 10^{-5}$ eV^2 and $\sin^2 2\theta_{12} = 0.82 \pm 0.07$. The CHOOZ experiment [6] (and SuperKamiokande) provide us with a limit on $\sin^2 2\theta_{13} < 0.18$. The CHOOZ limit is dependent on the input value used for $|\Delta m_{32}^2|$; for the current central value 2.5×10^{-3} eV^2, this limit is $\sin^2 2\theta_{13} < 0.14$, while for $|\Delta m_{32}^2| = 2.0 \times 10^{-3}$ eV^2, it is $\sin^2 2\theta_{13} < 0.18$ [6].

The appearance probability of ν_e in a ν_μ beam in vacuum is given, to leading order, by

$$P_{vac}\left(\nu_\mu \rightarrow \nu_e\right) = \sin^2\theta_{23}\sin^2 2\theta_{13}\sin^2\Delta_{atm}\,, \tag{2.2}$$

where

$$\Delta_{atm} \approx 1.27\left(\frac{\Delta m^2_{32} L}{E}\right), \tag{2.3}$$

where Δm^2_{32} is measured in eV^2, L is measured in km, and E is measured in GeV.

2.2.2 Matter Effects

The neutrinos in the NuMI beam propagate through the earth and matter induced contributions to the propagation amplitude are non-negligible. These matter effects have opposite sign for neutrinos and antineutrinos and for the normal versus inverted neutrino mass orderings. The matter effects can thus be used to distinguish the two possible three-neutrino mass orderings shown in Figure 2.1. If the experiment is performed at the first peak in the oscillation the matter effects are primarily a function of the energy of the neutrino beam and the transition probability in matter can be approximated by

$$P_{mat}\left(\nu_\mu \rightarrow \nu_e\right) \approx \left(1 \pm 2\frac{E}{E_R}\right) P_{vac}\left(\nu_\mu \rightarrow \nu_e\right) \tag{2.4},$$

where E_R is the matter resonance energy associated with the atmospheric Δm^2, that is

$$E_R = \frac{\Delta m^2_{32}}{2\sqrt{2}G_F N_e} = 12\ \text{GeV}\left(\frac{\Delta m^2_{32}}{2.5\times10^{-3}\ \text{eV}^2}\right)\left(\frac{1.4\ \text{g cm}^{-3}}{Y_e \rho}\right) \tag{2.5},$$

where N_e is the electron number density in the earth, ρ is the matter density (2.8 g.cm^{-3}) and Y_e is the average Z/A.

For the normal hierarchy, matter effects enhance (suppress) the transition probability for neutrinos (antineutrinos) and vice versa for the inverted hierarchy. For a 2 GeV neutrino energy, matter effects give a 30% enhancement or suppression in the transition probability.

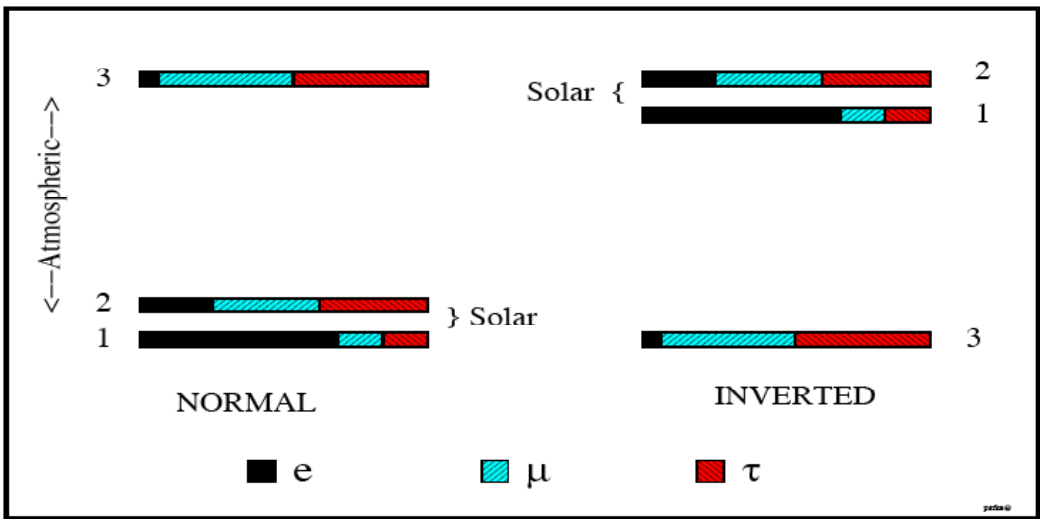

Fig. 2.1 The two allowed three-neutrino mass squared spectra that account for the oscillations of solar and atmospheric neutrinos. The normal spectrum has $\Delta m^2_{32} > 0$ and the inverted has $\Delta m^2_{32} < 0$. The ν_e fraction of each mass eigenstate is indicated by the black solid region, whereas the ν_μ (ν_τ) fraction is indicated by the blue-green right-leaning (red left-leaning) hatching. The ν_e fraction in the mass eigenstate labeled, 3, has been enhanced for clarity.

2.2.3 CP Violation

The $\nu_\mu \rightarrow \nu_e$ transition probability is sensitive to sub-leading effects and in particular to the CP violating phase δ. In vacuum, the shift in the transition probability associated with the CP violating phase is given by

$$\Delta P_\delta(\nu_\mu \rightarrow \nu_e) \approx J_r \sin \Delta_{sol} \sin \Delta_{atm}(\cos\delta \cos\Delta_{atm} -+ \sin\delta \sin\Delta_{atm}), \quad (2.6)$$

where the minus (plus) sign is for neutrinos (anti-neutrinos), $J_r = \sin 2\theta_{12} \sin 2\theta_{23} \sin 2\theta_{13} \cos\theta_{13}$, and

$$\Delta_{sol} = 1.27 \frac{\Delta m^2_{21} L}{E} = \frac{\Delta m^2_{21}}{\Delta m^2_{32}} \Delta_{atm} \approx \frac{1}{36} \Delta_{atm} . \quad (2.7)$$

At the first oscillation maximum of the atmospheric Δm^2 scale, the shift in the transition probability dependent on δ is of order

$$\left|\Delta P_\delta \left(\nu_\mu \rightarrow \nu_e\right)\right| \sim 0.6\% \sqrt{\frac{\sin^2 2\theta_{13}}{0.05}} \quad . \quad (2.8)$$

Note that the shift is proportional to $\sqrt{\sin^2 2\theta_{13}}$, while the leading term is proportional to $\sin^2 2\theta_{13}$. This means that the relative size of the CP-violating effect increases with decreasing values of θ_{13}.

2.2.4 Ambiguities

Since the matter effect is caused by the interaction of electron-type neutrinos with electrons in the earth and since it has the opposite sign for neutrinos and antineutrinos, it can be confused with a true CP-violating effect. This leads in some cases to an inherent ambiguity between the CP phase δ and the mass ordering.

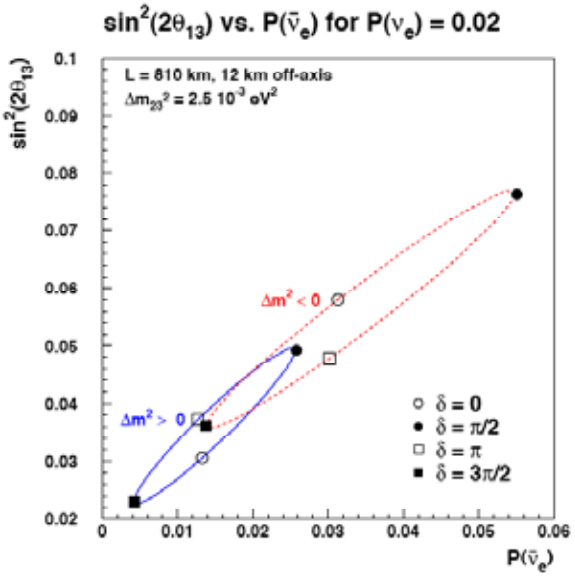

Fig. 2.2: Plot of the possible results for $\sin^2(2\theta_{13})$ vs. the oscillation probability observed for antineutrinos given a perfectly measured 2% neutrino oscillation probability. The blue curve is for the normal hierarchy mass ordering, and the read curve is for the inverted hierarchy. The values of the CP-violating phase δ are indicated in each case by the open and closed circles and squares with the key on the figure. This is for 12 km off-axis at an 810 km baseline.

NOνA is capable of making two measurements, the neutrino and the antineutrino oscillation probabilities near the first oscillation maximum. In some cases, these two measurements are capable, in principle, of measuring all three parameters, up to a two-fold ambiguity in the CP phase. For example a neutrino oscillation probability of 2% and an antineutrino oscillation probability of 4% or 1%, determine the mass hierarchy unambiguously. However, a neutrino oscillation probability of 2% and an antineutrino oscillation probability of 2% cannot resolve the inherent ambiguity shown in Fig. 2.2. A third measurement is needed in this case, either from an experiment done elsewhere at a different baseline, or from an additional measurement on the NuMI beamline, for example, on the second oscillation maximum.

Since the relative size of the matter effect does not depend on $\sin^2 2\theta_{13}$, while the CP-violating effect increases with decreasing $\sin^2 2\theta_{13}$, the fraction of possible δ values for which there is an ambiguity increases with decreasing values of θ_{13}. This is illustrated in Figure 2.3.

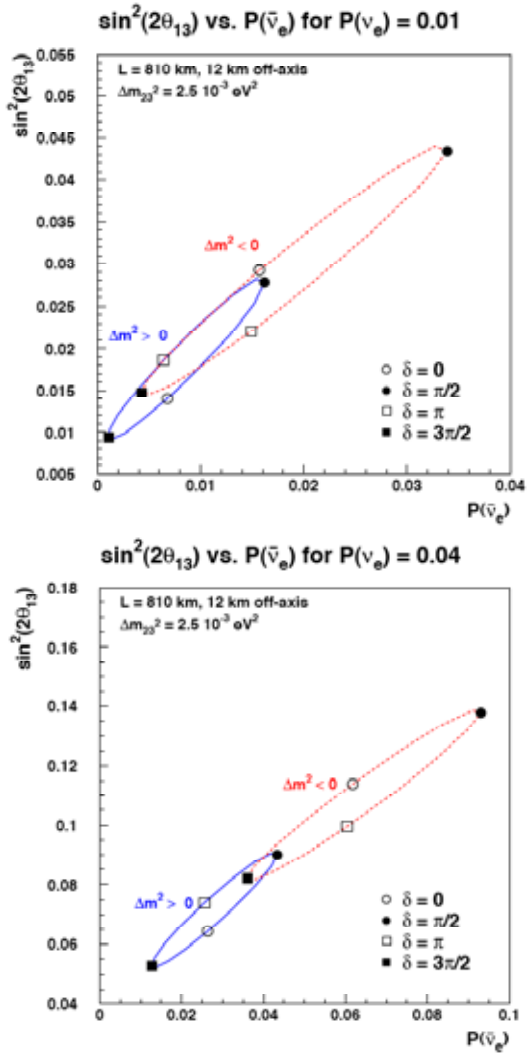

Fig 2.3: Plots of the possible results of measurement of a 1% neutrino oscillation probability (left) and a 4% neutrino oscillation probability (right), illustrating the increase in the ambiguity between the mass ordering and the CP as θ_{13} decreases.

2.2.5. Measurement of the Dominant Mode Oscillation Parameters

Although the primary NOνA physics goal is the study of $\nu_\mu \rightarrow \nu_e$ oscillations, NOνA will also be able to make significant measurements of the dominant mode oscillation parameters, $\sin^2(2\theta_{23})$ and Δm^2_{32}. Indeed, one of the most important measurements in neutrino physics today is the precise determination of $\sin(\theta_{23})$. The best current measurement comes from the SuperKamiokande study of atmospherically produced neutrinos [9]. This measurement is consistent with maximal mixing, $\sin^2(2\theta_{23}) = 1$, but with a considerable uncertainty. At the 90% confidence level, $\sin^2(2\theta_{23}) > 0.92$, which translates into a rather large range of possible values of $\sin^2(\theta_{23})$, namely $0.36 < \sin^2(\theta_{23}) < 0.64$.

There are three reasons why determining $\sin(\theta_{23})$ is of high interest: (1) If the mixing is maximal, it might be due to some currently unknown symmetry. (2) The $\nu_\mu \rightarrow \nu_e$ oscillation is mostly proportional to $\sin^2(\theta_{23})\sin^2(2\theta_{13})$ while $\bar{\nu}_e$ disappearance, measured by reactor experiments, is proportional to $\sin^2(2\theta_{13})$. Thus, if the mixing is not maximal, there is an ambiguity in comparing accelerator and reactor experiments, or conversely (3) whether θ_{13} is greater than or less than $\pi/4$, which measures whether ν_e's couple more strongly to ν_μ's or ν_τ's, can probably best be measured by comparing precise accelerator and reactor measurements.

The deviation of $\sin^2(2\theta_{23})$ from unity is measured by the depth of the oscillation dip in the ν_μ disappearance spectrum. Thus, precision in this quantity requires good statistics in this region, excellent neutrino energy resolution, and good control of systematics. NOνA offers the possibility of satisfying all of these requirements.

It appears that the best way to meet these requirements is to limit the analysis to totally contained quasielastic events, i.e., those events in which the geometrical pattern of energy deposition is consistent with the presence of only an energetic muon and a possible recoil proton. We have performed a preliminary study of how well NOνA can use these events to measure $\sin^2(2\theta_{23})$ and Δm^2_{32} using a parametric representation of the energy. This procedure is justified by the nature of these events, which are extremely clean.

The calculated one and two standard deviation contours are displayed in Figure 2.4 for assumed values of $\sin^2(2\theta_{23})$ of 0.95, 0.98, and 1.00 and a six-year neutrino run. The energy resolution has been assumed to be 2%, but the contours do not change markedly as one increases the resolution to 4%.

Note that the precision of the $\sin^2(2\theta_{23})$ measurement increases as the value of $\sin^2(2\theta_{23})$ approaches unity. For maximal mixing, the error on the measurement of $\sin^2(2\theta_{23})$ is about 0.004.

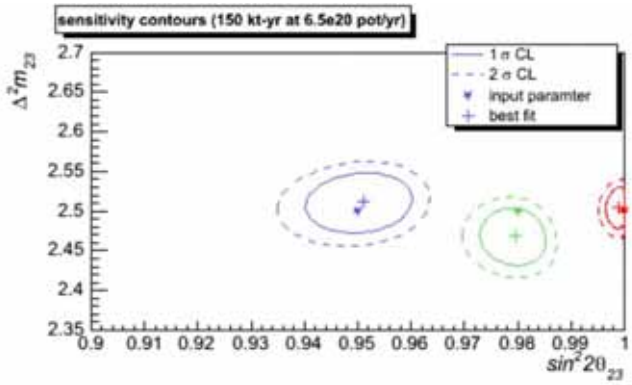

Fig. 2.4: One and two standard deviation contours for a simultaneous measurement of Δm^2_{32} and $\sin^2(2\theta_{23})$ for a six-year neutrino run in a 25 kt detector. The three input values are indicated by a star and the best fit for each is indicated by a plus sign.

2.3 The Off-Axis Neutrino Beam

2.3.1 The NuMI Beam

The NOνA experiment will use the existing NuMI neutrino beam [1]. The NuMI beamline brings 120 GeV protons extracted from the Main Injector onto a 0.95 meter-long graphite target. Two parabolic magnetic horns focus the resulting secondary beam, which is aimed at the MINOS far detector in the Soudan mine in northern Minnesota. Neutrinos are produced from pion and kaon decay in an evacuated pipe, which is 675 m in length and 2 m in diameter.

A unique feature of the NuMI neutrino beam is the ability to change the focusing optics configuration and hence the accepted neutrino energy band. Specifically, one can change the relative positions of the target and the first horn and the separation between two horns. These configurations are illustrated in Figure 2.5, together with the spectra for three possible beam element arrangements, referred to as low, medium, or high energy beam tunes. While the movement of the second horn is logistically complex and requires several weeks downtime, the target position can be varied remotely. Just moving the target provides a method of readily changing the energy spectrum in a continuous fashion at a small sacrifice of the neutrino flux as compared to a fully optimized configuration [10]. Our calculations indicate that the medium energy tune will give the best performance for the NOνA experiment.

Since Tevatron Collider operations will cease prior to the start of NOνA, components of the Fermilab accelerator complex now used for antiproton production, cooling, and storage will be available to the neutrino program. In particular, loading Booster batches into the Recycler can hide the Booster filling time from the Main Injector ramping cycle. We have based the projected NOνA performance on having 11 Booster batches of 5.5×10^{12} protons slip-stacked into the Recycler for transfer into the Main Injector every 1.467 seconds, yielding 0.8 MW and 6.5×10^{20} protons per year. More details can be found in Chapter 11 of the NOνA proposal and references therein[11].

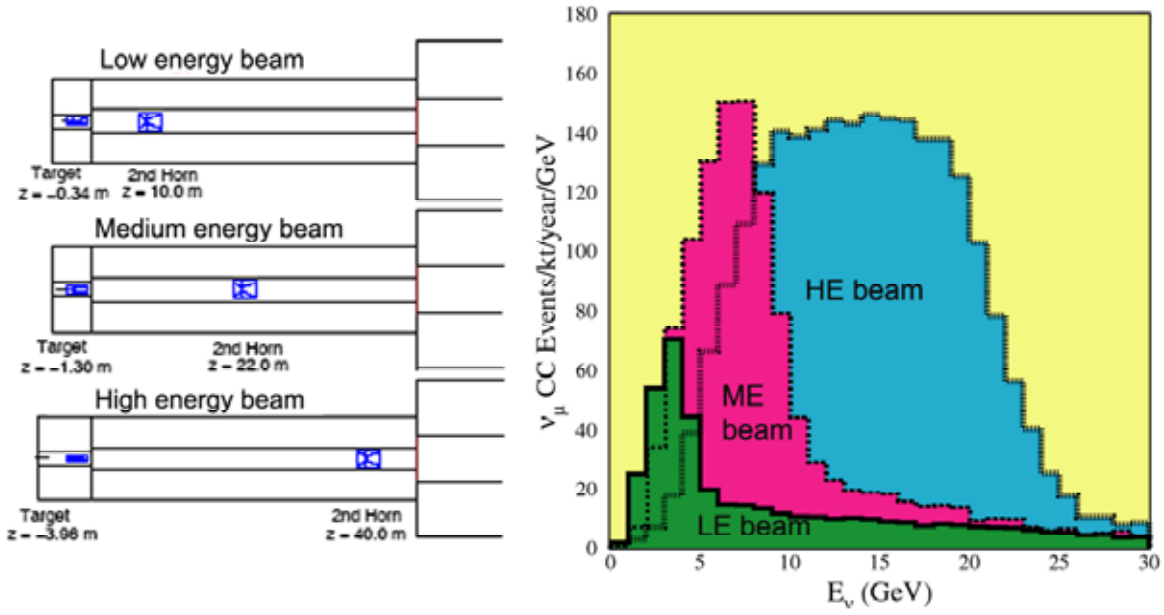

Fig. 2.5: Left: The locations of the target and second horn for the three NuMI beam configurations. Right: The expected neutrino interaction rates at the MINOS far detector site (on-axis at 735 km from Fermilab) for each of the three beam tunes assuming 2.5 x 10^{13} protons on target per year.

2.3.2 Off-Axis Concept

The NOνA Far Detector will be sited approximately 14 mrad off the NuMI beam axis, in contrast to the MINOS Far Detector, which is sited on the center of the NuMI beam. The rationale for this choice is explained below.

Pions and kaons decay isotropically in their centers of mass resulting in a relatively broad neutrino beam energy spectrum. For small angles, the flux and energy of neutrinos produced from the decay $\pi \rightarrow \mu + \nu$ in flight and intercepted by a detector of area A and located at distance z are given in the lab frame by:

$$F = \left(\frac{2\gamma}{1 + \gamma^2 \theta^2} \right)^2 \frac{A}{4\pi z^2} \tag{2.9}$$

$$E_\nu = \frac{0.43 E_\pi}{1 + \gamma^2 \theta^2}, \tag{2.10}$$

where θ is the angle between the pion direction and the neutrino direction, E_π the energy of the parent pion, m_π the mass of the pion and $\gamma = E_\pi / m_\pi$. The expressions for the neutrinos from the corresponding charged K decays are identical except that 0.43 is replaced by 0.96 resulting in a more energetic and broader distribution for identical meson energies.

Figure 2.6 shows the results of Equations. 2.9 and 2.10. The right portion of Fig. 2.6 shows that at 14 mrad the energy of the neutrino does not have a strong dependence on the energy of the parent pion. This is further demonstrated in Fig. 2.7, which shows the resulting number of neutrino events as a function of energy and angle. At approximately 14 mrad, the medium energy beam produces a narrow energy beam with approximately five times more neutrinos around the oscillation maximum than an on-axis beam.

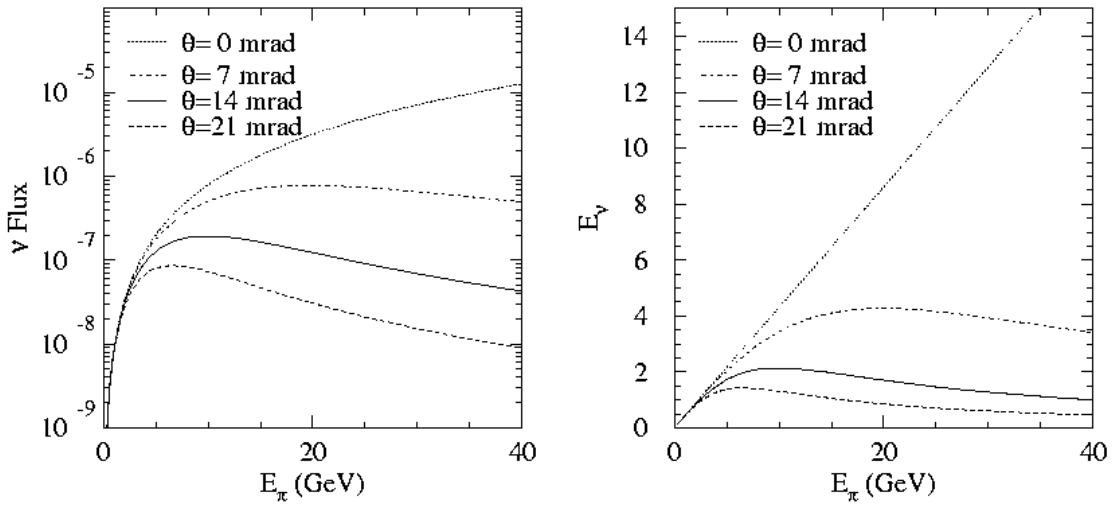

Fig. 2.6: Left: The neutrino flux from a pion of energy E_π as viewed from a site located at an angle θ from the beam axis. The flux has been normalized to a distance of 800 km. Right: The energy of the neutrinos produced at an angle θ relative to the pion direction as a function of the pion energy.

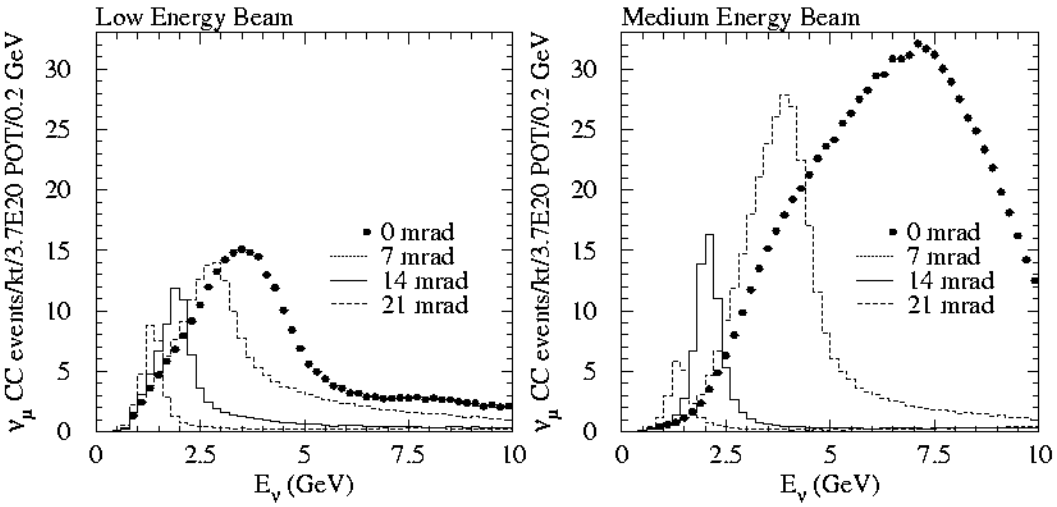

Fig. 2.7: CC ν_μ event rates expected under a no-oscillation hypothesis at a distance of 800 km from Fermilab and at various transverse locations for the NuMI low-energy beam configuration (left) and medium-energy beam configuration (right).

In addition to the increased flux, the off-axis position decreases the backgrounds compared to those in an on-axis beam. These events are diminished in an off-axis beam. One important source of background are neutral current events which simulate lower energy events since the outgoing neutrino is not observed. The neutral current events that are present are primarily found at lower energies than the signal events and thus easily eliminated, as can be seen in Figure 2.8.

Another important source of backgrounds are ν_e events that arise from muon and kaon decay. These events have a broad energy distribution, as also seen in Figure 2.8, with the muon decays tending to lower energies than the signal events and the kaon decays tending to higher energies. Thus, this source of background is also reduced by using an off-axis beam.

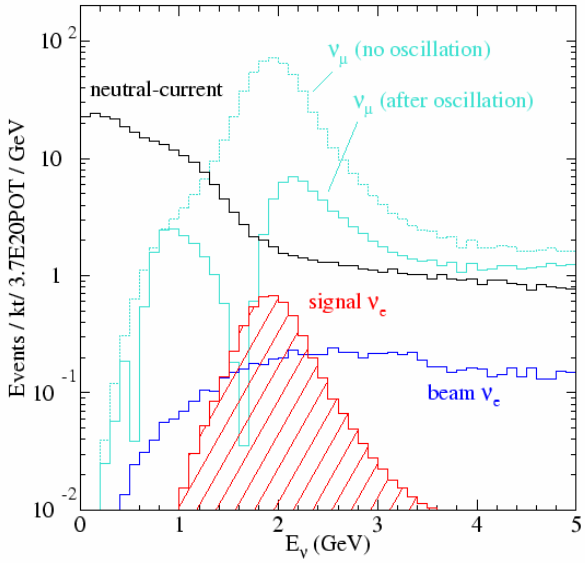

Fig. 2.8: Simulated energy distributions for the ν_e oscillation signal, intrinsic beam ν_e events, neutral-current events and ν_μ charged-current events with and without oscillations. The simulation used $\Delta m^2_{32} = 2.5 \times 10^{-3}$ eV^2, $\sin^2(2\theta_{23}) = 1.0$, and $\sin^2(2\theta_{13}) = 0.04$. An off-axis distance of 12 km at 810 km was assumed.

2.4 Siting Requirements

2.4.1 Transverse Siting

NOνA has multiple goals and these goals give different optima for the transverse (or off-axis) distance of the Far Detector. This is illustrated in Figure 2.9. The top half of Figure 2.9 shows the 3 standard deviation discovery limit of NOνA for $\nu_\mu \rightarrow \nu_e$ oscillations as a function of $\sin^2(2\theta_{13})$ and the off-axis distance. The bottom half of Figure 2.9 shows the 95% confidence level for NOνA to resolve the mass hierarchy as a function of $\sin^2(2\theta_{13})$ and the off-axis distance.

Since the unique feature of NOνA is the ability to measure the mass ordering, we optimize for a mass ordering measurement at a cost of having slightly smaller statistics for the signal reaction and set the requirement for transverse siting at 12 (+0, -0.5) km off-axis. This requirement is independent of the baseline since the relevant physics parameter is L/E, and E approximately scales inversely with the off-axis angle.

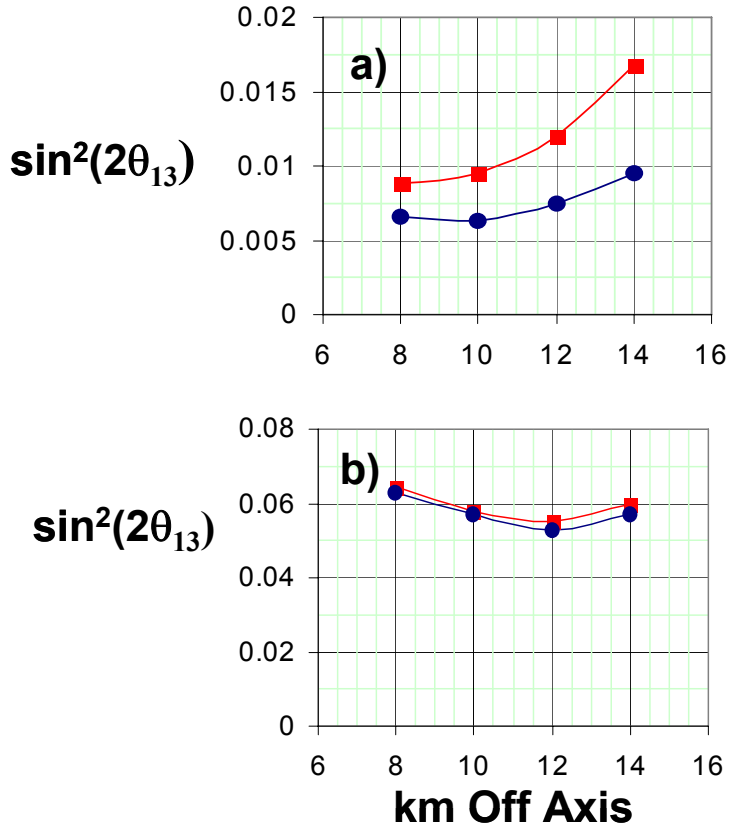

Fig. 2.9: a) Three standard deviation discovery limits for the observation of $\nu_\mu \rightarrow \nu_e$ oscillations versus the off-axis distance, and b) $\sin^2(2\theta_{13})$ versus the off-axis distance for the 95% confidence level resolution of the mass hierarchy. The upper red curve is for inverted mass hierarchy and the lower blue curve is for the normal mass hierarchy in both figures.

The curves in a) are for six years of neutrino running, while the curves in b) are for 3.6 years each of neutrino and antineutrino running. Both figures assume $\Delta m^2_{32} = 0.0025$ eV^2 and a 25 kiloton detector at 810 km. The curves in a) assume the typical CP phase δ, while the curves in b) are for δ such that 25% of δ values give a lower $\sin^2(2\theta_{13})$ limit and 75% give a higher limit since in this case the typical δ gives a limit above the existing experimental limit. See Chapter 13 in reference [11] for additional details.

2.4.2 Longitudinal Siting

Equation 2.4 indicates how the matter effect modifies the oscillation probability observed in the experiment. The differences between the normal mass hierarchy (blue curves) and inverted mass hierarchy (red curves) in Figures 2.2 and 2.3 depend on the size of the matter effect. This is displayed in a slightly different form in Figure 2.10. While Figure 2.2 shows the antineutrino oscillation probability versus $\sin^2(2\theta_{13})$ for a given value of the neutrino oscillation probability, Figure 2.10 shows these same three variables when $\sin^2(2\theta_{13})$ is fixed and plots the neutrino oscillation probability versus the antineutrino oscillation probability. Clearly any measurement of the mass hierarchy depends on the separation of the red and blue curves in Figure 2.10, and this is accomplished by inserting as much matter as possible in the path between the neutrino source and the NOνA detector.

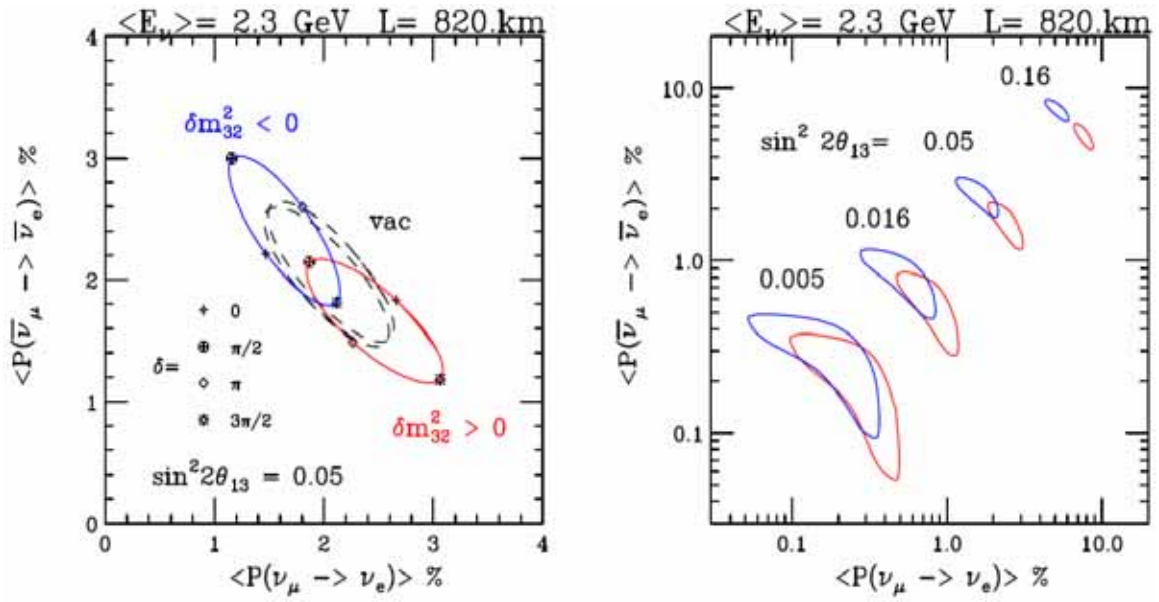

Fig. 2.10: The bi-probability plots $P\left(\nu_\mu \to \nu_e\right)$ versus $P\left(\bar{\nu}_\mu \to \bar{\nu}_e\right)$, assuming a constant matter density of $\rho = 2.8$ g. cm^{-3} at a distance of 820 km and an average energy of 2.3 GeV with a 20% Gaussian spread. The mixing parameters are fixed to be $\left|\Delta m^2_{31}\right| = 2.5 \times 10^{-3}$ eV^2, $\sin^2 2\theta_{23} = 1.0$, $\Delta m^2_{21} = +7 \times 10^{-5}$ eV^2, $\sin^2 2\theta_{12} = 0.8$ with the labeled values of $\sin^2 2\theta_{13}$ and δ. The left plot demonstrates how the matter effect modifies the two solutions relative to oscillations in vacuum for $\sin^2(2\theta_{13}) = 0.05$. The right plot shows how the overlap between the two mass orderings changes for four values of $\sin^2(2\theta_{13})$.

Since the sensitivity of the determination of the mass ordering depends on the distance the neutrinos travel through the earth, the NOνA Far Detector should be sited as far away from Fermilab as is practically possible. For a given detector mass, this longitudinal siting requirement is modified somewhat by the solid angle of the detector as seen from Fermilab and by the inherent divergence of the Off-axis beam. Modifications also occur because longer baselines with the same off-axis transverse distance have a higher energy neutrino beam and the interaction cross section for neutrinos is proportional to the beam energy. As an example, we have calculated the 95% confidence level for determining the mass ordering for detectors at 810 km and 775 km from Fermilab (sites at these distances are discussed in Chapter 4). In order to have the same sensitivity to the mass ordering, a detector at 775 km would have to have 40% more

mass than a detector at 810 km. It is difficult to make up for a shorter baseline with greater statistics.

2.5 Far Detector Requirements

The primary goal of the NOνA experiment is to measure $\nu_\mu \rightarrow \nu_e$ oscillations at the "atmospheric" oscillation length with a three standard deviation sensitivity to a $\sin^2(2\theta_{13})$ value of ~ 0.01. This goal is approximately an order of magnitude greater sensitivity than can be achieved by the existing MINOS experiment [12] now operating in the NuMI beamline. This goal is also approximately the same sensitivity expected in the T2K experiment in Japan [13] that would be running in the same time frame as NOνA. Relative to T2K, NOνA has the unique advantage of a long baseline and is thus complementary to T2K.

2.5.1 Figure of Merit

There are four multiplicative factors that determine the sensitivity of the NOνA experiment to ν_e appearance: The beam power (or number of protons delivered to the NuMI target), the mass of the NOνA detector, the detector's efficiency for identifying ν_e events, and the detector's ability to discriminate $\nu_\mu \rightarrow \nu_e$ oscillations from various backgrounds. The last two of these factors depend both on the detector design, such as its segmentation and light levels, and on the algorithms used to discriminate the signal from background.

The product of these factors can be expressed as a figure of merit (FoM), and its value is the basic scientific requirement for experimental sensitivity. The FoM is defined as the number of $\nu_\mu \rightarrow \nu_e$ signal events divided by the square root of the background for a six-year neutrino run with a 25 kt detector at 6.5 x 10^{20} protons on target per year for $\sin^2(2\theta_{13}) = 0.1$ and $\Delta m_{32}^2 = 0.0025$ eV^2, without regard to matter and atmospheric-solar interference effects.

To first order a FoM of 30 then corresponds to a three standard deviation sensitivity at the NOνA goal with $\sin^2(2\theta_{13}) = 0.01$. In reality the matter effects (mass hierarchy) and value of the CP violating phase δ would modify the sensitivity as shown in Figure 2.12. Figure 2.12 shows the range of results in a six year run with a 25 kiloton NOνA detector located 12 km off axis at a baseline distance of 810 km from Fermilab.

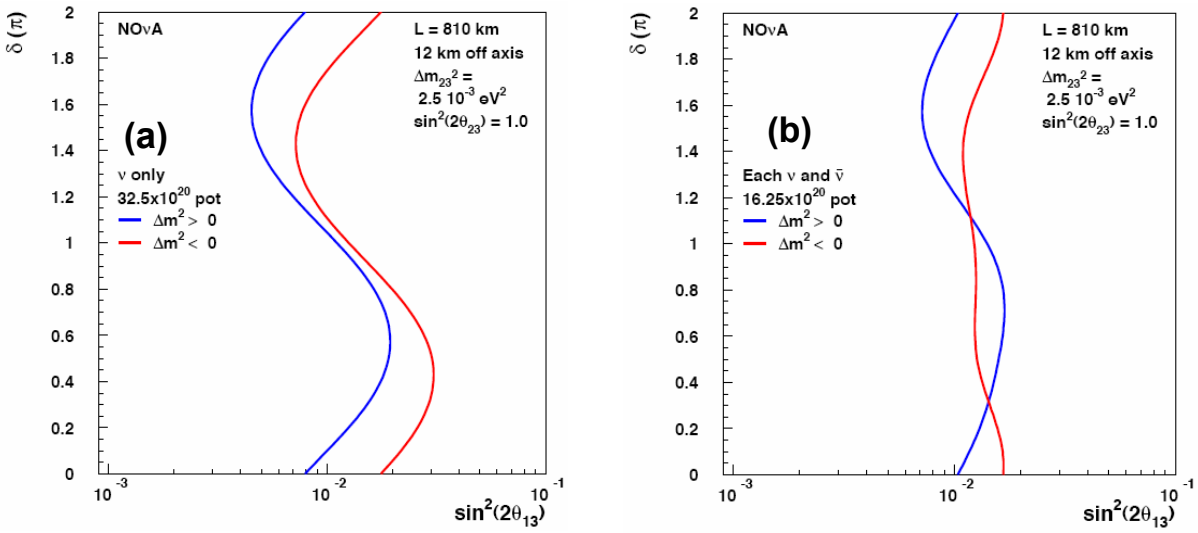

Fig 2.12: Three standard deviation sensitivity to $\theta_{13} \neq 0$ as a function of $\sin^2(2\theta_{13})$, δ, and the mass ordering for NOνA in a) a six-year neutrino run with a 25 kt detector, and b) a six year run evenly split between neutrino and antineutrino running. (The numbers of pot on the figures are incorrect, corresponding to a five year run with a 30 kt detector.)

2.5.2 Energy Resolution

As discussed in Section 2.3.2, one of the advantages of the off-axis siting is that the narrow-band beam can be used to eliminate backgrounds. The rms width of the off-axis beam is about 25%, as can be seen in Fig. 2.8. With the limited statistics expected for the $\nu_\mu \rightarrow \nu_e$ oscillation signal, dividing this narrow energy range further does not increase the sensitivity appreciably. Therefore, the main use of good energy resolution is to prevent a widening of the visible energy, which would increase the background. An energy resolution of one-third the beam width, or 8% is sufficient for this purpose.

Section 2.2.5 discussed the need for excellent energy resolution for quasielastic ν_μ charged current events for the precise measurement of $\sin^2(2\theta_{23})$. The required rms resolution is 4%.

2.6 Far Detector Hall Overburden Requirement

The physics requirement for the detector hall comes from the need to reduce cosmic ray backgrounds to a negligible level. The very low duty cycle of the NuMI beam aids greatly in cosmic ray rejection. We assume (see reference [11], Chapter 11) that the NuMI beam will run 1.2×10^7 cycles per year and that the spill will be 10 μs per cycle, yielding a live time of only 120 seconds per year.

To simulate a $\nu_\mu \rightarrow \nu_e$ signal event, a cosmic ray would need to appear to be a horizontal event from Fermilab within a 45^o cone, appear to have an electron-like track, and not leave any significant energy within 20 cm of the edges of the detector. Charged cosmic rays all fail the last requirement and thus are not a problem. Our simulation of the charged cosmic neutrino flux indicates that there would be less than one event simulating a signal event in a five-year run with no overburden over the detector.

Simulations of neutrons in cosmic rays also indicate NOνA should see only a fraction of an event from this source in a six-year run [11].

The major concern is the photon component of cosmic rays. These cosmic rays are strongly peaked towards the vertical as shown in Figure 2.13(a). Our acceptance for these events as ν_e interactions is limited to a 45^o cone around the horizontal in the direction of Fermilab, see Figure 2.13(b). The convolution of the two in our simulation of the photon flux with no overburden over the detector yields 2600 events in a six-year run with a 25 kt detector as shown in Figure 2.13(c).

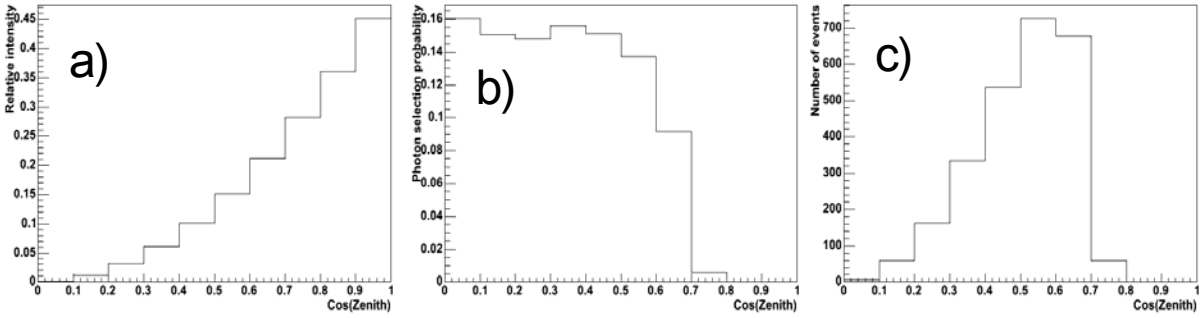

Fig 2.13: The photon component of cosmic rays. The incident cosmic rays are shown in (a) as a function of cos(Zenith). The NOνA selection probability for these events is shown in (b), and the convolution of production and selection yield the event distribution in (c).

We need 8 attenuation lengths of overburden to reduce these 2600 events to less than one event. The shower attenuation length of rock is about 125 g/cm^2. At an average density of 2.5 g/cm^3, this would correspond to approximately 4 m of overburden at normal incidence. Cosmic rays that simulate NOνA signal events do not enter the detector at normal incidence and instead

enter the detector at substantial angles at least $45^o - 75^o$ to one side of vertical as shown in Figure 2.13(c). Taking the slant height into account, the overburden requirement is reduced to 2 m.

2.7 Near Detector Requirements

The NuMI beam is not a pure ν_μ beam and has a small inherent admixture of ν_e which can simulate the $\nu_\mu \rightarrow \nu_e$ oscillation signal. In addition neutral current ν_μ events (events where there is no outgoing muon) can simulate the $\nu_\mu \rightarrow \nu_e$ oscillation signal. In order to measure these backgrounds to the oscillation signals, NOνA requires a Near Detector to measure neutrino interactions before they have had a chance to oscillate.

The primary Near Detector design requirement is that it should be as similar as possible to the Far Detector in material and segmentation. This requirement ensures that the efficiencies for signal and background events are identical to the NOνA Far Detector. Other requirements are that the fiducial volume be large enough to have well-defined boundaries and that the Near Detector be large enough to fully contain events from the fiducial volume. A transverse cross section of 4 m^2 is sufficient to meet the first requirement. Simulations have shown that a 70 cm wide border around the fiducial volume in the transverse dimensions and 4 m in the longitudinal dimension provides sufficient of containment of ν_e charged current events.

Placing the Near Detector on the Fermilab site in the range 1 – 2.5 km from the NuMI target will be adequate for the experiment. Ideally the Near Detector should be at the same off-axis angle as the Far Detector. At a 2.5 km site, this can be easily achieved since the Near Detector is far enough away to see approximately a point source of neutrino production from the NuMI decay pipe. At sites near 1.0 km a complication arises in that the detector sees a line source of neutrinos produced throughout the 675 m long NuMI decay pipe and therefore sees a range of off-axis angles. In addition, the beam ν_e backgrounds come primarily from muon decays which occur on average further downstream in the decay pipe and therefore effectively come from a higher off-axis angle. Meanwhile backgrounds from ν_μ neutral currents come from pion decays occurring on average closer to the NuMI target than the muon decays. As detailed in Chapter 10 of the NOνA proposal [11], this angular range problem can be overcome by moving the Near Detector through a range of positions ($\sim \pm$ 50m) at about 1 km to untangle the two background distributions. Such mobility imposes additional requirements on the Near Detector structure.

A Near Detector placed approximately 1 km from the NuMI target will be approximately 800 m from the typical pion decay. Since the neutrino flux falls roughly as the inverse of the distance squared, the flux per unit mass in the Near Detector will be approximately one million times higher than in the Far Detector. Thus, the fiducial volume of the Near Detector can be quite small. A twenty-ton fiducial volume in the Near Detector would produce about 800 times more events there than in the fiducial volume of the Far Detector. The requirement on the fiducial volume of the Near Detector is that the number of background events to the $\nu_\mu \rightarrow \nu_e$ oscillation signal be large enough to perform systematic studies over a period of about a year. A twenty-ton fiducial volume would produce approximately 1000 beam ν_e events in each of two detector locations (as discussed above) in one year, and this would be an adequate number for systematic studies.

A Near Detector at 2.5 km from the NuMI target has a slightly different mass requirement. Since the neutrino flux falls roughly as the inverse of the distance squared, the fiducial volume of the detector would need to be $(2.5)^2$ times as large or about 125 tons to get the same number of events as a 20 ton detector at 1 km. However, at 2.5 km the requirement of a mobile detector can be dropped and all the required background data can be acquired in one position. This means the fiducial volume at 2.5 km should be 62.5 tons.

Chapter 2 References

[1] The NuMI Technical Design Handbook, http://www-numi.fnal.gov/numwork/tdh/-tdh_index.html.

[2] SNO Collaboration, Q. R. Ahmad *et al.*, Phys. Rev. Lett. **87** (2001) 071301; S. N. Ahmed *et al.*

[3] K. Eguchi *et al.* [KamLAND Collaboration], Phys. Rev. Lett. **90**, 021802 (2003); T. Araki *et al*., hep-ex/0406035 (2004).

[4] S. Fukuda *et al.* [Super-Kamiokande Collaboration], Phys. Lett. B **539**, 179 (2002).

[5] M. H. Ahn et al. [K2K Collaboration], Phys. Lett. B **511**, 178 (2001), and Phys. Rev. Lett. **90**, 041801 (2003), and E. Aliu et al., hep-ex/0411038 (2004).

[6] CHOOZ collaboration, M. Apollonio *et al.*, Phys. Lett. B **466** 415.

[7] Kamiokande Collaboration, Y. Fukuda *et al.*, Phys. Lett. B **335** (1994) 237. Super-Kamiokande Collaboration, Y. Fukuda *et al.*, Phys. Rev. Lett. **81** (1998) 1562; S. Fukuda *et al.*, *ibid.* **85** (2000) 3999; Y. Ashie *et al., ibid*, **93** (2004) 101801; hep-ex/0501064 (2005).

[9] Y. Ashie *et al., Phys. Rev. Lett.* **93** (2004) 101801; E. Aliu *et al*., hep-ex/0411038 (2004); Y. Ashie *et al.,* hep-ex/0501064 (2005).

[10] M. Kostin *et al*., "Proposal for a continuously-variable beam energy," October 2001, Fermilab Report NuMI-783.

[11] The NOνA Collaboration, "Proposal to Build a 30 Kiloton Off-Axis Detector to Study $\nu_\mu \rightarrow \nu_e$ Oscillations in the NuMI Beamline," http://www-nova.fnal.gov/NOvA_Proposal/-Revised_NOvA_Proposal.html.

[12] "Proposal for a Five Year Run Plan for MINOS, May 2003, NuMI Note 530.

[13] T2K Letter of Intent, January, 2003. http://neutrino.kek.jp/jhfnu/.

3. Overview of the NOνA Design

3.1 Introduction

We describe here our recommended alternative design for NOνA. This overview describes the selected sites and selected detector technologies which satisfy the scientific requirements outlined in Chapter 2. A more detailed description of the sites and detector can be found in Chapters 7 through 16.

3.2 Far Detector Site: Ash River

We have chosen a location near Ash River, Minnesota as the NOνA Far Detector site. The site is on the Ash River Trail (St. Louis County Highway 129) near the entrance to Voyageur's National Park. The site is west of the NuMI beam centerline and about 810 km from Fermilab as shown in Figure 3.1. Ash River has the unique property of being the furthest site from Fermilab in the United States. It is about an hour drive from International Falls, about a 2 hour drive from Duluth, and about a 4 hour drive from Minneapolis. International Falls is presently served by a Northwest Airlines affiliate with four flights per day from Minneapolis.

Fig 3.1: Map of the central United States showing Fermilab, the NuMI beamline in red, and the selected NOνA site at Ash River, Minnesota.

The Ash River area is located about 40 km east south east of International Falls, Minnesota as shown in Figure 3.2. The selected site is about 11.8 kilometers west of the NuMI beamline. The NuMI beamline is itself about 4.2 kilometers above the surface at this point. The site is about 15 km east of U.S. Highway 53 along the Ash River Trail road (St. Louis County 129). Both U.S. 53 and County 129 are maintained year-round. County 129 does have 9-ton-per-axle load limits during spring thawing, March 15 until May 15.

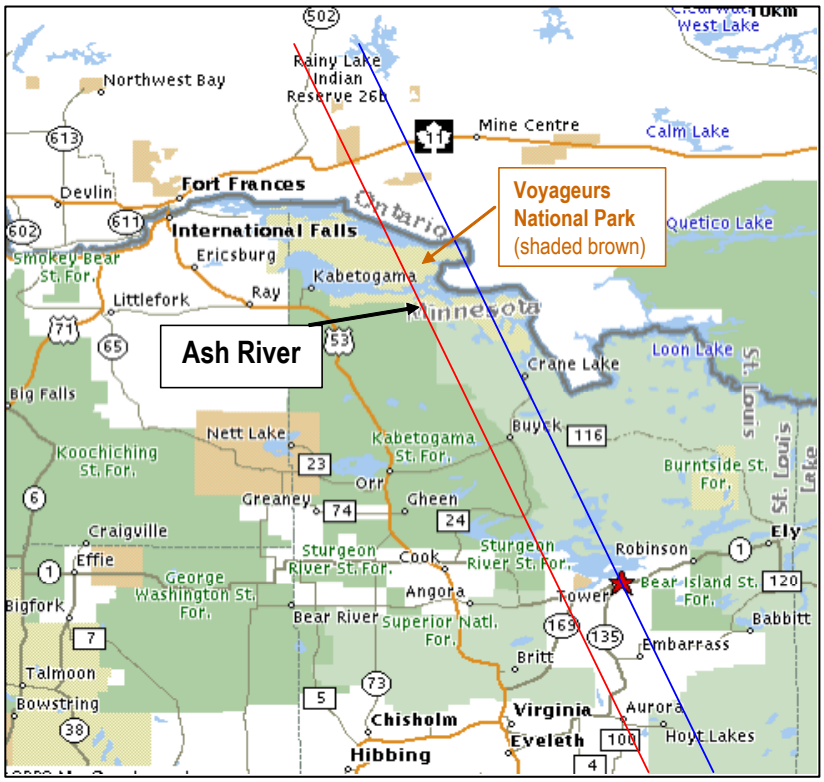

Fig. 3.2: Map showing our selected Far Detector site at Ash River. The NuMI beam centerline (blue) passes through the MINOS detector underground at Soudan (red star). The NOvA Ash River site is on the red line to the left (west) of the NuMI beam centerline, ~11.8 km (~ 15 mrad) off-axis. Voyageurs National Park and the US-Canada border are just north of the site.

The actual detector laboratory location at Ash River is in Section 18 of Township 68 North, Range 19 West, St. Louis County MN. This location is described in Table 3.1 and shown in Fig. 3.3 on a 1:24000 USGS topographic map. The site is located at an altitude of 1240 feet above sea level and is about 90 feet above the Ash River located to the south. Core borings at the site have determined [1] that the site has 5 – 15 feet of soil overburden and then is solid hard granite to a depth of at least 60 feet. Access to the site is currently via a 3.6 mile section of logging trail off St. Louis County 129.

Description	Latitude (NW corner)	Longitude (NW corner)	Distance from Fermilab (km)	Transverse distance from the NuMI beamline (km)	Altitude (ft)	Angle to the NuMI beamline (mr)
T68N, R19W, Section 18	48.37892°	-92.83272°	810.5	11.77	1240	14.52

Table 3.1: Parameters of the Ash River site. The angle in the table is the full space angle relative to the NuMI beam.

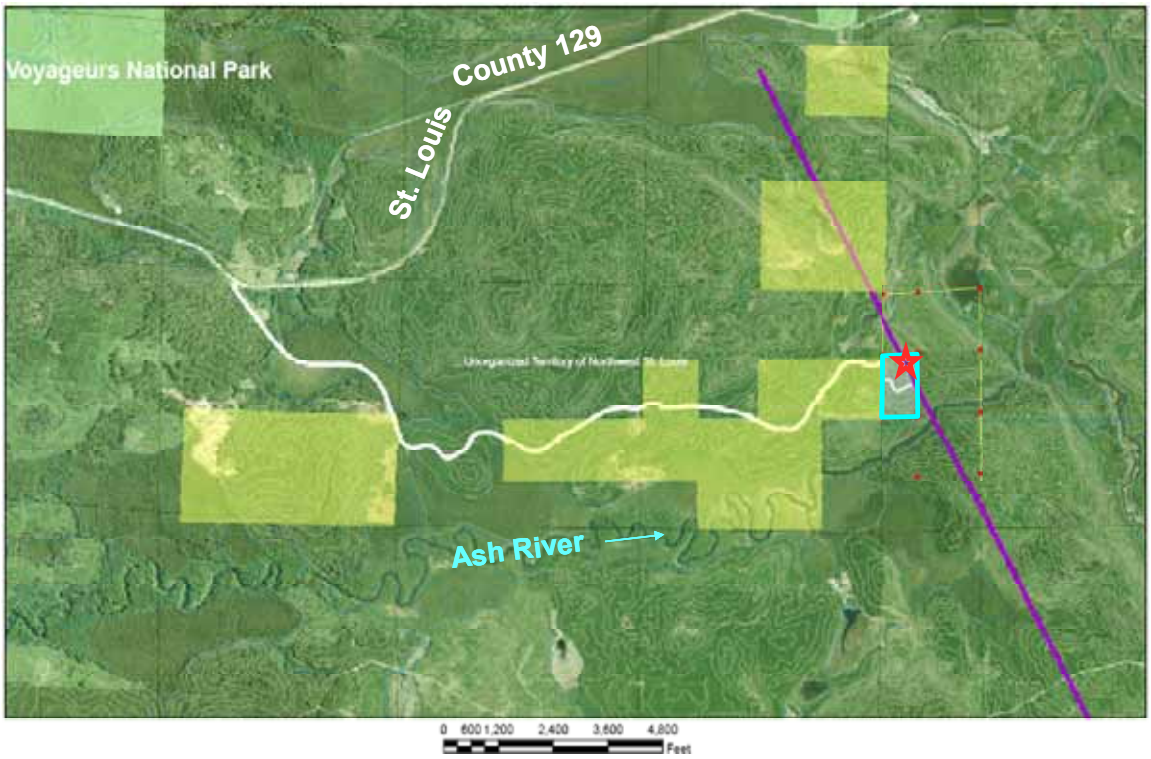

Fig. 3.3: Topographic map of the Ash River Trail site. The rectangle outlined in light blue is the selected site. Access to the site from the Ash River Trail road (St. Louis County 129) is along the white line. The yellow shaded land near the NOνA site belongs to Forest Capital Partners. The entrance road to the Ash River Visitor's Center in Voyageurs National Park is shown shaded in light green at the top right center of the map. The purple line is parallel to the NuMI beamline but 11.77 km off-axis.

The site is a 23.5 acre plot currently owned by the State of Minnesota and managed by the Minnesota Department of Natural Resources. Access to the site is currently via an old clay base logging road which crosses some land owned by Forest Capital Partners (formerly Boise Cascade). We have met at the site [2] with stakeholder representatives from the Minnesota Department of Natural Resources, Forest Capital Partners, and Voyageurs National Park to discuss locating the NOνA Detector in this area. The site is located about 1.5 miles south of an entrance to Voyageur's National Park but is not visible from the park due to intervening hills and trees. Public presentations of the NOνA planning process have been presented at various places in Minnesota during the last two years and the reception to the project has been positive [3]. Chapter 21 discusses this outreach effort in more detail.

The Acquisition Strategy [4] planned by the Department of Energy includes a solicitation of bids for a Cooperative Agreement. A selected bidder would be expected to acquire the site and access rights to the site and build the Far Detector Hall in a "design-build" approach. The selected bidder must also have a plan identifying an institution to be the "Responsible Government Unit" within the State of Minnesota with regard to environmental actions. These environmental issues are discussed in Chapter 17 as part of our NEPA documentation strategy. We expect at least one bidder for the Cooperative Agreement.

The access road passes through a wetlands area just as it leaves County 129 and we have met [5] with the Army Corps of Engineers to determine the permitting procedure required to upgrade this road to handle the NOνA construction traffic. A more detailed discussion of these ES&H concerns is presented in Chapters 7 and 17.

The conceptual design of the NOνA Far Detector Hall at Ash River is shown in cross section in Figure 3.4. The building is sunk into the granite about 40 feet and has supporting columns for trusses to hold a 3 meter overburden of excavation spoils above the detector as a cosmic ray shield. The density of the granite at Ash River is ~ 2.8 g/cc, so 3m of this material allows a 40% fraction of voids in the overburden relative to the scientific requirement (2 m of 2.5 g/cc material). Void fractions of 30-40% are typical for angular blasted rock which is not compacted. Details of this conventional construction are found in Chapter 8.

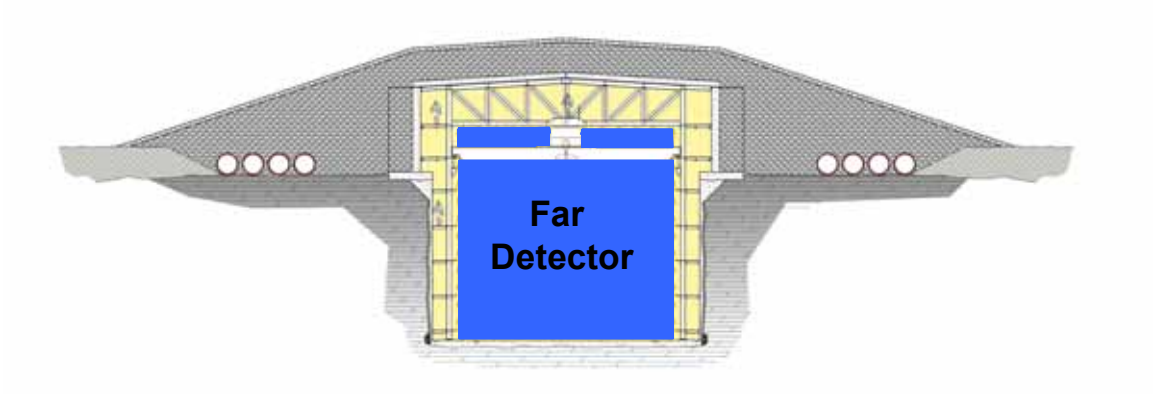

Fig 3.4: Neutrino beam view of the NOνA Far Detector Hall. The detector face is shaded blue. It is surrounded by access catwalks and open truss work in lighter yellow. The soil (light gray) has been removed at the detector site for excavation into the granite (block gray). The spoils from the excavation are loaded back on top of the detector to a minimum depth of 3m.

3.3 Near Detector Site: Fermilab NuMI Access Tunnel

We have chosen the existing NuMI Access tunnel at Fermilab as the NOνA Near Detector site. This site exists and therefore has the clear advantage of requiring no new civil construction. Figure 3.5 shows the NuMI Access tunnel in elevation and plan view with the NOνA Near Detector site indicated in red stripes just upstream and downstream of the vertical shaft from the MINOS Surface Building. The distance from the Target Hall to the MINOS shaft is about 960 meters and the NOνA Near Detector site (the red striped area in Figure 3.5) is about 75 meters long. The entire shaded area is on a level grade.

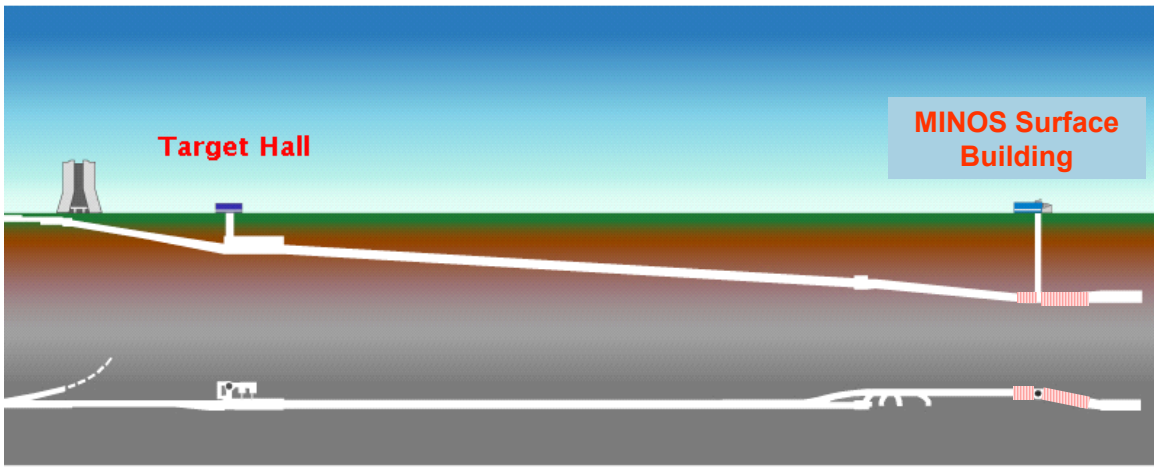

Fig. 3.5: Plan (bottom) and elevation (top) views of the NuMI beam line at Fermilab. The location(s) for the NOνA Near Detector would be in the red striped sections 340 feet beneath the MINOS Surface Building at the bottom of the access shaft to the NuMI tunnel.

Moving the Near Detector within the shaded area of Figure 3.5 allows a sampling of off-axis angles between 4 and 21 milliradians (mrad), bracketing the 15 mrad off-axis angle to the NOνA Far Detector site. The NOνA proposal [6] outlines how the Near Detector would be used in various positions in this access tunnel, including the possibility that a discovery by the MiniBooNE experiment may require use of the tunnel for another 150 meters upstream of the red shaded area. That upstream section is on a 10.85% grade. The underground access tunnel cross section is shown in Figure 3.6. The vertical MINOS access shaft to the surface is shown in Figure 3.7. The tunnel cross section, the vertical access shaft, and the sloped section of floor all serve to constrain the size of the NOνA Near Detector and its assembly. This is discussed in Section 3.4 and in Chapter 14.

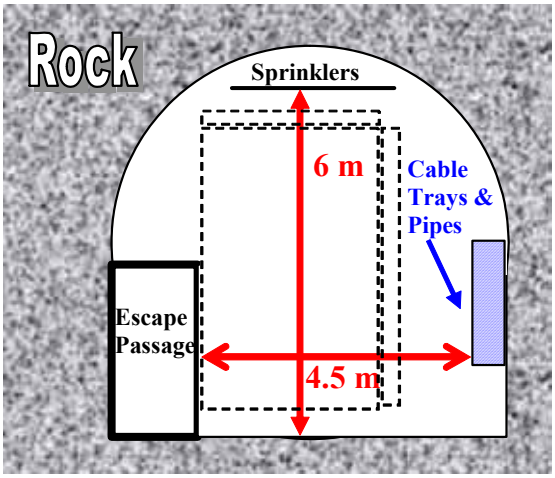

Fig. 3.6: A cross-section view of the NuMI access tunnel near the vertical MINOS shaft. The dotted outline shows the NOνA Near Detector cross section with the fiber manifolds sticking out the top and right side of the device.

Fig. 3.7: View from the bottom of the vertical D-shaped MINOS shaft as a MINOS near detector plane comes down the shaft. The MINOS module shown is ~4.5 m wide by ~3.5 m high by ~0.2 m thick (including the red strong-back frame).

3.4 Description of the NOνA Detector

3.4.1 The Basic NOνA Detector Element

The basic unit of the NOνA Detector is a simple rectangular rigid PVC plastic cell containing liquid scintillator and a wavelength-shifting fiber. This is illustrated in Figure 3.8. Charged particles traverse the cell primarily along its depth (D) and scintillator light is produced in the liquid. The light bounces around in the rectangular cell of width W, depth D, and length L until it is captured by a wavelength-shifting fiber. The fiber is twice the length L of the cell and is looped at the bottom so the captured light is routed in two directions to the end (top in the illustration) of the cell. Effectively there are two fibers in the cell, each with a nearly perfect mirror at the bottom so that nearly four times the light of a single non-reflecting fiber is captured. At the top of the cell both ends of the looped fiber are directed to one pixel on an Avalanche Photodiode photodetector and the light is converted to an electronic signal.

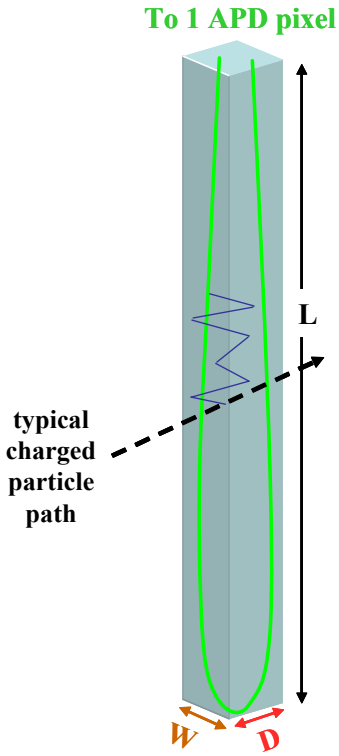

Figure 3.8: A PVC cell of dimensions (W, D, L) containing liquid scintillator and a wavelength-shifting fiber (green). A charged particle incident on the front face produces light (blue line) that bounces off the cell walls until absorbed by the fiber. The fiber routes the light to an APD.

The selected alternate for NOνA has a highly reflective titanium dioxide loaded rigid PVC cell with walls 2 to 4.5 mm thick. The cells have an interior width 3.87 cm transverse to the beam direction, an interior depth of 6.0 cm along the beam direction, and an interior length of 15.7 meters. The cell width and depth satisfy the scientific requirements and the cell length is sized to fit on a standard domestic 53-foot semi trailer truck. To achieve the 30 kiloton mass stipulated by the scientific requirements, we repeat the cell structure 643,000 times.

The cells are assembled in alternating layers of vertical and horizontal extrusions as shown in Figure 3.9. This layering organizes the detector into planes with 90^{o} stereo for tracking of particles produced in neutrino interactions originating in the PVC and scintillator mass. The

assembled set of cells acts as fully active or total absorption calorimeter since 80% of the mass is active liquid scintillator. Pulse height information is obtained from each cell and the total charged particle energy of a neutrino event is formed from the sum of the pulse heights. The cell structure makes the detector a tracking device as shown for a sample Monte Carlo generated event in Figure 3.10. This combination of calorimetry and tracking makes the NOνA detector capable of distinguishing signal neutrino events and of rejecting backgrounds to that signal as stipulated in the scientific performance requirements.

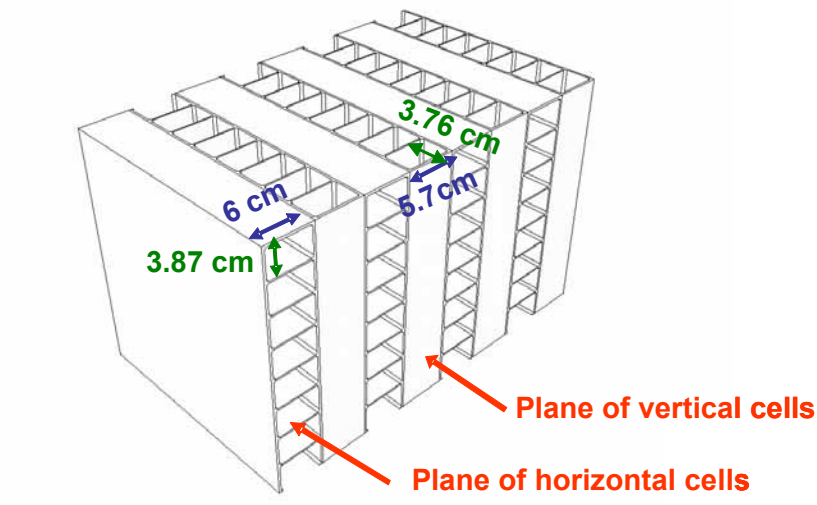

Fig 3.9: Close-up of the NOνA structure.

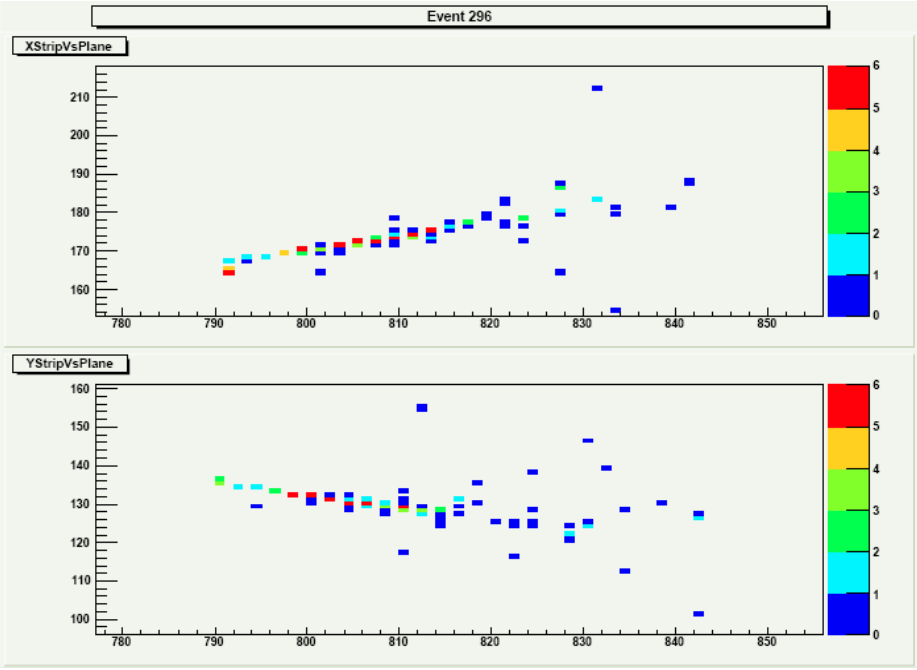

Fig 3.10: Example of a 2 GeV electron neutrino charged current Monte Carlo event in the NOνA detector. Both stereo views are shown. The event vertex is on the left hand side of the display and an electron shower develops to the right of the vertex. The colored boxes indicate pulse height in the individual cells.

3.4.2 Liquid Scintillator

Seventy-three percent (~18.5 kilotons) of the NOνA detector mass is the liquid scintillator held inside the NOνA cells. The 5.7 million gallons of liquid scintillator is composed primarily of mineral oil with a five percent pseudocumene [1,2,4-Trimethybenzene] as the scintillant. The pseudocumene produces light with a spectrum peaked at 360 - 390 nanometers (nm). The liquid also contains chemical additives to shift the scintillated light to 400 - 450 nm matched to the wavelength-shifting fiber absorption spectrum. Typical additives are PPO [2,5-diphenyloxazole], POPOP [1,4-bis(5-phenyloxazol-2-yl)benzene], and bis-MSB [1,4-di(methylstyryl)benzene]. Previous investigations [8] have shown that this scintillator does not attack the PVC containment structure or the wavelength-shifting fiber suspended in the liquid. Details of the NOνA liquid scintillator are discussed in Chapter 9.

Liquid scintillator mixtures like these are well known to have a ~ 20% decreased light output when exposed to oxygen, so the NOνA design requires only the lower oxygenated light level . Oxygen diffusion over time through our PVC walls is sufficient to produce the decreased light output effect. Since the scintillator light in a NOνA cell is captured locally by a wavelength-shifting fiber within about one meter path in the liquid, the attenuation length of the scintillator in NOνA is less of a performance driver than in previous experiments [8] where the light had to travel many meters through the liquid to the photodetector. Reference [8] also serves to point out that this technology has been used in many high energy experiments over a long time period and is therefore well understood.

3.4.3 Wavelength-shifting Fiber

The NOνA detector contains about 21,600 kilometers of wavelength –shifting fiber, with about 33.5 meters forming the loop inside each of the cells. The fiber captures the blue 400 – 450 nm light from the scintillator and wavelength shifts to green light in the range 490 - 550 nm. The fiber is 0.8 mm in diameter with a core of polystyrene mixed with about 200 parts per million R27 dye as the wave-shifter.

The fiber is double clad with material of a lower refractive index than the core to facilitate total internal reflection of the shifted light along the fiber to the APD. The first cladding is a thin acrylic layer (PMMA or polymethylmethacrylate) with a thickness of a few % of the fiber diameter, and the second cladding (~ 1% of the fiber diameter) of is a fluor-acrylic. A similar fiber (but diameter of 1.2mm) was used in the MINOS detector [9], so this is a well understood technology.

As the internally reflected light travels down the 15.7 meter long fiber, it is attenuated by about a factor of ten with red light (520 – 550 nm) preferentially surviving. This property puts a premium on use of a photodetector with good quantum efficiency in the red and the APD is such a device. Chapter 10 contains more details on the fiber.

3.4.4 Rigid PVC Extrusions

The mass of the rigid PVC extrusions is ~ 6.9 kilotons or about 27% of the mass of NOνA. Assembling 643,000 objects is achieved by using larger rigid PVC extrusions with 32 cells extruded together in a unit 1.3 meters wide. An example of this structure for 16 cells is shown in Figure 3.11. Two different extrusions are required. The horizontal cells have exterior PVC walls 3 mm thick and 2 mm thick interior webs between cells. The vertical cells contain more PVC with 4.5 mm thick exterior walls and 3 mm thick interior webs. About 20,000 of the 32-cell extrusions are needed for the full detector.

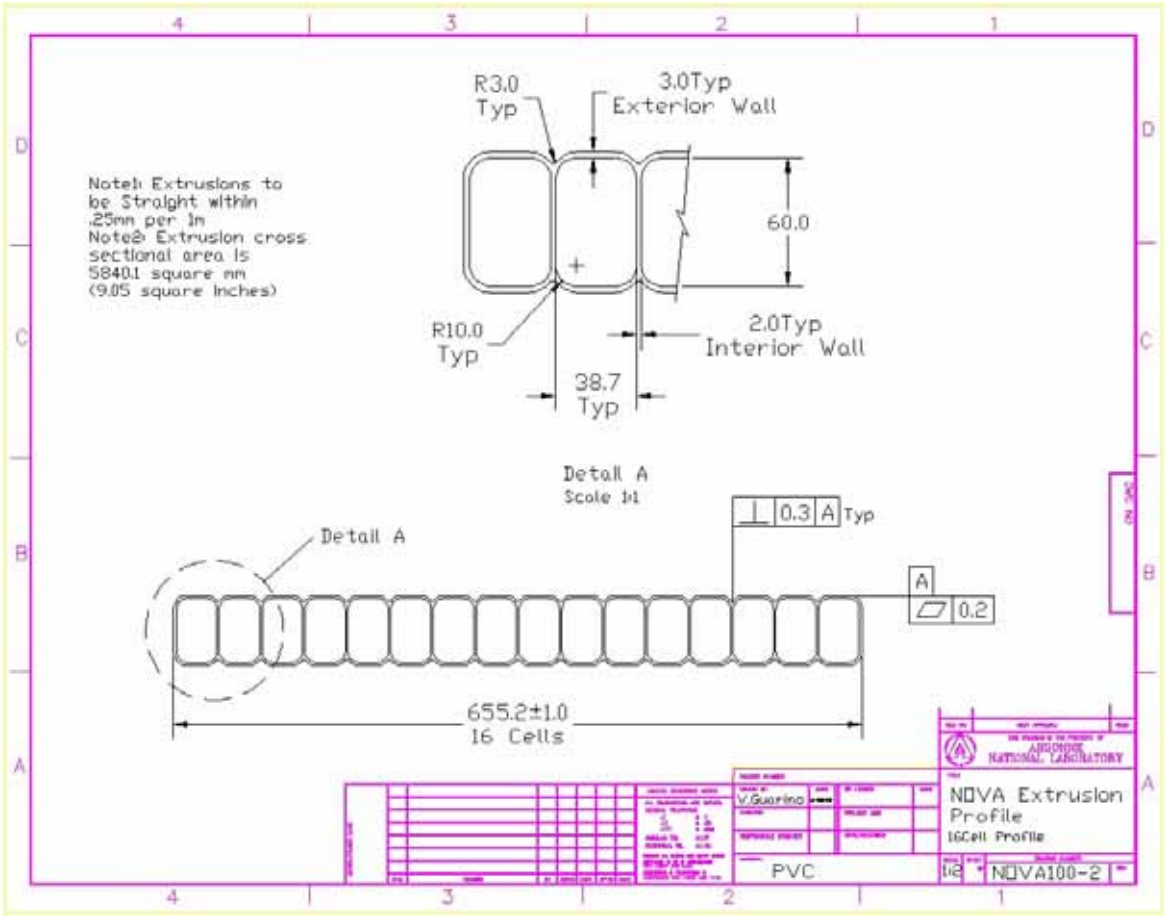

Fig. 3.11: Drawing of a 16 cell version of the NOvA rigid PVC extrusion

The material properties of rigid PVC strongly influence the NOvA design. Unlike metals, plastics under stress can creep and perhaps creep to failure. The NOvA vertical cells build up an interior hydrostatic pressure of 19.2 psi at the bottom of the 15.7 meter column of scintillator (only 1.6 psi is seen at the "bottom" of a horizontal extrusion which is only 1.3 meters "tall"), so creep is a relevant concern. The rounded corner design shown in Figure 3.11 is selected to minimize the maximum stress seen in the plastic and in fact keeps that stress force below 750 psi everywhere in the cell. At these values the plastic does behave linearly and effects of creep are minimized (see Chapter 11).

The other crucial property of the PVC is its reflectivity for scintillator light of 400 – 450 nm. The light typically bounces off the PVC walls about 10 times before being captured by the fiber, so the surviving light at that point is proportional to (reflectivity)^{10}. A 1% change in reflectivity translates into a 10% change in the amount of light seen by the fiber. Our baseline rigid PVC sample has demonstrated a reflectivity of 93% using a PVC mixture loaded with 15% titanium dioxide to boost the reflectivity in the blue region. Additional details of NOvA PVC properties and NOvA extrusions are covered in Chapter 11.

3.4.5 Extrusion Modules

The extrusions are capped at one end by a simple PVC closure plate to contain the liquid scintillator and are capped at the other end by a more complicated fiber manifold which contains the liquid (in horizontal modules) and routes the 64 fiber ends to 32 APD pixels, as shown in Figure 3.12.

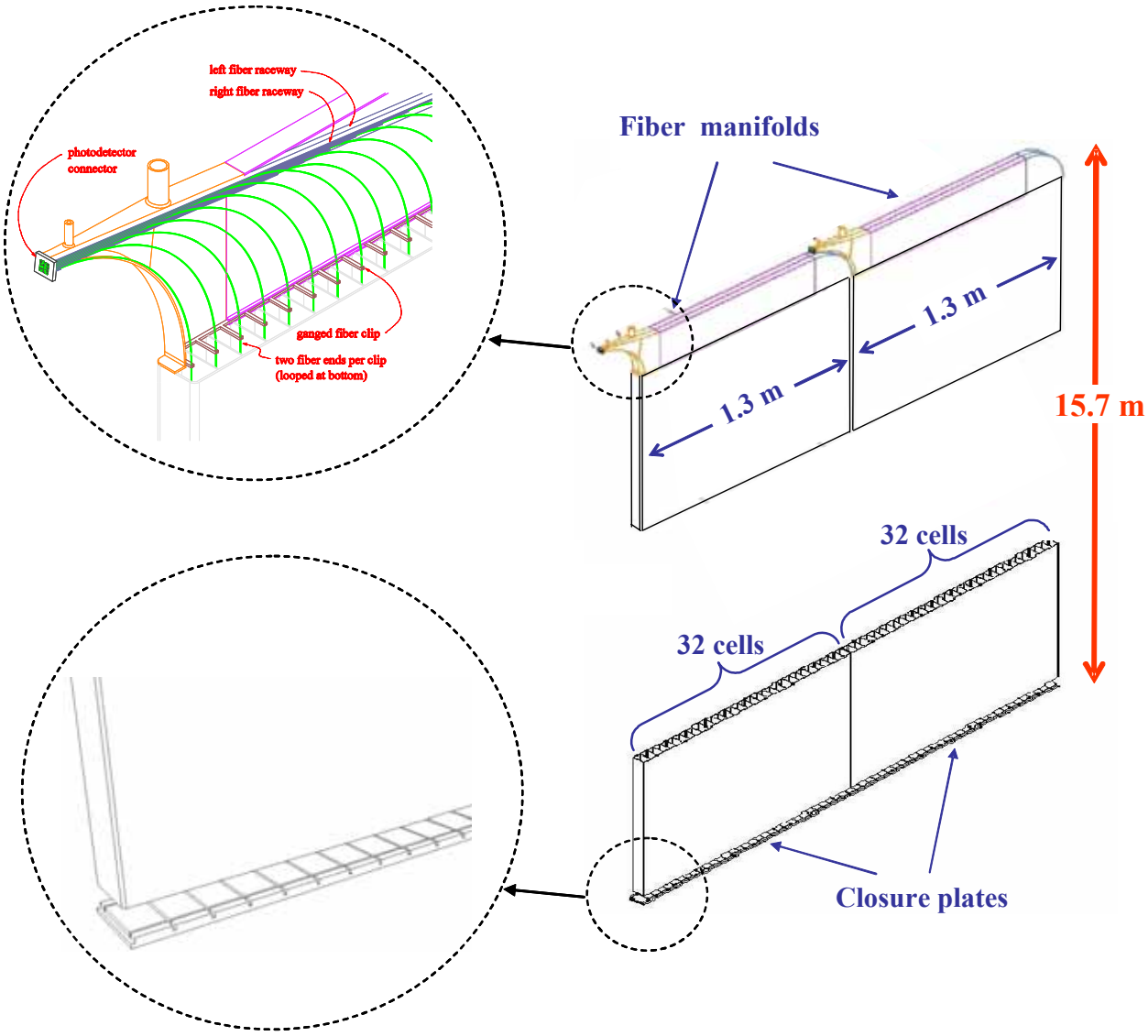

Fig. 3.12: Two vertical 32 cell extrusion modules side by side. The inset figures on the left show details of the fiber manifold and the closure plate.

The assembled modules with fiber manifolds and end caps are sized to fit inside a standard domestic 53-foot semi trailer truck. As part of the assembly procedure, the 64 fiber ends are constrained into a block to match the APD pixel array, potted in epoxy, and faced off with a fly cutter. In addition the closure end of the extrusion has small holes punched in the interior webs so that the entire extrusion forms a single volume for the scintillator. Thus the 1.3 meter by 15.7

meter extrusion module forms the primary containment for the liquid scintillator. Each vertical extrusion module holds about 275 gallons of scintillator and each horizontal module holds about 295 gallons. Chapter 12 contains more details on the extrusion module assembly.

3.4.6 Photodetector and Electronics

The NOνA photodetector is an Avalanche Photodiode (APD) manufactured by Hamamatsu and similar to the ones developed for use in the Compact Muon Solenoid (CMS) detector at the CERN Large Hadron Collider [10]. The APD has an 85% quantum efficiency for the 520 – 550 nm light exiting the fiber. We operate the APDs at a gain of 100 using an applied voltage of about 375 volts. The thermal noise generated in the APD is reduced by cooling the devices to -15^{o}C using thermo-electric (TE or Peltier-effect) coolers.

The signals from the APD are amplified by a special low noise pre-amp based on the Fermilab MASDA chip [11] and that pre-amp is combined in a new custom ASIC with 8:1 multiplexers, each running at 16 MHz. The signals are digitized by quad 40 MHz ADCs using the AD41240 from CMS.

There are ~20,000 APDs and front-end electronics boards in NOνA, one per extrusion module. Additional details on the APD and front-end electronics are in Chapter 13.

3.4.7 Data Acquisition System

The Data Acquisition (DAQ) for NOνA is based on a standard Gigabit Ethernet network and commercial processor. The 20,000 front-end boards are connected in groups of 64 to a custom Data Combiner board which then interfaces to the Ethernet network. The Ethernet network passes the data to a processing farm consisting of about 256 commercial PCs. Chapter 14 contains details of the DAQ.

3.4.8 Assembly and Structure of the Far Detector.

Twelve of the extrusion modules get placed side by side on a flat table to form one plane of the NOνA detector. Thirty-one such planes are glued together into a block to form the strong honeycomb-like structure already shown in Figure 3.9. Vertical planes of extrusion modules all have their readout fiber manifolds at the top of the detector. Horizontal planes of extrusions alternate the readout position, with one plane having all readouts on the left side of the detector and the next horizontal plane having its readouts on the right side of the detector. This alternating readout of the horizontal layers gives an additional handle on the horizontal position of a neutrino event and aids in the pattern recognition.

Each block is 15.7 meters wide by 15.7 meters high by 2.05 meters thick. The PVC in a 31 plane block has a mass of about 127 metric tons. When filled with scintillator, the mass of a 31-plane block is about 469 metric tons. Handling this size block is a challenge, so we plan to assemble the empty 31-plane blocks in a horizontal position and then stand each empty block up using a custom block raiser machine illustrated in Figure 3.13 below. Sixty-four of the 31-plane blocks get attached to one another to form the full NOνA Far Detector shown in Figure 3.14.

Filling the blocks with liquid scintillator is a separate assembly operation and takes place after the blocks are attached to the full detector. To avoid a long schedule for completion of the detector, we fill the structure with scintillator almost in parallel with the PVC plane erection, following the empty PVC module assembly front by about one month in a total 20 month schedule. The required scintillator fill rate of about 20 gallons per minute is accomplished with a custom metering machine which fills many extrusion modules in parallel, thus avoiding any build-up of bubbles or foam in the extrusion modules which would require a topping-off procedure later.

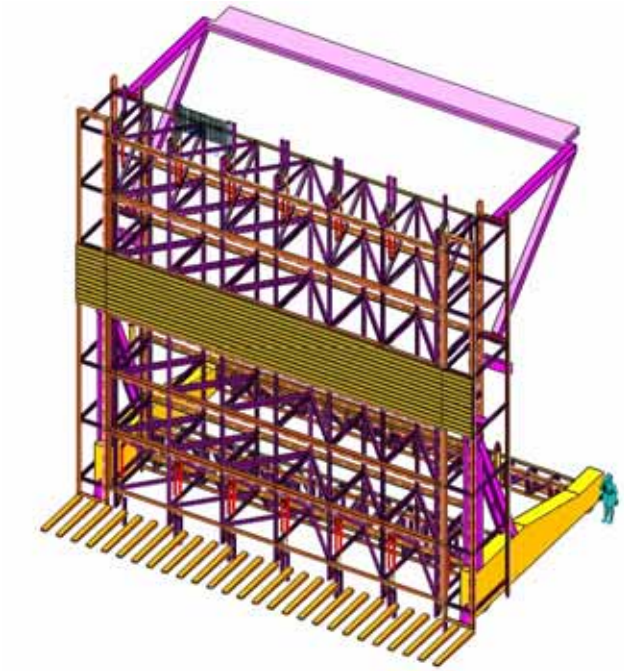

Fig. 3.13: The custom NOνA block raiser is shown. This object is like a giant fork-lift with 24 tines and is used to tilt a 31-plane block into the vertical position. Note the person on the lower right side for scale.

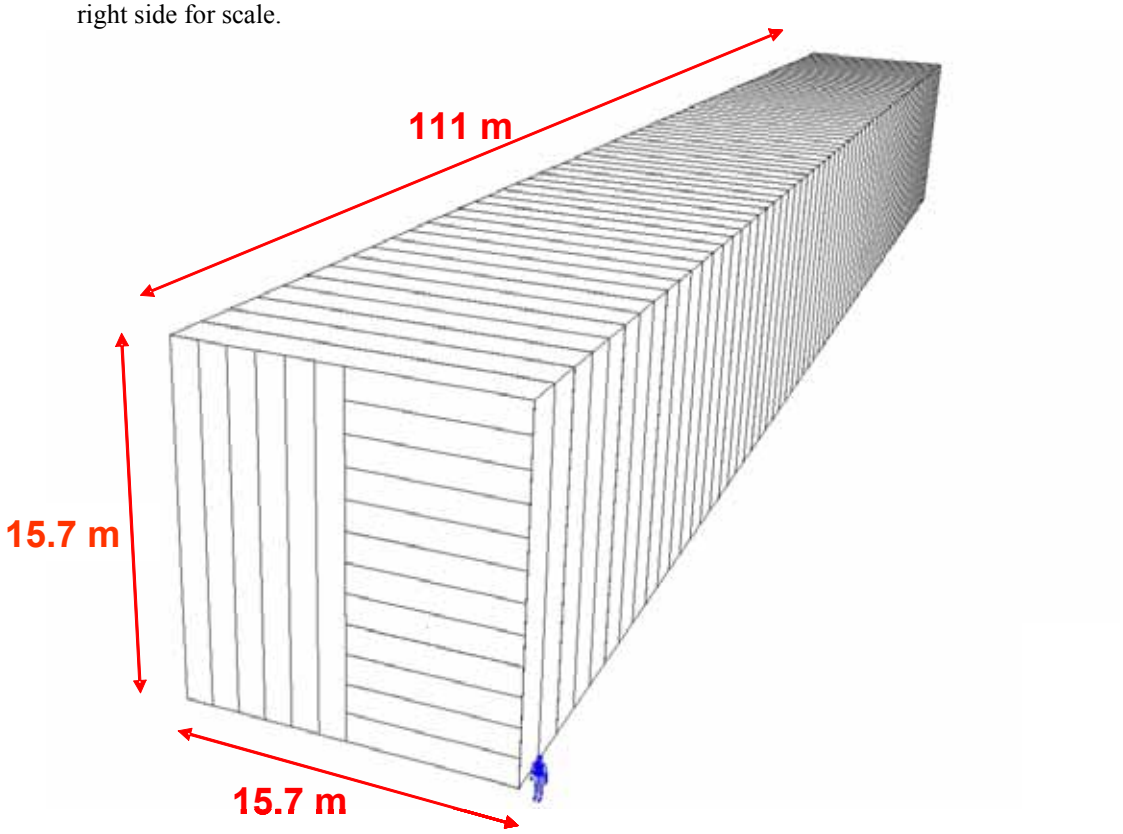

Figure 3.14: Overview of the NOνA Far Detector Structure showing fifty-four 31-plane blocks (1674 planes, each with 12 extrusion modules) organized into alternating layers of vertical and horizontal planes. Note the person in the lower right corner for scale.

The large NOνA PVC structure is unique and we have spent considerable time understanding the properties of rigid PVC and the properties of our structure. Many of these details are presented in Chapter 15. One unique structural property noted in this overview is the swelling of the plastic structure as the 342 metric tons of scintillator are added to the empty PVC planes. Our finite element analysis shows that a displacement of the plastic builds up by several mils per plane due to the hydrostatic pressure in the long modules (see Figure 3.15). The bottom of the detector is pinned to the floor of the building by friction, so a stress builds up in the detector during filling with scintillator. Our finite element analysis has determined that after about 80 planes, the stress in the PVC will build up beyond our self-imposed limit of 1000 psi maximum design stress. This requires the NOνA structure to have periodic expansion gaps to relieve this stress build up much like a concrete sidewalk has expansion gaps to accommodate the properties of concrete. We plan to have such an expansion gap every 31 planes so that every horizontal plane is trapped on both sides by a vertical plane.

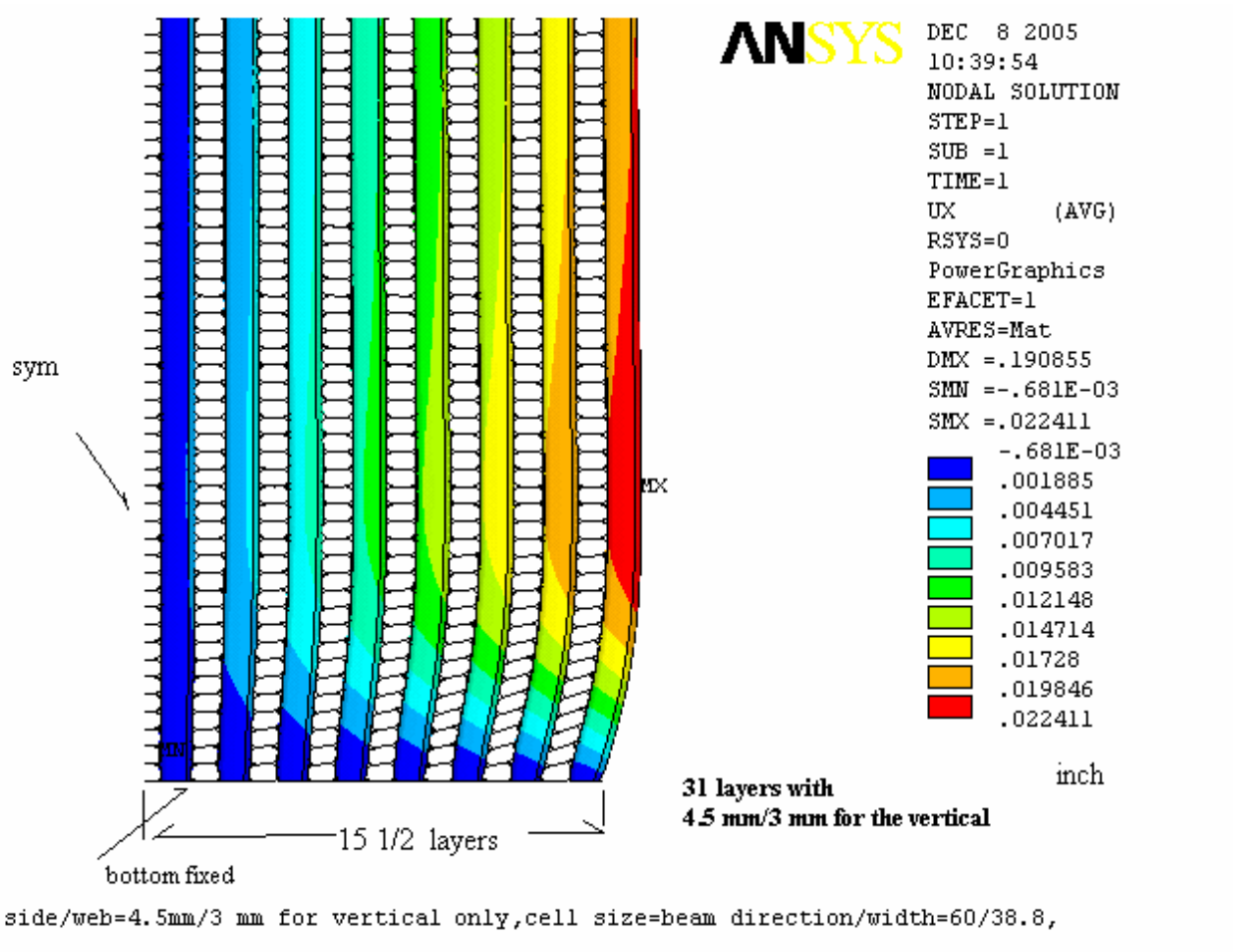

Fig. 3.15: The displacement along the beam direction after 31 planes are filled. Only the bottom 3 meters out of the 15.7 meter height is shown, and that the deformation is highly exaggerated. Fifteen and a half planes are shown since the analysis assumes a symmetry plane in the center of the 31-plane block. The deformation is largest at the bottom of the detector about 1 m off the floor (red area). The stress (not shown) is concentrated at the bottom of the detector about 10 cm off the floor.

A summary of the Far Detector parameters is given in Table 3.2 and more details of the structure and assembly are in Chapter 16.

Total mass	25,398 metric tons (includes epoxy and fiber)
Mass of rigid PVC extrusions	6,854 metric tons
Mass of liquid scintillator	18,463 metric tons
Liquid scintillator	Mineral oil base with 5% pseudocumene as the scintillant, PPO and bis-MSB waveshifters added.
Active mass fraction	73%
Active height × width	15.7 m × 15.7 m
Active length	111 m
Number of layers	1674 (864 vertical, 810 horizontal) 54 blocks of 31 planes each
Radiation length per layer	~ 0.15
Mass of epoxy between layers	~ 67 tons
Extrusions per layer	12
Extrusion outer wall thickness	3 mm in horizontal cells, 4.5 mm in vertical cells
Extrusion inner web thickness	2 mm in horizontal cells, 3 mm in vertical cells
Extrusion width	1.3 m
Extrusion length	15.7 m
Maximum pressure in vertical cells	19.2 psi
Cells per extrusion	32
Cell interior width × depth, horizontal cells vertical cells	 3.87 cm × 6.00 cm 3.76 cm x 5.70 cm
Total number of cells	642,816
Total number of extrusions	20,088
Wavelength-shifting fiber	0.8 mm diameter double clad fiber with K27 waveshifting dye
Total WLS fiber length	21,624 km
Total WLS fiber mass	13.8 tons
Photodetector	Avalanche Photodiode

Table 3.2: Summary of Far Detector parameters.

3.4.9 Assembly and Structure of the Near Detector

The Near Detector is an identical copy of the Far Detector except that the extrusion modules are shorter to accommodate the restrictions of the NuMI underground tunnel and MINOS access shaft described in Section 3.3. A diagram of the Near Detector is shown in Figure 3.16. The detector consists of planes that are 64 cells wide (2 extrusion modules) and 96 cells high (3 extrusion modules), arranged in alternating horizontal and vertical layers and in segments of 7 or 8 planes. An additional set of ten planes of 10 cm steel interspersed with 10 planes of extrusion modules serves to tag muons from ν_μ charged current events.

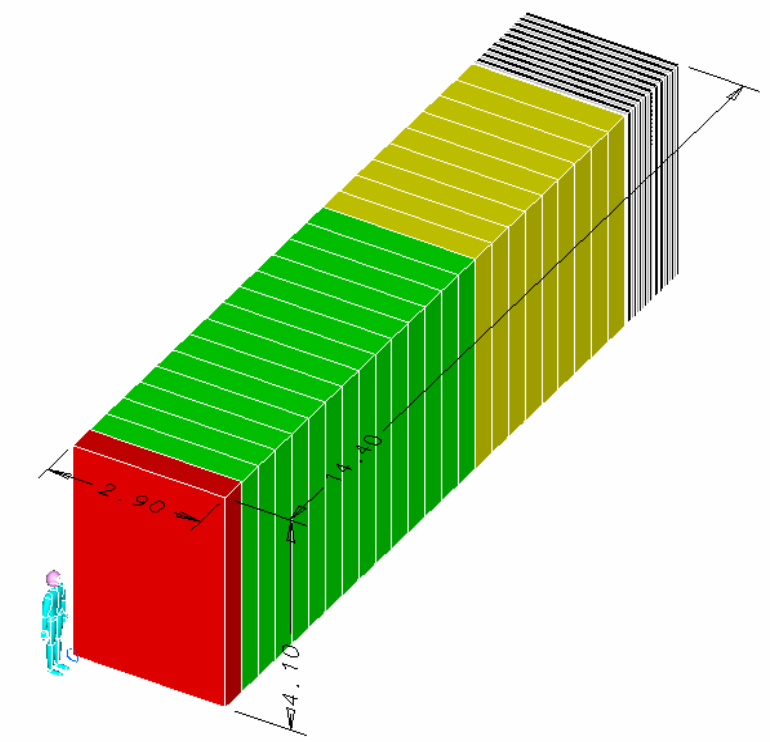

Fig. 3.16: The NOνA Near Detector. The beam comes from the lower left in this diagram. Each modular piece consists of 8 or 7 planes of extrusions, 4 vertical interleaved with 4 horizontal planes. Every 4th segment has on less horizontal plane so as to duplicate the Far Detector 31-plane configuration. The upstream section is a veto region (red), the next 14 sections are the fiducial region (green), and these are followed by a 9 section shower containment region (gold). All parts of these three sections are fully active liquid scintillator cells identical to the Far Detector and the colored areas just represent a logical assignment. Downstream of this active region is a 1.7 meter long muon catcher region of steel interspersed with 10 active planes of liquid scintillator (black and white).

An early prototype of the Near Detector will be assembled as part of the R&D effort for NOνA. This prototype is called the Integration Prototype Near Detector and it serves as a venue to test all the parts of NOνA together during calendar 2007. Our plan is to operate this prototype in the MINOS Surface Building shown in Figure 3.5 and Figure 3.17. The MINOS Surface Building is about 75 mrad off-axis to the NuMI beam and at this location a neutrino beam composed of 85% ν_μ of energy ~ 3 GeV and 15% ν_e of energy ~ 2 GeV is available [13] for study of the prototype. Since the prototype detector is on the surface, the location also allows us to measure the cosmic ray backgrounds in the detector and to vary the shielding from cosmic rays with standard Fermilab shielding blocks stacked around the detector to make a cave.

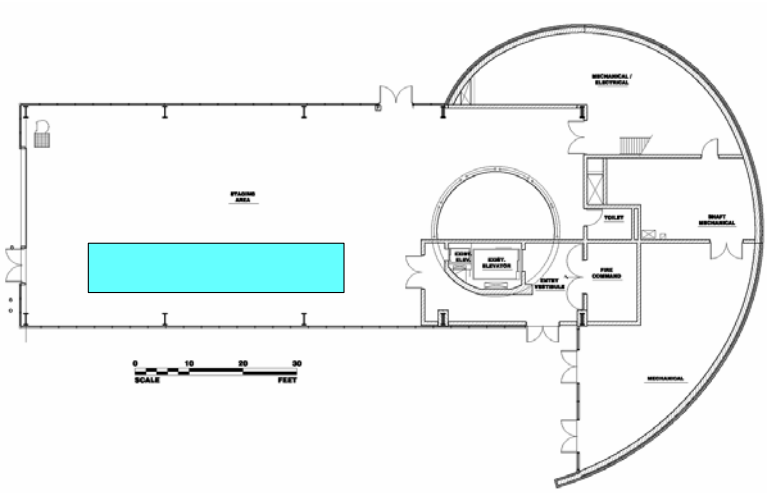

Fig. 3.17: Plan view of the NOνA Integration Prototype Near Detector in the MINOS Surface Building.

A summary of the Near Detector parameters is given in Table 3.3 and additional details are in Chapter 15.

Near DetectorParameter	ParameterValue
Total mass	209 metric tons
Active detector mass	126 metric tons
Fiducial mass	23 metric tons
Extrusion cells, liquid scintillator, waveshifting fiber, APD readout	Identical to the NOνA Far Detector
Number of channels	15,584
Total Liquid Scintillator	29,048 gallons
Detector Width (m and # of cells), Height (m and # of cells, length (m)	 2.9 m, 64 cells 4.1 m, 96 cells 14.4 m
Total active planes	196 planes, 95 horizontal & 101 vertical
Basic modular piece in the active section # planes, Thickness of 7 (8) plane segment Empty weight of 7 (8) plane segment Full weight of 7 (8) plane segment	 7 (or 8) planes, 46.2 (52.8) cm 1,203 (1,340) kg 4,504 (5,132) kg
Veto region, # of active planes	6 planes
Fiducial region, # of active planes	110 planes
Shower Containment region, # of active planes	 70 planes
Muon catcher Steel (m/section, # of sections) # of active planes	 0.1 m, 10 sections 10 planes
Muon catcher mass Steel Scintillator planes	 81 metric tons 6.5 metric tons

Table 3.3: NOνA Near Detector Parameters.

3.5 Performance of the Selected NOνA Design

3.5.1 Measured Performance of a Single Cell

Our R&D efforts during FY2005 led to prototype lengths of extrusions with 15% titanium oxide loaded rigid PVC in a 2.2 cm by 4.0 cm cell extruded in a 3-cell wide arrangement. We have used this material to form a NOνA cell of the standard interior size 3.87 cm by 6.0 cm as shown in Figure 3.19. A 33.4 meter length, 0.8 mm diameter, Kuraray, Y-11 fluor, S-type multiclad fiber has been inserted in this standard size test cell with a loop at the far end just like the NOνA design. The complete array of cells shown in Figure 3.18 was filled with fully oxygenated St. Gobain (Bicron) BC-517P liquid scintillator, a scintillator with a 5% pseudocumene content [14]. The fiber was connected to a commercially available Hamamatsu APD array which has pixels of dimensions 1.6mm by 1.6mm, well matched to the 0.8mm fiber used in the test setup. The APD was cooled to -15^{o}C using a TE cooler and was operated at a gain of 100 as in the NOνA design. The APD was readout using the MASDA chip [11] discussed in section 3.4.6. This was an existing version of the chip optimized for 70 picoFarad input capacitance rather than the APD's 10 pF, so the electronic noise in the system was 350 electrons vs. the < 250 electrons expected from a properly matched amplifier in the custom NOνA ASIC design.

A set of scintillator paddles were placed above and below the test cell and pulse heights were recorded from the test cell for cosmic ray muons crossing the 6.0 cm dimension of the test cell. This is the direction most tracks from neutrino events in NOνA will cross the cells. Cosmic tracks at angles to the cell were eliminated by vetoing on any events with observed pulse height in the adjacent cells. The distribution of pulse heights observed for these ~6.0 cm crossing tracks is shown in Figure 3.19. The mean pulse height is plotted vs. time in Figure 3.20. Figures 3.19 and 3.20 show that we have demonstrated a ~21 photoelectron (pe) mean pulse height from the far end of a standard NOνA cell. In the context of the Figure of Merit scientific performance requirement, this pe yield is adequate. Chapters 5 and 13 discuss this pe yield and Figure of Merit in more detail.

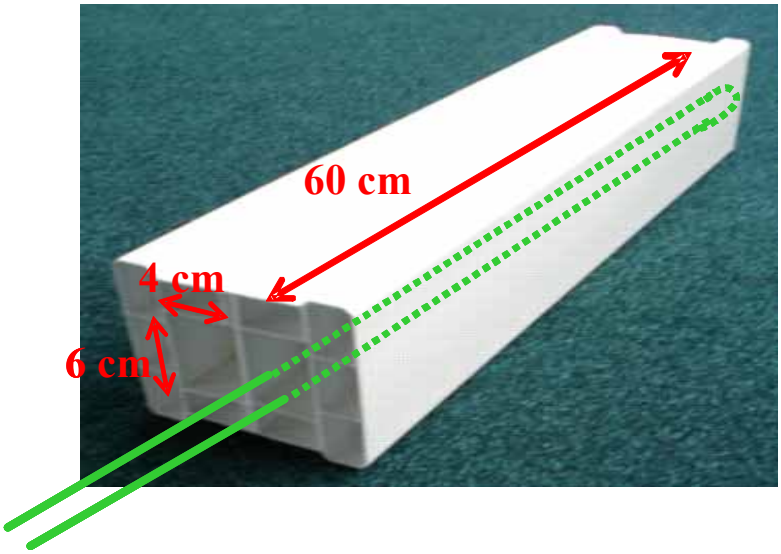

Fig. 3.18: A test cell of NOνA dimension 3.87 cm by 6.0 cm by 60 cm constructed of R&D rigid PVC loaded with 15% titanium oxide. The green line indicates the full length wavelength shifting fiber inserted in this cell for tests.

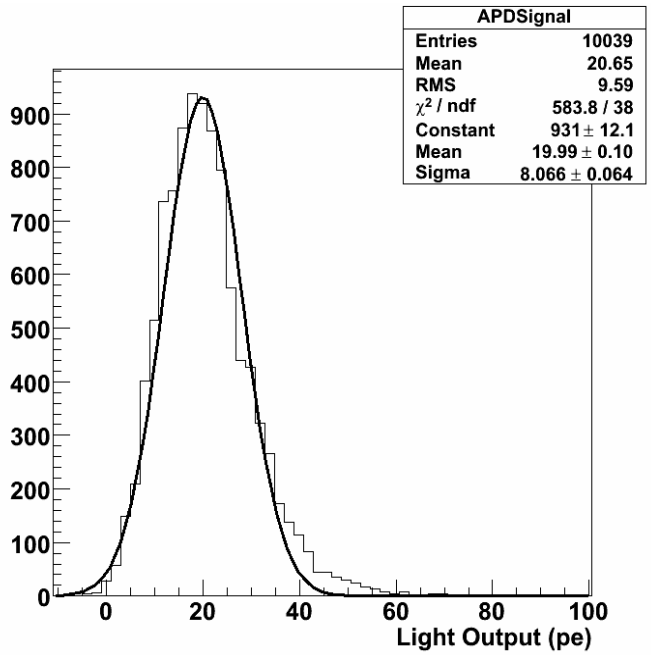

Fig. 3.19: Histogram of pulse heights observed in cosmic ray data with the test cell of Figure 3.18.

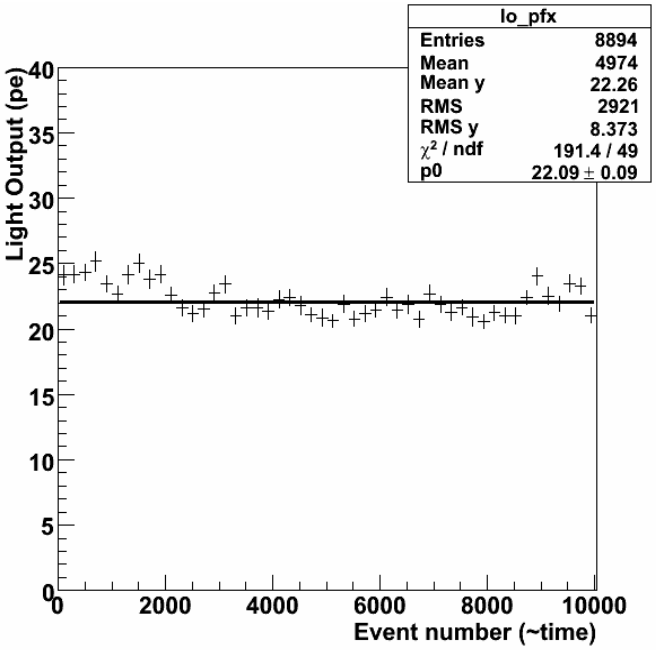

Fig. 3.20: Fits to the peak value of 50 independent histograms of data similar to that of Figure 3.19. These data represent about three months of continuous running of the test cell.

3.5.2 Simulated Performance of the NOνA Detector: A Visual Overview

About one-third of the neutrino interactions at the NOνA neutrino beam energy are quasi-elastic, with just a nucleon and a lepton in the final state. A second third of 2 GeV neutrino interactions are resonant processes in which a Δ resonance is created which then decays to a proton + pion, or a neutron + pion. The final third of neutrino interactions at 2 GeV are deep inelastic scattering events where multiple pions are produced. Figure 3.21 illustrates this mix of neutrino interactions as a function of the neutrino energy.

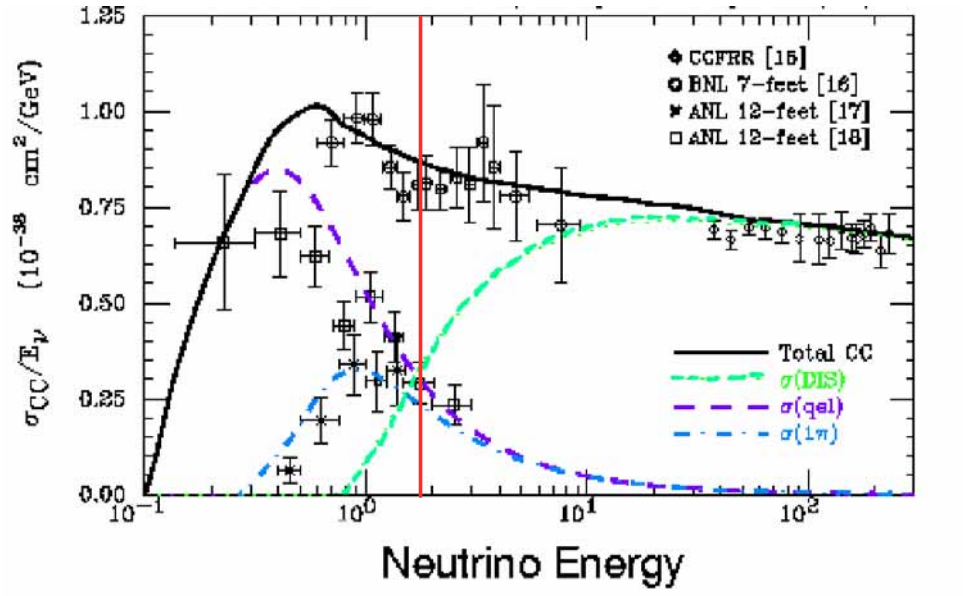

Fig. 3.21: A compilation of low energy charged current neutrino cross sections from G. Zeller [15]. The red line indicates the peak energy of NOνA events.

Some selected simulated NOνA events are shown in Figures 3.22 through 3.26 to illustrate properties of the detector. Figure 3.22 shows a simulated quasi-elastic ν_e charged current event and Figure 3.23 shows a simulated quasi-elastic ν_μ charged current event. Contrasting these two figures illustrates the NOνA detector's ability to distinguish electrons from muons. Electrons (Figure 3.22) tend to deposit more energy per plane and are more "fuzzy" in the transverse direction to the electron track, having more hits per plane of the detector. Muons (Figure 3.23) tend to be much longer tracks than electrons and typically have only one hit per plane. Muons are "not fuzzy" in the transverse direction to the muon track. Figures 3.22 and 3.23 also illustrate the response of the NOνA detector to protons of energy 1 GeV or less. The protons do not travel far and deposit a large amount of energy in a short distance, typically ending with a large spike of deposited energy (a red cell near the event vertex in the NOνA event display).

Figure 3.24 shows a resonant or single pion charged ν_e current event in NOνA. The typical pion has a low energy, but can be seen easily in the detector as a third track (assuming one recognizes the short length proton track in the event). Figure 3.25 shows a deep inelastic scattering ν_e charged current event in NOνA with several pions in addition to the outgoing electron. Such multiple pion events are harder to recognize as the 2 GeV of event energy gets divided into more and more parts, but the fuzzy electron can still be identified in many such events.

Finally, Figure 3.26 shows a neutral current event in NOνA. Neutral current events are a source of background. Typically a higher energy neutrino (3.86 GeV in this example) interacts with the nucleus and an outgoing neutrino takes good fraction of the incoming energy away and is unseen by the detector. The scattering produces additional particles which are seen by the detector and some of the time one of these particles is a π^0 which decays into two photons. One or more of these photons can fake an electron track and cause the detector to misidentify the event as a ν_e charged current event. In the sample event shown in Figure 3.26, one can see how the two photons line up in one view to simulate an electron track. In the other view the photons are separated and in fact those tracks do not continue all the way to the event vertex. This "gap" in the tracks is how one can distinguish a π^0 from an electron.

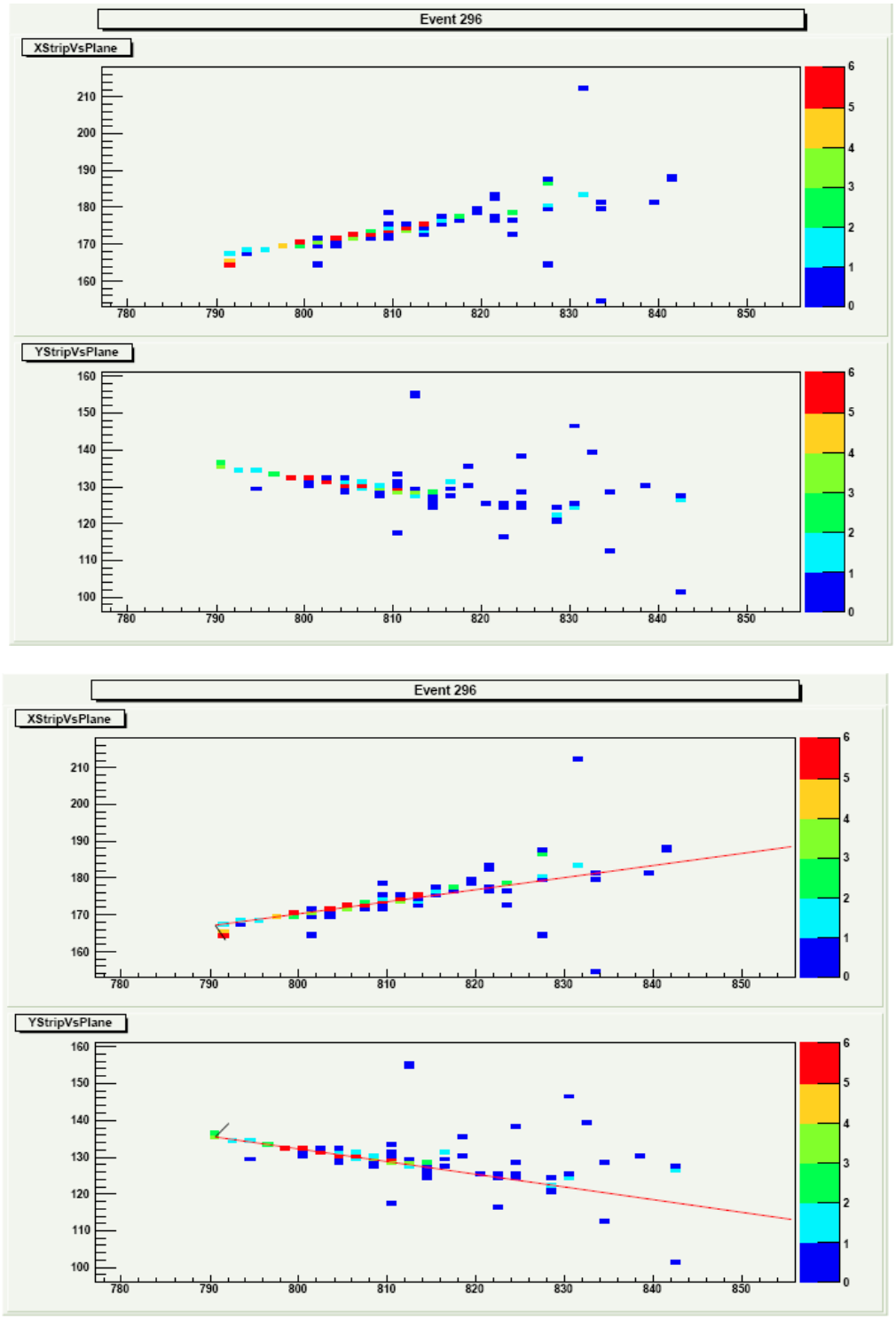

Fig. 3.22: A 1.99 GeV ν_e quasi elastic charged current event, ν_e A → p e^-. The raw pulse heights (in minimum ionizing particle units) are shown at the top of the figure for the y-z and x-z views. The event views are repeated at the bottom of the figure with lines representing the trajectories of the final particles. The line code is as follows: red for charged leptons, green for π^0, blue for charged π, black for protons. The length of the colored line is proportional to the energy of the particle, but is not its expected length in the detector.

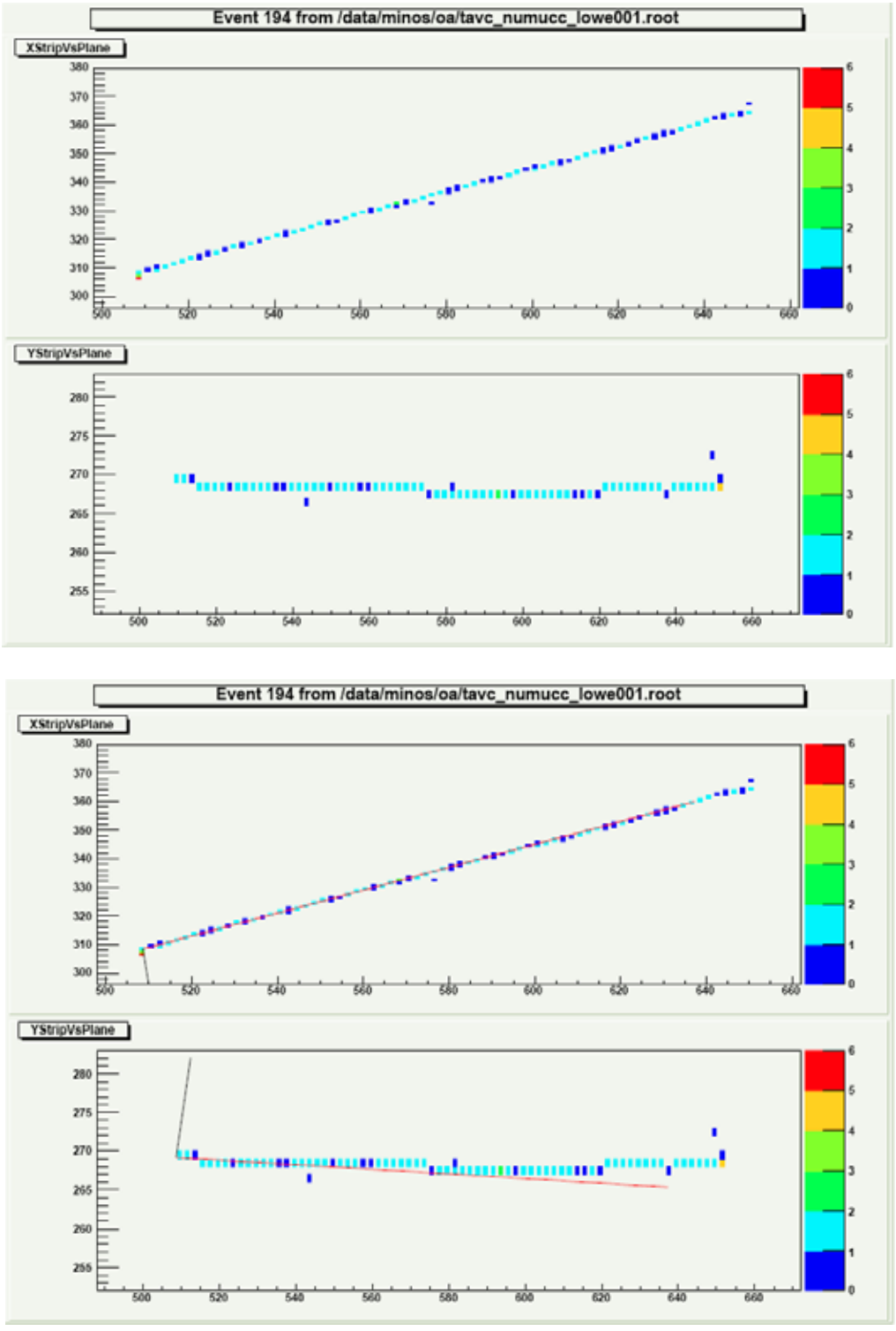

Fig. 3.23: A 2.2 GeV ν_μ quasi elastic charged current event, ν_μ A → p μ^-. The raw pulse heights (in minimum ionizing particle units) are shown at the top of the figure for the y-z and x-z views. The event views are repeated at the bottom of the figure with lines representing the trajectories of the final particles. The line code is as follows: red for charged leptons, green for π^0, blue for charged π, black for protons. The length of the colored line is proportional to the energy of the particle, but is not its expected length in the detector. Note the horizontal extent of this event is more than twice the length in Figure 3.23.

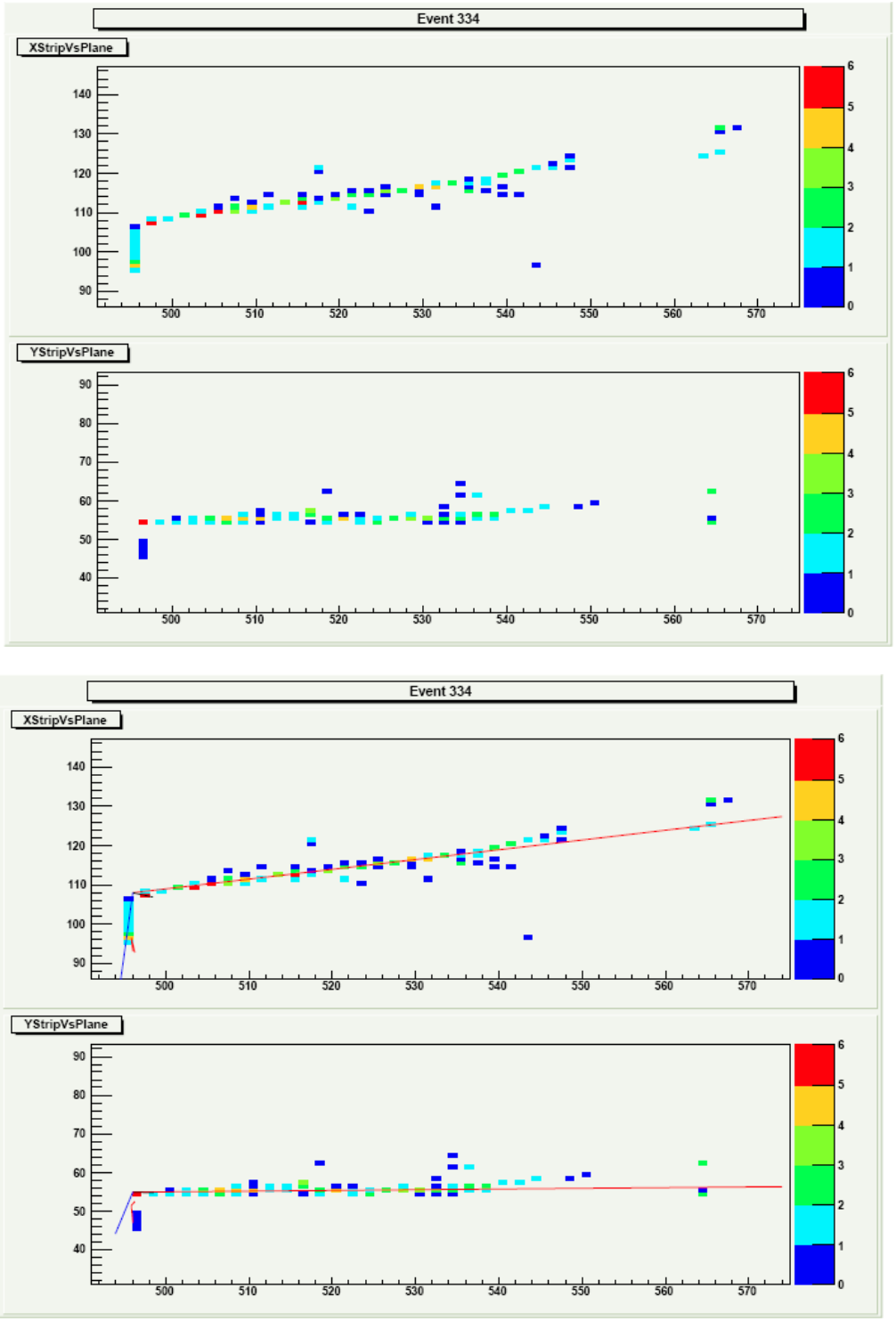

Fig. 3.24: A 2.28 GeV ν_e single pion charged current event, ν_e A → p π^+ e^-. The raw pulse heights (in minimum ionizing particle units) are shown at the top of the figure for the y-z and x-z views. The event views are repeated at the bottom of the figure with lines representing the trajectories of the final particles. The line code is as follows: red for charged leptons, green for π^0, blue for charged π, black for protons. The length of the colored line is proportional to the energy of the particle, but is not its expected length in the detector.

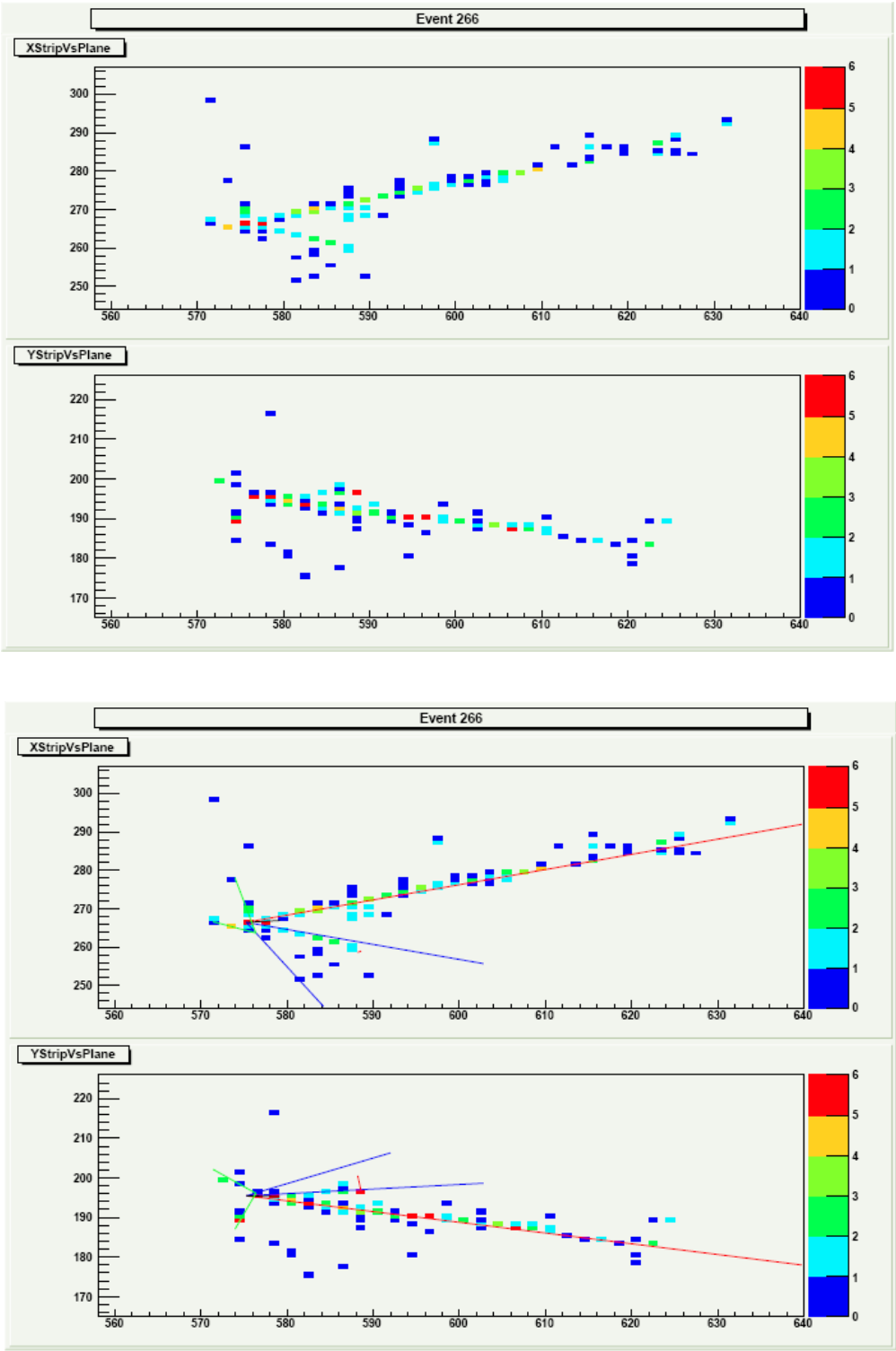

Fig. 3.25: A 2.57 GeV ν_e deep inelastic scattering charged current event, ν_e A → p e^- π^+ π^-. The raw pulse heights (in minimum ionizing particle units) are shown at the top of the figure for the y-z and x-z views. The event views are repeated at the bottom of the figure with lines representing the trajectories of the final particles. The line code is as follows: red for charged leptons, green for π^0, blue for charged π, black for protons. The length of the colored line is proportional to the energy of the particle, but is not its expected length in the detector.

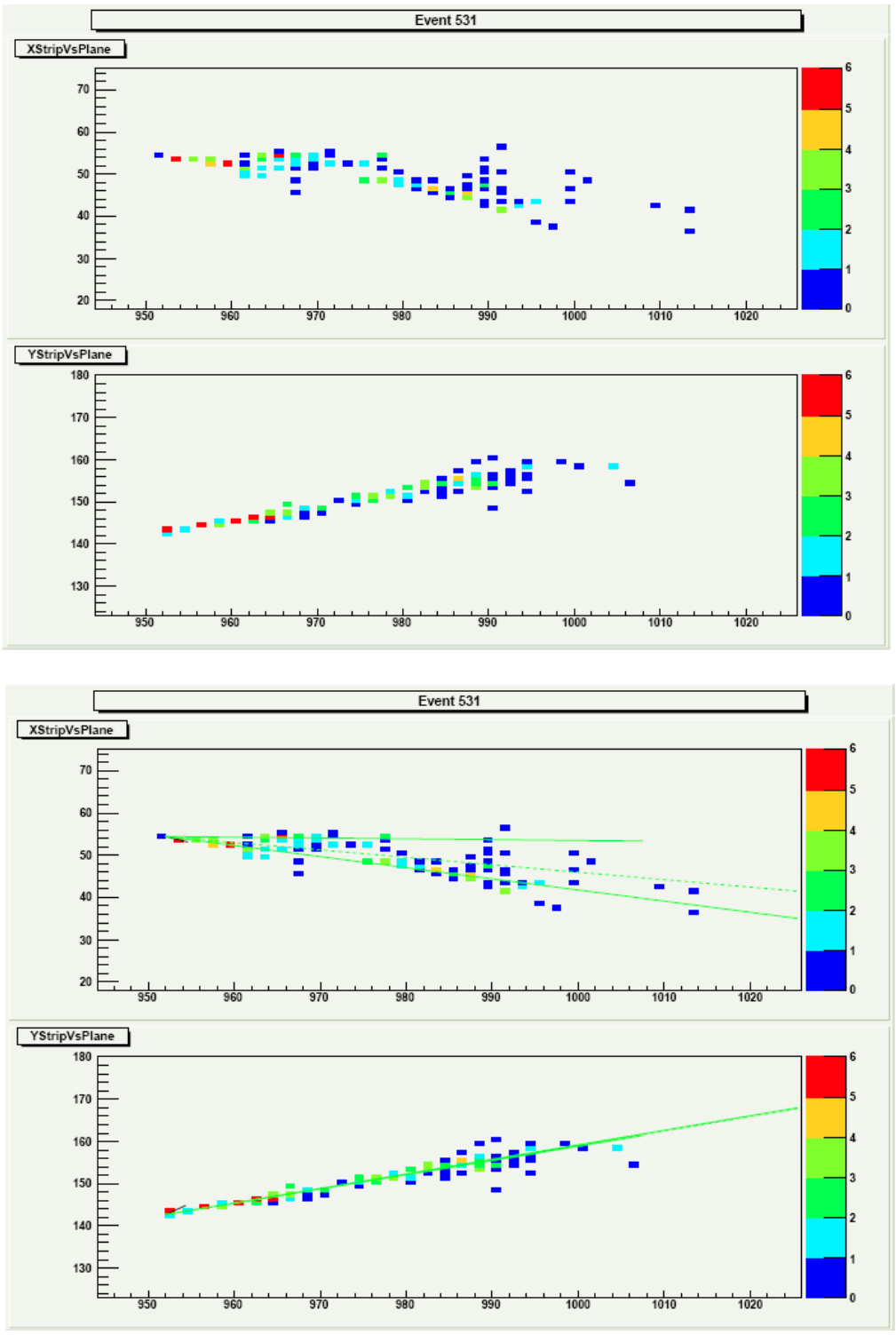

Fig. 3.26: A 3.86 GeV ν_μ neutral current event, ν_μ A → ν_μ p π^0(1.93 GeV), π^0 → γ γ. The raw pulse heights (in minimum ionizing particle units) are shown at the top of the figure for the y-z and x-z views. The event views are repeated at the bottom of the figure with lines representing the trajectories of the final particles. The line code is as follows: red for charged leptons, green for π^0, blue for charged π, black for protons. The length of the colored line is proportional to the energy of the particle, but is not its expected length in the detector.

3.5.3 Simulated Performance of the NOνA Detector: Quantitative Analysis

In a more quantitative way, Figure 3.27 shows the energy per plane and hits per plane distributions for electrons and muons in NOνA. The two types of particles can be cleanly separated in this detector.

The energy resolution of NOνA for electrons and muons is shown in Figures 3.28 and 3.29.

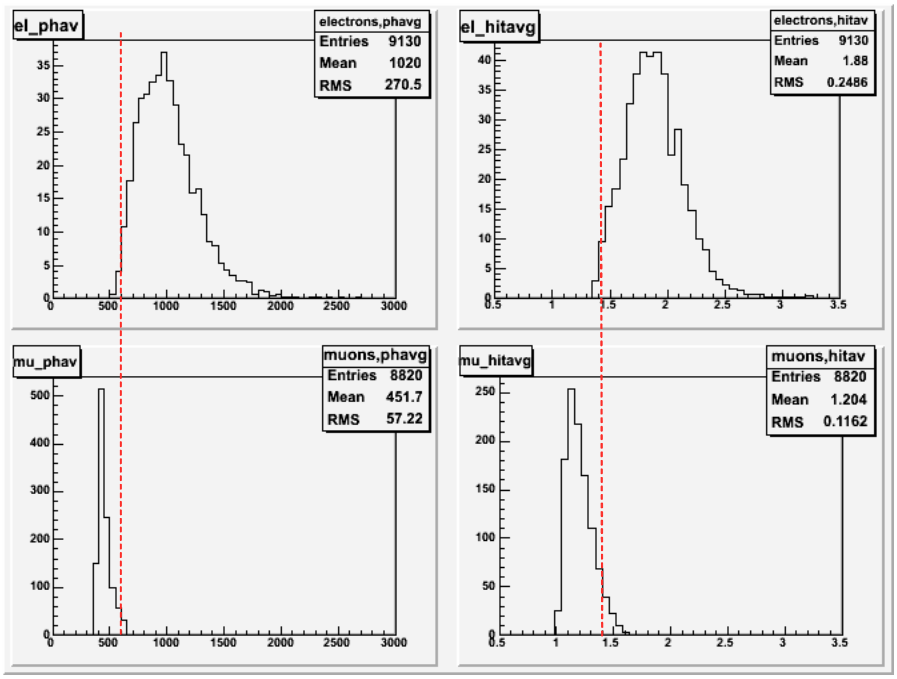

Fig. 3.27: Distributions of average pulse height/plane (left) and average number of hits per plane (right) for electrons in electron charged-current events (top) and muons in muon charged-current events (bottom).

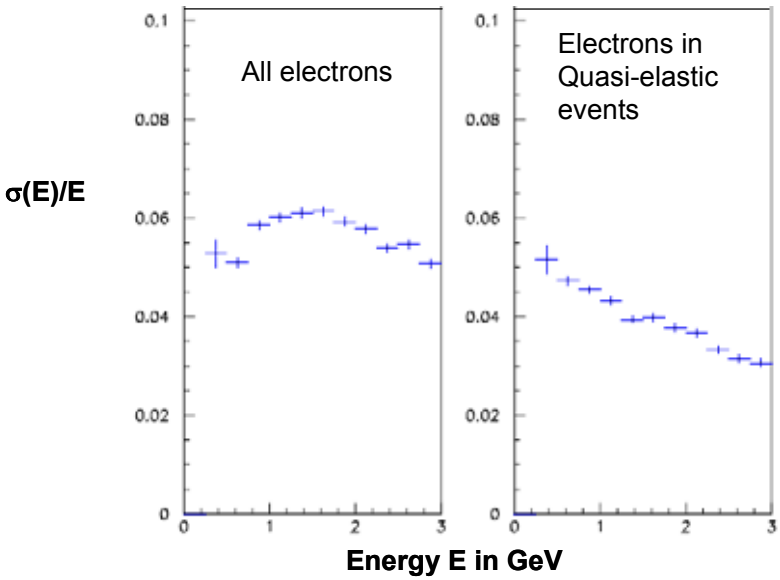

Fig. 3.28: σ(E)/E for electrons in NOνA. The left plot is for all ν_e events, while the right plot is for quasi-elastic events only.

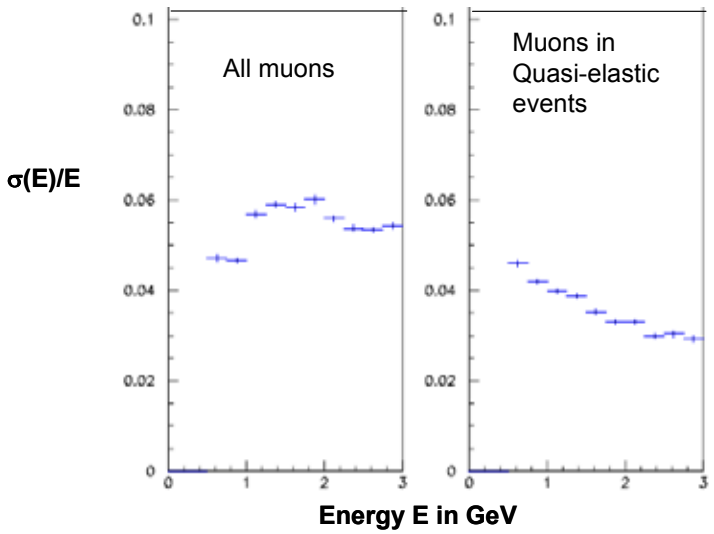

Fig. 3.29: σ(E)/E for muons in NOνA. The left plot is for all ν_μ events, while the right plot is for quasi-elastic events only.

The differences between all events and the quasi-elastic events reflect the mix of events as a function of energy shown in Figure 3.21. At about 0.5 GeV, the quasi-elastic events constitute 75% of all events so the left and right sides of Figures 3.28 and 3.29 agree at that energy. At 2 GeV, where most of the NOνA ν_e signal appears, the energy resolution σ(E)/E is about 6% for electrons. For 2 GeV muons, the energy resolution σ(E)/E is about 3.5% for quasi-elastic events.

The NOνA Far Detector performance for signals and backgrounds for $\nu_\mu \rightarrow \nu_e$ oscillations has been simulated using parts of the MINOS experiment software, the NEUGEN3 neutrino interaction generator and the GEANT3 detector simulation. The steps in the simulation were:

1) Generation of the event interaction.
2) Calculation of the detector response to the generated particles.
3) Reconstruction, i.e. track finding and fitting. A quadratic fit is made to each track using the pulse height-weighted cell positions in each plane.
4) Calculation of various parameters associated with each track.
5) Assignment of particle identity to each track (e, μ, p, γ, or hadron).
6) Calculation of the interaction vertex.
7) Preliminary identification of events with
   a) A measured energy within 25% of the nominal off-axis energy.
   b) No significant energy deposition near the detector boundaries.
   c) An electron candidate, which starts near the vertex and has no gaps near the vertex.
   d) No μ or γ in the event.
8) Separation of signal and background events using a maximum likelihood analysis with the following variables
   a) Total measured energy
   b) Fraction of total energy carried by the electron
   c) Mean pulse height near the origin of the electron
   d) Pulse height per plane for the electron
   e) Number of hits per plane for the electron
   f) Energy upstream of the vertex
   g) Curvature of the electron
   h) Missing transverse momentum
   i) Fraction of total electron energy contained in the first half of the electron track

j) rms deviation of electron hits from the fitted track
k) number of tracks identified as hadrons in the event

The maximum likelihood optimization was done by maximizing a Figure of Merit (FoM) defined as the signal divided by the square root of the background, assuming that the oscillation is given by the formula

$$P\left(\nu_\mu \rightarrow \nu_e\right) = 0.5\sin^2(2\theta_{13})\sin^2\left(\frac{1.27\Delta m^2_{32} L}{E}\right), \quad (1)$$

with Δm_{32}^2 =0.0025 eV^2, L = 810 km, and the energy spectrum given by the Off-Axis beam.

The results for a 6-year run at 6.5 x 10^{20} protons on the NuMI target per year are a signal of 142.4 events with a background of 19.5 events, giving a Figure of Merit (FoM) = 32.2. These event yields assume that $\sin^2(2\theta_{13}) = 0.10$, $\sin^2(2\theta_{23}) = 1.0$, and $\Delta m_{32}^2 = 0.0025$ eV^2. The number of signal events is proportional to $\sin^2(2\theta_{13})$, but the number of background events is essentially independent of $\sin^2(2\theta_{13})$.

In this analysis, the efficiency for accepting a ν_e event from $\nu_\mu \rightarrow \nu_e$ oscillations is 24%. The background of 19.5 events is about two-thirds from beam ν_e's produced in the NuMI beam via muon and kaon decay and one-third from neutral current events. The background from ν_μ charged current events is less than one event. The accepted fraction of ν_μ charged current background events is about 4 x 10^{-4} and the accepted fraction of neutral current background events is approximately 2 x 10^{-3}.

Figure 3.30 shows the number of each class of background events as a function of the number of accepted signal events generated by changing the cut on the likelihood function. The top half of Fig. 3.31 shows the resulting Figure of Merit (FoM) as a function of the number of accepted signal events, indicating that we have optimized this software-based analysis.

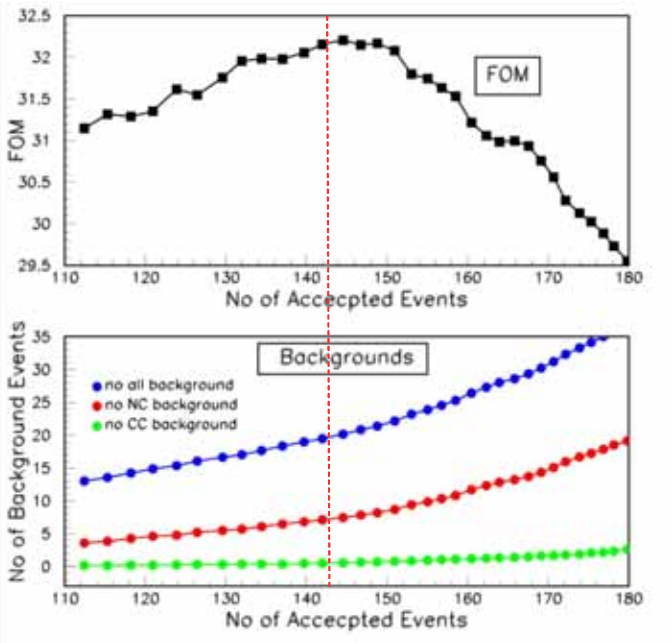

Fig. 3.30: The FoM (top figure) and the numbers of background events (bottom figure) as a function of the number of accepted signal events generated by varying the cut on the likelihood function. In the bottom figure, the green curve shows the number of misidentified ν_μ charged current events; the red curve shows the number of misidentified neutral current events; and the blue curve shows the total number of background events including the number of beam ν_e events.

3.5.3 Summary: Selected NOνA Design Performance vs. Scientific Requirements

Table 3.4 compares the simulated performance of the selected NOνA design to the scientific performance requirements discussed in Chapter 2. All the performance requirements are met by the selected design.

Design Parameter	**Scientific Performance Requirement**	**Performance of the NOνA Selected Design**
Distance off-axis	11.5 to 12.0 km	11.77 km
Distance from Fermilab	As far from Fermilab as practically possible.	810 km, farthest possible site in the United States along the NuMI beamline
Experimental Sensitivity	Figure of merit greater than or equal to 30 (The Figure of Merit is defined as the number of ν_e signal events divided by the square root of the background for 39 x 10^{20} protons on the NuMI target at a the oscillation values $\sin^2(2\theta_{13}) = 0.1$ and $\Delta m^2_{32} = 0.0025$ eV^2 without regard to matter and atmospheric-solar interference effects.)	32.2
Energy resolution for ν_e Charged Current events	Less than 8% at 2 GeV	6% at 2 GeV
Energy resolution for Quasi-Elastic ν_μ Charged Current events	Less than 4% at 2 GeV	3.5% at 2 GeV
Far Detector overburden	2 meters of rock with density 2.5 g/cc	3 meters of excavated granite rock, rock density of 2.8 g/cc mixed with 40% voids
Near Detector	At least a 20 ton fiducial volume located about 1 kilometer from the NuMI target with sufficient transverse and longitudinal size for neutrino event containment.	23 ton fiducial volume Located at 1.0 km from the NuMI target 2.9 m by 4.1 m by 14.4 m With a fiducial volume 1.65m by 2.85 m by 7.4 m, followed by a 4.75 m containment region.

Table 3.4: NOνA design parameters. The scientific performance requirements and the performance of the selected NOνA design are given for each parameter.

Chapter 3 References

[1] Steve Dixon, American Engineering Testing, Inc Report of Subsurface Boring and Piezometer Installation, NOvA Off-Axis Site, NOvA docdb note 162, November, 2005. See also NOvA docdb note 108, Preliminary Ash River Boring Logs, October, 2005.
[2] Bill Miller and Marvin Marshak, Ash River Site Visit and DNR Meeting of April, 2005, NOvA docdb note 168.
[3] Bill Miller, NOνA docdb note # 188, November, 2005.
[4] draft Acquisition Strategy.
[5] Marvin Marshak, email exchange with Jon Ahlness with the St. Paul District of the U.S. Army Corps of Engineer, July 8, 2005.
[6] D. Ayres et al., NOνA: Proposal to Build a 30 Kiloton Off-Axis Detector to Study $\nu_\mu \rightarrow \nu_e$ Oscillations in the NuMI Beamline, March, 2005, hep-ex/0503053.
[7] P. Border et al., NIM A463 (2001) 194-204, and L. Benussi et al., NIM A488 (2002) 503-516.
[8] Some examples are: M. Ambrosio et al., the MACRO detector at Gran Sasso, NIM A 486 (2002) 663-707, D. Harris et al., Precision calibration of the NuTeV calorimeter, NIM A447 (2000) 373-415, L. Ahrens et al., A Massive, Fine-grained Detector for the Elastic Reaction Induced by Neutrinos in the GeV Energy Region (BNL-734), NIM A254 (1987) 515-528.
[9] MINOS Technical Design Report, Fermilab, NuMI-L-337 (1998)
[10]K. Deiters et al., NIM A461 (2001) 574-576, NIM A453 (2000) 223-226, and NIM A442 (2000) 193-197.
[11] M. Maolinbay et al., NIM A485 (2002) 661-675, and T. Zimmerman, Fermilab Technical Note FERMILAB-TM-2063 (1998).
[12] B. Krieger et al., FERMILAB-PUB-030-489-E, (2003), also published in IEEE Trans. Nucl. Sci. 51(2004).
[13] D. Ayres et al., NOνA Proposal Chapter 9, hep-ex/0503053, March, 2005.
[14] M. Kusner, St. Gobain, private communication, April, 2004.
[15] G. Zeller, "Low-energy neutrino cross sections: comparison of various Monte Carlo predictions to experimental data", hep-ex/0312061, Proceedings of NuInt'02, Irvine CA, December 2002.

4. Alternative NOνA Designs Considered

4.1 Introduction

We describe here alternative designs considered for NOνA and discuss the reasons these alternatives were not chosen. This alternatives analysis overview describes the alternative sites, alternative detector technologies, and alternative detector structures considered. Additional alternatives considered for more detailed parts of the detector are discussed in sections of Chapters 6 - 15.

4.2 Alternative Far Detector Sites

The scientific performance requirements dictate a long baseline between Fermilab and the Far Detector site. Knowing that a long baseline was optimal for the science case, sites from Lake Superior into Canada were considered from the beginning of the NOνA design process. Figure 4.1 shows the area of possible sites explored along the existing NuMI beamline.

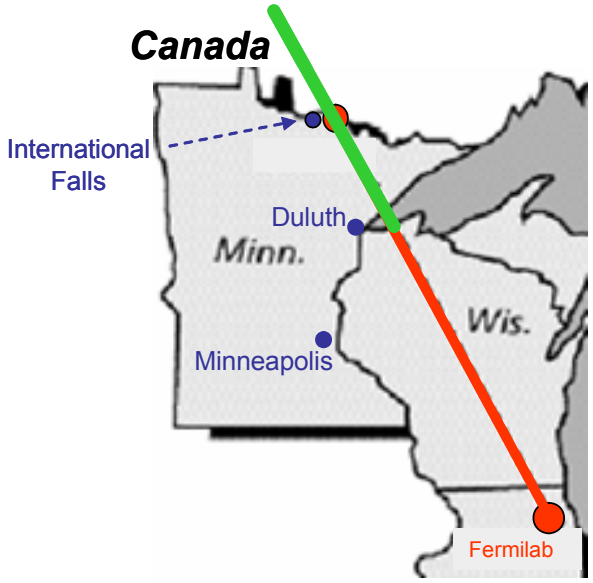

Fig 4.1: Map of the central United States and Canada showing Fermilab, the NuMI beam, and the area of sites considered for the Far Detector in green.

The criteria used to judge possible sites included the following:

a) The ability to have a detector ~ 12 km off-axis. See Section 2.4.1 of Chapter 2.
b) Access to the site by existing roads. Available sites in the green area of Figure 4.1 are rather restricted because there are relatively few east-west all weather roads in the area. Ability to do construction in all seasons on the experimental hall and on the detector is part of the critical path on any NOνA schedule.
c) Access to power, telephone lines, and fiber optic data connections.
d) The availability of a relatively flat area for construction.
e) The availability of high ground well above the water table with no wetlands.
f) The lack of features likely to provoke controversy or litigation. Examples are nearby high population density, visibility from a national park, on-site cultural resources like burial mounds or historical site and artifacts.

The intersections of appropriate all weather roads and the 12 km off-axis line are shown in Figure 4.2. There are only a handful of choices with all weather roads in this part of the world. Seven possible sites were considered: on Lake Superior, at an inactive surface mine at Cliffs-Erie in Minnesota, near the MINOS underground detector at Peyla, Minnesota, at a site along the Orr-Buyck Road in Minnesota, at Ash River, at a site along Trans-Canada 11 and Ontario 502 in Ontario, Canada, and at a site near Vermilion Bay on Trans-Canada 17. In some cases (not all) equivalent sites are available on the east side of the NuMI beamline at 12 km off-axis.

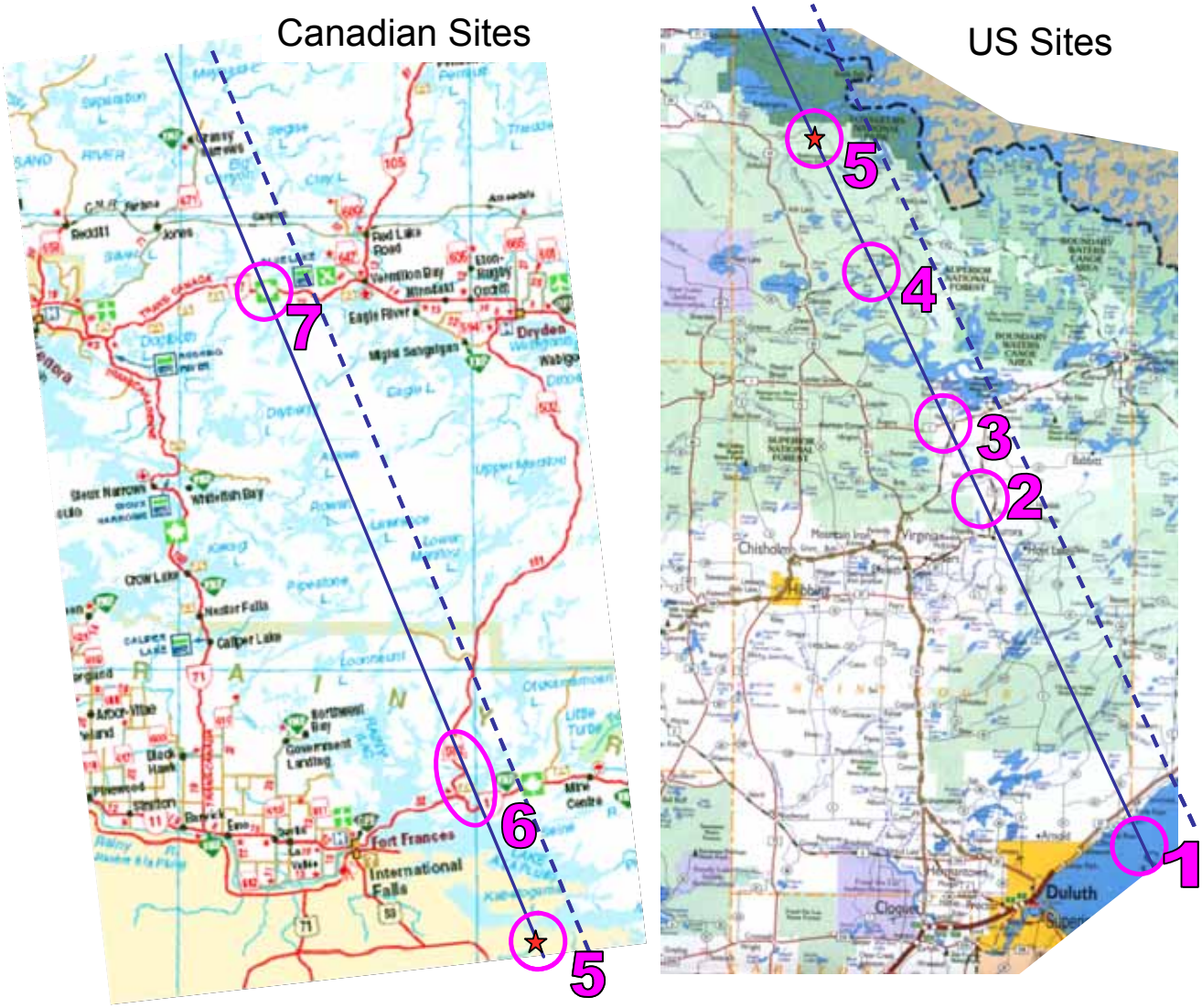

Fig. 4.2: Maps showing alternate Far Detector sites in Canada (left) and the United States (right). From south to north, the US sites are 1) Lake Superior, 2) Cliffs-Erie, 3) Peyla, 4) Orr-Buyck, and 5) Ash River, with all sites in Minnesota. From south to north, the Canadian sites are 6) Fort Frances-Mine Center, Ontario and 7) Vermilion Bay, Ontario. The NuMI beam centerline is shown as the dashed blue line and the 12 km Off-axis line is the solid blue line. The selected alternate Ash River site is marked with a red star on both maps.

4.2.1 Lake Superior Sites

Lake Superior was investigated as a site for an underwater Cherenkov detector (see section 4.2) or for a floating liquid scintillator detector as in the selected NOνA design. Since the water Cherenkov technology is not the NOνA selected alternate, the underwater feature is not particularly interesting. Lake Superior is less than 100 m deep at the far western end, so a water Cherenkov would have some restrictions as well. In addition the lake is only navigable about 9 months out of the year and freezes over during the winter. The baseline distance for these sites is in the range 560 – 630 km from Fermilab. This baseline is too short for the scientific performance requirement on the baseline. The navigability and baseline reasons eliminate this site from consideration.

4.2.2 Cliffs-Erie Site

This site is in an inactive LTV surface mine and was originally considered because loose tailings piles from the mine exist in large hills which could be easily excavated for an experimental hall. However, this site is only 712 km from Fermilab and therefore does not meet the scientific performance requirement on the baseline. The tailings offer an easy excavation, but this is balanced by the need for strong walls in an experimental hall to retain the tailings outside of the hall as a cosmic ray shield. These two reasons eliminate this site from consideration.

4.2.3 Peyla Site

This site is very near the Soudan Mine and MINOS detector and therefore offers the possibility of using the skilled MINOS mine crew on the NOνA project. On further examination the long overlap in time between the MINOS data run and the NOνA construction negate using the mine crew. In addition this site is only 735 km from Fermilab and therefore does not meet the scientific performance requirement on the baseline. This site has been eliminated from consideration.

4.2.4 Orr-Buyck Site

This site is located 774 km from Fermilab and is within the scientific performance requirement distance. It is the second longest baseline available in the United States. Three potential sites were examined in this area and are shown in Figure 4.3. The NOνA project team visited this area

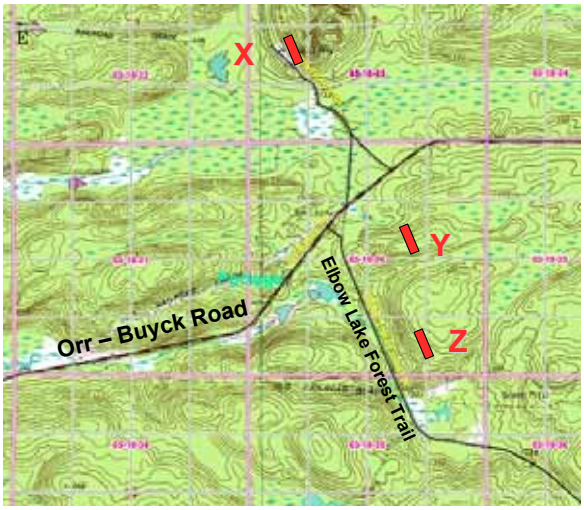

Fig. 4.3: Potential Sites along the Orr-Buyck road.

in September 2005 [1]. Site X at Orr-Buyck is in an existing gravel pit operation and looked attractive because the excavation would be simple. Unfortunately the water table is only a few feet below the surface here, so site X was eliminated from consideration. Site Y is south of the Orr-Buyck Road but the hilltop there did not seem large enough to accommodate the experimental hall easily and this site was also eliminated.

Site Z is a reasonable candidate. Access is via the Elbow Lake Road, a maintained gravel road heading south from the Orr-Buyck Road. There is no road from Elbow Lake Road to the site, but the distance is less than a mile and a road could be built. Borings [2] at Site Z indicate a ~ 5 foot soil overburden sitting on hard granite to a depth of 60 feet, much like the selected alternate site at Ash River. This site remains as a back-up site for NOνA if something is discovered in the environmental assessment process of if a problem develops with access rights to the Ash River selected alternate. See Chapter 7 for additional details.

4.2.5 Alternatives at the Ash River Site

The Ash River site is 810 km from Fermilab and is the longest baseline site available along the NuMI beamline in the United States. Several potential sites were examined [1] in the Ash River area in addition to the selected alternate discussed in Chapter 3. Figure 4.4 shows the additional 6 sites considered. Five of the sites (A – E) were further off-axis than the 12 km performance requirement even though they met the other criteria. Sites D and E are close to 12 km, but are inferior to the selected alternate because they are not as high above the surrounding water table as the selected alternate. Site F (in Figure 4.4, red rectangle near the top of the figure) is at the proper distance, but would require a new access road south off St. Louis County Road 129 (the Ash River Trail) through a wetlands area. The access road to the other sites also passes through a wetlands area, but it is an existing logging road, not a new road. In addition Site F and its access road would be within sight of Voyageurs National Park and Site F is not acceptable for that reason. There are no sites 12 km east of the NuMI beamline at Ash River because the Ash River Trail road does not extend east of the Ash River. All these alternative Ash River sites have been eliminated from consideration.

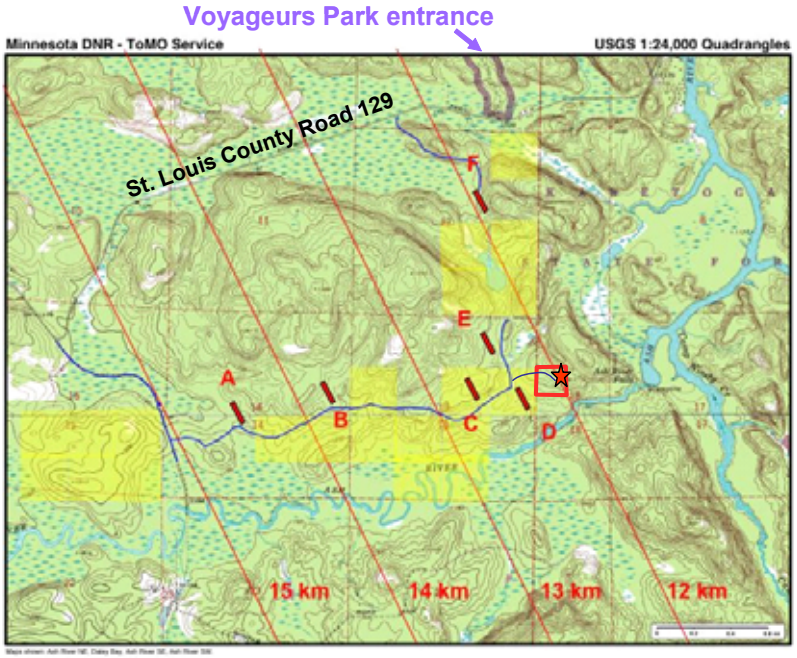

Fig. 4.4: Topographic map showing six alternate sites considered in the Ash River area in addition to the selected alternate (marked with a red star). The grid lines are 1 mile apart (section lines).

4.2.6 Fort Frances – Mine Center Site

This site is in Canada at a distance of 835 - 865 km from Fermilab on the first east-west road north of the US-Canada border. The northern end of this ellipse along Ontario 502 is in a very empty area with no available power. While the site may be feasible geographically, the lack of any Canadian participants in the NOνA collaboration indicated this area would be a politically complicated site to acquire and manage. This site has been eliminated from consideration.

4.2.7 Vermilion Bay Site

This site is in Canada at a distance of 950 km from Fermilab on the second all weather east-west road north of the US-Canada border. While the site may be feasible geographically, the lack of any Canadian participants in the NOνA collaboration indicated this would be a politically complicated site to acquire and manage. In addition, the NuMI beamline is about 15.6 km in the air at this site, so that an off-axis distance of 12 km cannot be achieved. See Figure 4.5 for an explanation of the beam altitude effect. This site has been eliminated from consideration since it cannot match the scientific performance requirement on the transverse off-axis position.

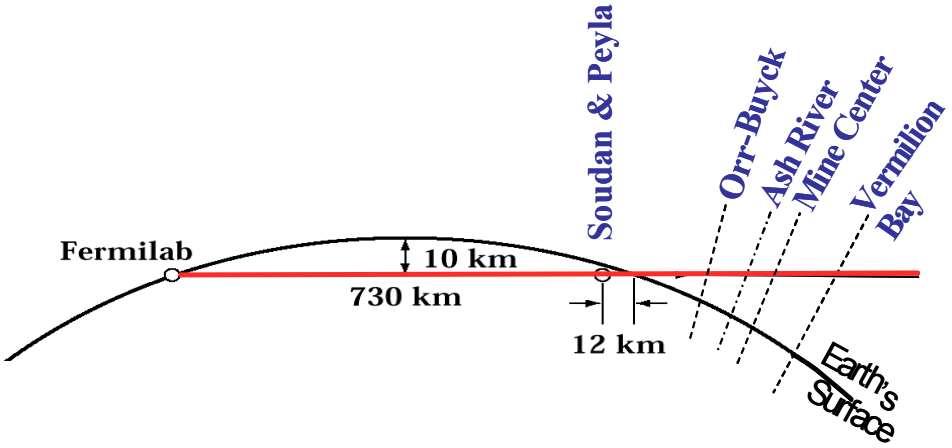

Fig. 4.5: Schematic (not to scale) showing the passage of the NuMI beam through the Earth and into the Earth's atmosphere north of the Soudan Mine.

4.3 Alternative Near Detector Sites

The scientific performance requirements indicate Near Detector sites between 1.0 km and 2.5 km from the NuMI target will be adequate for background measurements. It is possible to build a new detector hall as far away as 2.27 kilometers from the NuMI target and still be inside the Fermilab site boundary as shown in Figure 4.6. At 2.27 km site would have to be 145 meters deep, since that depth is then 15 mrad off-axis directly above the NuMI beam which continues into the earth at a 58 mrad downward slope. The good Platteville Dolostone rock at Fermilab continues down to 178 meters depth, so new shafts this deep are possible. We examined an alternative using directional drilling of two shafts 40 m apart(a 5.5 m diameter man and materials shaft and a 3.7 m diameter utility shaft). The two shafts could be linked by an excavated chamber at the required depth. The cost of such a new excavation would be of order $ 10 – 15 M. In addition, a detector at 2.27 km would have to be larger than our selected alternate Near Detector and would cost more.

The recommended alternative is in the existing NuMI / MINOS access tunnel and is cheaper, requiring no new construction and a smaller Near Detector. We are not considering any other sites for the NOνA Near Detector.

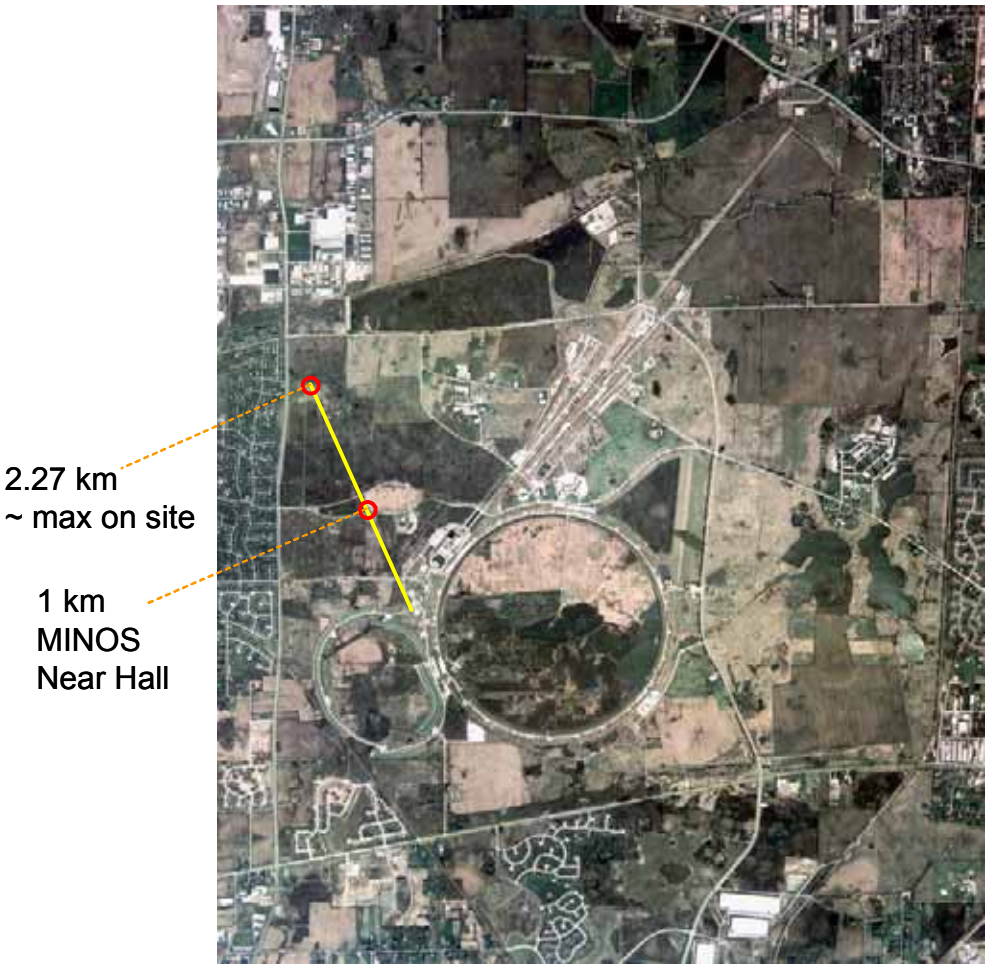

Fig. 4.6: Alternative Near Detector Sites at Fermilab.

4.4 Alternative Detector Technologies

The scientific performance requirements demand a robust and efficient detector for ν_e interactions at 2 GeV. Initially detector technologies including Water Cherenkovs, Low Z sampling Calorimeters with a variety of active elements with passive absorbers, and Liquid Argon Time Projection Chambers were considered along with the selected NOνA design described in Chapter 3. This section reviews the alternates and the reasons they were not chosen for NOνA.

4.4.1 Water Cherenkov Detectors

This technology was discussed in the NOνA Letter of Intent[3]. The concept is the same used in the Super Kamiokande (SK) detector [4] with a large water volume viewed by an array of large phototubes looking inward from the surface of the volume. This technology depends on seeing rings of Cherenkov light from each track produced in a neutrino interaction. The technology is not well suited for 2 GeV neutrino interactions due to the high number of secondary particles produced at this energy and the challenge of finding all the rings and determining the vertex in such events. The SK efficiency for charged current ν_e interactions is about 60% at 1.3 GeV where the fraction of quasi-elastic events is about 50% (see Figure 3.22). For NOνA at 2 GeV, only 33% of the neutrino interaction cross section is quasi-elastic and the efficiency for a water Cherenkov would be reduced.

In addition, the construction of a detector like SK with an array of photodetectors on the interior surface of the water volume has a downside because the fiducial volume must be restricted for events occurring close to the interior surface. SK has only a 45% fiducial volume inside the 50 kiloton detector, so it is effectively only 22.5 kilotons. Another disadvantage of a single volume is that a single cosmic ray lights up a fair fraction of the photodetector array on the surface of the volume, making operations of such a detector without a robust cosmic ray shield problematic. SK is a deep underground detector, and such a deep excavation would drive the cost of a NOνA detector well beyond reasonable funding assumptions.

For these reasons of event identification efficiency, fiducial volume, and required cosmic ray shielding, a water Cherenkov detector technology has been eliminated from consideration.

4.4.2 Liquid Argon TPC

Liquid Argon TPCs like the ICARUS detector [5,6] have fine resolution for charged tracks in three dimensions with an effective pixel size of ~5 x 5 x 5 mm^3. This resolution promises enormous potential for use in neutrino physics and Liquid Argon TPCs appear to have the greatest efficiency for identifying ν_e interactions. However, the largest detector operated to date (ICARUS) has about 500 tons of imaging mass and would need to be scaled up by about a factor of thirty to be useful in the NuMI beam intensities projected for NOνA. The NOνA collaboration judged this technology to require additional R&D beyond our envisioned time scale and this technology has been eliminated from consideration.

4.4.3 Low Z Sampling Calorimeters

A wide variety of Low Z sampling Calorimeter alternatives were considered for NOνA. This scheme is quite similar to the selected NOνA design described in Chapter 3 except that a large fraction of the active scintillator mass is replaced by an inert absorber. Sampling calorimeters still track charged particles, but the smaller number of active samples reduces the track information and reduces the energy information available from the calorimeter.

The NOνA Collaboration considered a wide variety of low Z absorbers: recycled plastics, shredded automobile tires, nutshells, cracked dried corn, particle board, oriented strand board, gypsum drywall sheets, and air entrained foam concretes. The particle board and oriented strand boards emerged as the favorites because of their structural properties which could be used in assembling a large detector.

Three types of active detectors were considered for alternative Low Z Sampling Calorimeter designs: solid plastic scintillator with phototube readout (like that used in MINOS [7]), liquid scintillator in PVC plastic cells with APD readout [8], and glass resistive plate chambers(RPCs) with strip readout (like those used in the BELLE experiment [9]). As indicated in the references, all three of these alternative active detectors have been used in previous experiments and are considered conservative choices based on existing technologies. The RPC scheme had two variants, one with a single X view or Y view RPC per sample, and one with both X and Y views in every sample. All the sampling calorimeter alternative designs investigated had a sampling approximately every 0.5 radiation lengths. The scintillator options were about 13% active detectors, while the RPC option using gas amplification was effectively zero% active detector.

The first draft 2004 version of the NOνA proposal [10] had information on all of these sampling devices and serves as a value management study of the four designs. A summary of the four sampling calorimeter schemes for cost and performance is shown in Table 4.1. When evaluated with the same Monte Carlo event generation program, performances of the four alternative detectors were similar. The solid and liquid scintillator versions include pulse height information from every cell, while the RPC versions have only digital on/off hit information. Table 4.1 compares the performance via the Figure of Merit [= Signal / √(Background)] for the

four schemes [10, 11, 12]. The costs of all four alternative technologies were also studied in detail. The liquid scintillator was clearly cheapest with the RPC single view per sample as a close second. Optimization efforts to make each of these alternatives cheaper failed to reduce the cost by more than 10% in any case.

Alternative Sampling Calorimeter Scheme	**Relative Cost** (compared to Liquid Scintillator)	**Relative Performance** (Figure of Merit compared to Liquid Scintillator)
Solid Scintillator	1.79	1.00
Liquid Scintillator	1.00	1.00
Glass RPC, 2 views per sample	1.39	0.89
Glass RPC, 1 view per sample	1.22	0.78

Table 4.1: Relative Cost and relative Figure of Merit Performance for four alternative sampling calorimeter designs considered.

4.4.4 Performance of Alternative Low Z Sampling Calorimeters vs. the Selected NOνA Design

The selected NOνA design described in Chapter 3 is superior to these alternative sampling calorimeter designs in many ways and we illustrate the differences in this section. When judged by ν_e identification efficiency based on the same Monte Carlo event generation program, the sampling devices have about half the efficiency of the selected NOνA design. This efficiency deficit arises because the sampling devices struggle to identify events with several tracks. Figure 4.7 shows this effect in a plot of the number of identified ν_e events vs. (1-y), where y is the fraction of energy carried away by all the charged particles in the event except the lepton. Both the scintillator sampling and RPC sampling devices require a cut in (1-y) restricting the events found to mostly quasi-elastic events. The selected NOνA design is able to find more single pion events and even some deep inelastic scattering events at low values of (1-y). See Chapter 3, section 3.5.2 for a description of these three types of events.

This higher efficiency for the selected NOνA design means the scientific requirements can be met with about 50% of the mass of the sampling calorimeter alternatives. This in turn means that the Far Detector experimental hall can be smaller for the selected NOνA design than for the alternatives. The cost of the selected NOνA design is more expensive per unit mass, but it requires less mass and less building to achieve the same scientific performance. Overall, the cost of the selected NOνA design for 30 kilotons is within 5% of the cost of the cheapest 50 kiloton sampling calorimeter alternative.

The electron / muon separation performance of the sampling calorimeter alternatives is also inferior to the selected NOνA design. Figure 4.8 shows the number of hits per plane for muons and electrons for the sampling devices and should be compared to Figure 3.28. With a simple cut at 1.4 hits per plane, the selected NOνA design cleanly separates electrons from muons while the same cut in the sampling alternatives keeps all the electrons but also retains 40% of the muons.

The energy resolution of the sampling calorimeters is also inferior. $\sigma(E)/E$ for the selected NOνA design is about 6% at 2GeV (see Figure 3.29). For the RPC sampling calorimeter (with only digital information from each plane) the $\sigma(E)/E$ at 2 GeV is only about 16%. For the scintillator sampling calorimeters (with pulse height information from the sampled planes) the $\sigma(E)/E$ is about 10%.

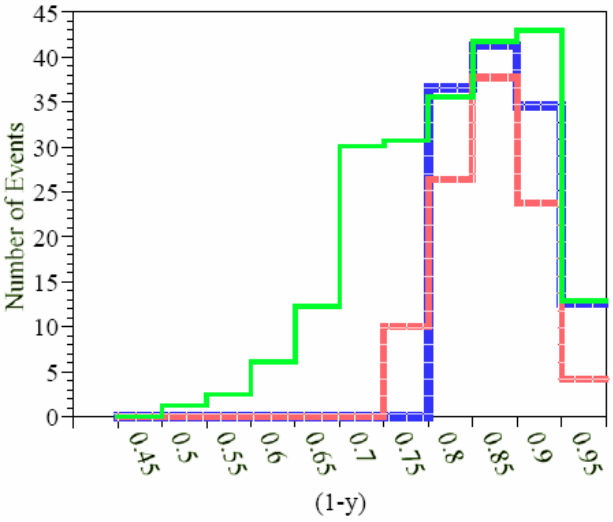

Fig. 4.7: Efficiency for ν_e identification as a function of (1-y). A value of 1.0 in (1-y) means the outgoing lepton in the charged current neutrino event took all the energy of the incoming neutrino. The scintillator sampling calorimeter efficiency is shown as the blue dashed line, the RPC sampling calorimeter is shown as the red dashed line, and the totally active selected NOνA design is shown as the solid green line.

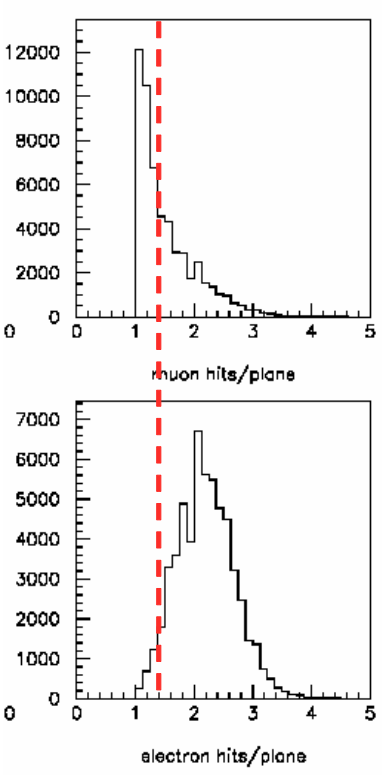

Fig. 4.8: Distributions of the average number of hits per plane for electrons in charged current events (bottom) and muons in muon charged current events (top) for the liquid scintillator sampling calorimeter alternative. Compare to Figure 3.28 for the selected NOνA design.

4.4.5 Risk Analysis of Low Z Sampling Calorimeter Alternatives

In addition to the cost and performance evaluations described above, the alternate designs were evaluated for risks.

The RPC sampling calorimeter design depends on gas amplification via electron avalanches in a mixture of 8% isobutene, 61% R134a (tetrafluoro-ethane), and 31% argon. This is a non-flammable mixture, but RPCs have experienced severe aging effects with these mixtures. The glass RPC technology seems less susceptible to aging in the BELLE experiment[9] example and glass RPCs were chosen based on that experience. BELLE did still experience other problems with the gas due to effects from water vapor contamination in the gas plumbing system. The NOνA alternative RPC design sought to reduce these risks by having two chambers at each sample with each chamber fed by a separate gas supply. The steps required to mitigate the risks of a gas system are serious and expensive. The RPC technology also depended on scaling up the experience of the BELLE detector from 5,000 square meters of glass chambers to ~ 600,000 square meters. This large amount of glass presents risks in manufacturing, shipping, and assembly of the devices.

All the sampling calorimeter alternatives were designed with particle board as the absorber and therefore there were fire protection issues in each case. The polystyrene solid scintillator flammability would require mitigation via a metal sheathing as in MINOS. The liquid scintillator sampling calorimeter option (like the selected NOνA design) has the smallest fire protection risk. PVC is self-extinguishing and liquid scintillator burns without flame spreading.

All the sampling calorimeter alternatives also suffer from a potential cosmic ray background of charged particles entering the detector vertically in one of the thick absorber sections and interacting in the absorber to produce a fake neutrino event. All the sampling calorimeters require a shield of veto counters around the detector mass to tag such incoming cosmic rays, and it is difficult to achieve 100% tagging cheaply. The totally active selected NOνA design is self-shielding from this background because such cosmic ray tracks are seen entering the device and can be followed all the way to any potential background interaction vertex.

4.4.6 Conclusions on Low Z Sampling Calorimeter Alternatives

Compared to the selected NOνA design, the RPC sampling calorimeter option has inferior performance, is more expensive to construct, and has higher risks from the gas handling system. RPCs have been eliminated from consideration. The solid scintillator sampling calorimeter option is too expensive and has been eliminated from consideration. The liquid scintillator sampling calorimeter alternative has inferior performance relative to the selected NOνA design, approximately equal cost to the selected NOνA design, and has been eliminated from consideration.

4.5 Alternative Structures for the Selected Totally Active NOνA Design

As described in Chapter 3, section 3.4.8, the selected NOνA design is a unique plastic structure with properties that require a complete analysis of the assembly and filling processes. The build up of stress in the plastic as the empty PVC extrusions are filled with scintillator is a particular problem in the design and several alternative structural proposals have been considered in attempts to deal with the problem. Those alternatives are described in this section.

4.5.1 Less Vertically Challenging Alternative Detectors

Alternatives were considered with shorter vertical cells in order to lessen the stress problem in the vertical cells from the hydrostatic pressure in the cell. For example, an alternative detector that is 7.8 meters tall vs. the 15.6 meter in the selected NOνA design has half the hydrostatic

pressure and half the stress problem. However, the stress effect does not disappear and any such design still has to consider and deal with these same effects.

A detector only 7.8 meters tall must now be either a longer or a wider detector if it is to have the same mass. Longer detectors require longer buildings and an increased cost. The excavation costs remain approximately constant, but the overburden cost increase with length. A longer building becomes increasingly difficult to site parallel to the NuMI beamline. The example considered here would require a building ~1000 feet long.

The selected NOνA design presents a square face to the neutrino beam because this minimizes the fiducial cut to remove events near the edge of the detector (~ 0.2 meters in the present analysis package). A detector that is rectangular, with a 7.8 m by 15.6 m face, has a 2.5% smaller fiducial volume (more edge to beam face fraction) that would have to be compensated by additional mass at additional cost.

Wider detectors require the horizontal cells to be longer and induce a longer attenuation length requirement on the wavelength shifting fibers. The selected NOνA design has the maximum length transportable cell and longer cells are not possible. Wider detectors could be composed of two distinct horizontal cells which touch in the center and are read out at opposite ends. This introduces a dead zone vertical strip in the center of the detector and the analysis would probably require a fiducial cut to eliminate events near the center. Wider detectors require wider buildings and holding the 3 meter thick overburden above a wide span introduces additional building costs. A set of columns could be installed along the centerline of the detector, worsening the dead zone problem.

The selected NOνA design optimizes the fiducial volume, but some deviation from a square front face could be tolerated. The bottom line for such schemes is that the stress effect does not completely disappear if the detector is less than 15.6 meters high, and any such design still has to consider and deal with the exact same effects as the selected design. Detectors with widely different aspect ratios have been eliminated from consideration for this reason.

4.5.2 A "Vee" Design Alternative

Since the stress build up in the vertical cells filled with scintillator derives from the hydrostatic pressure in the cell, a design was considered with the detector rotated by 45^{o} as shown in Figure 4.9. This alternative "Vee" design preserves the optimal square front face but again

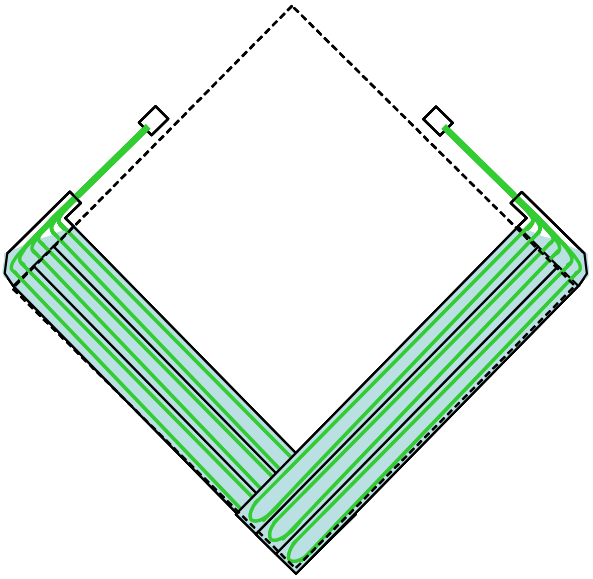

Fig. 4.9: A "Vee" design alternative for NOνA with the entire detector rotated by 45^{o} as seen by the neutrino beam.

only reduces the hydrostatic pressure problem by √2. The stress effect does not completely disappear if the detector is effectively only 11.0 meters high, and this alternative design still has to consider and deal with the same stress effects as the selected NOνA design. Analysis of the stress effects becomes more complicated since every cell now has aspects of both the horizontal and vertical cells in the selected NOνA design. Any building housing the "Vee" detector would have to be wider and taller, causing increased building costs. The support structure to hold the detector in this shape has been analyzed and found to require full support over 100% of the two bottom surfaces of the "Vee". Thus this design would restrict access to two of the four sides of the detector while the selected NOνA design allows access to three of the four sides. Vee structures have been eliminated from consideration.

4.5.3 A Bathtub Design Alternative

Another alternative design puts all the extrusion modules in a large bathtub and the bathtub is filled with scintillator. In this design, the extrusion modules are open at the end, so the inside and outside pressures on the modules are equalized. Since the extrusions no longer contain the scintillator, the bathtub must now serve as the primary containment vessel.

An X –Y (vertical – horizontal) readout is not possible in this scheme because the electronics on the horizontal cells must either be immersed in the scintillator or some 12,000 feed-throughs would be required through the walls of the bathtub containment vessel. The electronics require cooling to -15^{o}C, so immersion is not an option. The scintillator cannot be chilled to the TEC level without developing wax paraffin precipitates. An alternate scheme could have the horizontal fibers turn and continue to the top surface of the scintillator, but that adds too much extra attenuation length and additional fiber costs. A "Vee" scheme with 45^{o} or shallower stereo is a solution and such an example is shown in Figure 4.10. A shallow stereo angle is preferred or the detector builds up large dead areas on the sides (red areas in Figure 4.10). The dead areas must be filled with scintillator and drive up the cost of this alternative design. Shallow stereo systems tend to suffer from decreased pattern recognition and the example in Figure 4.10 has poor resolution for the vertical position of tracks from neutrino events when compared to the selected NOνA design.

The main containment bathtub must now be a rather substantial and expensive structure interior to the secondary containment of the excavation. All access to electronics is now on only one side of the assembly. Since the assembly tables and block raiser are still required, this alternative scheme requires assembly of 6 kilotons of plastic before the containment vessel can be completed and before any filling of the detector can begin. Multiple smaller bathtubs can reduce these effects, but bathtub alternatives have been eliminated from consideration.

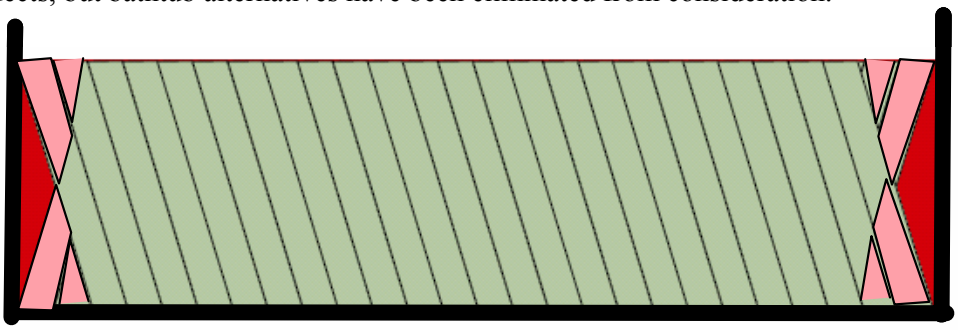

Fig. 4.10: A schematic bathtub alternative design. Alternate planes of extrusion modules are at ±12^{o} stereo. The triangular red areas on the sides of the detector are not instrumented yet still must be filled with scintillator. The two readout views do not overlap at the edges (pink area).

4.5.4 A Design Alternative based on International Shipping Containers

Another alternative design considered for NOνA is based on a steel construct derived from the design of intermodal shipping containers or ISO (International Standards Organization) containers [13]. These boxes have a strong steel frame made of vertical posts and horizontal rails. The bottom of the container is an arrangement of steel channels with a plywood floor to hold the container load. The entire structure is sheathed in thin 2mm thick steel to provide a weathertight structure. In international trade the containers are stacked 10 high in container ships with the strong vertical posts taking the load of the containers in the stack. The containers can be as long as 53 feet since they are sized for domestic trucks just as our extrusion modules have been kept below 53 feet for transportation reasons.

Figure 4.11 shows a custom container design alternative for NOνA. This container is the same length and height as an ISO container, but is only half as wide (4 ft vs. standard 8 ft) so that it can support the weight of the NOνA detector. Like the ISO version, the alternative NOνA version has 4 corner posts and 4 interior posts. Since the floor of the standard ISO container is a thick 15 cm steel channel superstructure, this alternative NOνA custom container has a trusscore floor only 1.3 cm thick (see Figure 4.12).

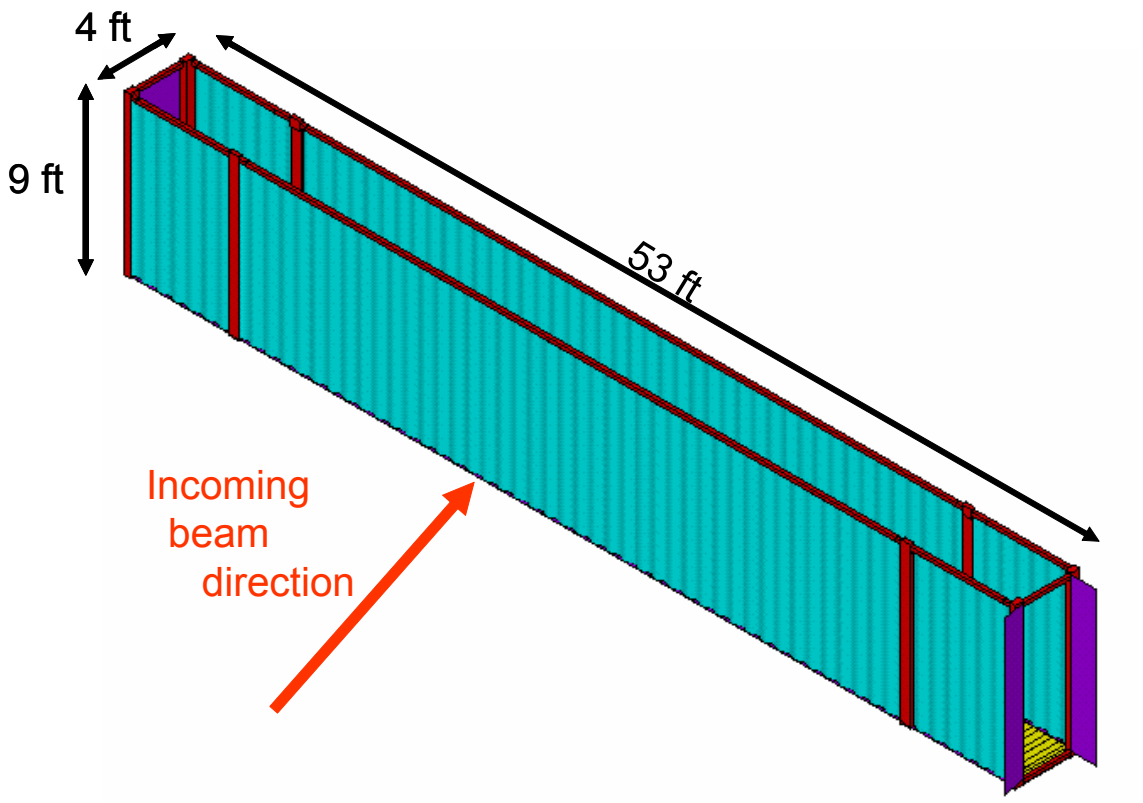

Fig. 4.11: A custom ISO container alternative design. The 8 strong vertical posts are shown in red, the trusscore floor is shown in yellow, and the two ends have doors for access. The top of the container is not shown.

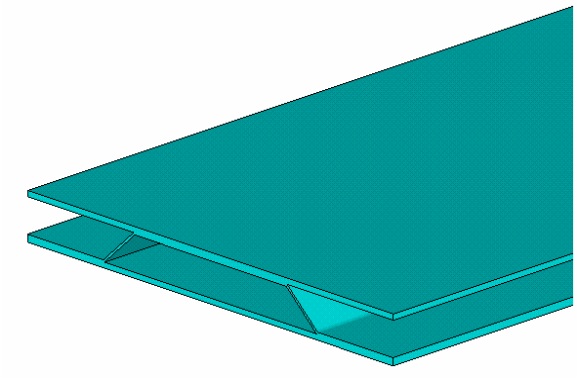

Fig. 4.12: A section of the thin trusscore steel floor used in the custom ISO container design of Figure 4.11. The top sheets are 3mm thick steel and the truss is 2 mm thick steel. This package has sufficient strength for the container and is only 13 mm thick.

The final detector in this alternative scheme is formed by stacking the containers 6 high in ~ 100 rows as shown in Figure 4.13. The trusscore floors transmit the load of each container to the strong steel corner posts and those posts are strong enough to bear the load of 5 containers stacked on one. Access to the containers is limited since the doors cannot be opened when a container has additional containers on top. Repairs of electronics would require removal of containers in a stack to expose the one to be repaired. Full (50 ton) containers can be moved with a standard building crane.

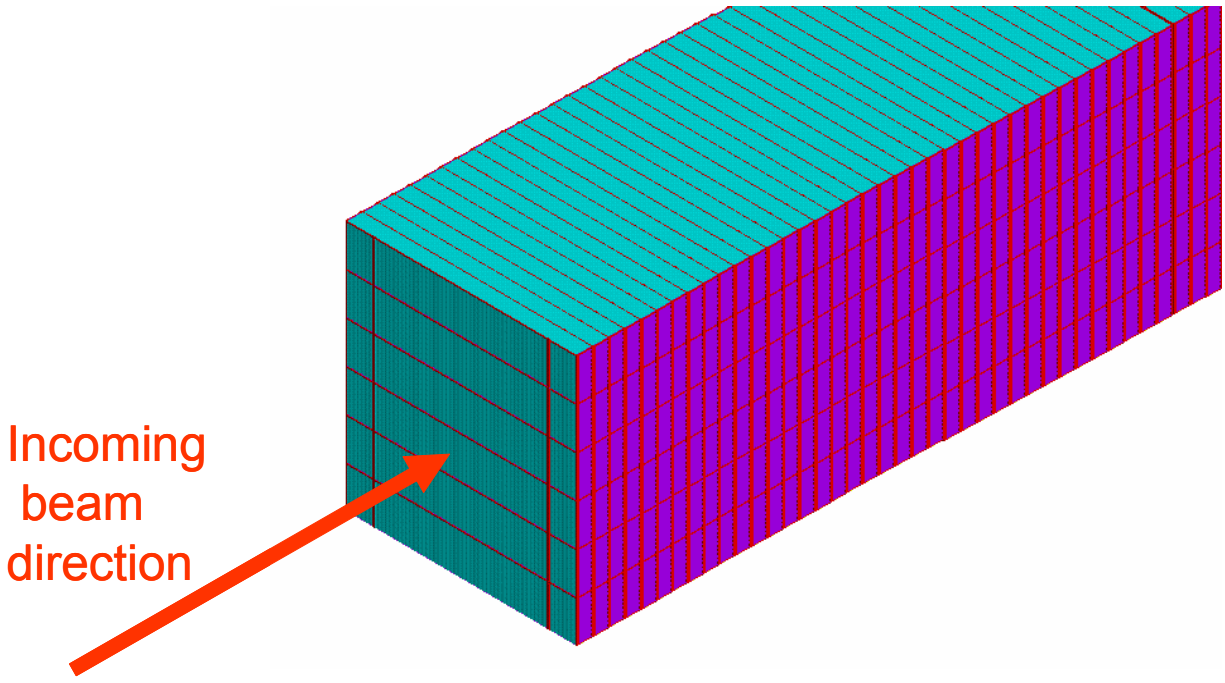

Fig. 4.13: The final arrangement of containers in the alternative design. Containers like the one in Figure 4.11 are stacked six high in ~ 100 rows along the beam direction.

This alternative NOνA design has several advantages. The vertical extrusion modules are only 2.7 meters long and can use thinner (cheaper) fibers to achieve the required light level. The vertical pressure in a 2.7 meter tall object is reduced to ~ 3 psi and the stress effect on the plastic is considerably reduced. The steel frame holds the modules in the proper orientation and the layers can be assembled without adhesive. Disassembly is straightforward. All the filling of extrusion modules can occur in one place and a building-wide distribution system for liquid scintillator is not required. The containers serve as secondary containment modules, reducing the containment requirements on the building periphery. Fire protection issues are reduced with all the flammable parts held inside a metal box. The containers help provide a light-tight box for the detectors.

The containers provide a natural shipping box to move the completed empty extrusion modules from the factories to the Far Detector site. When loaded with empty extrusion modules, two such containers can be transported side by side (2 x 4 feet) within the load limits for US trucks. With all the extrusion modules full of scintillator, the module weighs 50 tons and can be moved by crane. If the scintillator is removed from the horizontal extrusion modules, the half-full container still meets the truck load limits, making the detector mobile for a future experiment.

This alternative NOνA design also has two significant disadvantages. Since the vertical extrusions are effectively split into 6 separate parts, there are more APD channels and the electronics cost is six times higher for the vertical cells in this detector than in the selected NOνA design. This increased cost is partially offset by savings in fiber, scintillator distribution, and adhesives, but a close accounting has shown that this alternative design is ~ 10% more expensive than the selected NOνA design. The stack of six containers also means that there are 5 horizontal dead areas in the detector around the five cracks shown in Figure 4.13. In our simulations, the detection efficiency for ν_e interactions in such a device is reduced by 5% - 10% due to these cracks, depending on the total size of the crack (trusscore floor + gap for routing the fibers out of the vertical modules). The general conclusion is that the alternative container scheme costs slightly more and likely has a somewhat lower efficiency for neutrino interactions. This alternative is no longer being pursued.

Chapter 4 References

[1] Steve Dixon, Trip Report: Visit to Potential Sites for Far Detector in St. Louis County on September 1-2, 2005, NOνA docdb note 68, 2005

[2] Steve Dixon, American Engineering Testing, Inc Report of Subsurface Boring and Piezometer Installation, NOνA Off-Axis Site, NOνA docdb note 162, November, 2005. See also NOνA docdb note 108, Preliminary Ash River Boring Logs, October, 2005.

[3] D. Ayres et al., Letter of Intent to build and Off-Axis Detector to Study $\nu_\mu \rightarrow \nu_e$ oscillations in the NuMI Beam, hep-ex/021005, June 2002.

[4] Y. Fukuda et al., Phys. Lett. B335, 237 (1998).

[5] C. Rubbia, The Liquid Argon Time Projection Chamber: a New Concept for Neutrino Detector, CERN-EP/77-08(1977)

[6] S. Amerio et al., Design, construction and tests of the ICARUS T600 detector", NIM A527 329-410 (2004)

[7] MINOS Technical Design Report, Fermilab, NuMI-L-337 (1998)

[8] P. Border et al., NIM A463 (2001) 194-204, and L. Benussi et al., NIM A488 (2002) 503-516.

[9] BELLE KLM Detector group, NIM A 449, 112-124 (2000).

[10] D. Ayres et al., March 2004 NOνA Proposal, http://www-nova.fnal.gov/reports_page.html

[11] S. Wojicki and T. Yang, NOνA Note 25, November 2003.

[12] P. Litchfield and R. Ray, NOνA Note 40, June 2004.

[13] International Standards Organization, ISO 668, Freight Containers, 5th edition, 1995.

5. Optimization of the Selected NOνA Design

5.1 Introduction

In addition to the site, technology, and structure alternatives discussed in Chapter 4, the selected NOνA design itself has been extensively optimized. This chapter gives a general overview of this optimization, concentrating on the totally active liquid scintillator detector technology in the basic NOνA cell. Optimizations of the cell segmentation and of the cell light level are examined in detail. Performance, cost, performance risk, and cost risk are considered for each part of the selected design. The iterative process of systems engineering and the best value techniques of value management methodology were applied in this optimization process. Additional quantitative optimizations of the detector cell technology are described in Chapters 9 – 14, while this chapter focuses on how each part of the selected technology interacts with other parts.

Optimizations of the site and conventional construction are not presented here and are discussed separately in Chapters 7 and 8. Optimization of the detector assembly is discussed separately in Chapters 15 and 16. Further value management studies are anticipated in all areas as the NOνA design moves from the conceptual phase to a technical design report and a performance baseline.

5.2 Optimization of the NOνA Detector Segmentation

Consider a single basic NOνA cell illustrated again in Figure 5.1. There are four basic components: a PVC extrusion, liquid scintillator, a wavelength shifting fiber, and an avalanche photodiode (APD) photodetector. Performance of this basic cell is characterized by the APD signal detected from the far end of the long cell.

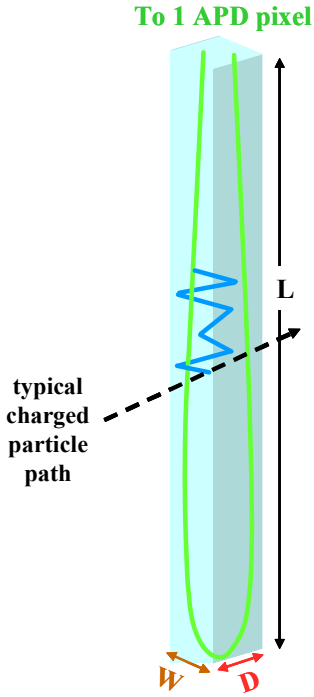

Fig. 5.1: The NOνA PVC cell of dimensions (W, D, L) containing liquid scintillator and a wavelength-shifting fiber (green). A charged particle incident on the front face produces light (blue line) that bounces off the cell walls until absorbed by the fiber. The fiber routes the light to one APD pixel.

The selected NOνA design has a cell width of 3.9 cm and a cell depth of 6.0 cm. The simulated relative experimental sensitivities for identifying $\nu_\mu \rightarrow \nu_e$ oscillations for different cell widths and depths are shown in Table 5.1. In these simulations the light level per cell was kept constant and the Figure of Merit (event signal divided by the square root of the background level) was computed.

Cell Width (W)	3.9 cm	5.0 cm	8.0 cm	12.0 cm
Cell Depth (D)				
4.5 cm	1.00	0.99	0.98	
6 cm	**1.00**	1.02		0.87
9 cm	0.92		0.92	
15 cm	0.80			0.71

Table 5.1: Relative Figure of Merit for various combinations of cell depth and width. Different combinations are compared to the selected NOνA design of 3.8 cm by 6.0 cm shown in red. The statistical uncertainty for each entry is 0.015, so variations of 0.02 or less may not be significant. This simulation assumed the light level per cell was constant for all configurations.

In the longitudinal direction, the simulation results in Table 5.1 indicate that the performance would fall off beyond depths of 6 cm. Based on these simulation results, we extended our original design of 4.5 cm depth to 6 cm.

The simulation results indicate that the selected design width of 3.9 cm could be expanded by around 30% without loss of sensitivity. However, such an expansion would not reduce the cost of the experiment for several reasons. First, the light level per cell would be lower since the average path length between reflections would increase and the light would be attenuated by the scintillator. The light level would also be lower because the average solid angle subtended by 0.8mm fibers would decrease if the wall were on average further from the fiber. Additional reflections and additional path in the attenuating liquid would be required to reach the fiber. Simulation results for the light level in cells corresponding to Table 5.1 are shown in Table 5.2.

Cell Width (W)	3.9 cm	5.0 cm	8.0 cm	12.0 cm
Cell Depth (D)				
4.5 cm	0.89	0.74	0.58	0.44
6 cm	**1.00**	0.83	0.67	0.52
9 cm	1.15	1.02	0.81	0.66
15 cm	1.39	1.20	1.02	0.83

Table 5.2: Relative light observed in a looped fiber for various combinations of cell depth and width. Different combinations are compared to the selected NOνA design of 3.8 cm by 6.0 cm shown in red. The simulation assumed the two fibers were in diagonally opposite corners of the cell.

Wider cells do not increase the path length of track incident on the front face of the cell (see Figure 5.1) and therefore do not increase the light level. Table 5.2 indicates that a cell 30% wider would have 17% less light than the selected NOνA design. Recovering this lost light output via thicker wavelength shifting fibers or increased pseudocumene and waveshifter content in the scintillator is expensive (see Section 5.4).

Second, the PVC extrusion walls would need to be thickened to provide additional strength. To keep the PVC stress level constant relative to the selected design while under pressure from the 19 psi liquid loading, a cell width of 5.0 cm requires PVC walls that are about 50% thicker than in the selected design. This is because the span between the interior webs increases and yet still must resist the internal pressure without a larger outward deflection. Handling heavier extrusions at the extrusion module factories and at the far site assembly would increase the overall cost.

Third, even though the channel count would decrease by 20%, the cost would not decrease. In principle wider cells implies fewer cells in the detector, but thicker walls mean the mass and cost of PVC would increase. The amount of fiber would be reduced by 20%, so fibers with 12% larger diameter (mass of fiber is proportional to the square of the diameter) could be used at neutral cost. The larger diameter would deliver more light, but less than 12% more since the path length in the attenuating scintillator would still be longer. The electronics cost would be decreased by 20%, but this is not enough to offset the increased cost of PVC. All these arguments assume a 30% wider extrusion, still with 32 cells, could easily be obtained in industry. This may not be the case, meaning the electronics board count would not be reduced at all.

One final note on segmentation: Even if our present simulations indicate no or little loss in increasing the segmentation, we are reluctant to change the segmentation for small reductions in the cost of the experiment since the change could potentially limit our ability to improve the efficiency of the signal pattern recognition and of the background rejection. The NOνA detector relies on its fine-grained measurements to identify the relatively rare $\nu_\mu \rightarrow \nu_e$ oscillation events. The electron in these events is identified as a fuzzy track with the characteristic longitudinal and transverse energy profiles discussed in Chapter 3, section 3.5.3. Electrons can be discriminated from neutral pions by the transverse energy distribution, gaps before the event vertex, and double pulse height at the start of the track. All these event selection variables are related to the width and depth of the cell.

5.3 Optimization of the NOνA Cell Light Threshold Level

The number of photoelectrons from the far end of a cell is a parameter that can be controlled by a number of different factors including the reflectivity of the PVC walls, the diameter of the wavelength-shifting fiber, the positioning of the fiber, and the amount of pseudocumene and wave shifters in the scintillator. Since some of these parameters may significantly affect the cost of the experiment, it is necessary to carefully consider the minimum requirement for this quantity. Sections 5.4 and 5.5 discuss the costs in more detail. This section describes the simulation work done to establish the light level in the selected NOνA design.

The NOνA front-end electronics simply transmits all signals above a preset threshold to the data acquisition (DAQ) system. There are two considerations with regard to the minimum allowable threshold. First, the data rate must be low enough to not overwhelm the DAQ system. Second, the noise must be sufficiently low so as to not affect the pattern recognition of the signal events.

The scale of the data to the DAQ system is set by the cosmic ray rate. We estimate the cosmic ray rate to be approximately 400 Hz per channel. With 643,000 channels and 10 bytes per hit, this corresponds to a data rate of 2.6 GB/s. A conservative goal would be to limit the noise rate to one-quarter of this value, or an additional 0.65 GB/s. The noise will be dominated by the the amplifier noise, but a long tail of noise is seen due to excess noise of the APDs, shown in Figure 5.2. Taking the relevant time window to be 1ms, this requirement corresponds to a noise hit probability of 10^{-4}. From Figure 5.2, this gives a minimum threshold of 15 photo electrons. The largest events of relevance have a domain of interest approximately 2 m in width and 18 m in length. This corresponds to 15,000 cells, so a random noise probability of 10^{-4} would yield an average of 1.5 noise hits per event. This is clearly an acceptable level.

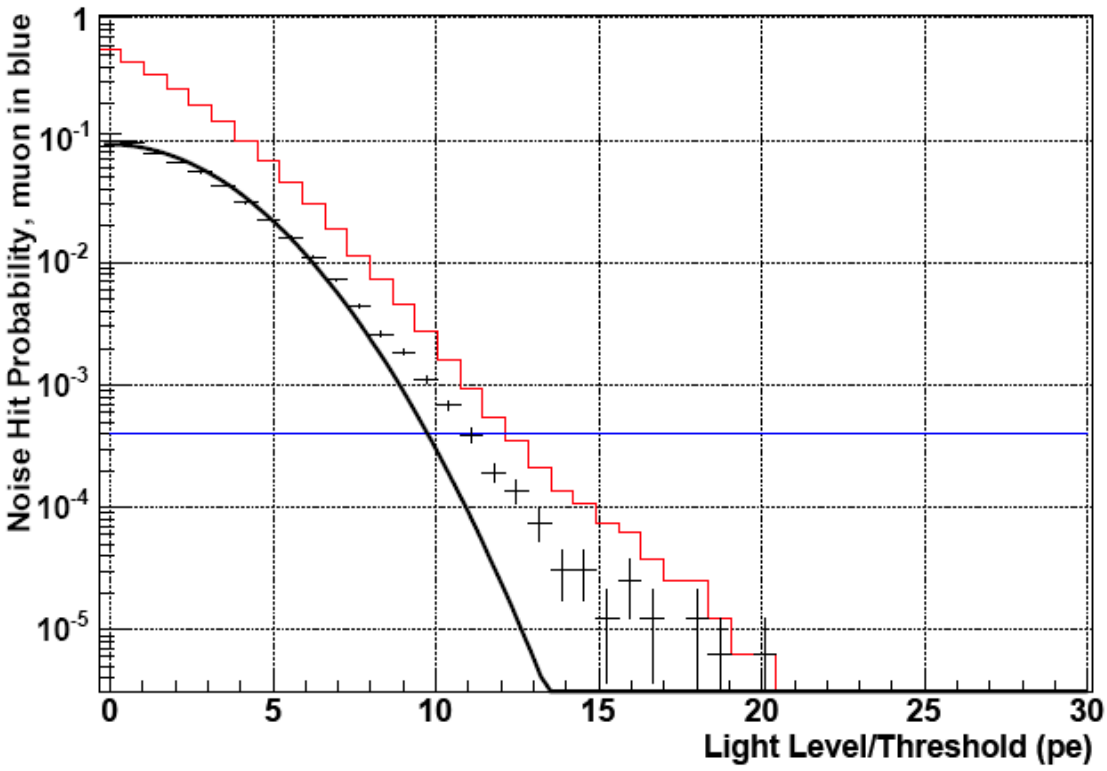

Fig 5.2: Noise hit probability versus the light threshold in photoelectrons. The top (red) histogram gives the integrated hit probability and the (blue) horizontal line is the expected hit probability from cosmic rays. The data points are shown as crosses and the best fit Gaussian is the black line.

Figure 5.2 shows the noise hit probability for the amplifier in our test cell which has a mismatched capacitance to the APD. A new matched ASIC amplifier has been designed and submitted for prototype quantities. We expect that amplifier to be much quieter with a noise level of ~ 150 electrons compared to the higher noise level measured and presented in Figure 5.2. Figure 5.3 shows our expectations for the noise hit probability with the new ASIC amplifier. In this case the same noise hit probability of 10^{-4} leads to a minimum threshold of 10 photo electrons.

Given that the threshold is 10 - 15 photoelectrons, the next issue is what light level is required to give adequate pattern recognition. Figure 3.20 in Chapter 3 shows the results of a measurement of the light output of cosmic ray muons from the far end of a prototype NOνA cell. Gaussians with means of 20 - 22 photoelectrons fit the distributions. Note that a threshold of 15 would prevent the readout of a substantial fraction of normal incident minimum ionizing particles from this area of the detector. Further note that some signals will be split between two cells in a given plane.

Nonetheless, our current simulations do not seem to have a strong dependence on the light output. Table 5.3 gives the relative Figure of Merit for different combinations of thresholds and minimum ionizing particle light outputs from the far end of the cells. Although we are wary of setting too low a light requirement, which could compromise our efforts to improve our analysis algorithms, these simulations indicate that our scientific performance requirement on the Figure of Merit translates into a requirement of 20 photoelectrons from the far end of the cell.

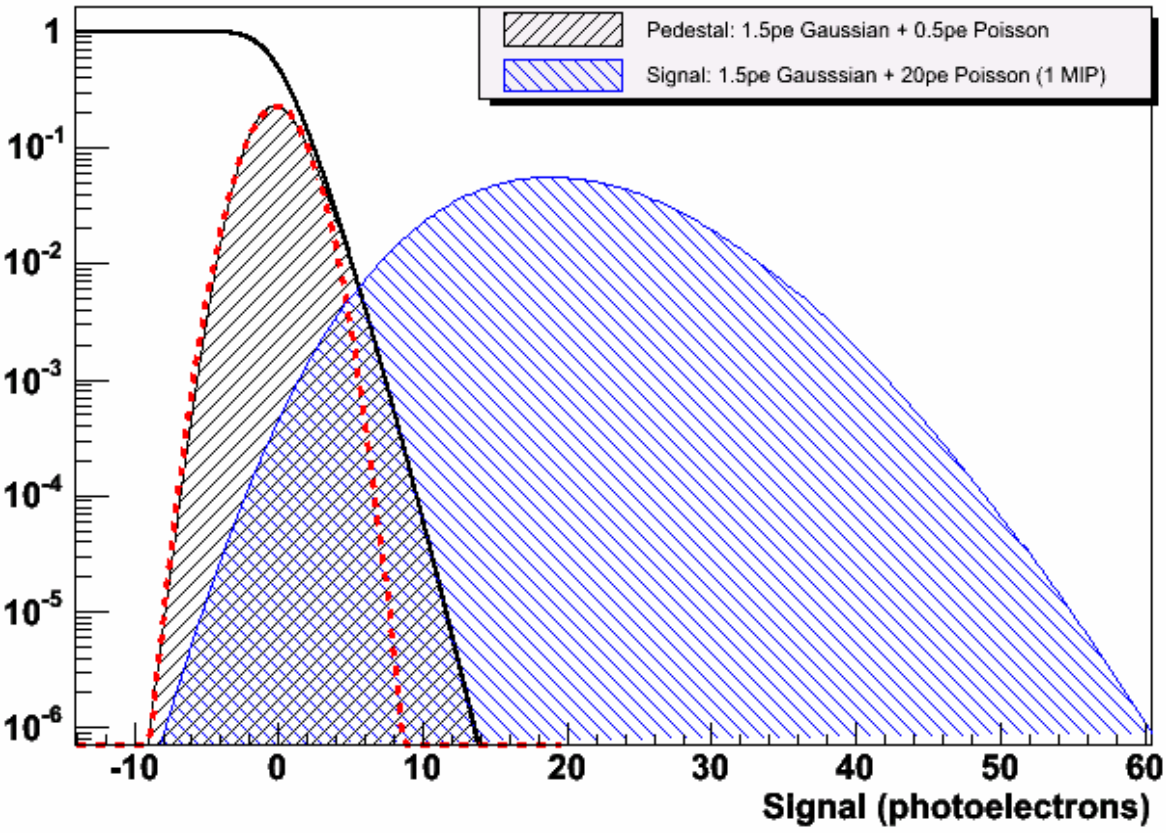

Fig 5.3: Expected noise hit probability versus the light threshold in photoelectrons with the new ASIC amplifier being prototyped. The top (black) curve gives the integrated hit probability and the dashed (red) curve is the expected noise distribution from the amplifier. The blue area indicates the expected signal from minimum ionizing particles.

Signal (pe)	10	15	20	25
Threshold (pe)				
10	0.95	1.00	1.02	1.00
15			1.00	
20			0.98	1.00

Table 5.3: Relative Figure of Merit for a given threshold and average light output in photoelectrons from a minimum ionizing particle transiting the far end of a NOvA cell.

5.4 Optimization of the Horizontal Cell Readout Orientations

Why is the Figure of Merit so insensitive to high thresholds on the average light output levels as shown in Table 5.3? First recall that we have been talking about the light level from the very far end of the 15.7 meter long NOvA cell. On average, most events have much more light than the minimum 20 - 22 pe. This is illustrated in Figure 5.4 where the number of photoelectrons is shown in a color code as a function of distance along the cell. The average number of pe in the cell is about 45 if the light level at the far end is 20 pe. In addition, the

threshold is not being set on just one piece of information but separately on many pieces of information. The NOνA detector is a calorimeter, and the average events extend over many planes and many cells as shown in the sample event displays in Chapter 3, Figures 3.23 – 3.27. The loss of a few cells does not have an immediate effect on the pattern recognition in this tracking calorimeter.

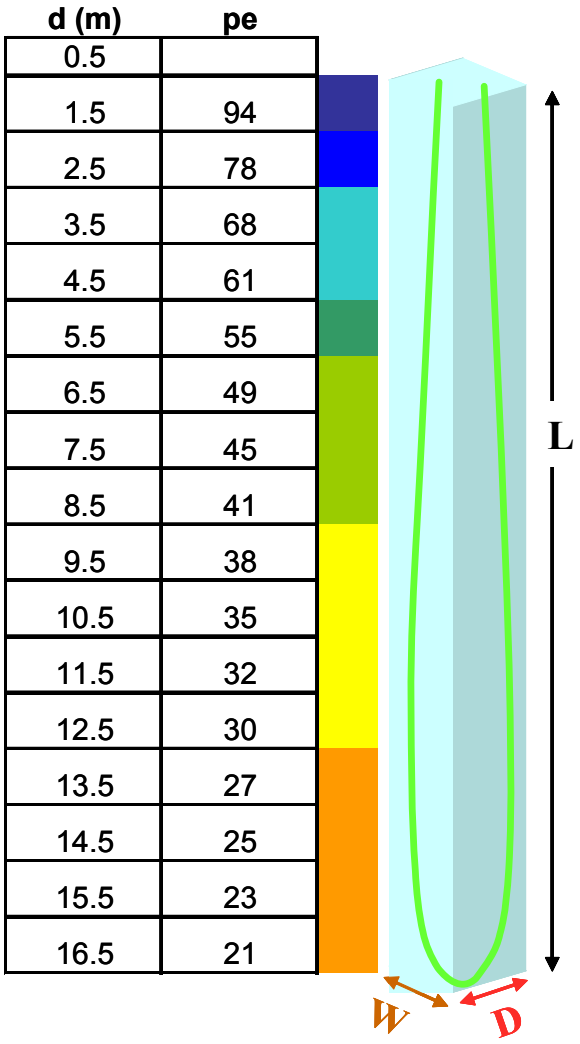

Fig. 5.4: The average number of photoelectrons in a NOνA cell as a function of distance d from the APD. The cell is broken up into 1 meter long sections. Note the fiber has to exit the cell and run a short distance to the APD, so the effective length of the cell is longer than the physical 15.7 meters filled with scintillator.

The NOνA design has also been optimized by alternating the readout direction on successive horizontal planes of cells. If we read out the detector on the top and the right sides only, then the average number of photoelectrons per plane would have the response function shown in Figure 5.5. This shows a wide variation in average pulse height per plane from 21 pe in the lower left corner to nearly 100 pe in the upper right corner. By instead reading out on the left and right and top sides of the detector, the response function is more even with the average number of photoelectrons per plane shown in Figure 5.6. This optimization flattens the response to a range from 30 pe in the lower center to 75 pe in the upper left and right corners.

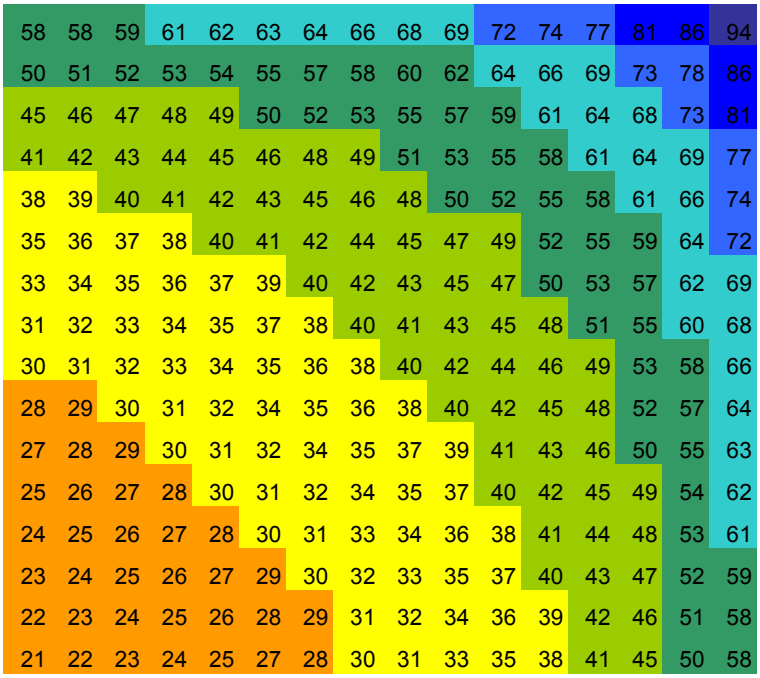

Fig 5.5: The average number of photoelectrons per plane in 1meter by 1 meter sections of the NOνA calorimeter as seen by the neutrino beam. This is the distribution seen if the detector is read out on the top and the right hand side for vertical and horizontal cells. The color code is the same as in Figure 5.4.

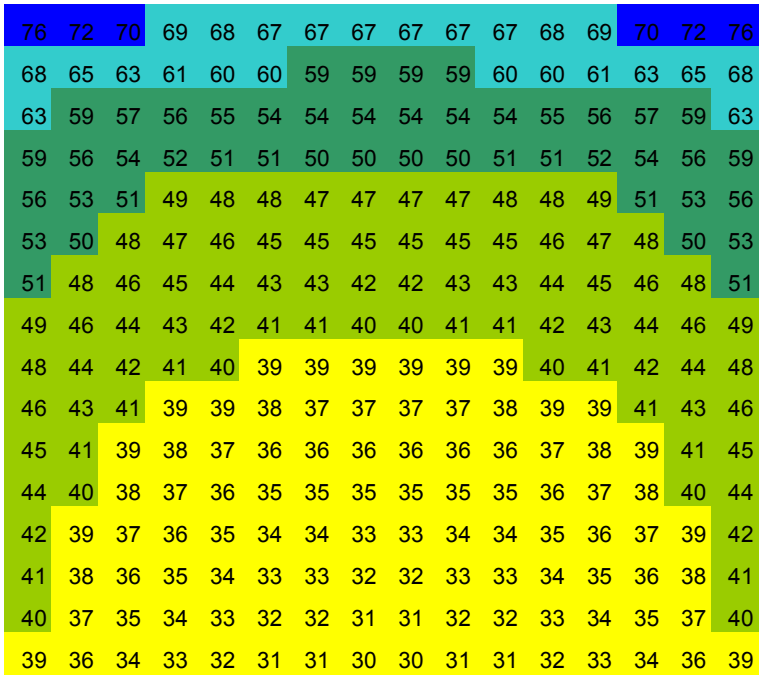

Fig 5.6: The average number of photoelectrons per plane in 1meter by 1 meter sections of the NOνA calorimeter as seen by the neutrino beam. This is the distribution seen if the detector is read out on the top for vertical cells but with alternating left and right side readouts for the horizontal cells. The color code is the same as in Figure 5.4.

5.5 Further Performance / Cost Optimization of the NOνA Cell Design

Section 5.4 illustrates that the scientific performance requirement on the Figure of Merit translates into a performance requirement for the basic cell to see an average of 20 photoelectrons (pe) from the far end of the cell. The characteristics of each component of the selected cell design are examined here and optimization of that component for the 20 pe performance requirement is discussed. During the design optimization, particular attention has been given to the interactions among the components and those inter-relationships are discussed. The four simple NOνA cell parts (PVC, scintillator, fiber, photodetector) have been divided into 23 separate variables and each of these variabless is evaluated in sections 5.4.1 – 5.4.5 below. Many of the 23 variables have no possible performance increase but will have performance risk and cost risk attributes discussed in Section 5.5. Sections 5.4 and 5.5 keep the same numbering in an attempt for clarity.

Each variable is evaluated below with increased light output performance ranked as low, moderate, or high according to the classification scale in Table 5.3. Since the detector has been optimized, a large swing in cost is typically required to realize a particular performance gain. For the purposes of this section, we classify the cost using the scale outlined in Table 5.3. Approximate base costs are used for this analysis. Since this Conceptual Design Report is a public document, specific detailed costs are not given here so that competition in the marketplace can realize the best possible prices. Our Basis of Estimate and Resource Loaded Cost and Schedule documents contain the actual cost numbers obtained to date via official quotes acquired by the Fermilab Business Services Section.

	Low	Moderate	High
Increased Performance Level	Less than 10% increase in performance	10 -20 % increase in performance	Greater than 20% increase in performance
Associated Cost	Required cost increase is less than ~ $ 1M	Required cost increase is in the range ~ $ 1 – 5 M	Required cost increase is greater than ~ $ 5 M

Table 5.4: Performance and cost level definitions used in Section 5.5.

5.5.1 Performance Optimization for PVC Extrusions.

Seven aspects of the PVC extrusions are considered in this performance - cost study. Chapter 11 contains additional details of the NOνA PVC extrusions.

1) PVC Raw Resin. The rigid PVC is made via an extrusion process from a raw resin. The light output performance of the cell can't be increased with changes to the basic resin, so this variable is ranked as a neutral. The associated cost is also neutral.
2) PVC Reflectivity. The reflectivity is linked to the amount and type of titanium dioxide (TiO_2) in the PVC. A 1% change in reflectivity gives ~ a 10% increase in light output. The selected design already has 93% reflectivity with a 15% TiO_2 (in rutile form) admixture, so additional reflectivity gains are difficult. The rutile TiO_2 cost per pound is only about $ 0.01 per pound more than rigid PVC resin and our design calls for ~ 15 M pounds of PVC. Higher percentages of TiO_2 are more difficult to extrude and lead to increased extrusion costs. Above about 15% TiO_2 the extrusion machines run more slowly (time = money) and somewhere around 20% TiO_2 the extrusion process does not work with existing manufacturing equipment. A 20% admixture may give a 2 -3 %

increase in reflectivity and this is under study in our R&D program. This variable has the potential for a high performance gain with a low associated cost.

3) Other PVC Additives. Rigid PVC extrusions use a complicated mixture of raw PVC resin with additives designed to facilitate the extrusion (heating) process. Additional additives have low cost, and appear to have a negative effect on reflectivity performance, reducing 93% reflectivity to as low as 88% reflectivity. However, the extruded PVC surface quality can be enhanced with the addition of some additives, giving perhaps 1-2% additional reflectivity. Experience so far shows mixed performance results from additional additives. More experience with R&D samples may lead to a different view of this variable, but it is now rated as a neutral performance gain for a low associated cost.
4) PVC Extrusion Process. Recall that we have optimized the design with the scalloped cell shape and with an outside wall to inside web ratio of 3:2 as advised by extruder vendors. Changes to the optimized cell scalloped profile or wall / web thickness do not hold any promise for increased performance of the cell for light collection. This variable is rated as a neutral performance gain for a neutral associated cost.
5) PVC Cell Length. The light reaching the APD must travel through the long fiber and is attenuated along that length. The maximum cell length is set by the fiber, not by the PVC. Shorter cells could be contemplated, giving more light from the far end of each such shorter cell. In the spirit of this section we consider reducing the cell length by 25%, from 15.7 m to 11.8 m. At 75% of the cell length, the light is increased by ~ 50%, so this would be a high performance gain. Reduced cell length would imply 33% more PVC cells to reach the same detector mass, requiring 33% more ends for the assembled extrusion modules, more assembly labor, and more APD / electronics channels. In addition the Far Detector building would have to be less wide, less deep, but longer. The excavation costs for such a modified building are about the same as the selected design, but the cost of a longer overburden is higher. Overall this variable has a high performance gain with a high associated cost.
6) PVC cell profile. The NOνA cell size is ~ 4 cm by 6 cm. As discussed in Section 5.2, the scientific performance requirement on the Figure of Merit allows increasing the cell width by 30% but does not allow an increase in cell depth. The wider cell leads to reduced light output performance due to the increased light path lengths. These wider cells imply 20% fewer cells in the detector and this does lead to a reduced cost of fiber and electronics. Following Section 5.2, the fiber savings would be used to regain the lost light output. The wider cells would require ~ 50% more PVC per cell to keep appropriate structural safety factors. The 50% more PVC would be accompanied by a reduced amount of scintillator to keep a constant detector mass. Overall this cell profile change would have at best a neutral performance gain at an associated cost of ~ $ 1 M.
7) PVC Adhesive. This variable cannot improve the light collection performance and has no associated cost.

5.5.2 Performance Optimization for the Liquid Scintillator.

Seven aspects of the scintillator are considered in this performance – cost study. Chapter 9 contains additional details of the NOνA liquid scintillator.

8) Scintillator Scintillant. The basic amount of scintillator light produced is critical to the cell performance. The NOνA design has been optimized by studying light output from scintillators with 5% - 10% pseudocumene as the scintillant and a 5.5% mixture has been selected. Our optimization has chosen a pseudocumene level just adequate for the scientific performance requirement, largely because pseudocumene is an expensive component (~ $5 per gallon for ~ 0.3 M gallons) and we have minimized the cost. The light output can be increased by 18% with a 10% pseudocumene mixture but only if the

scintillator waveshifters are increased at the same time (see variable #9 below). So a moderate increase in performance can be had for a moderate increase in cost according to the definitions in Table 5.4.

9) Scintillator Mineral Oil. The dominant component of liquid scintillator is mineral oil used as a solvent and constituting 95% of the liquid in the selected design. Most of the detector mass is in this component, and the cost is high at several dollars per gallon for about 6.4 million gallons. The selected design assumes a mid-grade of mineral oil, oil with attenuation lengths in the 2.5 – 10 meter range. Increased performance to attenuation lengths of > 10 meters is possible and gives a ~5% increase in light output associated with an additional cost of ~ $1 - $2 per gallon. This variable has low performance increase with an associated high cost.
10) Scintillator Internal Waveshifters. These waveshifter concentrations scale roughly with the amount of pseudocumene, and one in particular (PPO) is quite expensive, approximately twice the price of the pseudocumene scintillant. As discussed above for the pseudocumene variable #8, an 18% gain in light output can be realized by doubling the amount of waveshifters and pseudocumene. This variable has a moderate performance increase with an associated very high cost increase.
11) Scintillator Blending. If done correctly, mixing of the scintillator components has no effect on the light output performance level. The components do have to be mixed, but there is no associated cost related to performance.
12) Scintillator Attenuation Length. The light produced by the traversing charged particle must pass through the scintillator over a mean path of ~ 50 - 100 cm, so the attenuation of the light by the composite mix of scintillator components is a crucial parameter. The selected NOνA design has an attenuation length > 2 meters. This variable is driven by the clarity of the pseudocumene when the mineral oil is of high quality and is driven by the clarity of the mineral oil when the mineral oil is of low quality. As in item 9), choosing a higher quality mineral oil can lead to a low increase in performance with an associated high cost.
13) Scintillator Oxygenation. The selected design assumes the lower level of light output produced by fully oxygenated scintillator, approximately 20% less light than un-oxygenated scintillator. Air diffusion through the PVC walls will naturally oxygenate the NOνA scintillator. The performance could be increased 20% by bubbling nitrogen though the vertical cells, but this does not work for the horizontal cells. Overall this variable is ranked as a low performance increase with an associated moderate cost.
14) Scintillator Flashpoint. This variable is not related to light output performance and there is no associated cost.

5.5.3 Performance Optimization for the Fiber.

Five aspects of the wavelength-shifting fiber are considered in this optimization description. Chapter 10 contains additional details.

15) Fiber Diameter. The wavelength-shifting fiber captures more light in direct proportion to its diameter, while its cost goes as volume (= diameter squared times the (fixed) length). Our selection of 0.8 mm diameter is matched to the APD pixel size, but diameters up to 0.9 mm may be possible, giving a 13% performance increase. The associated cost would be 26% more and in the high range.
16) Fiber Flexibility. The fibers lose a few percent of the light when bent sharply. Relaxing the bend requires a larger cell width or depth and is not possible. There is no particular cost break for flexible fibers.
17) K27 Wave-shifting Dye Concentration. With more K27 dye, the fiber captures more light. However, the dye is also self-absorbing for short wavelengths, dominating the

attenuation length of the fiber. The selected design has 200 parts per million of K27 and exactly follows the MINOS experience for 1.2 mm diameter fibers of length ~ 8 m. Expectations are that the light output performance cannot be influenced by more than 10% by the amount of K27 (of course one can make the performance zero with zero K27). The dye is not expensive. K27 concentrations continue to be the subject of NOνA R&D work.

18) Position of the Fiber in the Cell. In the horizontal cells, the fiber will gravitate to the PVC walls. In the vertical cells, the fiber has no particular constraint except near the bottom of the cell where it wants to snap into opposite corners to maximize the bend radius. The scalloped PVC cells in the selected design have corners of radius 3 mm and are in a middle range between a sharp corner and a flat wall relative to a 0.8 mm diameter fiber. Simulations indicate about a 10% loss of light when a fiber is against a wall or a 20 – 30% loss in a sharp corner, but actual measurements find no observable effect. Controlling the position of the fiber does not have any potential performance gain even though cheap positioning devices might be imagined.

5.5.4 Performance Optimization for the Photodetector and Electronics.

Four aspects of the photodetector / electronics are considered in this optimization overview. Chapter 13 contains additional details.

19) APD pixel size. The APD pixels are a rectangular shape (1.1 mm by 2.3 mm) sized to hold two 0.8mm fibers from one cell. Performance of the pixels cannot be enhanced, though larger pixels would make larger fiber diameters (variable 15) possible. The cost of the APD is not strongly linked to the pixel size.
20) APD gain. The selected design operates the APD at a gain of ~100. The electronic noise from the device is optimized at about a gain of 90, so our selected design is near the noise optimum. Additional performance gains are not possible with this variable.
21) Thermoelectric Coolers (TEC). The NOνA design operates the APD at -15^0C to minimize the APD noise. Lower temperatures would give lower noise, but only by a few percent. One can consider operating at higher temperatures, but above 0^oC the noise increases by more than 33%, increasing the high tail in Figure 5.2 and increasing the required threshold in the detector. There is no associated cost savings from operations at slightly higher temperatures.
22) Electronics Amplifier Noise. Performance of the detector cell depends on recognizing a hit cell above the electronic noise background level. The selected design has minimized the amplifier noise in a new ASIC chip design and further gains do not seem possible. Multiple correlated sampling could be implemented in FPGA software to control the noise level even further. This might give as much as a 25% reduction in noise at almost no cost.

5.5.5 Performance Optimization and Cost Summary.

Figure 5.7 shows the Performance versus Cost vs. Performance for each of the 23 variable discussed above. Only twelve of the variables are shown on the plot since all the rest cluster in the neutral performance increase / neutral cost area (white area where the axes intersect). Variables in the green area (lower right corner) of the plot are candidates for further R&D to increase performance at little cost. Variables in the red are (upper left corner) of the plot are clearly not cost effective candidates for increased performance. Variables in the area between the two corners may be cost effective depending on details of the performance increase and cost.

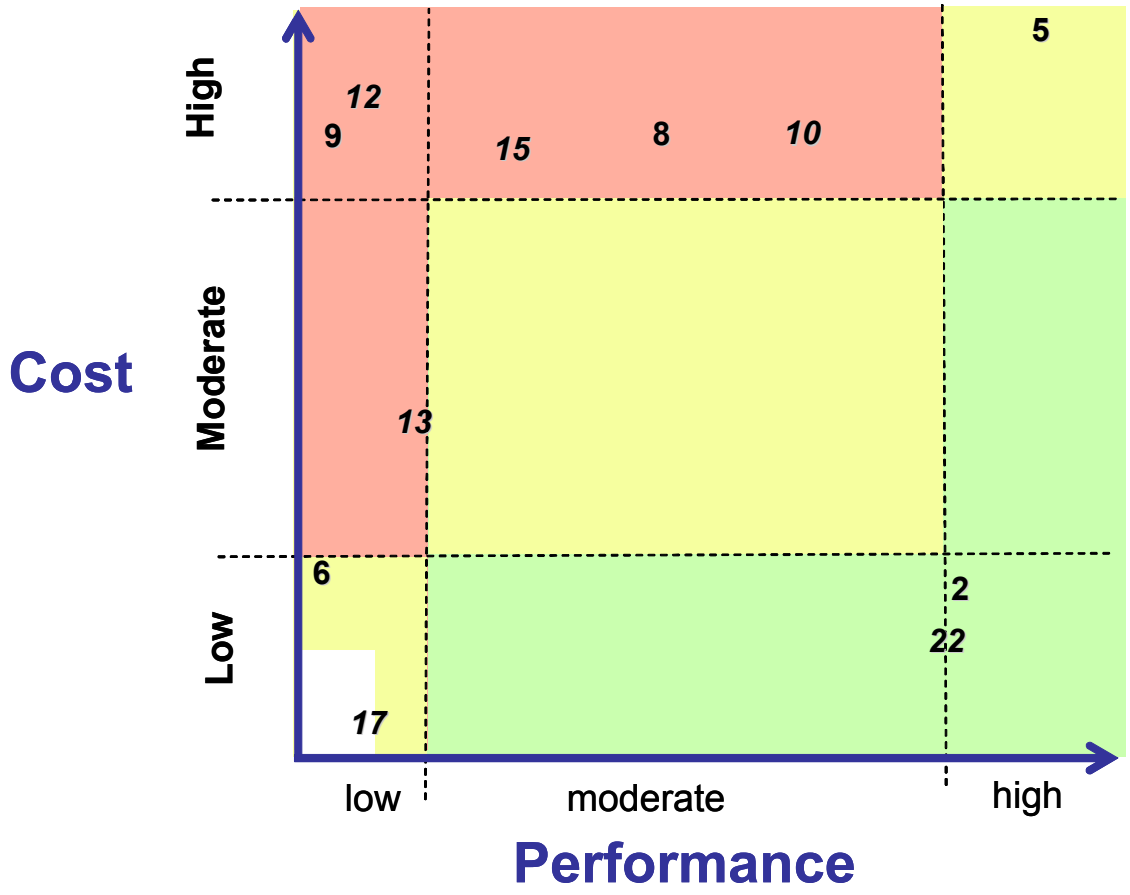

Fig. 5.7: Performance increases and associated cost plotted for the 22 variables in the basic NOνA scintillator cell. Only 11 of the 22 variable are shown since the other 11 variables would all cluster in the white area (lower left corner).

5.6 Risk Optimization of the NOνA Cell Design

Consider again the basic single NOνA cell illustrated in Figure 5.1. This section examines the same 23 characteristics of the cell with an eye to understanding of the links between technical risk and cost risk. Coupled with the discussion in previous section on performance and associated cost, these two views will guide future value management studies as the NOνA design moves from the conceptual design level to the technical design level.

The cost risk for each component is evaluated below with each cost and technical risk ranked as low, moderate, or high. For cost risk, the cost uncertainty is the quantized using the scale outlined in Table 5.5. This chapter groups performance risk, ES&H risk, project schedule risk, and detector lifetime risk into one technical risk category as shown in Table 5.5. The relative weights for four segments of Technical Risk are assigned so that one moderate risk segment makes an overall moderate risk, multiple moderate risks push the overall risk higher, if all four segments have moderate risk the total risk is evaluated as an overall high Technical risk.

The risk analysis presented in this chapter and in Table 5.5 is not a substitute for a complete formal risk management plan. The NOνA Risk Management Plan is discussed separately in Chapter 19.

		Low	Moderate	High
Cost Risk	Cost Uncertainty	Cost uncertainty of less than ~ $ 1 M.	Cost uncertainty in the ~ range $ 1M – 5 M	Cost uncertainty greater than ~$ 5 M
Technical Risk	Performance	No performance degradation: Loss of detected light less than ~ 10%	Significant performance degradation: Loss of detected light in the range of 10 -30%.	Performance effectively useless for attaining physics objectives: Loss of detected light greater than ~ 30%
	ES&H	No ES&H risk foreseen	Some ES&H risk	Potential for a large ES&H risk
	Schedule	Schedule risk small, less than a few months for the total project	Schedule risk in the range of ~ 3 -9 months	Schedule risk greater than ~ 9 months for the total project
	Detector Lifetime	No effect	Could limit detector lifetime to less than 10 years	Potential severe effect: performance requirement of an initial 5 year data run at risk

Table 5.5: Cost Risk and Technical Risk definitions used in Section 5.6.

5.6.1 Risk Optimization of the PVC Extrusions.

Seven aspects of the PVC extrusions are considered in this optimization description. Chapter 11 contains additional details of the NOνA PVC extrusions.

1) PVC Raw Resin. The PVC is made via an extrusion process from a raw resin. The resin is a derivative of crude oil, so the potential fluctuations in the price of crude oil introduce a moderate to high cost uncertainty for this variable. On the performance side the risk is low: there are modest ES&H issues due to the chlorine in PVC, but NOνA fire protection issues are not dominated by this component.
2) PVC Reflectivity. Scintillator light bounces off the PVC walls an average of ~ 10 times before hitting a waveshifting fiber, so maximizing reflectivity maximizes the light output of the cell. A 1% change in reflectivity gives ~ a 10% increase in light output. The reflectivity is linked to the amount and type of titanium dioxide (TiO_2) in the PVC, and PVC samples with 8%, 12%, and 15% of the rutile form of TiO_2 have been examined. The reflectivity of the 15% TiO_2 sample is the best of the samples obtained to date but is adequate for the performance requirement light output from the far end of the cell. Technically this component is near the edge between low / moderate performance risk boundary. 15% TiO_2 concentrations have been extruded for NOνA, so manufacturing also has low cost risk.
3) Other PVC Additives. Rigid PVC extrusions use a complicated mixture of raw PVC resin and additives designed to facilitate the extrusion (heating) process. Typically the exact amounts of additives are a proprietary recipe and the levels of additives in our existing samples are only known to ~ 1%. Our first procured sample had higher levels of

additives and a reflectivity more than 5% lower than in our selected design. However, the additives also govern the surface quality of the PVC and we have samples where the surface quality varied the reflectivity by 1-2%. The cost uncertainty risk for additives is low but non-zero since we cannot now exactly specify a single product to more than one vendor and this restricts competition. The technical risk is low since any procurement will involve (and has involved) quality assurance to determine the reflectivity before production runs.

4) PVC Extrusion Process. The PVC extrusion process involves heating the raw resin, pushing it through a die, and then cooling the product carefully to maintain the desired profile. Our original R&D attempts involved rectangular cells with equal thickness interior webs and exterior walls and proved difficult to extrude. We have optimized the design with the scalloped cell shape and by maintaining an outside wall to inside web ratio of 3:2 as advised by extruder vendors. This mitigation has lowered the technical risk, but we do not yet know how hard it is to do the 32-cell profile. The extrusion costs are substantial, but the cost uncertainty is moderate since this is a simple manufacturing process.
5) PVC Cell Length. The light reaching the APD must travel through the long fiber and is attenuated along that length. The selected NOνA design started with a 17.5 meter long extrusion which just satisfied the scientific performance for light from the far end. Practical considerations of shipping costs have led to a 15.6 m length matched to US truck sizes. This optimization results in low cost risk and low technical risk in the selected design.
6) PVC cell profile. The NOνA cell size has been optimized during the R&D period from a rectangular cell 2.2 cm deep along the beam direction, to a cell 4.5 cm deep, to the selected design of 6.0 cm deep with a scalloped cell (see Figure 3.11). Wider cells will lead to less light. Deeper cells give more light, but as the cell shape moves from square to rectangular the light gain is less than linear with depth. The NOνA cell profile is well within the size limits and wall thickness limits used in the extrusion industry and has low cost risk and low technical risk.
7) PVC Adhesive. The end closures and fiber manifolds must be attached to the PVC extrusions with an adhesive which gives no leaks and does not interact with the scintillator. The cost risk for this component is low because we plan to use an existing product. The technical risk is low since we mitigate any scintillator damage risk through testing of the product before use. There are modest ES&H risks, e.g. volatile adhesives have ventilation issues, and epoxies have skin sensitivity issues for workers. Several candidate products and processes exist to mitigate the ES&H risks.

5.6.2 Risk Optimization of the Liquid Scintillator.

Seven aspects of the scintillator are considered in this optimization description. Chapter 9 contains additional details of the NOνA liquid scintillator.

8) Scintillator Scintillant. The basic amount of scintillator light produced is critical to the cell performance. The NOνA design has been optimized by studying light output from scintillators with 5% - 10% pseudocumene as the scintillant and a 5.5% mixture has been selected. Our optimization has chosen a pseudocumene level adequate for the scientific performance requirement and we have minimized this large cost. Pseudocumene is an environmentally sensitive component in scintillator, so minimizing it minimizes the ES&H risks into the moderate range. The cost of pseudocumene is not strongly linked to the price of crude oil, so this component has moderate cost risk.

9) Scintillator Mineral Oil. The dominant component of liquid scintillator is mineral oil used as a solvent and constituting 95% of the liquid in the selected design. Since mineral oils are derivatives of crude oil, this component also has a high cost uncertainty. Our selected design described in Chapter 9 uses a mid-quality clear technical grade white mineral oil, and its performance is adequate. The density of mineral oil is ~ 0.86 gm/cc, so the use of mineral oil dictates a foam or dry chemical fire suppression system. We treat this as a moderate ES&H risk.
10) Scintillator Internal Waveshifters. The scintillator also contains compounds which shift the light to wavelengths that can be captured by the fiber. These waveshifters are expensive, so there is a moderate cost risk associated with the contingency level. We have optimized the scintillator for just enough light from the far end, reducing the amount of waveshifters needed. This has reduced the cost and reduced the schedule risk from a critical path to a simple task for the vendor. We classify this scintillator component at the low-moderate performance risk boundary.
11) Scintillator Blending. The selected NOνA design involves mixing of the scintillator components at Fermilab. This has a moderate cost risk since it involves construction and operation of a mixing facility. There is some ES&H risk in operating a mixing facility at Fermilab, but these risks have straightforward mitigation via 100% secondary containment, proper ventilation, and proper fire protection. From a detector lifetime point of view each component can be tested for adherence to its specification before mixing, and the final result can be tested against the specification after mixing. Lifetime effects on light output from unknowns in the components or mixing process are more difficult to detect. As noted in Chapters 3 and 9, other experiments have successfully done such mixing and we believe this is a low risk enterprise.
12) Scintillator Attenuation Length. The light produced by the traversing charged particle must pass through the scintillator over a mean path of ~ 50 - 100 cm, so the attenuation of the light by the composite mix of scintillator components is a crucial parameter. The selected NOνA design has an attenuation length in the range 2.5 - 10 meters and has low technical risk. The cost of this scintillator property is driven by the clarity of the pseudocumene if the mineral oil has 10 m attenuation, but by the mineral oil if it has 2.5 m attenuation. We set the cost risk at moderate - midway between the contingencies of these two components.
13) Scintillator Oxygenation. The selected design assumes the lower level of light output produced by fully oxygenated scintillator, approximately 20% less light than un-oxygenated scintillator. Air diffusion through the PVC walls will naturally oxygenate the NOνA scintillator. Since we assume the minimum performance there is no technical risk and no cost risk.
14) Scintillator Flashpoint. Liquid chemical flashpoints below 100 ^{o}C require more expensive partitioned fire protection systems. The flashpoint of liquid scintillator is strongly correlated with the % pseudocumene in the mix, and at 10% pseudocumene the flashpoint of the mixture is just above the 100 ^{o}C limit. Our choice of 5% pseudocumene has minimized this performance risk and there is no additional cost risk for this choice.

5.6.3 Risk Optimization of the Fiber.

Five aspects of the wavelength-shifting fiber are considered in this optimization description. Chapter 10 contains additional details.

15) Fiber Diameter. The wavelength-shifting fiber captures more light in direct proportion to its diameter. Larger diameter fibers can crack when bent in the loop inside the cell. Smaller fibers are more fragile and easily broken during assembly of the extrusion modules. We are at an optimum diameter in terms of handling the fibers. There is a high

technical risk here since damaged fibers can expose the polystyrene core to a dissolving agent (pseudocumene) in the scintillator. There is a modest schedule risk since individual vendors need 3 years to produce the 22,000 km of fiber for NOνA. This component carries a moderate cost risk since only two vendors exist. In addition, one of the potential vendors is outside the U.S. and currency fluctuations can come into play.

16) Fiber Flexibility. The bend diameter of the fiber at the far end of the cell is set by the cell dimensions and has a maximum = $\sqrt{(W^2 + L^2)}$. The NOνA design has bend diameter of 6.8 cm. This is just below the borderline of recommendations from Kuraray for 0.8 mm S-type (flexible) fiber, so this component has a moderate to high technical risk with some possibility of forming micro-cracks with time. Micro-cracks can lead to the pseudocumene reaching the polystyrene fiber core and dissolving the core, so this is a detector lifetime issue. The cost risk for the most flexible fiber is small, but additional mitigation of risk may drive up the cost.
17) K27 Wave-shifting Dye Concentration. Since the attenuation length of the fiber is a critical parameter for the design and driven by the K27 concentration, this component has low to moderate technical risk. The cost of the dye is not a cost driver.
18) Position of the Fiber in the Cell. In the horizontal cells, the fiber will gravitate to the PVC walls and simulations indicate about a 10% loss in light when the fiber is against a wall and a 20-30% loss when the fiber is in a sharp corner. However, our measurement detect no effect at all. The position has no technical risk and no cost risk.

5.6.4 Risk Optimization of the Photodetector and Electronics.

Four aspects of the photodetector / electronics are considered in this optimization overview. Chapter 13 contains additional details.

19) APD pixel size. The APD pixels are a rectangular shape (1.1 mm by 2.3 mm) sized to hold two 0.8mm fibers from the cell. Performance of the pixels falls off near the edges, so this arrangement requires alignment of the fibers to the pixel at the ± 25 micron level and implies some technical risk. The APDs are available from only one vendor and are subject to currency fluctuations. This gives a cost uncertainty risk near the low/moderate border.
20) APD gain. The selected design operates the APD at a gain of ~100. The electronic noise from the device is optimized at about a gain of 90, so our selected design is near the noise optimum. A gain of 100 is in the middle of the operating range of the APD and has a low technical risk. Gain and cost are not particularly coupled in this product, so the cost risk is very small.
21) Thermoelectric Coolers (TEC). The NOνA design operates the APD at -15^0C to minimize the APD noise. The temperature control is supplied by a TEC for each 32-channel APD. The TECs are standard commercial devices with very little cost risk. The lifetime of the TECs is not well specified by the manufacturers and our large number of devices (24,000) may imply replacement of a few devices per day. The electronics package design must satisfy the requirement to be easily swapped out to remove these failures. Removal of heat from the hot side of the TEC adds a requirement to the building infrastructure. Some TECs contain encapsulated Lead Telluride and are a small ES&H concern. The technical risk is moderate.
22) Electronics Amplifier Noise. The selected design minimizes the amplifier noise in a new ASIC chip with a small technical risk (near the moderate boundary until we have a prototype in hand) and with low cost risk.

5.6.5 Risk Optimization Summary.

Figure 5.8 shows the Cost Risk vs. Technical Risk for each of the 22 points discussed above. The points tend to cluster towards the lower left corner as expected for an optimization effort. The selected NOνA design has optimized this complicated array of variables for low to moderate cost risk and for low to moderate technical risk.

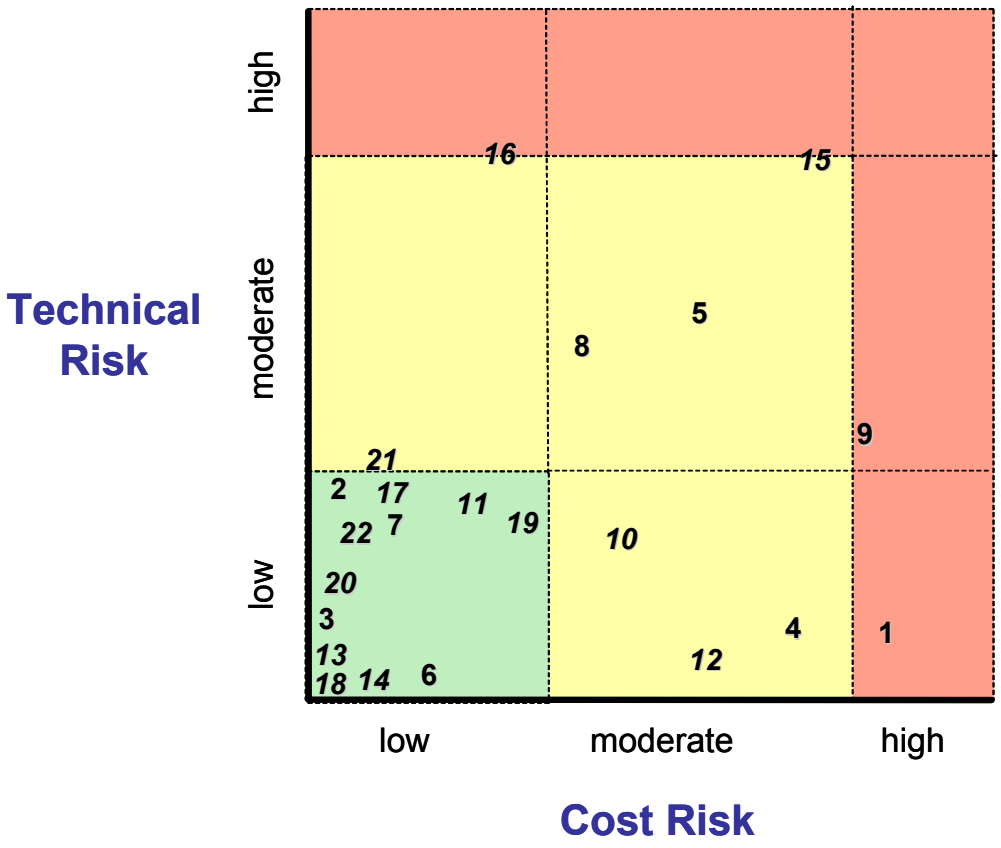

Fig. 5.8 : Plot of cost risk versus technical risk for the selected NOνA design. The 22 points correspond to the 23 variables of the selected design discussed in Section 5.5 and 5.6.

5.7 Indications for Additional Value Management Studies

Sections 5.5 and 5.6 each describe two-dimensional projections of a multi-dimensional problem in cost, cost risk, performance, and performance risk for twenty-two variables of the basic NOνA cell. The simple detector cell composed of PVC, scintillator, fiber, and a photodetector still has a very large set of variables, and the previous sections demonstrate that the selected NOνA design has been extensively optimized.

Further cost-effective value management choices are anticipated as the NOνA design moves from the conceptual phase to a technical design report and a performance baseline. This process will depend on judgments by the integrated project team to optimize the detector among the parameters discussed above. Figure 5.8 indicates that the following variables need additional investigation:

16 and 15 – Fiber cost, delivery, and flexibility.

9 – Cost of mineral oil.

1 – Cost and additive mixture for PVC.
4 – Manufacturability of the NOνA cell profile and of the 32-cell structure (linked to item 1)

Figure 5.7 indicates investigations into the following variables:
2 – PVC reflectivity (linked to item 1)
22 – Multiple correlated sampling in the electronics

The figures are just indications, and we need to keep our focus on all the variables as we move to a final Technical Design. This analysis was intended to demonstrate that we are aware of these effects, have already optimized the detector, and continue to investigate additional optimization.

5.8 Optimization and Possible Further Improvements in the Analysis Algorithm

The current NOνA analysis algorithm is described in Chapter 3, Section 3.5.3. Versions of this analysis were developed by two separate groups within the NOνA Collaboration and give similar results, with one version giving a Figure of Merit (FoM) approximately 8-9 % larger (with errors in these FoM values at the level of ±2%). We have optimized the reach of the experiment using the algorithm version with the larger FoM as our default.

Hand scans of simulated NOνA events have yielded even larger FoMs (~ 20% higher than our default algorithm), indicating that further improvements in the analysis may be possible. The current algorithm suffers when the main vertex is not well defined, typically because there are multiple hits from low energy particles behind the main vertex. The algorithm also suffers from confusion if the electron shower track is short or if multiple π^0s are produced. Hand scans have also indicated that correlations between the horizontal and vertical event views can be employed to advantage, but the algorithm currently treats each view independently. In particular, electromagnetic shower tracks should have the same length in both views, the pulse height profile of the shower tracks should be similar in both views, and if the shower track has gaps along the length of the shower then each segment of the shower track should have the same length in each view.

Implementing new code to address these problems is not trivial. We have to increase the ν_e event identification fraction from its current value of 24% without adding additional background events or the FoM will decrease, not increase. In addition simulated NOνA events do not necessarily contain all the details we will observe in the real detector. Improvement in the analysis algorithm is not part of the NOνA Project, but the Integration Prototype Near Detector discussed in Chapter 3, section 3.4.9 is crucial for progress in this area by the NOνA Collaboration. A one year run in the MINOS configuration of the NuMI beam will yield [1] a sample of ~ 750 ν_e charged current events with the NOνA off-axis neutrino energy distribution. The Integration Prototype Near Detector completion is a goal of the NOνA Project R&D effort and it is expected to be operational during calendar 2007, given sufficient R&D funding in FY06 and FY07.

Chapter 5 References

[1] D. Ayres et al., NOνA Proposal Chapter 9, hep-ex/0503053, March, 2005. See also J. Cooper presentation to the Fermilab PAC, April 2005, http://www-nova.fnal.gov/reports_page.html

6. Work Breakdown Structure

6.1 Introduction

The NOνA Work Breakdown Structure (WBS) defines the total set of items to be developed and produced to accomplish the scientific goals set out in Chapter 2 with the detector described in Chapter 3. The integrated project team has identified ten major components to the project at Level 2 as shown in Table 6.1. Chapters 7 through 15 of this Conceptual Design Report focus on each of these WBS Level 2 elements in detail. The WBS in Table 6.1 and its lower level tree structure form the basis for the NOνA resource-loaded Cost and Schedule. The Project is developing the Cost and Schedule using the Open Plan® software package [1].

WBS elements at Level 2		Task Name
R&D	Construction	
1.1	2.1	Site and Building
1.2	2.2	Liquid Scintillator
1.3	2.3	Wavelength Shifting Fiber
1.4	2.4	PVC Extrusions
1.5	2.5	PVC Modules
1.6	2.6	Electronics Production
1.7	2.7	Data Acquisition Systems
1.8	2.8	Near Detector Assembly
	2.9	Far Detector Assembly
1.9	2.10	Project Management

Table 6.1 NOνA Level 2 WBS tasks. 1.x are the R&D tasks and 2.x are the construction project tasks.

6.2 WBS Dictionary at Levels 2 and 3

This section defines the WBS tasks for a NOνA Construction Project through Level 3. WBS 2.0 is for the design and construction of the NOνA Near and Far Detectors and the Far Detector Hall. NOνA R&D is covered in WBS 1.0 and that dictionary is attached in Appendix A.

WBS 2.1 Site and Building

This Level 2 element covers the design and construction of the Site and far Detector Enclosure and Building.

WBS 2.1.1 Develop Design/Build Criteria

This WBS element contains the tasks necessary to complete the design criteria to produce a set of documents suitable for use in a competitive bid situation to obtain a Design/Build subcontractor.

WBS 2.1.2 Design/Build
This WBS element contains the Design/Build contract for the far Detector Hall.

WBS 2.1.3 Shield Wall
This WBS element includes the design, procurement and installation of the precast shield wall that separates the Detector Enclosure from the Assembly Space after the detector is fully assembled.

WBS 2.1.4 Site Logistics
This WBS element includes site support functions for the Far Detector site including utilities, site maintenance and safeguards and security.

WBS 2.1.5 Management
This WBS includes the tasks required to support and manage WBS 2.1 activities including quality assurance, value management, risk management, ES&H, monitoring of vendor performance and schedule, preparation of reports and related activities.

WBS 2.2 Liquid Scintillator

This level 2 summary element covers the procurement, production, QA and shipping of the liquid scintillator required by the project for both the Near and Far Detectors.

WBS 2.2.1 ISO Tankers

This WBS element provides for vendor selection and lease agreements for the ISO tanks.

WBS 2.2.2 Infrastructure
This WBS element provides for the development of the infrastructure required to perform the blending of the liquid scintillator components into the final product. This task includes the development, documentation, review and implementation of equipment and procedures necessary for safe operation, consistent with Fermilab ES&H guidelines.

WBS 2.2.3 Mineral Oil
This WBS element provides for vendor selection and procurement of mineral oil as well as a QA and shipping.

WBS 2.2.4 Pseudocumene
This WBS element provides for vendor selection and procurement of pseudocumene as well as a QA and shipping plan.

WBS 2.2.5 Wave-Shifters
This WBS element provides for vendor selection and procurement of wave-shifters as well as a QA and shipping plan.

WBS 2.3 Wavelength Shifting Fiber

This level 2 summary element covers the procurement, QA and shipping of wavelength shifting fiber.

WBS 2.3.1 Procurement
This WBS element provides for vendor selection and procurement of WLS fiber as well as a QA and shipping plan.

WBS 2.3.2 Production
This WBS element provides for production of fiber QA testing equipment as well as the development of procedures, documentation and reporting requirements. Delivery of fiber spools to the module factories on a schedule consistent with factory schedules and available storage must also be organized and managed.

WBS 2.3.3 Management
This WBS element includes the tasks required to support and manage WBS 2.3 activities including quality assurance, value management, risk management, monitoring of vendor performance and schedule, preparation of reports and other related activities.

WBS 2.4 PVC Extrusions

This level 2 summary element covers the procurement, QA and shipping of the PVC extrusions.

WBS 2.4.1 Procurement:
This WBS element provides for vendor selection and procurement of the PVC extrusions.

WBS 2.4.2 Extrusion Pre-Production:
This WBS element includes manufacture and evaluation of pre-production extrusions. Determination of the quality assurance methods for use in production is also included.

WBS 2.4.3 Extrusion Production:
This WBS element provides for supervision and quality assurance monitoring of PVC extrusion production.

WBS 2.4.4 Edge Stiffeners
This WBS element provides for the production of edge stiffeners.

WBS 2.4.5 Shipping & Handling
This WBS element provides for the development of a shipping and handling plan for delivering extrusions to module factories, for supervising trucking schedules and for managing the equipment necessary for shipping and handling.

WBS 2.4.6 Management

This WBS element includes the tasks required to support and manage WBS 2.4 activities including quality assurance, value management, risk management, monitoring of vendor performance and schedule, preparation of reports and other related activities.

WBS 2.5 PVC Modules

This level 2 summary element provides for construction and QA of the PVC modules for both the Near and Far Detectors and shipping of the completed and tested modules to their respective detector sites.

WBS 2.5.1 End Seal Production

This WBS element includes the production of the fiber manifolds that cover and seal the readout end of a PVC module and route the WLS fibers to the photodetector interface, and the production of the bottom plates that seal the other end of the PVC modules.

WBS 2.5.2 Photo Detector Interface Production

This WBS element includes the hardware necessary to connect the WLS fibers from the PVC modules to the APD modules.

WBS 2.5.3 Factory Module Assembly

This WBS element covers the set up and operation of the module factories as well as the procurement and construction of the various machines necessary to assemble and test the modules.

WBS 2.5.4 Management

This WBS element includes the tasks required to support and manage WBS 2.5 activities including quality assurance, value management, risk management, monitoring of factory performance and schedule, preparation of reports and other related activities.

WBS 2.6 Electronics Production

This level 2 summary element includes the Avalanche Photo Diode (APD) optical sensors, the thermo-electric (TE) coolers for the APDs, the custom ASIC that amplifies and multiplexes the APD signals, the ADC that digitizes the signals and the FPGAs that zero suppress and time-stamps the data. Also included is the low-voltage system for the TE coolers and the front-end electronics, the high voltage system for the APDs and a cooling system to remove the heat from the TE coolers. These systems will be provided for both the Near and Far Detectors.

WBS 2.6.1 APD Module Production

This WBS element includes procurement of the APD chips, the APD carrier boards, the TE coolers and the APD housing hardware. This task includes managing the flow of components for assembly and development and execution of a QA plan.

WBS 2.6.2 Readout-Front-End Board (FEB)
This WBS element provides for delivery of the specified system to receive signals from the APD modules, digitize them and deliver them to the Data Acquisition (DAQ) system.

WBS 2.6.3 Readout Infrastructure
This WBS element includes design, production and installation of the infrastructure required to deliver power and cooling to operate the FEBs and APDs.

WBS 2.6.4 Management
This WBS element includes the tasks required to support and manage WBS 2.6 activities including quality assurance, value management, risk management, monitoring of performance and schedule, preparation of reports and other related activities.

WBS 2.7 Data Acquisition System

This level 2 summary element includes the hardware and software to record the data to archival storage and to control and monitor both the Near and Far Detectors. It includes the fiber, cable, switches and memory necessary to move and buffer the data, a PC farm for online filtering, local disk storage, a system for moving data to permanent storage at Fermilab, software and testing.

WBS 2.7.1 DAQ Software
This WBS element includes software to run on buffering/triggering hardware for archival of data within selected time frames. Databases are also included in this WBS element.

WBS 2.7.2 DAQ Hardware
This WBS element includes the design and installation of the hardware for receiving signals from FEB, buffering and archival, delivery of clock/timing signals.

WBS 2.7.3 Integration
This WBS element includes the integration testing of DAQ and trigger electronics hardware and software.

WBS 2.7.4 Slow Control System
This WBS element includes the controls required to receive and archive monitoring data as needed.

WBS 2.7.5 Management
This WBS element includes the tasks required to support and manage WBS 2.7 activities including quality assurance, value management, risk management, monitoring of performance and schedule, preparation of reports and other related activities.

WBS 2.8 Near Detector Assembly

This level 2 summary element provides for the engineering design of the mechanical devices and tooling needed to install the NOνA Near Detector. Fabrication of the necessary tooling, installation and commissioning of the near Detector in its underground location at Fermilab is also included.

WBS 2.8.1 Underground Tunnel Infrastructure

Complete the engineering design, procurement, fabrication and installation of the utilities and infrastructure required to install and operate the Near Detector in its underground tunnel location. These systems include lighting, HVAC, electrical power, fire protection, chilled water and liquid scintillator containment. This task covers the technical and ES&H reviews and approvals of equipment and assembly procedures.

WBS 2.8.2 Mechanical Systems

Complete the engineering design, procurement and fabrication of the Near Detector muon steel segment, the detector support structure and the systems for moving the detector subassemblies underground and to different positions along the MINOS access tunnel. This task includes any shipping and moving costs and the final optimization, review and approval of equipment and assembly procedures.

WBS 2.8.3 Assembly Equipment

Complete the engineering design, procurement and fabrication of the Near Detector plane assembly tables, the detector subassembly fixtures, the adhesive dispensing system and the alignment fixtures. This task includes any shipping and moving costs and the final optimization, review and approval of equipment and assembly procedures.

WBS 2.8.4 Liquid Scintillator Filling Equipment

Complete the engineering design, procurement and fabrication of the Near Detector liquid scintillator supply system, the filling machine and the plumbing that connects these together and to the detector modules. Secondary containment of the liquid scintillator is included in this task as well as any shipping and moving costs and the final optimization, review and approval of equipment and assembly procedures.

WBS 2.8.5 Installation

This WBS element includes installing readout electronics, cabling, plumbing, filling with liquid scintillator, final component QA tests, detector alignment, the implementation of safety systems, the review and approval of equipment and installation procedures, and the documentation and initial commissioning of the assembled detector and its moving system.

WBS 2.8.6 Management

This WBS element includes the tasks required to support and manage WBS 2.8 activities including quality assurance, value management, risk management, schedule monitoring, preparation of reports and other related activities.

WBS 2.9 Far Detector Assembly

This level 2 summary element provides for the engineering design of the mechanical systems and tooling needed to install the NOνA Far Detector. Fabrication of the necessary tooling, installation and commissioning of the detector in the detector building in Northern Minnesota is also included.

WBS 2.9.1 Mechanical Systems

This WBS element includes the engineering design, procurement and fabrication of the Far Detector support structure and machines for moving materials and equipment into and within the detector building. This task includes any shipping and moving costs and the final optimization, review and approval of associated equipment and assembly procedures.

WBS 2.9.2 Assembly Equipment

This WBS element includes the engineering design, procurement and fabrication of the block raiser, the 31-plane block assembly fixtures, the adhesive dispensing system and the detector alignment systems. This task includes any shipping and moving costs and the final optimization, review and approval of associated equipment and assembly procedures.

WBS 2.9.3 Liquid Scintillator Filling Equipment

This WBS element includes the engineering design, procurement and fabrication of the Far Detector liquid scintillator filling machine and the plumbing that connects it to the supply system and to the detector modules. This task includes any shipping and moving costs and the final optimization, review and approval of equipment and assembly procedures.

WBS 2.9.4 Installation

Finalize the procedures, schedules, resources and cost estimates for the installation of the Far Detector at the detector building in Minnesota. Move components and equipment into the building assemble 31-plane blocks and raise and attach them to the previously erected blocks. This task includes installing readout electronics, cabling, plumbing, filling with liquid scintillator, final component QA tests, detector alignment, the implementation of safety systems, the review and approval of equipment and installation procedures, and the documentation and initial commissioning of the assembled detector.

WBS 2.9.5 Management

This WBS element includes the tasks required to support and manage WBS 2.9 activities including quality assurance, value management, risk management, schedule monitoring, preparation of reports and other related activities.

WBS 2.10 Project Management

This Level 2 summary element consists of reviews, reports, site visits, local supervision, running technical board meetings, standards preparation, tracking and analysis, schedule preparation tracking and analysis, change control. It also includes procurement of relevant software and computers, the cost of running the project office and the salaries of non-scientists working on the project.

WBS 2.10.1 FY08 Project Management

WBS 2.10.2 FY09 Project Management

WBS 2.10.3 FY10 Project Management

WBS 2.10.4 FY11 Project Management

WBS 2.10.5 FY12 Project Management

Chapter 6 References

[1] Open Plan is a product of Deltek, see www.welcom.com.

7. Site Description

7.1 Introduction

We describe here additional details of the Ash River site, and an additional discussion of alternatives considered leading to the scientific choice of the Ash River site. See Chapter 4 for a wider overview of alternative sites considered. This chapter also looks at optimization of the site, ES&H concerns, risks, and opportunities for value management.

7.2 Details of the Recommended Ash River Site

7.2.1 Site Maps and Features

The Ash River site is 810 km from Fermilab and offers the longest possible baseline along the NuMI beam within the United States. Figure 7.1 is a relief map of the general area around the selected site with an inset map showing how this area is situated in the State of Minnesota. Voyageurs National Park dominates the northern half of Figure 7.1. U.S. 53 runs north-south on the western edge and the city of International Falls is off the map towards the northwest. The red line from the Ash River Trail to the Project Site is an existing logging road which must be upgraded for truck traffic as part of the project. The project would require about 23.5 – 40 acres for the Far Detector Hall and about another 20 acres for the upgraded access road. The access road would be 30 feet wide with 10 foot clear areas on either side. Utilities would be run underground along the access road from the Ash River Trail to the project site.

Figure 7.2 is a US Geological Survey 7.5 minute, 1:24,000 scale map showing the topology of the Ash River area. The inset figure shows that the selected site is on a hilltop, roughly 70 feet above the level of the Ash River. The details of the building in the inset are explained in Chapter 8. The red line on Figure 7.2 is again the access road to the site, now with details showing how it deviates from the logging road in a few places so as to increase the curve radius for truck traffic to the site.

Figure 7.3 is an aerial photograph of the area with map details overlaid. The inset map of the Project Site area shows that this particular 23.5 acre section has been logged over within the last 10 years, leaving larger trees in the adjacent land sections. The Project Site boundary in this figure is a working estimate, not a final outline.

Figure 7.4 is the same aerial photograph of the area with additional map details overlaid. In particular, the type of vegetation is identified, and the 100 year floodplain of the Ash River is marked. The inset figure shows the required setback from the 100 year floodplain just touches the Project Site in the southeast corner. This figure also shows how the access road crosses through an area of wetlands (bog) that will require mitigation through purchase of equivalent area in a wetlands bank. The road will require permits from the US Army Corps of Engineers under Section 404 of the Clean Water Act and from St. Louis County under the requirements of the Wetland Conservation Act of Minnesota. None of the impacted area is designated as a Protected Water or Wetland by the Minnesota Department of Natural Resources.

Figure 7.5 shows the core samples from one of the two core drillings done on the Project Site. The surface deposits are about 7 feet deep and include soil over a layer of clay. Below the surface soils is a layer (at least 65 feet thick) of hard granite bedrock down to the proposed bottom of the NOνA excavation for the Far Detector building (see Chapter 8). These core samples were taken at the two points in the inset to Figure 7.3 (marked by small red circles). Both cores show the same granite base. A packing test (seal boring site, overpressure with water, wait for leak rate) was done in one of the borings at a depth of 36 – 41 feet below the surface. No pressure loss was observed, indicating that the granite is not very fractured within the tested zone.

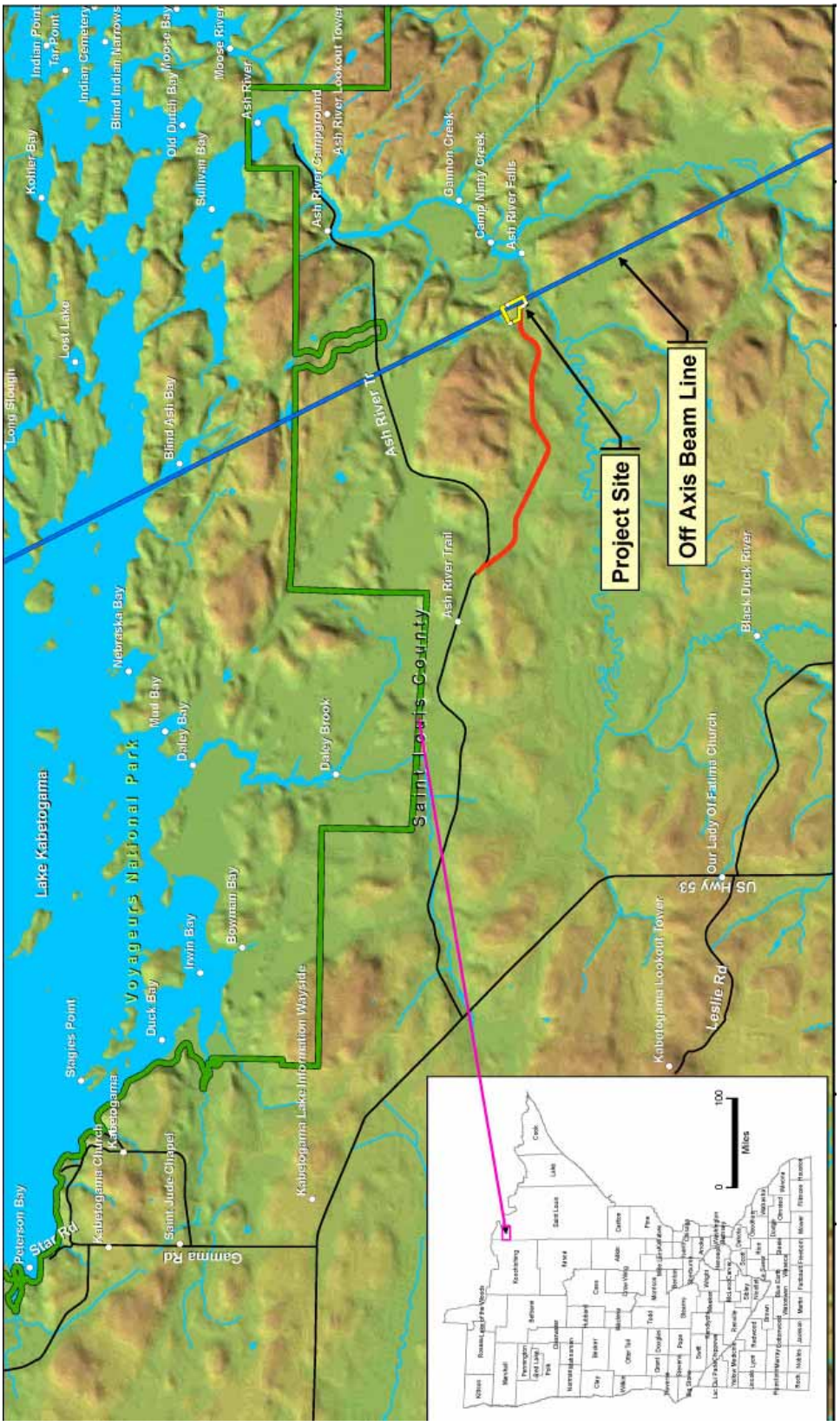

Fig 7.1: Shaded relief map of the Ash River site. The inset black and white figure indicates the site position within the State of Minnesota. North is to the left side of the page in this figure.

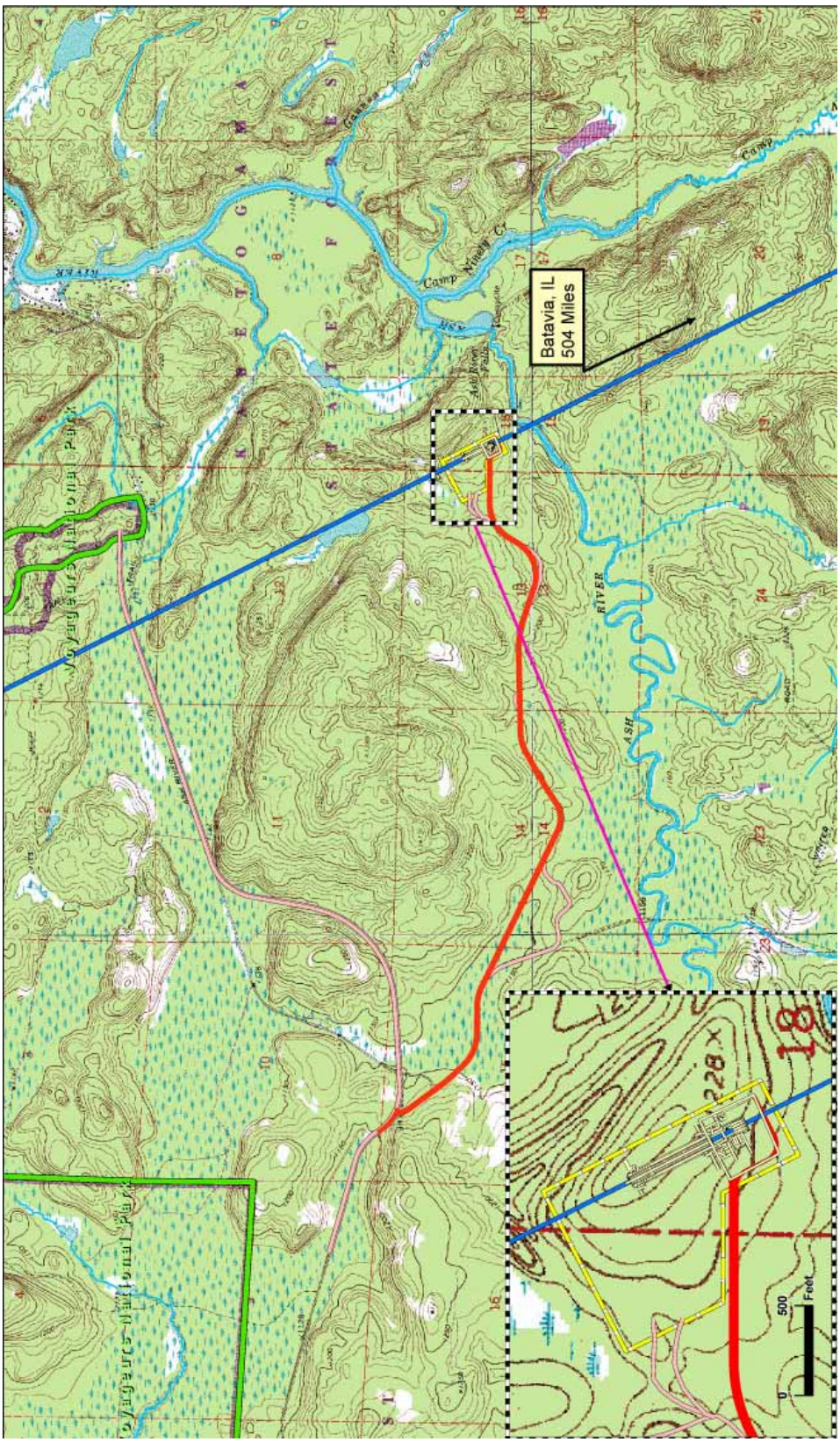

Fig. 7.2: U.S Geological Survey 7.5 minute, 1:24,000 scale map indicating the project area at Ash River. Section boundaries (1 mile by 1 mile) are indicated by the grid.

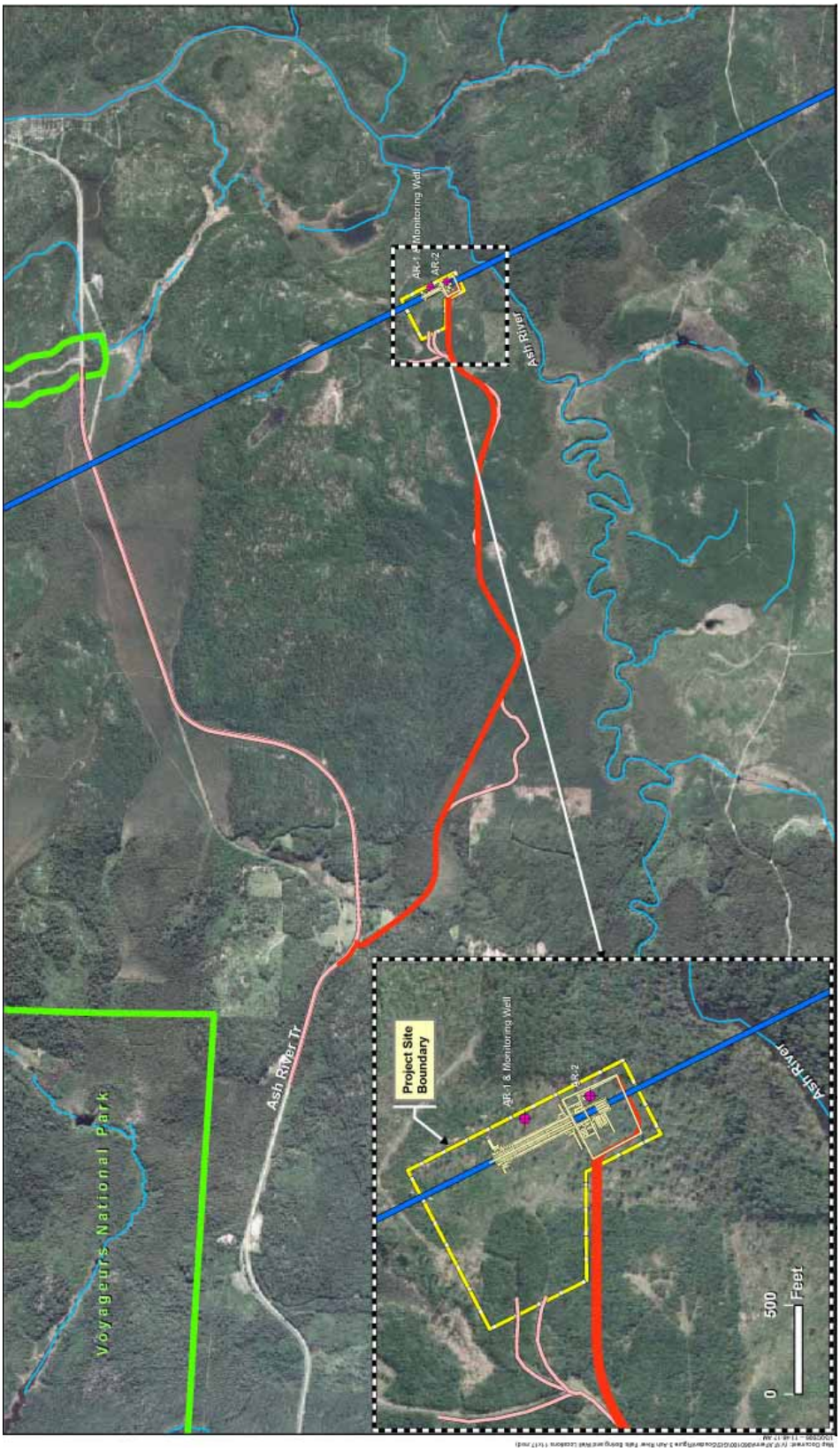

Fig 7.3: A more detailed aerial picture of the Ash River site area with and overlay of the roads and rivers.. Dark blue line is 11.77 km off-axis to the NuMI beamline. The inset figure shows how the site area has been logged over.

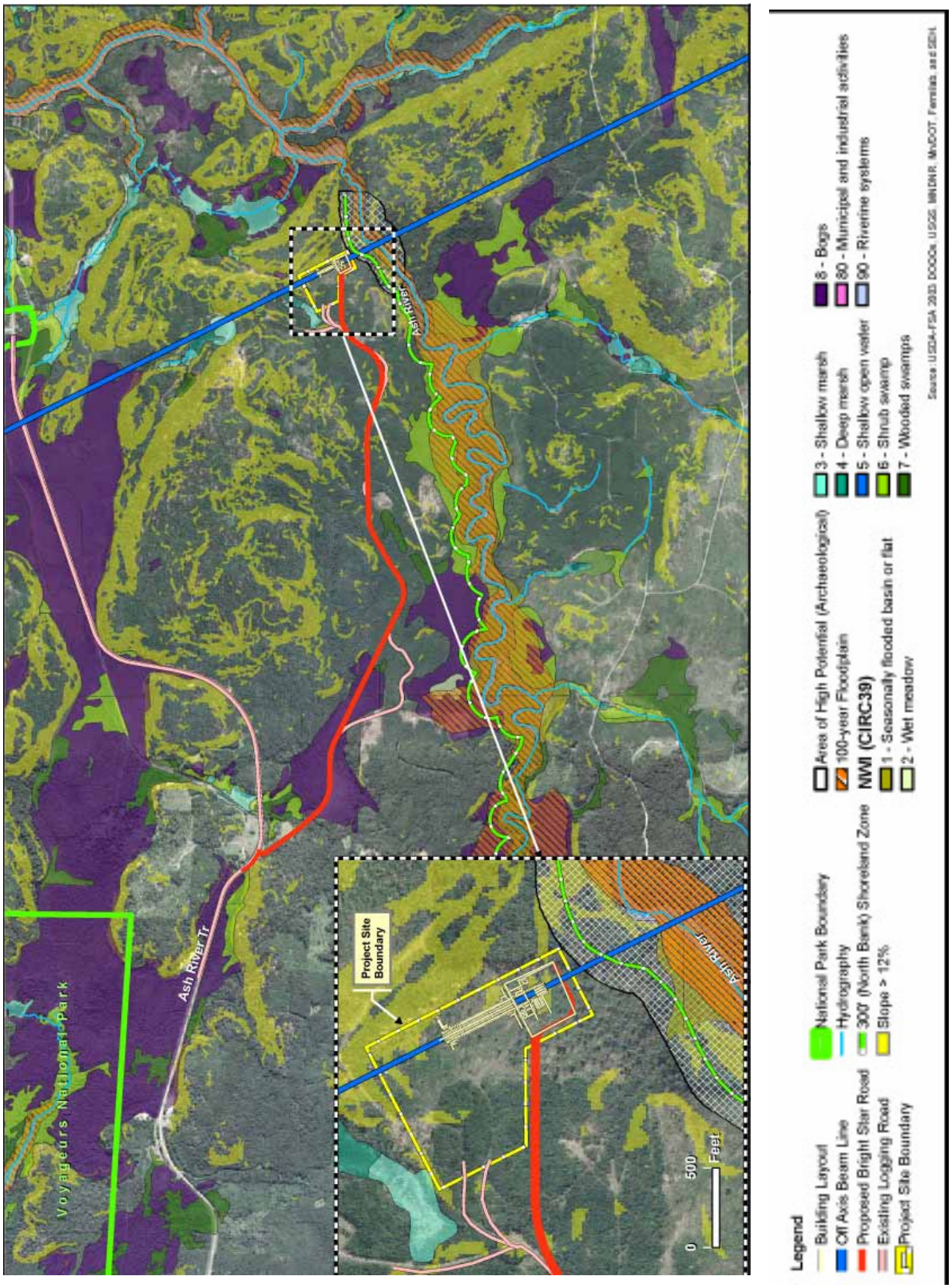

Fig. 7.4: A detailed map of the Ash River site shown wetlands, required wetlands setback lines, and other land characteristics in the area. The yellow shading in the forested areas indicates places with a > 12% slope.

Fig. 7.5: Core samples from the boring sites indicated in the inset to Figure 7.3. See text.

7.2.2 Roads, Power, Data Communications

Highway US 53 does not have road restrictions in any season. The normal limits are 10 tons per axle, see Figure 7.6. The Ash River Trail (St. Louis County Road 129) between US 53 and the NOνA site access road does have road restrictions during the spring thaw, limiting trucks to 9 tons per axle for a 60 day period, March 15 – May 15 each year. In northern Minnesota it is common to then use trucks with an extra axle. For example, the chassis trailers discussed in Chapter 9 for scintillator transport come in 2 and 3 axle versions, so the delivery of liquid scintillator to the site should not be interrupted except during actual severe storm conditions.

There is limited power available along the Ash River Trail at present, only 300 kVa versus our estimated need of 1,000 – 1,500 kVa. The power company is North Star Electric, a part of of MinnKota Power, with about 6,000 customers in this part of Minnesota. North Star Electric Cooperative has provided an estimate [1] to upgrade the power lines (re-insulation and transformers) from the Kabetogoma Substaion some 35 miles from the NOνA access road turn-off from St.Louis County 129. See Figure 7.6. The power in this area is fed from a single direction, so there can't be any automatic feeding from another route in case the overhead power lines from Kabetogoma are knocked out by storms. The NOνA site will therefore require on-site capability for emergency power from a backup generator powered by propane.

Data communications in the Ash River area are provided by the Blackduck Telephone company, a small company with 2 telephone exchanges and less than ten employees. Fiber has been run along the Ash River Trail (St. Louis 129) and we don't foresee any problems.

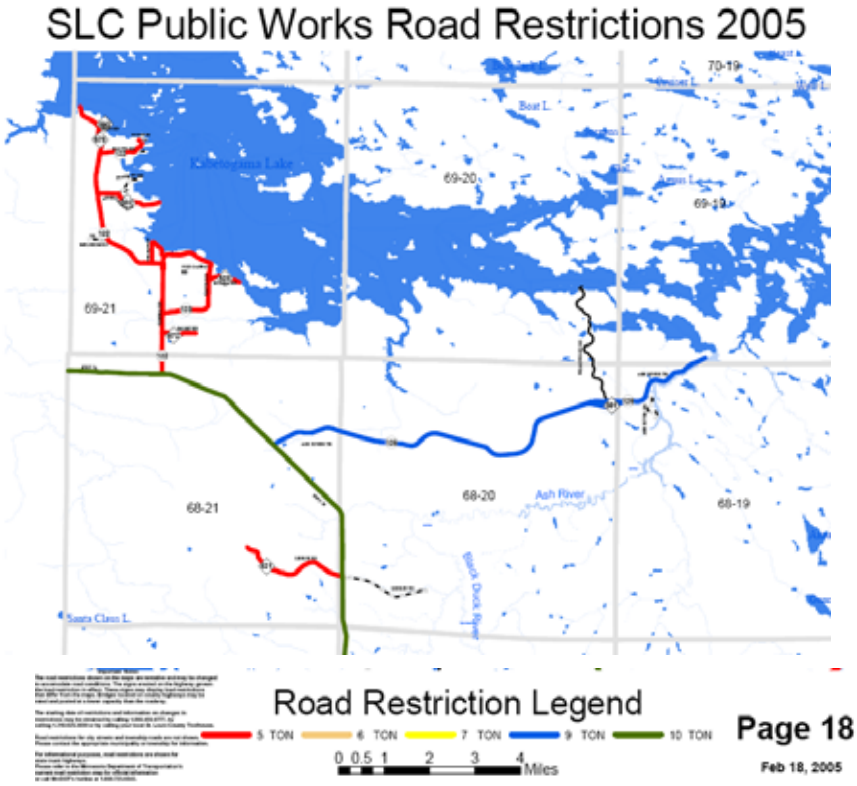

Fig. 7.6: St. Louis County Public Works Road Restictions published for 2005.

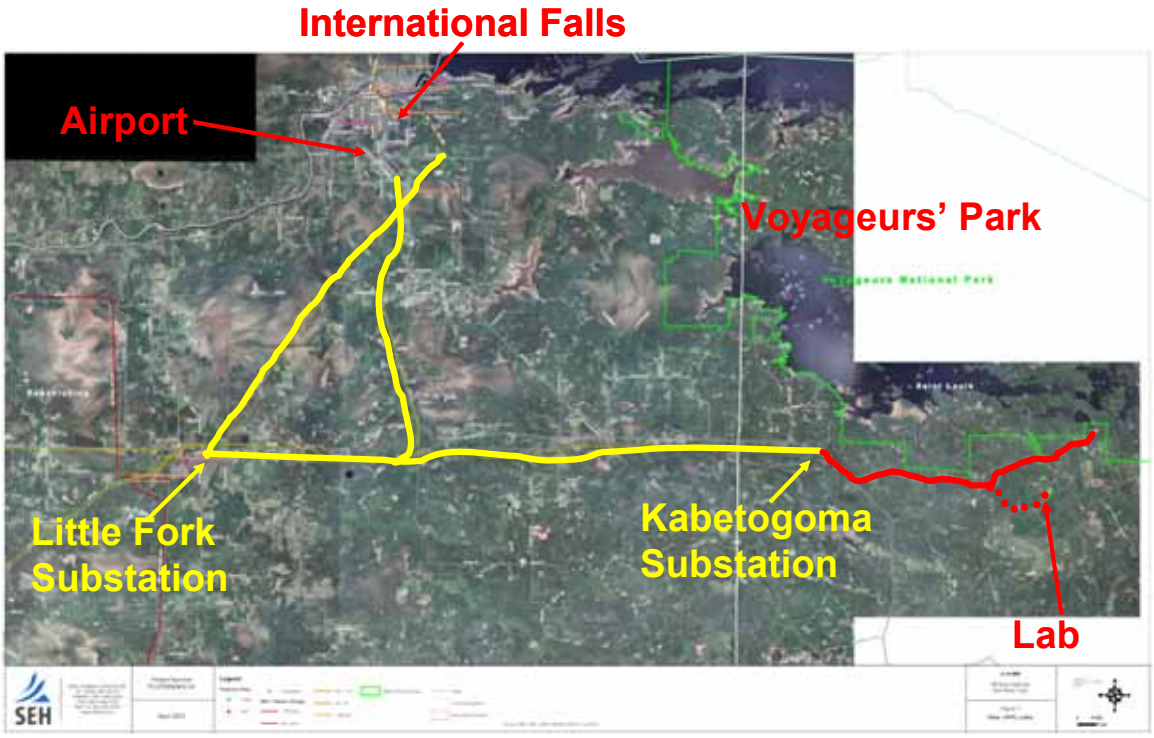

Fig. 7.7: Power distribution lines in the Ash River area.

7.2.3 Proximity to Voyageurs National Park

The Ash River site is just south of Voyageurs National Park and the Park Superintendent has several concerns about NOνA that were explained to us [3] during an outreach meeting to stakeholders in April 2005. The first worry is that a NOνA structure might be seen from the park, since their mission is to provide a wilderness experience free of man-made objects. Figure 7.8 (provided by Voyageurs National Park) shows the viewshed from inside the park boundaries. Once the NOνA design of an earth covered overburden was described, this concern was lessened. In addition the NOνA plan is to put the entry to the Far Detector building on the south end of the site so that only the overburden should be visible from the north. Figures 7.9 and 7.10 are pictures taken facing north and south from a position near the south end of the site. Voyageurs Park is not visible to the north because of the intervening hill and trees.

The Park's second concern was noise from the site during ~ two years of civil work, and from truck traffic delivering the NOνA detector components. Figure 7.11 shows the distances from the NOνA site to parts of the park. We note that the noisiest part of the construction is the period of excavation which should only last during about a 2 – 4 month period, not two years. We intend to restrict our construction activities to 0700 – 1900 hours to help mitigate the noise impacts during the rest of the construction period. The current traffic level on the Ash River Trail has been measured at 310 vehicles per day and the NOνA plan would add about 90 trips to that total, a 33% increase.

The final concern was light pollution. Since our only need for light will be at the southern end of the NOνA building down the hill from the Park, this concern is easily mitigated by appropriate choice of dark sky[3] lighting equipment that lights the ground, not the sky.

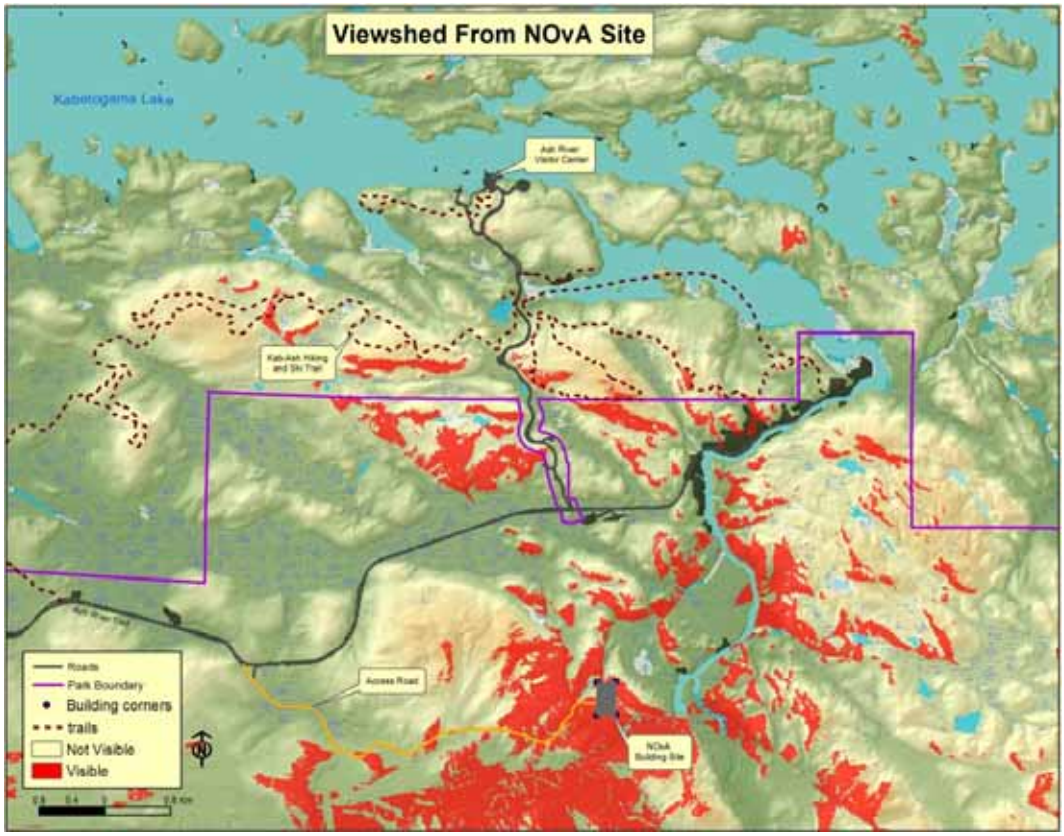

Fig. 7.8: Viewshed map as seen from Voyageur National Park. The red areas can be seen from parts of the Park, but the map does not take into account any intervening trees.

Fig. 7.9: Picture at the Ash River site facing towards Voyageurs National Park in September 2005. This was taken from about the position of the southern bore hole marked in Figure 7.3.

Fig. 7.10: Picture at the Ash River site facing towards Fermilab in April 2005.

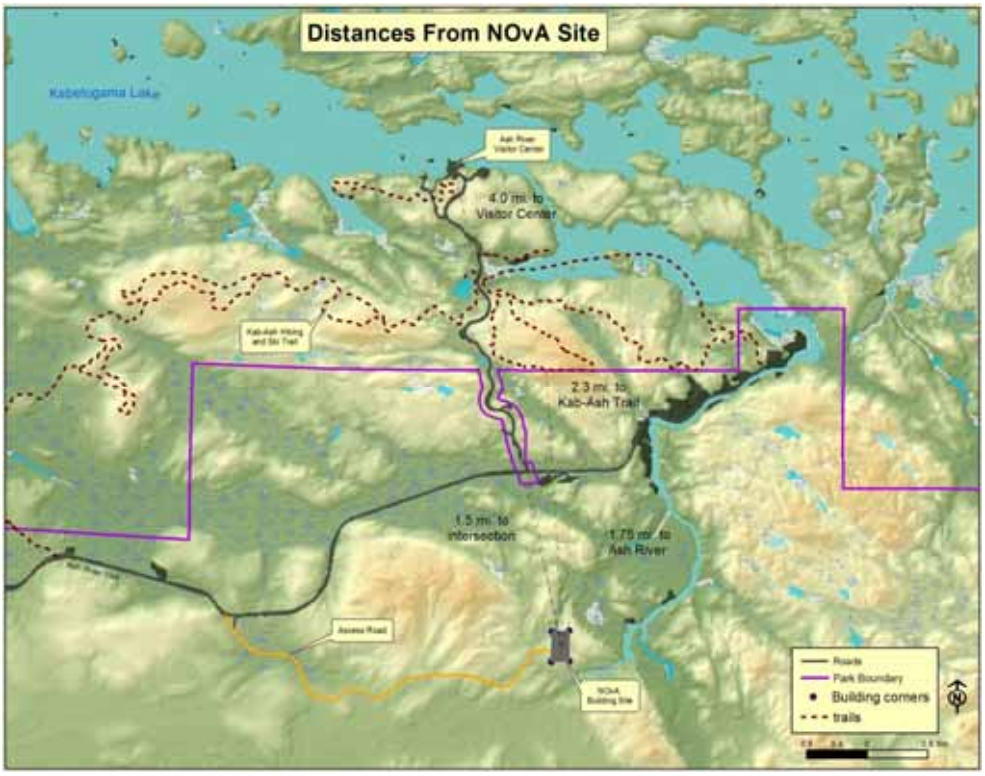

Fig. 7.11: Soundshed map for Voyageurs National Park. Distances from the NOνA site to the Park are indicated.

7.3 Alternatives: Comparisons with the Orr-Buyck Site

The Orr-Buyck site is 774 km from Fermilab and would have the second longest baseline available in the United States. The general conditions at these two sites are nearly identical with the core boring showing the same thin soil covering over solid granite. Orr-Buyck would not have any of the concerns raised above for Ash River and its proximity to Voyageurs National Park, but we believe those concerns at Ash River can be appropriately addressed and mitigated. This leaves two variables to contrast the two sites: Construction Cost and Scientific Performance.

7.3.1 Construction Cost Comparison between Ash River and Orr-Buyck

Other than the baseline length from Fermilab, the differences between the sites are contained in three cost drivers: Construction of the access road to the NOνA building site Required electrical power upgrades, and Wetlands mitigation.

The access road at Ash River is about 3.3 miles long and changes grade by about 70 feet over that length. In contrast the access road at Orr-Buyck also has a grade change of about 70 feet, but over only 1.2 miles. Half the grade change is on the Orr-Buyck site proper and half is on the Elbow Lake Trail Road between the Orr-Buyck Road and the site. We estimate that the final road at Orr-Buyck would require some removal of soil and rock to provide a grade suitable for truck traffic. In addition we would require improvements to the Elbow Lake Trail portion of the access. The base construction cost comparison between the two sites indicates the Ash River access road would cost about $ 1,300 K more than Orr-Buyck.

The electrical power available at Ash River is inadequate and will require an upgrade of the transformer at the Kabetogama Substation some 35 miles away and an upgrade of the insulators and transformers from the substation to the NOνA site. The North Star Electric Cooperative has estimated the customer's share of the cost for this work at about $ 0.8 M. Both sites would

require new direct buried service along their respective access roads and a new transformer at the building site. The base construction cost comparison between the two sites indicates the Ash River electrical power would cost about $ 650 K more than Orr-Buyck.

The initial report from our environmental consultant (see section 7.6) indicates that the Ash River site will have approximately 60% more wetlands area mitigation than the Orr-Buyck site. This mitigation is most easily accomplished by the purchase of equivalent amount of land from commercially available wetlands banks in Minnesota. The base construction cost comparison between the two sites indicates the Ash River wetlands mitigation would cost about $ 125 K more than Orr-Buyck.

Overall, the base construction costs at Ash River are estimated to be about $ 2 M more than the access costs at Orr-Buyck. With appropriate overhead and contingency, this difference might be as much as $ 3 M.

7.3.1 Scientific Comparison between Ash River and Orr-Buyck

Since the sensitivity of the determination of the mass ordering depends on the distance the neutrinos travel through the earth, the NOνA Far Detector should be sited as far away from Fermilab as is practically possible. This is one of the Scientific Performance Requirements detailed in Chapter 2. Figure 7.12 shows that in order to have the same 95% confidence level sensitivity to the mass hierarchy, a detector at the Orr-Buyck site would have to have 40% more mass than a detector at Ash River. Due to the ambiguity discussed in Section 2.2.4, it is difficult to make up for a shorter baseline with greater statistics.

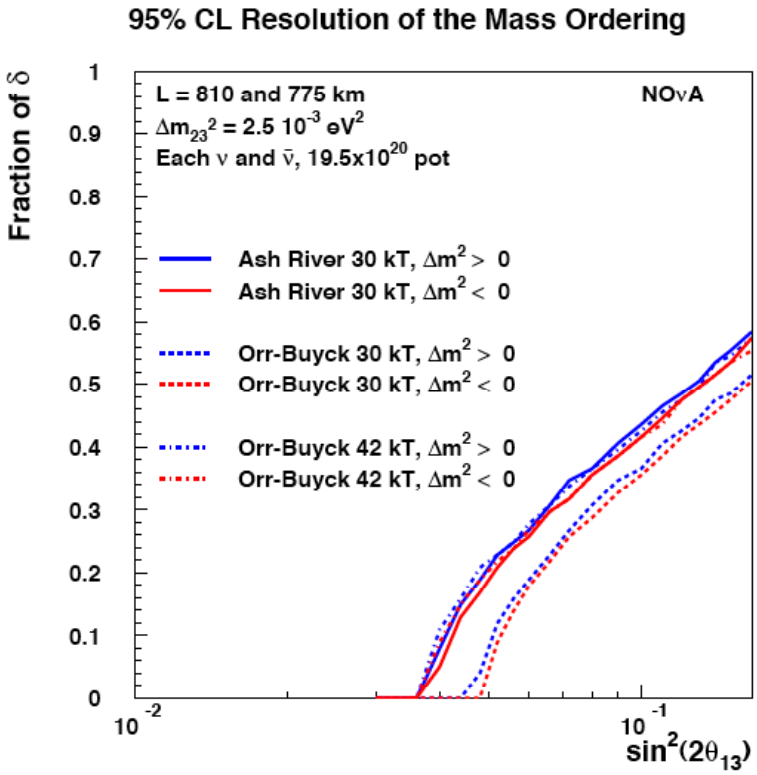

Fig 7.12: The 95% confidence level resolution of the mass ordering versus $\sin^2(2\theta_{13})$ for three years of running each neutrinos and antineutrinos. The vertical axis represents the fraction of δ values for which mass ordering is resolved. The curves are for a 30 kt detector at the Ash River site and for 30 and 42 kt detectors at the Orr-Buyck site.

Our Resource Loaded Cost and Schedule work is still in progress, but indicates that the cost of the NOνA Far Detector is about $ 6 M per kiloton of mass constructed. Thus 40% additional mass (~ 10 kt additional) at Orr-Buyck would mean the Orr-Buyck site costs would be of order $ 60 M more than a scientifically equivalent detector at Ash River.

Clearly the scientific comparison between the two sites overwhelmingly favors Ash River over Orr-Buyck when converted to a common currency. The modest advantages of the access and electrical power construction costs at Orr-Buyck are completely overshadowed by the cost of a detector capable of the same scientific measurements. In fact if the detector were placed at Orr-Buyck, we could not afford to build the extra mass and instead the detector capability for the mass hierarchy measurement would be compromised by about 5% in reach. We retain the Orr-Buyck site only as a second-string backup in case unexpected environmental or land acquisition problems occur.

7.4 Site Design Optimization

As discussed above in section 7.2, the Ash River site has been optimized for the best scientific performance. At the site itself, we have optimized the building position as shown in Figures 7.1 – 7.4 so as to mitigate any impacts on Voyageurs National Park. Our choice to follow the existing access road is also an optimization. Not only does the road already exist, using this road instead of a shorter road off the Ash River Trail also mitigates the NOνA impact on the National Park.

7.5 Quality Assurance

Our main concern at Ash River will be to follow through on the mitigation actions discussed above. This is a clear responsibility for the NOνA Project.

7.6 ES&H

Within Minnesota, environmental assessments for large construction projects proceed via an Environmental Assessment Worksheet (EAW) [4] submitted to the Minnesota Environmental Quality Board. This worksheet contains 31 specific items including

1) Project Title
2) Proposer
3) Responsible Governmental Unit submitting the EAW
4) Reason for EAW Preparation
5) Project Location
6) Project Description
7) Project Magnitude Data (area, buildings)
8) Permits and Approvals Required
9) Land Use(past use and potential conflicts with existing surrounding land uses)
10) Cover types (acres of land cover before and after the project)
11) Fish, Wildlife & Ecologically Sensitive Resources (endangered habitats)
12) Physical Impacts on Water Resources
13) Water Use
14) Water-related Land Use Management Districts
15) Water Surface Use (boating)
16) Erosion and Sedimentation
17) Water Quality: Surface Runoff
18) Water Quality: Wastewaters
19) Geologic Hazards and Soil Conditions
20) Solid Waste, Hazardous Waste, Storage Tanks

21) Traffic
22) Vehicle-related Air Emissions
23) Stationary Source Air Emissions
24) Odors, Noise and Dust
25) Nearby Resources (archaeological, historic, unique farm lands, parks, scenic views)
26) Visual Impacts
27) Compatibility with Plans and Land Use Regulations
28) Infrastructure and Public Services (new or expanded sewers, water mains, power lines, ...)
29) Cumulative Impacts (potential effects of related or anticipated future projects)
30) Other Potential Environmental Impasts
31) Summary of Issues

We have hired the Minnesota firm of Short Elliot Hendrickson, Inc.(SEH) as consultants to fill out the EAW for both the Ash River and the Orr-Buyck sites. SEH sees no issues that would keep the EAW for either site from being accepted by the Minnesota Environmental Quality Board as sufficient documentation for a determination that a full Minnesota Environmental Impact Statement will not be required. The Ash River draft EAW is available[5]. We expect the University of Minnesota, St. Louis County, or the Minnesota Environmental Quality Board itself to serve as the Responsible Government Unit submitting the EAW.

Following the example of the MINOS project done by DOE / Fermilab in the Soudan Mine, we expect the State of Minnesota EAW to be accepted as the basis for a Finding of No Significant Impact (FONSI) by DOE for the Minnesota portion of the project.

7.7 Risks

We still have to navigate the road permitting process with the Corps of Engineers, we have to acquire access rights to the site, we have to submit the EAW to the Minnesota Environmental Quality Board, we have to enter a public comments phase with the EAW, and we have to satisfy the DOE and obtain a FONSI for the Minnesota work.

7.8 Value Management

Section 7.3 serves as a formal Value Management Study of the two final candidate sites for the NOνA detector. We also expect to continue looking at the access road design to see if all or some of the wetlands area could be avoided.

Chapter 7 References

[1] Bill Miller and Marvin Marshak, NOνA note docdb#384, May 2005
[2] Bill Miller, NOνA note docdb#168, November 2005.
[3] International Dark Sky Association, www.darksky.org/fixtures/fixtures.html
[4] EAW Guidelines are available at http://www.eqb.state.mn.us/review.html
[5] draft EAW for the Ash River Site, NOνA docdb note #204.

8. Conventional Facilities

8.1 Introduction

Conventional construction work for NOνA includes work in three main areas: the access road and site work, the below grade excavation, and the above grade support areas. This chapter describes the design, alternatives to the design, and optimization of the design. Quality assurance issues, ES&H concerns, risks, Safeguards and Securities issues, and opportunities for value management are also discussed.

8.2 The Recommended Building Design

8.2.1 Access Road and Site Work

The site work consists of a new road from St. Louis County 129 to the Ash River Far Detector Hall as shown in Figure 8.1. The road follows the existing logging trail but smoothes the curves for 53-foot trailer truck traffic.

The road right of way will include a utility corridor to bring power and communication lines to the site. The utilities will be buried. The Ash River site requires a power upgrade and the local electrical cooperative will upgrade the electric service to site by replacing an existing transformer at the Kabetogama substation, replacing existing insulators and step down transformers along the route as well as installing a new transformer and related accessories at the project site. The project bears the cost for this electrical work with a small cost sharing from the utility company.

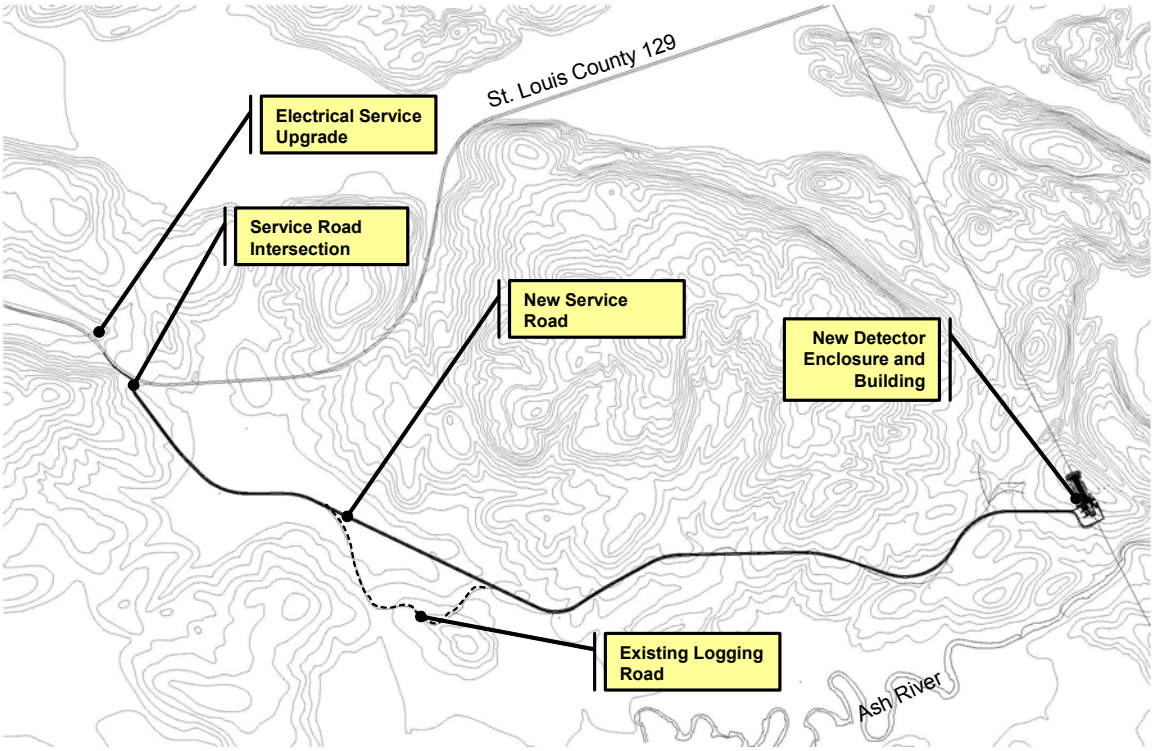

Fig. 8.1: Topology of the Ash River area showing the access road and utility corridor.

The site design includes two (2) 125 kvA emergency generators. One generator will provide emergency power for life safety systems while the other will power elevators, sump pumps and building heating. These generators will use propane as a fuel source.

The site work also includes the parking and hardstand areas for personnel and material deliveries.

8.2.2 Below Grade Areas

The areas at 13.5 meters below grade consist of the Detector Enclosure and the Assembly Area. The two areas together are a single cast-in-place concrete enclosure 155.5 meters long, 20.4 meters wide and 20 meters high (511 feet long, 67 feet wide and 65'-6" high) shown in Figures 8.2 and 8.3. The south end of the Assembly Area, shown at the far right in Figure 8.2, provides vertical access to a grade level loading dock for movement of equipment and detector modules.

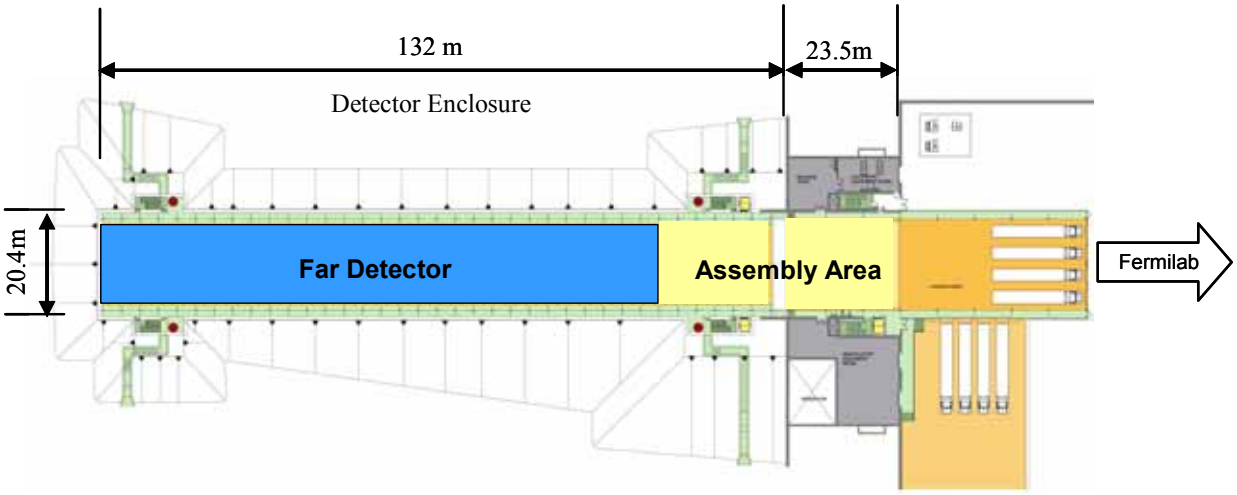

Fig. 8.2: Floor Plan of the Far Detector (blue) and Assembly (light yellow) areas at 13.5 meters below grade. The light green areas around the Far Detector are catwalks for detector access. The darker gold areas are loading docks at grade level.

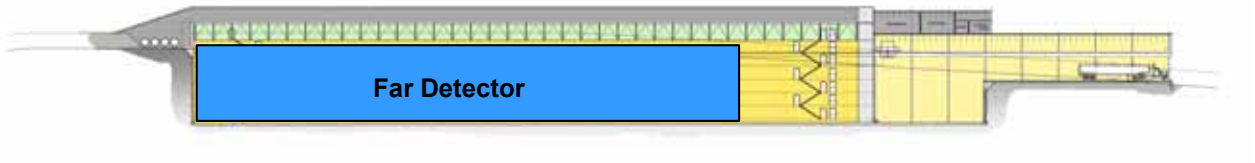

Fig. 8.3: Elevation View of the Detector Enclosure, Assembly Area and Loading Docks. The 3m thick overburden and the 3m thick final shield wall in the middle of the Assembly Area are visible in this view.

The NOνA detector is assembled from left to right in Figures 8.2 and 8.3, and the Detector Enclosure is sized to accommodate the apparatus required to assemble the detector. This equipment includes a block raiser, a glue machine and related support devices described in Chapter 16. This assembly apparatus requires approximately 49 meters of floor space south of the detector face being assembled. As the assembly nears completion at the far right of Figures 8.2 and 8.3, some of the assembly apparatus will be moved up onto the loading dock area so that the last part of the NOνA detector can be shoehorned into the deep enclosure. When the detector

assembly is complete, the Assembly Area will also contain a 3 meter (10 foot) thick precast concrete block shield wall to complete the physics driven overburden requirement.

The Detector Enclosure is serviced by four (4) code compliant exit stairs that provide two (2) means egress for each level of the enclosure. These stairs, located in the approximate corners of the enclosure also serve a detector catwalk system. The Assembly Area is serviced by two (2) code compliant exit stairs. One (1) standard sized elevator will provide vertical access to the lowest level of the Assembly Area, loading dock level as well as the support spaces.

Figure 8.4 shows an cross section view of the Detector Enclosure. The below grade areas will be excavated to approximately 13.5 meters (44'-6" feet) below grade to accommodate existing terrain as well as provide a below grade containment volume sized to contain the 100% of the liquid scintillator and a full discharge of the fire suppression system.

The material removed during excavation activities will be stockpiled on site and used to create a berm over the top of the Detector Enclosure that will provide the required cosmic ray shielding. This 3 meter (10 foot) thick overburden is shown in Figure 8.4.

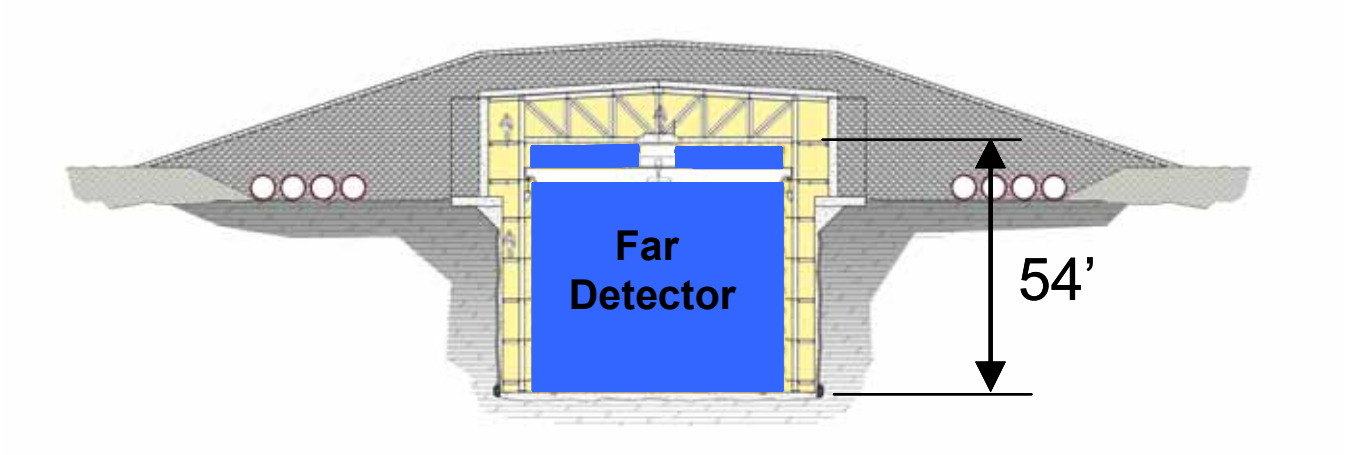

Fig. 8.4: Cross section through the Detector Enclosure.

A subsurface investigation [1] has indicated that the top of that the site has 5 – 15 feet of soil overburden and then is solid hard granite to a depth of at least 60 feet. Based on these conditions, the walls of the Detector Enclosure and Assembly Area have been designed to be cast-in-place concrete. For the portion of the walls in contact with the rock, the walls will be formed on one side utilizing the excavated rock face as the other form. For the portion of the walls in overburden, the cast-in-place concrete walls have been designed as retaining walls tied to the rock below. This system provides a uniform surface suitable for treatment and use as a secondary containment for the liquid scintillator.

The roof support structure will consist of a steel framed truss system supported by two (2) columns at each bent. The truss system will be almost 3.5 (11'-8") meters high at the mid-point to allow access to the top of the detector through the truss work. The trusses will be sloped to prevent to accumulation of standing water above the roof. The columns have been designed and located to reduce the span of the trusses. The columns are also used to provide support for the crane rails and a support for the catwalk system that provides access to the sides of the detector. Metal deck and concrete fill span between the trusses to provide the roof envelope for the Detector Enclosure.

Access to the sides of the detector is provided by means of a steel framed catwalk system that runs the length of each side of the detector. The design includes seven (7) levels of catwalks on each side of the detector spaced to provide access to 2 rows of modules per catwalk. Each level of the system will accessible from two of the exit stairs. Figure 8.5 indicates a typical column bay at the catwalk level with the service platform adjacent to detector.

Access to the top of the detector is provided by means of a steel grating system that spans the bottom chord of the roof trusses. This system is based on a light weight expanded metal grating in sections sized to be removed by two people. Access to the system is from either side of the top catwalk level. Figure 8.6 indicates the relationship of the top catwalk to the detector.

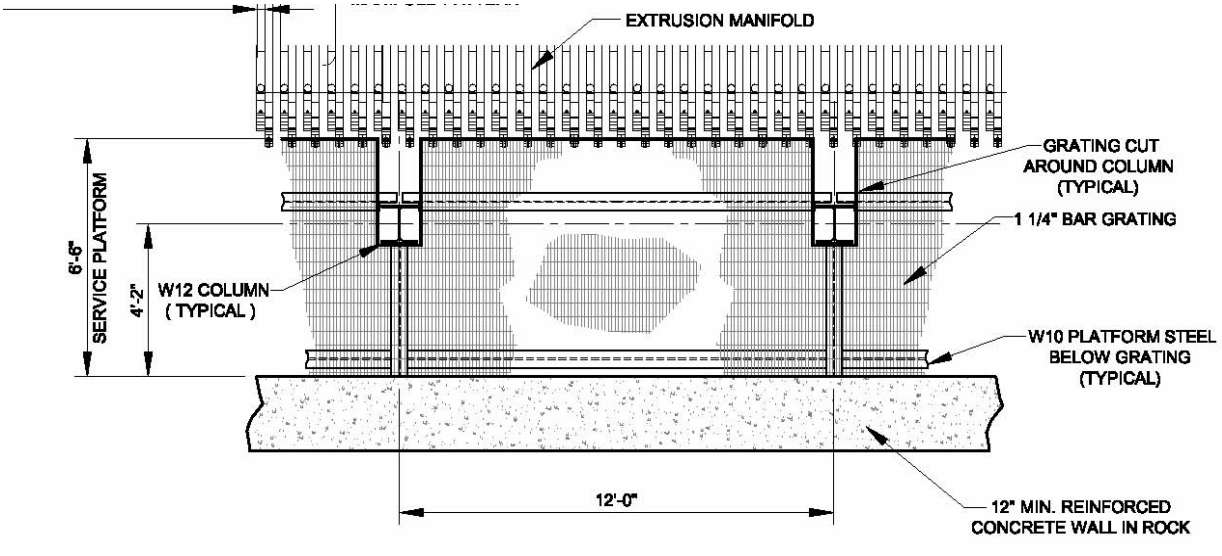

Fig. 8.5: Plan view of a typical column bay at a catwalk level.

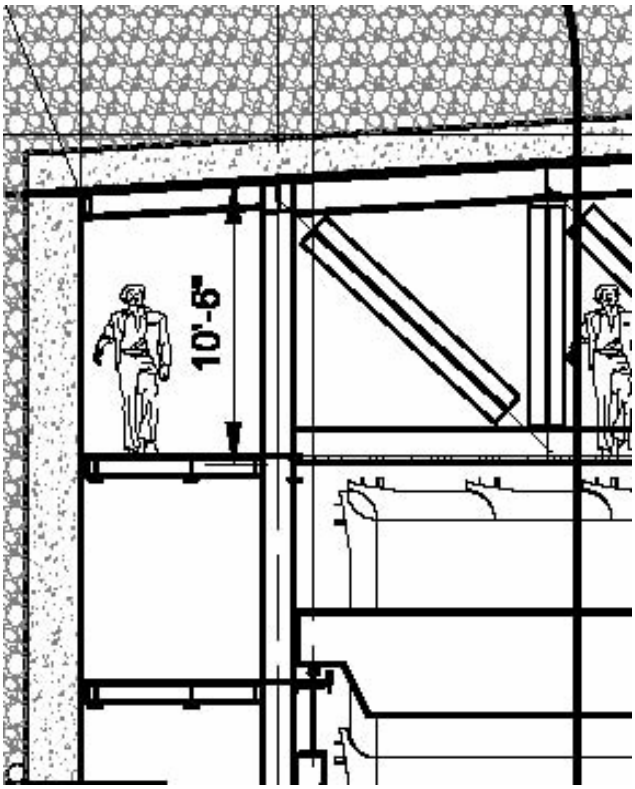

Fig. 8.6: Catwalk and truss at the top of the detector.

Since the Detector Enclosure and Assembly Area will be located below grade, ground water control has been included in the design. The roof construction will include a water resistant membrane installed above the concrete deck to direct water to the sides of the enclosure. The retaining wall will include provisions for damp proofing to be applied to the exterior face of the walls. Drainage strips ("dimple mats") will be located along the excavated rock face prior to placement of concrete for those walls in rock. These strips will divert accumulations of ground water to an underdrain system that encircles the Detector Enclosure. Water from these underdrains will be routed to one of four sealed ground water sump basins where it will be discharged to the surface away from the enclosure.

A separate sump basin or basins will be installed for the interior portion of the Detector Enclosure and Assembly Area. This sump system will catch any unexpected scintillator leaks from the detector and route the discharge to a holding tank. The interior walls of the Detector Enclosure and Assembly Area will be coated with an epoxy-based paint to help contain any scintillator leaks.

A 25 ton overhead bridge crane will be installed to facilitate movement of materials and supplies related to the detector assembly. The crane bridge is located below the top of the detector (see Figures 8.3 and 8.4) to reduce the excavation cost of the building. The crane stops will be moved to match the face of the detector assembly front. Two (2) material hoists, one serving each side of the detector, will provide a means of vertical movement of materials and supplies to each catwalk level.

The mechanical systems in the Detector Enclosure and Assembly Area have been designed to support the installation and operation of the detector. The HVAC systems will conform to ASHRAE 90.1, ASHRAE 62 and applicable NFPA requirements and applicable sections of the local codes and ordinances. The Detector Enclosure will be conditioned to provide 20 ^{o}C +/- 3 ^{o}C (68 ^{o}F +/- 5 ^{o}F) dry bulb air temperature and will maintain a 13 ^{o}C (55 ^{o}F) dew point. The Assembly Area will be conditioned to provide an environment range of 18 - 25 ^{o}C (65 - 78 ^{o}F). The outdoor air requirements are based on a normal operational occupancy of 10 people and are based on ASHRAE 62.

A process water system for support of the detector will be installed in the Detector Enclosure to provide 10 ^{o}C (50 ^{o}F) chilled water to the tertiary detector loops throughout the length of the enclosure. This system will include a 30-ton air-cooled chiller with built-in economizer, heat exchanger and associated piping.

The Detector Enclosure will be provided with an automatic foam sprinkler system installed in accordance with NFPA 11, NFPA 13 and NFPA 16 at a design concentration of at least 3%. A foam system is required because the liquid scintillator density is 0.86 g/cc. Fire Alarm systems will be installed in accordance with NFPA 72. To prevent accidental discharge, the activation of the suppression system will occur in a two step process. Air sampling systems will alarm on smoke detection and provide early warning to occupants. The foam sprinkler system will discharge only on activation of a line type heat detection device spaced at a maximum of 25 feet on center. The system has been designed to provide an application rate of 0.10 gallons per minute per square feet over the detector for a foam discharge time of 15 minutes. Upon activation of the smoke or heat alarm, the system will shunt trip the power to the electrical and mechanical devices in the enclosure. The depth of the below grade areas provide a containment volume sized to hold 100% of the NOνA detector liquid scintillator plus a full discharge of the fire suppression system.

Electrical service to the Detector Enclosure and Assembly Area will provide general house power and lighting for the installation and operation of the detector as well as power for the detector components. The design accommodates the 120 v power for the electronic racks spaced along the upper level of each side of the detector. Code required emergency lighting and exit lighting will be provided in the enclosure.

8.2.3 Above Grade Areas

The above grade portion of the facility consists of the Loading Dock and support spaces required to deliver, assemble and operate the Far Detector. Figures 8.7 and 8.8 indicate the relationship of the Assembly Area to the above grade portion of the building as well as the 25 ton overhead bridge crane that will be used to transport material and detector components from the upper level to the lower level.

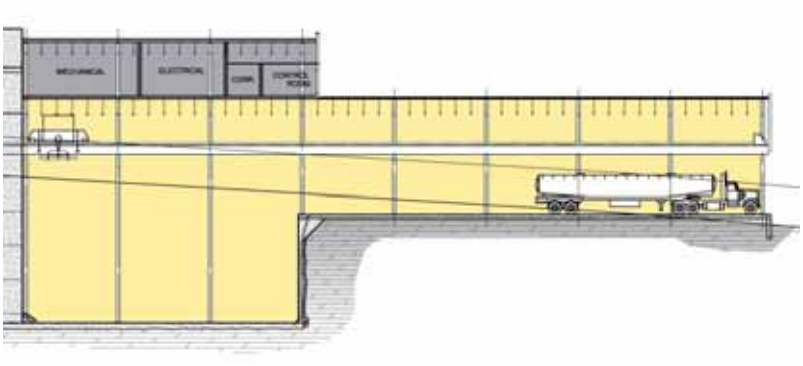

Fig. 8.7: Detail elevation view showing the relationship of the loading dock and upper level mechanical support spaces to the deep Assembly Area.

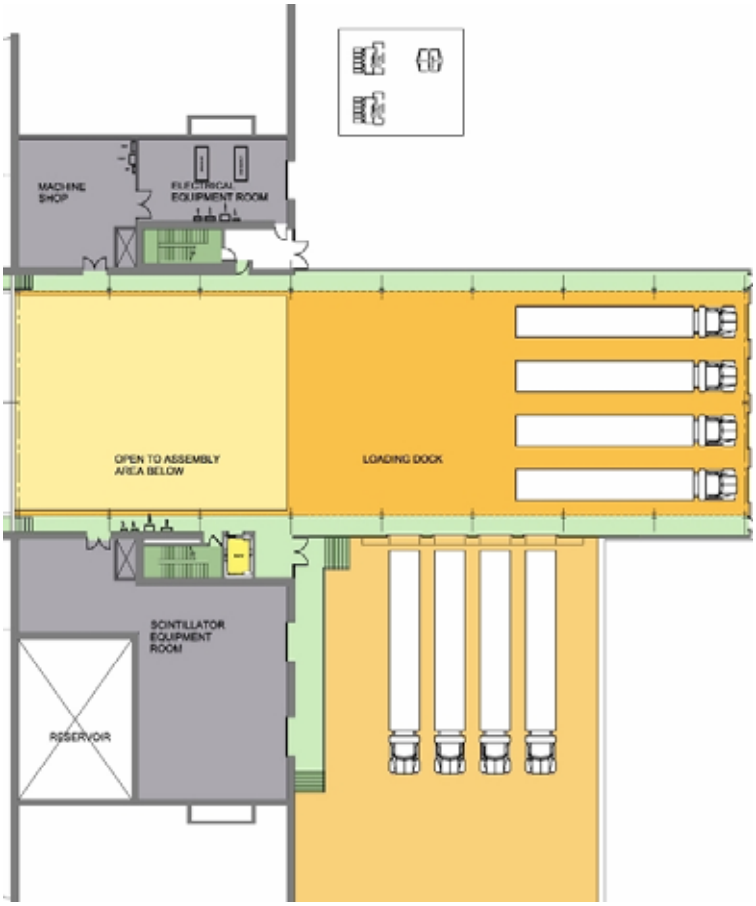

Fig. 8.8: Detailed plan view showing the relationship of the loading docks to the mechanical support spaces and the deep Assembly Area.

The Loading Dock has been designed to accommodate deliveries of detector components, liquid scintillator and related materials. The Loading Dock will have a four bay recessed loading dock along the west side and a four-bay at-grade dock to allow trailers to be located inside the building and underneath the coverage of the overhead crane. Adjacent to Loading Dock are the support spaces for the facility. These include an Electrical Equipment Room, Machine Shop and Scintillator Equipment Room shown in Figures 8.7 and 8.8.

The upper level of the building will provide space for Mechanical and Electrical equipment, a Control Room, Conference, Kitchenette and toilet room. Figure 8.9 shows the general arrangement of the spaces on the upper level.

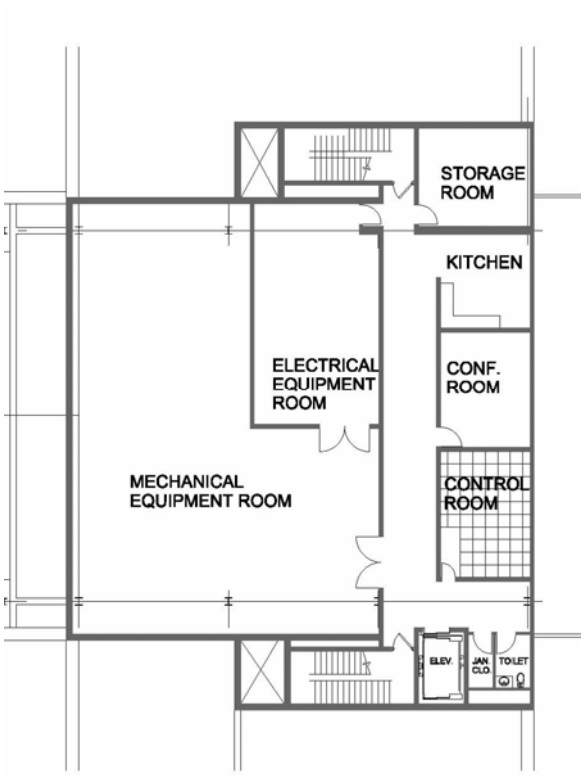

Fig. 8.9: Detailed plan view of the upper level of the building located above the deep Assembly Area.

The above grade portion of the building will be steel-framed metal sided construction on a cast-in-place concrete foundation and floor slab. The upper levels of the building will have cast-in-place concrete floor slabs on metal deck with steel framed floor structure. The roof structure will be built-up roofing over tapered insulation on metal deck with steel framing.

The HVAC systems in the above grade portion of the building will conform to ASHRAE 90.1, ASHRAE 62 and applicable NFPA requirements and applicable sections of the local codes and ordinances. The Loading Dock will be conditioned to provide an environment temperature range of 15 - 32 ^{o}C (60 - 90 ^{o}F). The building support spaces will be conditioned to provide 20 +/- 3 ^{o}C (68 +/- 5 ^{o}F) air temperature. The occupied spaces on the upper level will be conditioned to provide a 20 +/- 3 ^{o}C (68 +/- 5 ^{o}F) temperatures. The Control Room will provide space for eight computers racks and related equipment. The room will include a computer room air conditioning unit to provide 22 +/- 3 ^{o}C (72 +/- 5 ^{o}F) dry bulb air temperature and will maintain a 45% +/- 5% relative humidity. The outdoor air requirements are based on a normal operational occupancy of 10 people and are based on ASHRAE 62.

The Above Grade portion of the building that will contain liquid scintillator during truck deliveries and filling of the detector will be provided with an automatic foam sprinkler system installed in accordance with NFPA 11, NFPA 13 and NFPA 16 at a design concentration of at least 3 percent. Fire Alarm systems will be installed in accordance with NFPA 72. To prevent accidental discharge, the activation of the suppression system will occur in a two step process. Air sampling systems will alarm on smoke detection and provide early warning to occupants. The foam sprinkler system will discharge only on activation of a line type heat detection device spaced at a maximum of 25 feet on center. The system has been designed to provide an application rate of 0.10 gallons per minute per square feet over the detector for a foam discharge time of 15 minutes. Upon activation of the smoke or heat alarm, the system will shunt trip the power to the electrical and mechanical devices in the enclosure. The remaining areas of the above grade building will be protected with a conventional water based sprinkler system. Containment of any liquid scintillator spills and of any fire suppression system discharge will be provided.

Electrical service to the above grade portion of the building will provide general house power and lighting for the installation and operation of the detector as well as power for the the overhead crane. Code required emergency lighting and exit lighting will be provided in the above grade portion of the building.

8.3 Alternative Designs Considered

8.3.1 Building on the Surface with No Excavation

The first NOνA proposal [2] in March 2004 included a surface building shown in Figure 8.10 with no overburden and no underground containment system. This is a simple and cheap steel-framed metal sided construction on a cast-in-place concrete foundation and floor slab [3], At that time the photon component of cosmic rays was not understood as a shielding problem and instead an active detector veto system was proposed. Such an active shield will not eliminate the penetrating photon component of cosmic rays to the level required for the experiment.

At that time an outdoor containment system with berms like those around tanks at oil refineries was imagined. We have abandoned that scheme because it does not appear to work at low temperatures like those which can be encountered in northern Minnesota. The need to also contain any fire suppression system runoff also drove up the size and cost of such a scheme.

This above ground alternative has been discarded since it does not satisfy the scientific and ES&H performance requirements as they are now understood.

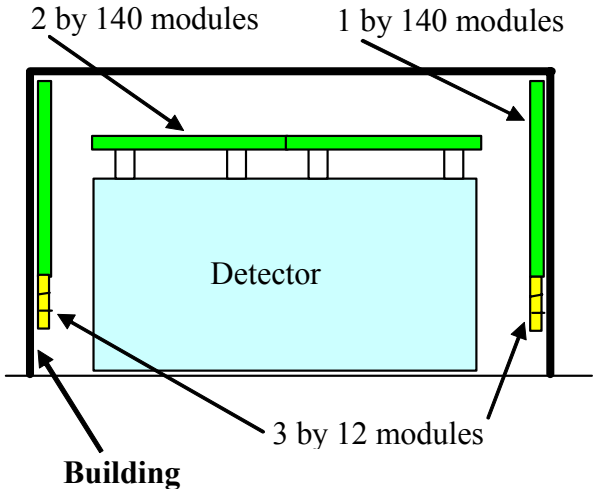

Fig. 8.10: An above ground building design.

8.3.2 Building Partially in the Ground for Containment

The final revised NOνA proposal [4] of March 2005 was based on a building that included a portion located below grade as shown in Figures 8.11 and 8.12. This design does provide the necessary means of secondary containment for the liquid scintillator. The above grade portion of the building was designed to be a pre-engineered metal building. This alternative has been discarded since it does not meet the scientific requirement for cosmic ray shielding. This alternative also does not provide enough staging area for assembly of the detector given our more complete understanding of the assembly process, nor does it have enough loading dock area to accommodate the incoming truck traffic during the assembly of the detector.

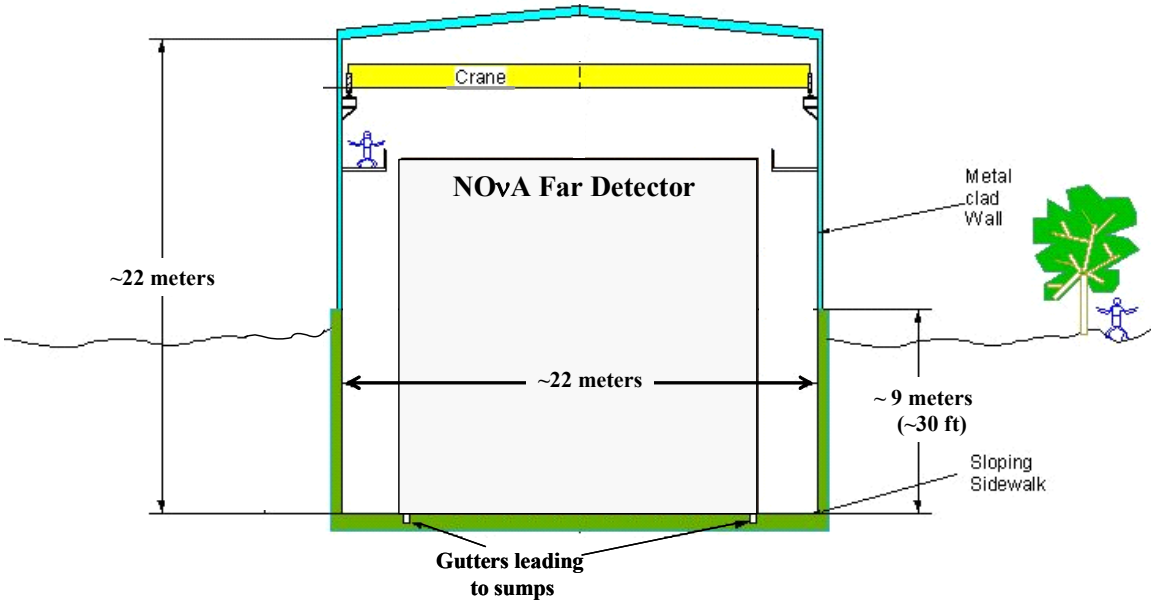

Fig. 8.11: Cross section of a building design with underground containment but no cosmic ray overburden.

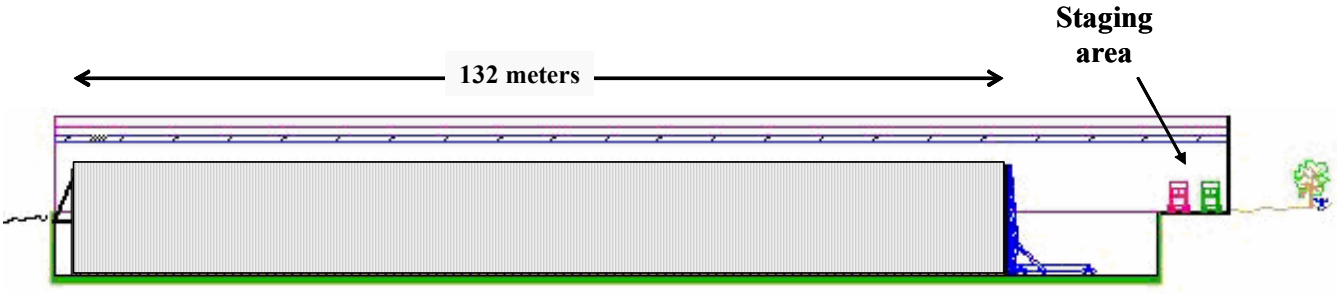

Fig. 8.12: Elevation view of the building in Figure 8.11.

8.3.3 Building with a 10 meter Overburden

A January 2003 Off-Axis detector study [5] commissioned by the University of Minnesota group investigated methods of providing a detector enclosure with a 10 meter overburden as shown in Figure 8.13. Cut and cover construction in bedrock was the favored solution in this study. This alternative has been discarded because a 10 meter overburden is not required and the cost of this alternative is more than 2.5 times the recommended NOvA building design.

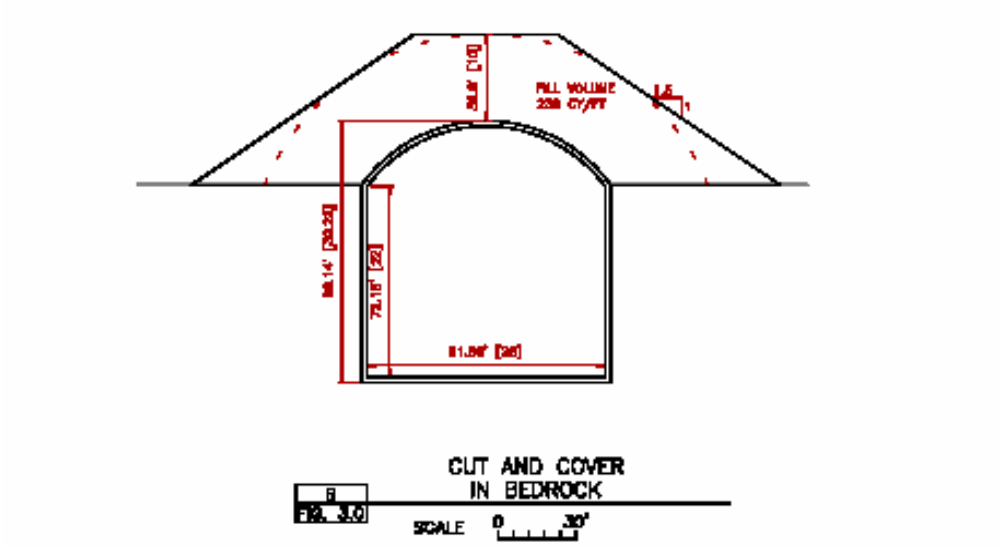

Fig. 8.13: Cross section of a building design with a 10 meter overburden.

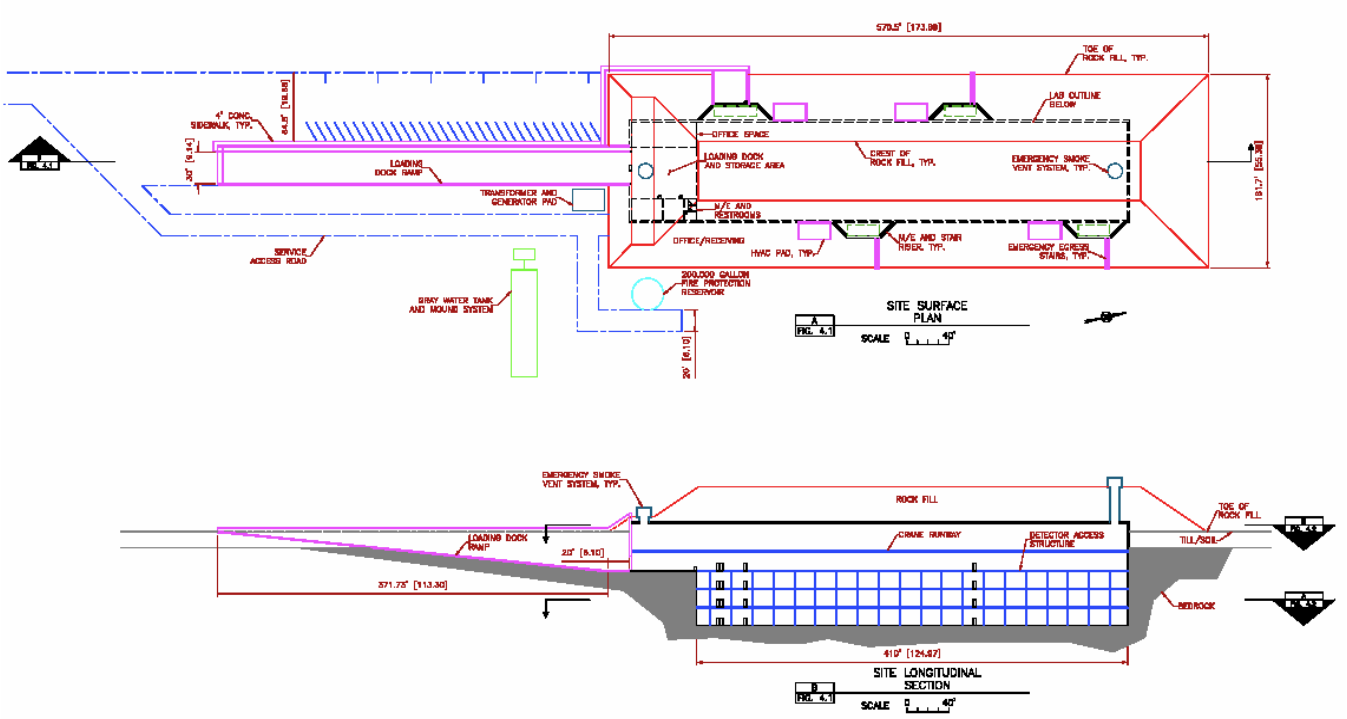

Fig. 8.14: Plan and elevation views of the building design shown in Figure 8.13. Access to this deep structure required a long truck ramp shown at the left of the diagrams.

8.3.4 Alternative Construction Techniques

Alternative construction techniques were also considered during 2003 in the NOνA design process, and these efforts are documented in reference [6]. This study included special buildings for the shipping container alternative structure discussed in Chapter 4, automatic building systems, and a tension fabric system design. The study included quotes from vendors and full detailed cost estimates for all the building options.

The study explored the cost of building designs as a function of building width to help bound the practical size an Off-Axis detector designs. The study considered the relative costs of building at different below grade depths in the bedrock so that our later design process was a cost informed process.

8.4 Optimization of the Selected Building Design

The size of the building is driven by the physical and infrastructure requirements of the Far Detector and related installation components. The volume of the building has been minimized to reflect the known spatial requirements to assemble and operate the detector in a safe manner.

Documentation of the optimization of the building design already complete includes the incorporation of the Value Analysis recommendations [7] for the roof structure of the Detector Enclosure and for one of two detector access systems considered.

8.5 Quality Assurance

All aspects of this project will be periodically reviewed with regard to Quality Assurance issues from Conceptual Design through Title III completion. This review process will be completed in accordance with the applicable portions of the Fermilab policies. The following elements will be included in the design and construction effort:

- An identification of staff assigned to this project with clear definition of responsibility levels and limit of authority as well as delineated lines of communication for exchange of information;
- Requirements for control of design criteria and criteria changes and recording of standards and codes used in the development of the criteria;
- Periodic review of design process, drawings and specification to insure compliance with accepted design criteria;
- Identification of underground utilities and facility interface points prior to the commencement of any construction in affected areas;
- Conformance to procedures regarding project updating and compliance with the approved construction schedule;
- Conformance to procedures regarding the review and approval of shop drawings, samples test results and other required submittals;
- Conformance to procedures for site inspection by Fermilab personnel to record construction progress and adherence to the approved contract documents;
- Verification of project completion, satisfactory system start-up and final project acceptance.

8.6 ES&H

A life safety consultant, Schirmer Engineering was retained to perform a life safety analysis of the facility [8]. This analysis included criteria and requirements that were incorporated into the design of the facility.

Fire Alarm/Fire Suppression systems shall be designed in accordance with the applicable codes, regulations and ordinances. Automatic sprinkler systems shall be designed to a minimum

of a Use Group F-1 (moderate hazard occupancy) classification of the International Building Code and National Fire Protection Association (NFPA) latest edition. The most commonly used NFPA standards relative to automatic sprinkler systems are: 13, 20, 25, 231, 231C, 318, and 750.

Fire alarm systems shall be designed with a minimum standby power (battery) capacity. These batteries shall be capable of maintaining the entire system in a non-alarm condition for 24 hours, in addition to 15 minutes in full load alarm condition. The most commonly used NFPA standards relative to fire alarm systems are: 70, 72, 90A, and 318.

Combination horn/strobe devices will be provided throughout the facility spaces no greater than 75 feet apart. Manual pull stations will be provided at each egress door.

Stairways will be provided with a Class 1 Standpipe and two-way fire department communication.

The below grade portion of the Detector Enclosure will serve as secondary containment in the event of leak or spill of the liquid scintillator and is sized to contain the 100% of the liquid scintillator and a full discharge of the fire suppression system. The concrete walls and floor will be coated with a field applied epoxy system to seal the surface of the wall. A system of trench drains will collect and direct spilled liquid scintillator to an isolated monitored sump system. Once collected, the liquid scintillator will be pumped and disposed. This system will require manual activation.

8.7 Risks

While the design of the conventional facilities has been progressed to a point where a cost and schedule range can be estimated, the design requires iteration with the other Level 2 tasks to respond to an evolving detector design. This process will continue in the coming months.

The site and subsurface conditions present a cost and schedule risk. This risk will be mitigated by developing and executing a site exploration program consisting of a detailed topographic study of the terrain and features as well as a thorough subsurface investigation including soil/rock borings to better understand the conditions and their impact on the planned construction.

The construction methodology presented is just one possible design solution. It is recognized that other methods of achieving the scientific driven requirements are possible. This risk will be mitigated in additional value management studies leading to a “design-build” bid process for the construction project.

The conventional facilities are seen as a cost and schedule driver the project. Increased costs and/or schedule slippage has the potential to negatively impact the project. These risks will be mitigated by obtaining an independent cost and schedule estimate for comparison to the range presented in this report. The two estimates/schedules will be compared and reconciled and used as the input for further design iterations.

8.8 Safeguards and Security

The project follows Fermi National Accelerator Laboratory, Argonne National Laboratory, and University standards during construction at those institutions. When the whole detector comes together in Ash River, the project has the greatest value-added cost sitting in one place. The assembled detector will be located beneath the overburden and relatively secure, but the loading dock end is a point of vulnerability. Security measures like berms, fencing, gates, and card readers on doors are being considered.

8.9 Value Management

Three formal value analysis studies related to the conventional facilities have been completed [7]. These studies incorporated a professionally applied, function-oriented, systematic

team approach to analyze and improve value of the detector enclosure roof system and access to the detector. Focused on reducing the cost of the structural system while achieving the same quality level, these studies resulted in recommendations that were presented to the NOνA Technical Board. Two of the three recommendations (Detector Enclosure Roof Study and Detector Side Access Study) were accepted by the NOνA Project Manager and incorporated into the design documents. The study on single sided access to the detector was rejected.

Additional value analysis studies are being considered. These include methods of coating the below grade concrete walls to provide secondary containment, a "cut and fill" study to balance the amount of excavated material with the volume of the overburden, and a detector enclosure length study that will examine the implications of a shorter or longer detector enclosure which may speed the detector assembly period.

Chapter 8 References

[1] Report of Subsurface Conditions and Piezometer Installation. See NOνA docdb Note # 162.
[2] I. Ambats et al., NOνA Proposal, March 2004, see the first entry for 2004 at http://www-nova.fnal.gov/reports_page.html
[3] Steve Dixon, Building Alternate Study, NOνA docdb Note # 128, September 2005
[4] D. Ayres et al., Revised NOνA Proposal, March 2005, see http://www-nova/fnal.gov/NOvA_Proposal
[5] Off-Axis Neutrino Detector prepared by CNA Consulting Engineers, Dunham Associates Miller-Dunwiddie Architects, University of Minnesota Project No. 298-03-1113, January 2003. Experiment Facility. See DocDB Document #252.
[6] J. Cooper, S. Dixon, H. Jostlein, and T. Lackowski, Off Axis Detector Enclosure Design Study Report, Fermilab FESS Engineering Project No. 6-2-22, June 2003.
[7] T. Lackowski and R. Alber, FESS/Engineering, NOνA docdb Note #140.
[8] Rick Glenn, Schirmer Engineering, Fire Protection/Life Safety Analysis for the NuMI Off-Axis Ve Appearance (NOνA), NOνA docdb Note #252.

9. Liquid Scintillator

9.1 Introduction

NOνA intends to use a liquid scintillator equivalent to Saint-Gobain (Bicron) BC-517P [1] or Eljen Technology EJ-321P [2], essentially 5% pseudocumene scintillant in a 95% mineral oil base with small amounts of UV waveshifters and small amounts of anti-oxidants. Most of these components have been known since the 1950s [3]. These scintillators have a moderate light output, 28% of anthracene when fresh and 21% of anthracene when fully oxygenated [1,2]. The advantages of this mixture include stability, low cost, availability in large quantities, low toxicity, high flashpoint and low potential as an environmental hazard. Previous work has shown that this scintillator attacks neither wavelength shifting fiber nor PVC over lifetimes exceeding this experiment (see Chapter 10, Section10.4).

9.2 The Recommended Design

9.2.1 Scintillator Composition

The NOνA detector requires 21.9 kilotons of liquid scintillator. The components of the scintillator we plan to use are shown in Table 9.1.

Component	Purpose	% (mass)	Gallons	Total Mass (kg)
Mineral oil	Solvent	94.4	5,432,962	17,481,099
Pseudocumene	Scintillant	5.5	306,358	1,015,891
PPO	Waveshifter	1.2×10^{-1}	-	22,356
bis-MSB	Waveshifter	1.7×10^{-3}	-	313
Anti-oxidant	Prevents yellowing	$\sim 2 \times 10^{-6}$	-	0.4
Total			**5,739,320**	**18,519,659**

Table 9.1: Composition of NOνA liquid scintillator.

This mixture has been measured by NOνA to give the same light output as BC-517P / EJ-321P for muons crossing through a NOνA PVC cell with a wave-shifting fiber read out via a phototube. Similar measurements of the light output have been done with a small sample and an alpha source. Both methods show that the composition in Table 9.1 has the same light output as the commercial scintillators to within a few percent.

The emission spectra of BC-517P and EJ-321P are shown in Figure 9.1. Pseudocumene [1,2,4-Trimethybenzene] is the primary scintillant. It is a benzene derivative with many uses in the plastics and paint industries. Pseudocumene is excited by traversing ionizing particles and the de-excitation produces light in the UV range as shown in Figure 9.1. PPO [2,5-diphenyloxazole], bis-MSB [1,4-di(methylstyryl)benzene] and POPOP [1,4-bis(5-phenyloxazol-2-yl)benzene] are wavelength shifters in the scintillator mix that shift UV light from the pseudocumene to the visible region. POPOP is used in some scintillators (BC-517L is an example), but it is not used in our selected alternative of BC-517P / EJ-321P. The absorption and emission spectra of all three wavelength shifters are shown in Figure 9.1 with data from [4]. These scintillators also typically contain anti-oxidants such as BHT or tocopherol (Vitamin E).

Oxygen will pass through the NOνA PVC cell walls so that the scintillator will become oxygenated. Oxygenation generally proceeds to a stable light output within a few months. Our design assumes fully oxygenated scintillator.

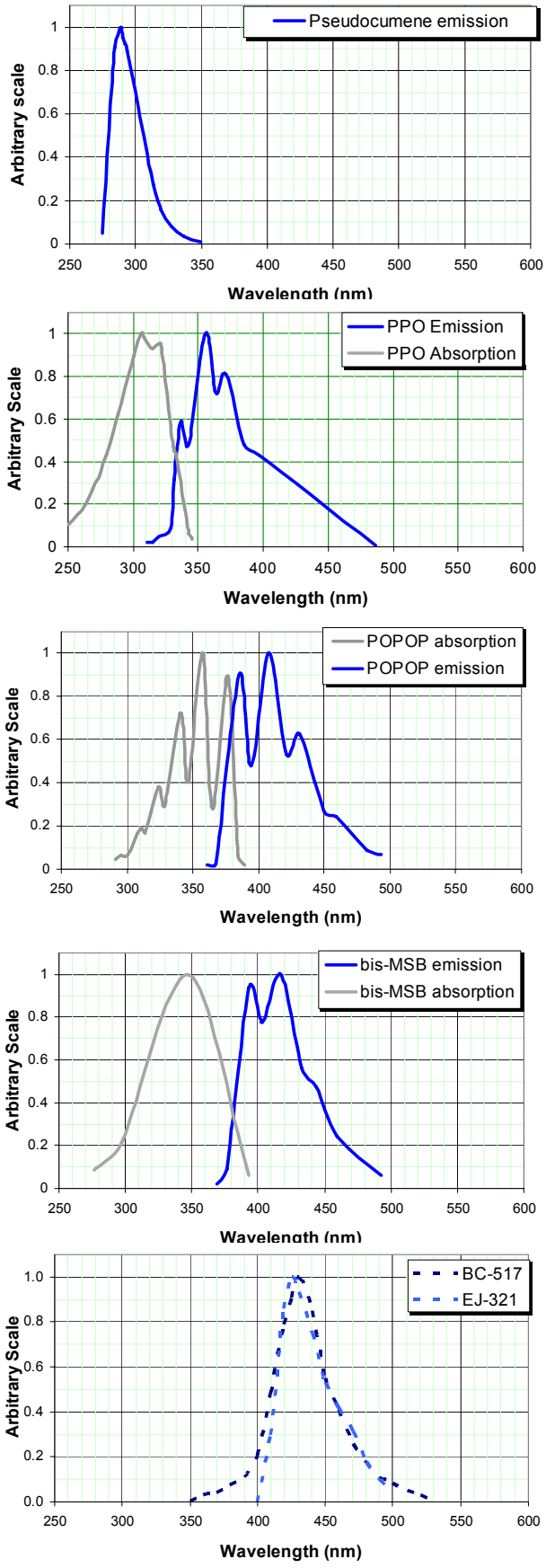

Fig. 9.1: The emission spectrum of pseudocumene, the absorption and emission spectra of PPO, POPOP, and bis-MSB, and the resulting emission spectra of BC-517P and EJ-321P scintillators. The spectra have all been normalized to an arbitrary scale with a peak at 1.0 to illustrate the wavelength shifting from pseudocumene to final scintillator.

The actual scales are important and the absolute values of the Molar Extinction Coefficients for each component are relevant. for absorption. Long tails on the absorption distributions (not shown) have the effect of shifting the final scintillator output to the higher wavelengths shown in the bottom figure. Similarly, the actual relative values of the Fluorescence Emission yields for each component are important to the final result.

9.2.2 Scintillator Blending at Fermilab

NOνA intends to purchase the scintillator component ingredients in Table 9.1 and blend them at Fermilab. Mineral oil and pseudocumene are both liquids. The wavelength shifters are produced in power form. The wavelength shifters will not dissolve in mineral oil and must first be dissolved in the pseudocumene. The pseudocumene/fluor mix is then blended together with the mineral oil. We use the word "blending" to emphasize that this mixing operation is not a chemical reaction. Instead the operation involves dissolving powders in one step and then mixing two liquids together in a final step.

The wavelength shifting powders will be delivered to Fermilab in 5 – 25 kg fiber drums. The mineral oil and pseudocumene will arrive at Fermilab by truck on leased ISO tanks like the one shown in Figure 9.2. An ISO tank is just a special kind of international shipping container conforming to the container standards set by the International Standards Organization. On land the tanks are moved by truck on container chassis as shown in Figure 9.3. The tanks can also be moved by rail.

Fig. 9.2: A standard 20 ft by 8 ft ISO tank container. The tank shell is made of stainless steel and holds 6,341 gallons of liquid. Lifting blocks are provided in the upper four corners of the frame.

Fig. 9.3: An ISO tank on a container chassis. The four bottom corner blocks are used to hold the tank to the chassis frame during transport

At Fermilab the wavelength shifting powders will first be dissolved in an ISO tank of pseudocumene to form a fluor concentrate. This blending can be done in a closed loop (powders in an empty ISO tank which is then connected to pseudocumene in a second ISO tank) to capture all vapors. The second step of blending the fluor concentrate with mineral oil can be done with in-line blenders in a second closed loop system or by metering appropriate amounts of fluor and mineral oil from two ISO tanks into a third empty ISO tank. A conceptual time and motion study [5] indicates that one finished ISO tank of scintillator can be produced in about two hours of blending operations by a crew of three technicians, including time for rudimentary QA checks. Additional time will be required to move the ISO tanks to the blending stations, but we believe a rate of 3 ISO tanks per day of blended scintillator can be achieved easily. We expect this operation to occur in an outdoor transfer pump station fitted with the same level of fire protection as that applied to the Fermilab vehicle fueling station located near Site 38. This facility looks like your local gas station. The pseudocumene has flash points higher than or equal to gasoline and diesel fuels transferred at the fueling station, so similar fire protection means are adequate.

The blending plan described above is a concept and requires additional study. Once the details of the plan are fully developed we intend to have the entire process reviewed by independent consultants with relevant backgrounds in petroleum blending and industrial chemical engineering.

9.2.3 Shipping Components and Scintillator

Three separate ISO tank transportation loops convey the scintillator components to Fermilab and the mixed scintillator from Fermilab to Ash River as shown in Figure 9.4. Separate sets of dedicated ISO tanks will be used in each loop to reduce the possibility of contamination.

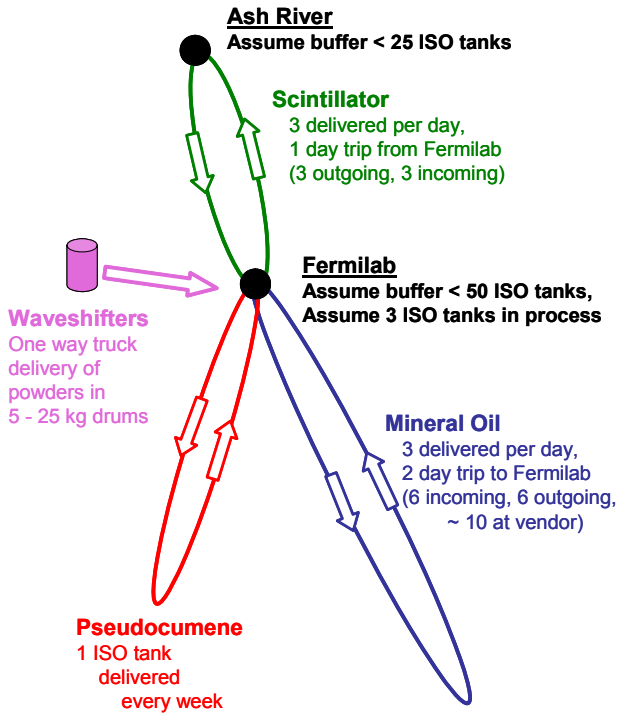

Fig. 9.4: Diagram indicating the assumed NOvA shipping and staging model. Three loops operate with dedicated equipment, ~25 in a mineral oil loop, ~ 6 scintillator in a scintillator loop to Ash River, and ~3 in a pseudocumene loop. Wavelength shifting fluors arrive in packed form by standard truck delivery. Up to 50 ISO tanks are staged at Fermilab and about 25 ISO tanks are staged at Ash River waiting to go into the detector. Approximately 110 ISO tanks and about 30 ISO chassis are required in this model.

It will be necessary to stage some amount of mixed liquid scintillator, both at Fermilab and at the Far Detector Hall so that the scintillator filling at Ash River can follow the detector assembly in all seasons without downtime due to transportation difficulties in poor weather. Figure 9.4 indicates a model with up to 50 ISO tanks buffered at Fermilab and up to 25 ISO tanks buffered at Ash River waiting to be offloaded into the NOνA detector. While 5.7 million gallons of scintillator are required in the NOνA Far Detector at Ash River, we expect no more than 350,000 gallons to be staged at Fermilab at any one time. In fact this limit can be set administratively if required. ISO tanks can be stacked up to five high when fully loaded as shown in Figure 9.5, providing an efficient means of temporary buffer storage at the two ends of the scintillator transportation loop. Such stacking is probably not required at Fermilab but is required at Ash River where floor space in the Far Detector Hall will be at a premium. When stacked 5 high, 25 ISO tanks need only 800 square feet of space and constitute about a one week buffer in the filling operation.

Fig. 9.5: ISO tanks stacked on a container ship in the Port of Houston. The corner blocks are used to tie the stack layers together with standard ISO twistlocks.

9.3 Alternatives Considered

Other liquid scintillators were considered in addition to the selected pseudocumene/ mineral oil based alternate. There are other liquid scintillators available higher light yields, but there is a direct correlation between light yield and chemical activity since typical scintillants contain aromatic rings. A family of biodegradable scintillators based on phenyl-ortho-xylylethane(PXE) was tested during MINOS prototype efforts tested [6]. An example is Ecoscint-O, a biodegradable PXE based scintillator which unfortunately dissolves double-clad wavelength-shifting fibers within a day at elevated temperatures.

Purchasing pre-blended scintillator was investigated but no vendor was willing to supply the quantities required by NOνA within the time frame required by NOνA. St.Gobain-Bicron and Eljen are really in the medical scintillator business dealing with batch sizes of tens of gallons. They could build up their infrastructure to handle NOνA volumes, but do not see a sustained future market to justify the effort.

9.4 Scintillator Design Optimization

9.4.1 Mineral Oil

The NOνA liquid scintillator constitutes 73% of the NOνA detector mass and is itself 95% mineral oil by weight. The mineral oil is inert and acts as a solvent for the scintillant and waveshifters. The primary performance feature of the mineral oil for NOνA is its attenuation length for light near 430 nm. Mineral oil is a cost driver and the attenuation length of different grades and qualities of mineral oil must be compared to the costs of those different grades.

Experiments like MiniBooNE and MACRO have used large quantities of mineral oil and mineral oil based liquid scintillator, respectively, but required very long attenuation lengths because of the detector technologies and geometries employed. The NOνA geometry is very different from those detectors since the light is collected locally by the wave shifting fiber. Typical light path lengths in the NOνA scintillator are about 1 meter so that long attenuation lengths are not required. This allows us to relax the mineral oil specifications for NOνA.

The most highly refined mineral oils are classified as food grade and meet the FDA requirements for consumption by humans. US Pharmacopoeia (USP) mineral oil is considered a heavy food grade mineral oil and has a large viscosity. National Formulary(NF) mineral oil is considered light food grade mineral oil and has a smaller viscosity. Higher viscosity means higher price. The step from USP to NF is about a 5 - 15% reduction in price. MiniBooNE used an NF mineral oil for their detector since an attenuation length of 20-25 meters was required.

Technical grade mineral oils are the next grade down from food grade. Technical grade mineral oils are not as highly refined as food grade mineral oils, but are approved by the FDA for indirect food contact and are typically used as lubricants for food processing machinery. The cost of technical grade mineral oil is less than NF mineral oils by about another 10 - 40%, depending on the viscosity.

The petroleum industry is not familiar with attenuation length as a specification and instead uses the Saybolt scale to characterize the color range of petroleum products including aviation fuels, kerosene, white mineral oils, hydrocarbon solvents and petroleum waxes. The Saybolt color index scale runs from -16 (darkest) to +30 (lightest) and unfortunately attenuation lengths above a few meters all lie at +30 on this scale. NOνA has blended scintillators using Saybolt +26 Technical Grade Mineral Oil and found such scintillator to be unacceptable for the experiment.

Mineral oils are derived from petroleum feedstocks called Parafinic Group II Base Oils. The American Petroleum Institute has defined the broad Base Oil group categories to create guidelines for licensing engine oils. All the groups cover a wide range of viscosites, but sovent-refined base oils typically fall into Group I , while hydropocessed base oils fall into Group II. Hydroprocessing [7] is a way of adding hydrogen to the base oil at elevated temperatures in the presence of a catalyst to stabilize the most reactive components in the oil, improve the color, and increase the working life of the oil. Several hydroprocessing steps have been introduced in recent years to advance this industry: Hydrocracking was introduced in 1969 and adds hydrogen at high temperatures and pressures to crack feedstock molecules into smaller molecules. Catalytic dewaxing was added in 1984 and catalytically removes n-paraffins and other molecules with waxy side chains by cracking into smaller molecules. In 1993 hydroisomerization was added to this string of processing steps to reshape the n-pariffins and other molecules with waxy side

chains into desirable compounds instead of cracking them completely away. This third step has resulted in distinctive Parafinic Group II base oils which typically have no color.

An increasing fraction of the base oil manufacturers use this full range of technology, but as recently as 2003 less than half used the full three step package. This technology is proprietary and several competing ones now exist, each using different catalysts and different temperatures and pressures for the various steps. We have obtained identically classified (and similarly priced) mineral oils with attenuation lengths for 430 nm light in the range 2m to 10m. While our current state of knowledge is incomplete, we suspect that the range is due to the technologies being applied and we will continue to evaluate these oils for NOνA.

We have determined that the 2 m attenuation length mineral oil is adequate for the NOνA experiment and find that the 10 m mineral oil gives only about 5% more light in our test cell. It is clear that a Technical Grade (cheaper) oil will meet our needs and that we have a range of appropriate vendors.

9.4.2 Pseudocumene

We have investigated the light yield of Bicron BC-517 / Eljen EJ-321 families of mineral oil based scintillators to tune the light yield via the amount of pseudocumene in the mix. Figure 9.6 shows the Bicron and Eljen light yields and some of our investigations with pseudocumene concentrations around 8 – 15%, while holding the waveshifters constant.

As demonstrated in Chapter 3, a 5% pseudocumene fraction is adequate for the NOνA scientific performance requirements. We note here that a 5% mix is a factor of two reduction from the liquid scintillator described in the NOνA proposal [8]. This reduction in pseudocumene has achieved a major cost reduction and reduced the ES&H risk (see section 9.7).

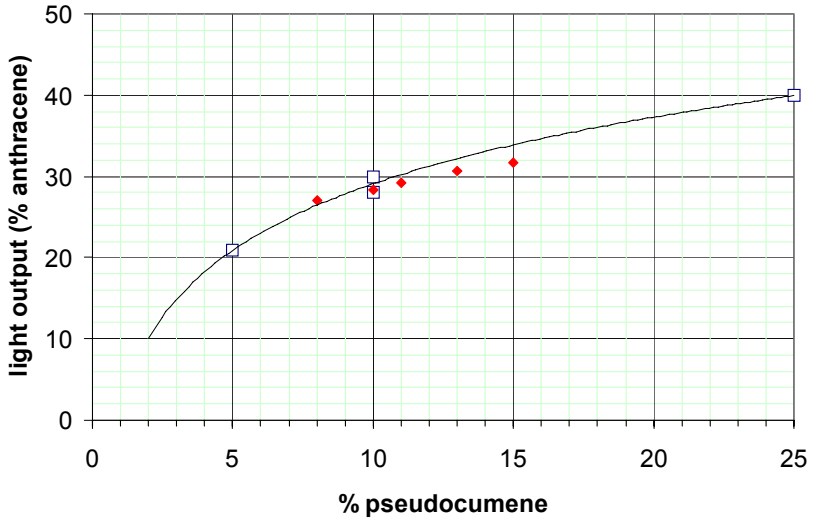

Figure 9.6 The light output vs. pseudocumene concentration in a variety of commercial Bicron and Eljen mineral oil based liquid scintillators is shown with the open squares and a line to guide the eye. NOνA investigations with pseudocumene concentrations in the 8 – 15% range are shown as red diamonds. The NOνA points varied only the pseudocumene and did not change the amount of waveshifters in the blend.

9.5 Quality Assurance and Quality Control

The liquid scintillator is the heart of the NOνA experiment. In combination with the wavelength shifting fiber and PVC cells, the scintillator is crucial to the performance of the

detector. We must be sure that the scintillator is free of impurities and properly blended. Quality Control (QC) and Quality Assurance (QA) are fundamental to the construction of this detector.

9.5.1 Comparison with QA / QC in Other Experiments

During the 1980s and 1990s at Fermilab a similar blending operation demonstrates how QA/QC can depend on local control of the process. When ionization drift chambers became common in Fermilab experiments, the drift chamber gas of choice converged on argon – ethane mixtures with additives like Freon or alcohols. This product was initially specified by experiments as a mixture to be delivered in gas cylinders from vendors. In spite of everyone's best efforts to write a tight specification, the fact that ethane was a by-product from oil fields meant that the feedstock for this product varied with time. At one point several experiments were damaged by argon-ethane mixtures with unknown impurities that led to deposits on the drift wires. Tracking down the problem was difficult because these experiments typically fed their chambers from a ganged set of low pressure gas cylinders and the offending cylinder was difficult to identify. Even when isolated, the component in the gas causing the problem was difficult to identify.

Several experiments and particularly the Collider Detector at Fermilab (CDF) experiment [9] took a different tack in response to this problem and began purchasing ethane in bulk to mix at Fermilab with boil off gas from liquid argon to form the drift gas. The ethane was transported in dedicated Fermilab-owned trailers. Samples from each incoming trailer of ethane were chemically analyzed at Argonne National Laboratory for any impurities before that trailer's ethane was allowed into the local mixing facility. Molecular sieves, cold traps and other protective schemes were devised to remove any known or unknown impurities. Stainless steel piping of the gas was the default for the CDF complex and the pipes were all put through a cleaning procedure before assembly. The mixing process was controlled by programmable logic controllers and a trained technician force guided the process on a daily basis. The resulting mixture was tested in-line in multiple test cells before being allowed into the CDF drift chamber. The exhaust gas was also tested. Extensive records were kept of the entire process so that when any anomaly appeared, similar batches could be immediately rejected in favor of batches known to be good. Some samples of the gas mixture were tested in accelerated aging cells to look for longer term effects. This attention to detail has kept the original CDF drift chamber and its high luminosity upgrade replacement functioning well over a period of 20 years. Not all problems were avoided, but the record keeping allowed a diagnostic process to guide the investigation of problems. The sustained effort over two decades was successful and eventually all other Fermilab experiments adopted similar mixing schemes.

The problem with these petroleum based products (ethane, mineral oil, pseudocumene) is that they come out of oil fields from a variety of wells, so the base material is variable. High gain ionization in drift chambers is more sensitive to impurity problems than light output of scintillator is for NOνA. However, ethane used in drift chambers is a relatively simple byproduct of distillation, while mineral oil and pseudocumene are often distilled by many successive vendors via proprietary processes in a long supply chain. These products are blended by the vendors to meet specifications having little to do with our applications in high energy physics.

Other experiments using liquid scintillator have blended their own product. One particular example is the MACRO experiment [10] which used 600 tons (about 120,000 gallons) of liquid scintillator. MACRO used a mixture with 3.6% pseudocumene. The wave-shifters were added to the pseudocumene at Drexel University and quality assurance of this fluor concentrate was done at Cal Tech. The blending with mineral oil took place at INFN Frascati and used mineral oil shipped to Frascati from the U.S. The blending for MACRO was done in a tanker truck at Frascati and then shipped to the Gran Sasso Laboratory.

9.5.2 NOνA QA / QC plans

We believe scintillator blending at a local venue (like Fermilab) with a dedicated NOνA technician work force offers the best possible way to assure a quality product. Since we know that light output and attenuation length are crucial parameters, we will measure those parameters in our own maintained and calibrated test apparatus. The required QC / QA will require a relentless and dogged pursuit of information, database entries, samples, and personnel training over several years. Accelerated aging tests of some samples should continue well beyond the initial installation and filling of the NOνA experiment.

Before any blending is done quality assurance will be performed on each incoming batch of the various raw materials. This will involve chemical analyses and well as attenuation length measurements. Records of these tests will be kept in a database and samples of each incoming batch will be kept available for long term testing. Once the materials are demonstrated to meet our specifications, the blending will proceed in two stages using a dedicated set of ISO tanks for each stage. Dedicated equipment will be used at all times for the mixed scintillator as well as the raw materials. Dedicated ISO tanks, pumps, hoses and fittings will be used for all of the liquids. Scoops and measuring cups for the powders will be used once and discarded.

In the first blending step, the wavelength shifting powders will be measured into an empty ISO tank, and the appropriate amount of pseudocumene will be added to the tank. The resulting pseudocumene/fluor product will then undergo another QA step to make sure the blend has been done properly. Samples of each fluor batch will be kept available for long term testing. The second step will blend the fluors with the mineral oil and once again the final product will be tested, records entered, and samples kept. When an ISO tank arrives at the Far Detector site, time and temperature records from the trip will be entered and each tank mix will be tested one more time before the contents are transferred to the PVC extrusions.

Ideally the pedigree of scintillator in each of the ~20,000 extrusion modules will be known in detail. If the response of a module changes, we can only change the electronics package on the outside of the detector. We can't change the scintillator, the fiber, or the PVC extrusion. If swapping the electronics does not cure the problem, we will immediately begin to worry that this offending module is the beginning of a problem due to the other components. With the QC / QA records we can immediately look for modules which might show similar effects and begin to work the problem and understand its ramifications. Table 9.2 illustrates the problem of matching extrusion modules to blended ISO tank batches.

Object	Scintillator (gallons)	Mineral Oil (gallons)	Pseudocumene (gallons)
1 extrusion module			
Horizontal	299	282	16
Vertical	273	258	15
1 plane of 12 modules			
Horizontal	3,587	3,394	193
Vertical	3,280	3,099	181
1 ISO tank	6,341	6,341	6,341
2 planes of modules	6,867	6,493	374
1 block of 31 planes	106,285	100,494	5,791

Table 9.2: Relative amounts of the scintillator blend in different units relevant to the detector and raw material delivery system. Horizontal modules have more liquid because the fiber manifold is full of liquid.

9.6 ES&H

Liquid scintillator of the type to be used by NOνA is commonly used in laboratory settings and can be used safely by following a few precautions. Chemically impervious gloves must be worn at all times when working with the scintillator. In addition, the workspace must be well ventilated and no open flames may be present. The flashpoint of commercial Bicron 517P / Eljen EJ-321 liquid scintillator[1,2] is 115°C making it safe for use in large volumes. Foam, carbon dioxide or dry chemical fire suppression systems are recommended. The Minnesota Pollution Control Agency has ruled that this scintillator is not considered a hazardous material in the State of Minnesota (see Appendix B).

Pseudocumene appears on only one US federal regulatory list, the US Environmental Protection Agency (EPA) Toxic Release Inventory Program [11], since it is toxic for aquatic organisms and can induce long-term damage to the aquatic environment. Spills must be contained and isolated from the groundwater. We are aware of the Borexino Detector problems at the Gran Sasso Laboratory in Italy, and take that as a lessons learned experience[12] for NOνA. As a result, full secondary containment of the liquid scintillator is built into the design of the Far Detector Hall, the Near Detector area, the Integration Prototype Detector area, and the blending facility.

NOνA plans to blend the liquid scintillator components together at Fermilab. The blending operation introduces additional concerns because of the presence of large quantities of pure pseudocumene. The flashpoint of pure pseudocumene is variously reported as 44 - 54°C, making it a Class II combustible liquid according to the National Fire Protection Association. We cannot handle this liquid inside a building, so this has led to the blending scheme outlined in Section 9.2.2 where the work is performed outdoors at a facility like a neighborhood gasoline fueling station. The blending all occurs in closed loop ISO tank systems where the vapors are controlled. It is even possible to start all the pseudocumene / wave-shifter blending ISO tanks with a purge of nitrogen gas to further reduce any risk of fire. Open flames and other sources of ignition will be excluded in the area where the pseudocumene is used or stored.

One of the advantages of ISO tanks is that there is never a need to off-load the product from one transportation system to another. Instead one just lifts the ISO tank off its railcar or truck chassis and places it directly where needed. No hoses are involved and no possibilities for spills are introduced.

Pseudocumene as a human heath hazard [13] is noxious to inhale, an irritant for the eyes, the respiratory tract and the skin. Bronchitis, headache, fatigue and drowsiness are experienced by 70% of the workers exposed to high concentrations. Given that the major route of entry of pseudocumene is the lungs, it is important to prevent it from entering the breathing zone. Our blending scheme where the work is performed outdoors (under a canopy) provides appropriate ventilation. Any open containers will be kept covered or closed when not in use. To cover the risk of accidental leakage a containment scheme will have to be developed for the blending site that includes specific measures for pseudocumene spills.

Outdoor work is itself an ES&H concern and our work plan has to allow for excessively cold and hot days when worker time outdoors may be limited.

9.7 Risks

Once the PVC modules are filled with liquid scintillator it is difficult to drain the extrusions and replace the scintillator. Thus, the greatest risk associated with the scintillator is the possibility that extrusion modules are filled with contaminated or improperly mixed scintillator. This risk is mitigated by the extensive QA procedures described in Section 9.5.

There is the additional risk that a long-term, unanticipated chemical reaction takes place between the liquid scintillator (or low-level impurities in the liquid) and the detector materials

with which it comes into contact. There is some precedent for this from the NuTeV experiment where BC517L reacted with brass fittings over a 10 year period to ultimately reduce the light output by nearly a factor of two [14]. NuTeV was able to replace their 4,000 gallons of liquid scintillator but replacing the 5.7 million gallons in NOνA is a much tougher financial and logistical problem. To mitigate this risk, NOνA will do accelerated aging tests of liquid scintillator in PVC modules that includes the endcaps, fiber manifolds, fibers and adhesives that will be used in the final detector.

9.8 Value Management

It may be possible to tune the light output of the liquid scintillator by adjusting the amounts of pseudocumene and the wavelength shifting fluors even further than our optimization so far. Other value management studies, for example resulting in an increased reflectivity of the PVC, may allow a re-optimization of the scintillator with a lower cost. Without changes in the other NOνA components, the mixture detailed in Table 9.1 has been optimized in the context of the NOνA cell variables as outlined in Chapter 5.

We will continue to explore cheaper mineral oils to search for the minimum cost solution. The R&D Integration Prototype Near Detector is a crucial part of these investigations. This detector requires ~29,000 gallons of scintillator and we are putting together several different procurements from several different vendors to learn more about the properties of their bulk deliveries over time and to learn how various blended combinations perform.

We need to continue studies of the pseudocumene as delivered from vendors to understand if the impurities cause any problems with PVC, fiber, or epoxies or if those impurities can cause any degradation of the scintillator light output. Pseudocumene is the reactive component in our scintillator and its impurities have similar properties. Accelerated aging studies will be done with blended scintillators using pseudocumene from several vendors. Chemical analysis of the pseudocumene samples will be done to confirm the impurities as stated by the manufacturers.

We believe our blending model using ISO tanks at Fermilab will give the best QC / QA product, but we will continue to investigate other options. There are commercial blending facilities where this work could be done, but it appears to be expensive, partly because of the cost of shipping the 5.7 million gallons of liquid anywhere but on a nearly direct path between the source and Ash River. We are uneasy about the QC / QA of the blended product in a remote location and would likely have to station our own technicians at the scene. Based on our current estimate, blending at Fermilab is the most cost effective solution, but we will continue to investigate this question. As a value management effort, we intend to have the entire blending process reviewed by independent consultants with relevant backgrounds in petroleum blending and industrial chemical engineering.

The risks of some unrecognized contaminant damaging the scintillator in the longer term might be mitigated by increasing its light output in such a circumstance. We will investigate the possibility designing the extrusion modules to allow bubbling nitrogen through the liquid scintillator to recapture the light yield lost to oxygenation. Figure 9.7 shows that the oxygenation loss is reversible. Such schemes have to allow bubbling through the entire liquid volume of an extrusion and this would seem to limit such schemes to the vertical extrusions. The horizontal extrusion might be designed to allow draining, bubbling, and reloading of the scintillator. These options would involve modification of the PVC module endcaps, include a new cost for fittings, and introduce the possibility of leaks. Such schemes would have to be easily repeated 20,000 times or they would introduce new risks of their own. We will have to analyze the costs vs. the probability of various risks for any such designs.

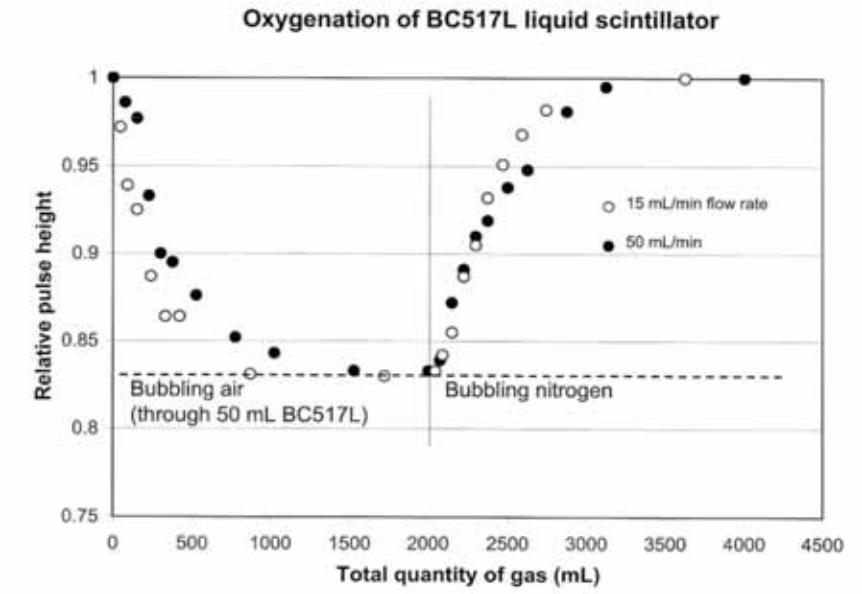

Fig. 9.7: Light output vs. time (quantity of gas bubbled) for a 50 mL sample of Bicron BC-517L. Air was bubbled to oxygenate the scintillator, then nitrogen was bubbled to reverse the effect. Two different flow rates gave the same overall result once the time-integrated total quantity of gas reached the same level in the two cases.

Chapter 9 References

[1] Mineral Oil Based Liquid Scintillators, www.bicron.com
[2] Mineral Oil Based Liquid Scintillators, www.eljentechnology.com/index.html
[3] For example, see Berks et al., Brit. J. Appl. Phys, vol 14, 141 (1963) for the absorption and emission spectra of PPO and POPOP. There are references in this paper to work by Kallman and others from the early 1950s. See also H. Rheinberger, "Liquid Scintillation Counters, 1950-1970, Max Planck Institute for the History of Science, 1999.
[4] See Berks et al. in ref [3], the Oregon Medical Laser Center at www.omlc.ogi.edu/spectra, and Back et al., the Borexino Collaboration, arXiv:physics/0408032 v1 6 Aug 2004 for sample data.
[5] Draft Plan for Scintillator Mixing at Fermilab, Dave Pushka, NOvA document database # 191, November 2005.
[6] P. Border et al., Nucl. Instrum. Meth A 463, 194 (2001).
[7] See Kramer, Lok, and Krug, "The Evolution of Base Oil Technology", in "Turbine Lubrication in the 21st Century", edited by Herguth and Warne, American Society for Testing and Materials, ASTM STP#1407, 2001. See also Kramer et al., Machinery Lubrication Magazine, May 2003.
[8] The NOνA Collaboration, "Proposal to Build a 30 Kiloton Off-Axis Detector to Study $\nu_\mu \rightarrow \nu_e$ Oscillations in the NuMI Beamline," http://www-nova.fnal.gov/NOvA_Proposal/-Revised_NOvA_Proposal.html.
[9] Bob Wagner, Fermilab, CDF Collaboration, private communication.
[10] S. Mufson, private communication, 2006. See aslo M. Ambrosio et al., the MACRO detector at Gran Sasso, NIM A 486 (2002) 663-707.
[11] EPA Toxic Release Inventory Program, www.epa.gov/trinter/chemical/index.html, 2001.
[12] Borexino Safety Handbook, August 2002.
[13] See the National Institute for Occupational Safety and Health (NIOSH) and Centers for Disease Control (CDC) chemical safety card (1994) at www.cdc.gov/niosh/ipcsneng/neng1433.html, 1994, or the EPS chemical summary at http://www.epa.gov/chemfact/s_trimet.txt , 1994.
[14] R. Bernstein, private communication.

10. Wavelength Shifting Fiber

10.1 Introduction

Plastic wavelength shifting (WLS) fiber provides an efficient method for collecting light from the long narrow cells used in this detector. After capture, the WLS fiber shifts the wavelength of the light from violet (400-450 nm) to green (500-600 nm) and traps it within the fiber by total internal reflection. The MINOS Far Detector provides considerable experience on the construction and operation of this light collection design.

10.2 The Recommended Design

To maximize light collection and transmission per unit cost and to satisfy the experiment's mechanical constraints, NOνA will use a 0.8 mm diameter, looped fiber inside of each PVC extrusion cell. The looped fiber design shown in Figure 10.1 effectively provides two fibers with a no cost, each with a perfect mirror 15.7 meters from the end. This gives a factor of two more light from the far end of each cell, where light output is most important, than from the far end of two individual fibers with nonreflecting far ends. The overall factor is only 3.6 times the light output of one fiber because two fibers in the same cell shadow each other.

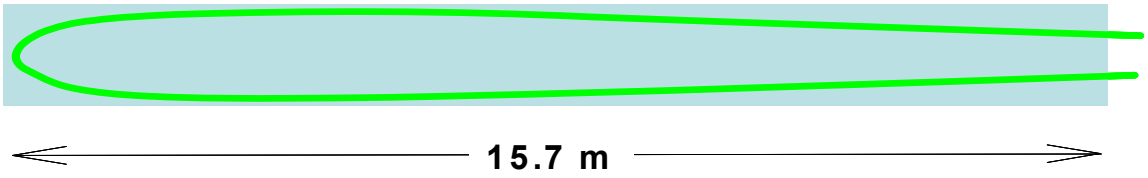

Fig. 10.1: A single NOνA cell with a looped WLS fiber, shown in green.

Suitable multiclad WLS fiber is available from Kuraray, the same type of fiber and the same vendor used for MINOS. St. Gobain Crystals (Bicron) also produces a similar fiber. The fiber core material is polystyrene followed by an acrylic inner cladding and a fluorinated-polymer outer cladding. The combination cladding increases the total internal reflection (see refractive indices in Table 10.1) and transmission of the fiber. The thickness of the inner cladding is ~3% of the fiber diameter and the thickness of the outer cladding varies from 1% to 3% of the fiber diameter, depending on the vendor. The polystyrene is doped with ~ 200 parts per million of K27 wave-shifting dye.

Material	Refractive Index
Polystyrene	1.59
PMMA (acrylic)	1.49
Fluorinated polymer	1.42

Table 10.1 Refractive indices of the of multiclad fiber layers.

Figure 10.2 shows the progression of light from the scintillator through absorption and emission by the K27 dye, and through attenuation by the polystyrene and effective attenuation via re-absorption by the K27 dye. The 425 nm scintillator light is shifted to a peak of ~ 510 nm for light at the near end of the fiber, and is shifted (and attenuated) to a peak ~ 545 nm for light coming from the far end of the 15.7 m long cell. The data for K27 and for the attenuation lengths of polystyrene and fiber are from Kuraray [1] for 1.0 mm diameter Y-11(200) fiber.

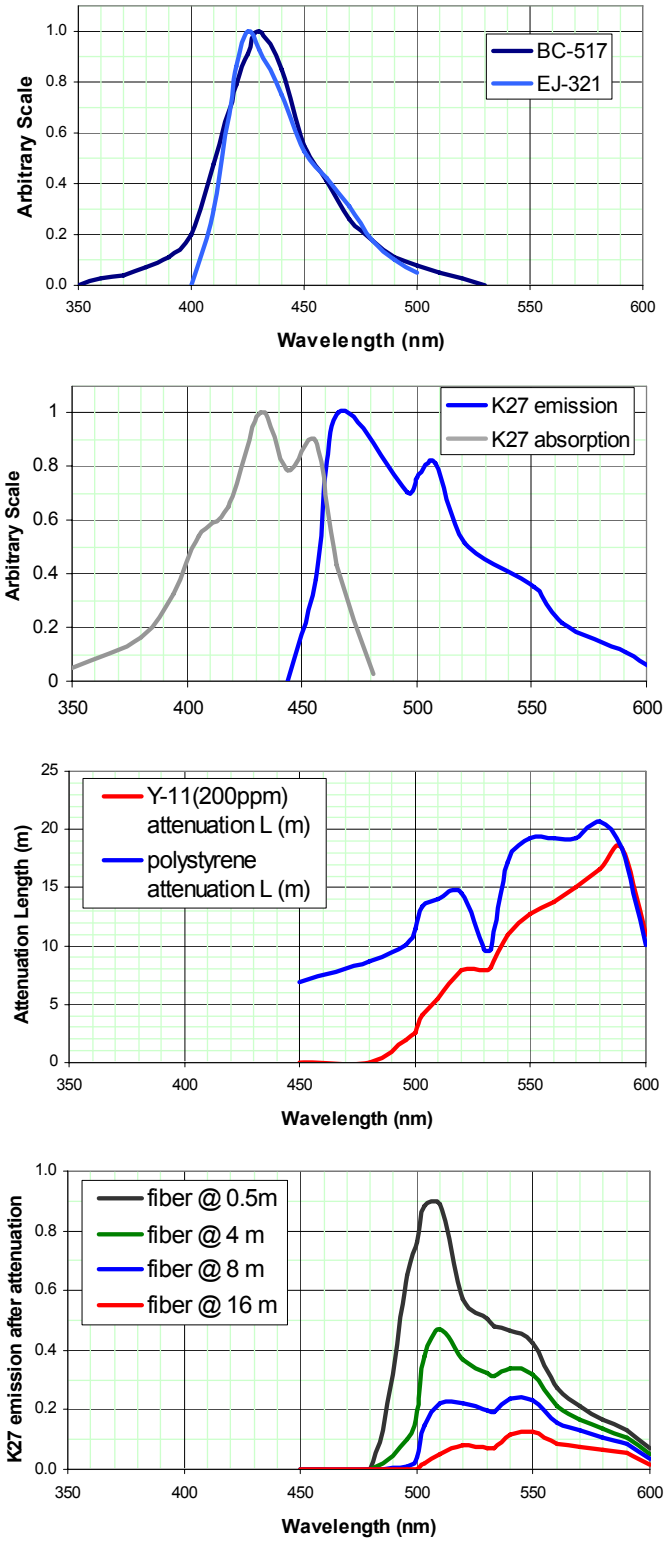

Fig. 10.2: The emission spectrum of NOvA liquid scintillator (top), the absorption and emission spectra of K27 wave-shifting dye (next to top), the attenuation length vs. wavelength for polystyrene fiber and K27-doped polystyrene fiber (next to bottom), and the expected surviving spectrum of wavelengths at 0.5m, 4m, 8m, and 16 m down the fiber (bottom).

The measured spectrum of the wavelength-shifted light that survives transport through a fiber as a function of the fiber length for 1.2 mm diameter MINOS fiber is shown in Figure 10.3. The measured data are in good agreement with the step by step multiplicative model in Figure 10.2. The shift of surviving light in the fiber to 550 nm and higher puts premium on a photodetector with high quantum efficiency at these wavelengths.

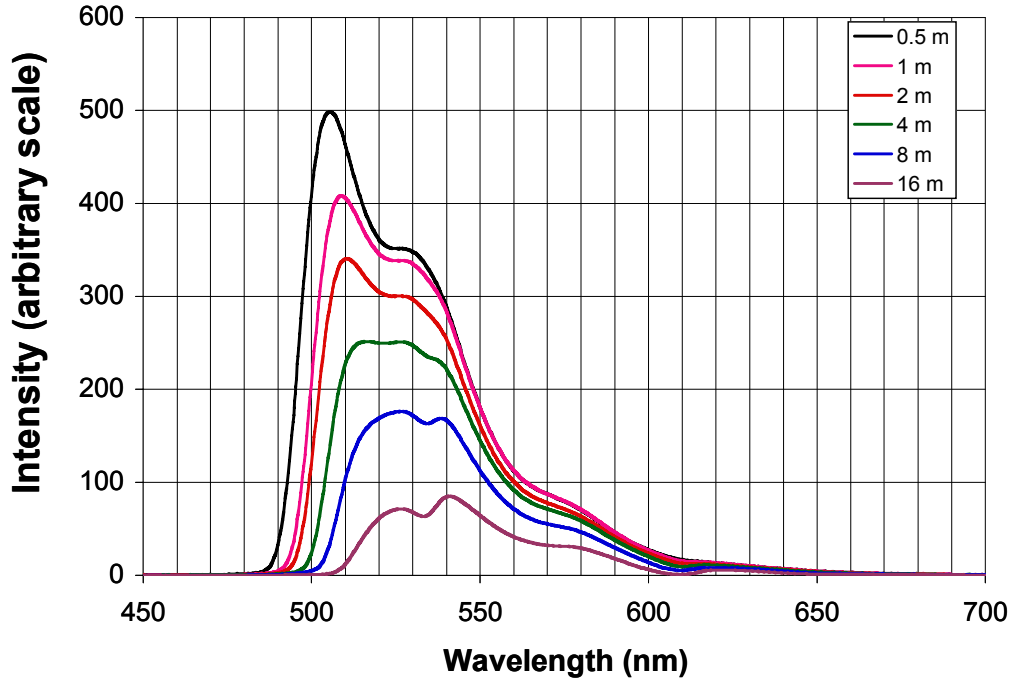

Fig. 10.3 The spectrum of wavelength shifted light that survives transport through a fiber as a function of the fiber length. These measurements were made with a MINOS 1.2 mm diameter fiber for fiber lengths of 0.5 m, 1 m, 2 m, 4 m, 8m and 16 m.

10.3 Alternatives Considered

WLS fibers with other wave-shifting dyes are available, but K27 has the best attenuation length (least self-absorption) and is therefore the best choice for our 15.7 meter long application.

An alternate was considered to boost the light from the far end of the NOvA vertical cells by adding a fiber that is wave-shifting in the bottom 5 meters of the cell then spliced to a clear un-doped polystyrene fiber in the top 10 meters since polystyrene has a better attenuation length (see Figure 10.2). This would mean a 0.8 mm diameter bond of fibers would have to be quite robust since we cannot access this bond once the detector is assembled, and we cannot replace the fiber once the detector is assembled. The wave-shifting fiber density is that of polystyrene (1.05 g/cc), so there is a net downward force on the fiber as it hangs in the 0.85 g/cc liquid scintillator. Another disadvantage of this spliced fiber scheme is that it would introduce a discontinuity in performance of the cell at the splice where suddenly the response would be doubled, complicating the analysis algorithm for any event spanning the splice region.

10.4 Fiber Optimization

An adjustable parameter is the fiber diameter. Fibers of diameter greater than ~1.5 mm are difficult to spool and ship, while fibers of diameter less than 0.5 mm are difficult to handle and break easily. For fiber diameters around 1 mm, the light collection efficiency depends approximately linearly on the radius of the fiber as shown in Figure 10.6, while the cost of the

fiber depends on its volume (r^2 times constant length). Thus, in terms of photons per dollar, two thinner fibers are more efficient than one thicker fiber. The NOνA design with two 0.8 mm fibers is therefore more cost effective than a design with one 1.6 mm fiber.

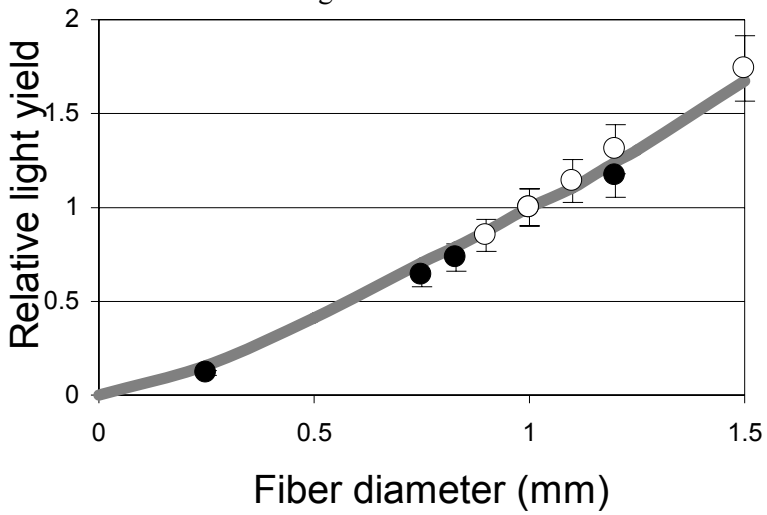

Fig. 10.6: Relative light yield as a function of WLS fiber diameter. The open circles are from measurements made for the MINOS Detector, the closed circles are more recent measurements and the solid line is a Monte Carlo simulation. (Data are normalized to unity at 1 mm diameter.)

An additional consideration, related to diameter, is the minimum-bending radius of the fiber. Smaller diameter fibers allow a smaller bending radius and can loop inside the NOνA PVC cells more easily than a fiber with a larger diameter. Kuraray manufactures two types of fibers known as *S type* and *non-S type*. S type fiber is stronger against cracking, has a smaller bending radius but has an attenuation length that is 10% shorter than non-S type. Based on the geometry of the NOνA PVC module cells, the maximum bend radius of the NOνA fibers is 71.4 mm in the horizontal cells and 68.3 mm in the vertical cells. The minimum bend radius as a function of fiber diameter for S type and non-S type Kuraray fibers is shown in Figure 9.7. The NOνA requirement is superimposed. As can be seen in the figure, the required bending radius for NOνA is very close to the recommended minimum for S type fiber.

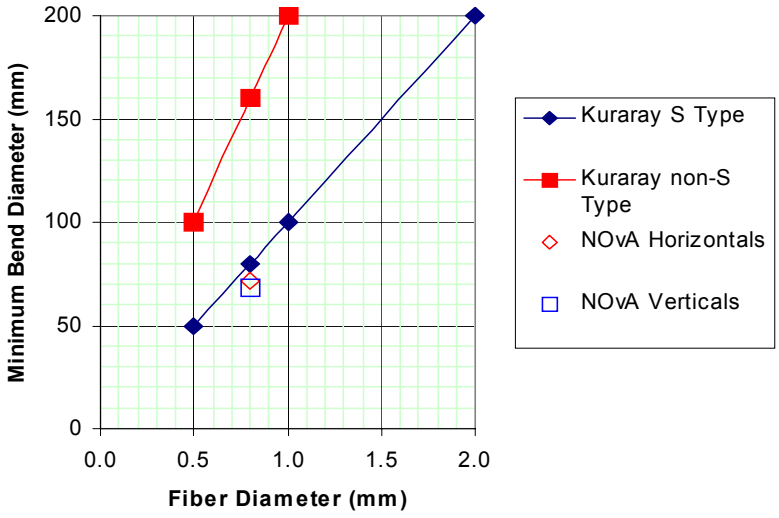

Figure 10.7 Minimum recommended bending radius vs. fiber diameter for S type and non-S type fiber from Kuraray. Superimposed are the NOνA vertical and horizontal cell diagonals.

10.5 Quality Assurance

QA information from the vendor will arrive with each unit as part of the shipment. Typically the information supplied includes measurement of the diameter every few centimeters, records of bumps in the diameter beyond some specification at the few percent level of the diameter, periodic measurements of the eccentricity of the fiber, measurements of the light yield for periodic samples, and measurement of the attenuation length of the fiber for periodic samples. The periodicity of the samples is about one per 1,000 meters Checks of this information will be done at the Module Factories discussed in Chapter 12. We will concentrate on confirmation of the vendor measurements for the crucial parameters of light yield and attenuation length.

10.6 Risks

The primary risk associated with the WLS fibers is the liquid scintillator environment in which they operate. Plastic fibers with single and double claddings have been shown to operate in mineral oil based liquid scintillator with up to 10% concentrations of pseudocumene for long periods of time.

Accelerated lifetime testing of single clad WLS fiber in BC-517L with ~10% pseudocumene has demonstrated a lifetime 16 ± 1 years by performing accelerated aging tests for 3 months at 42°C [2,3]. MINOS tested double clad WLS fiber in BC-517L for 8 months at 50°C and saw no effect [4]. A CERN group has also performed tests on WLS fiber in BC-517L [5], and fibers immersed at 60°C for 80 days saw no effect.

In addition to accelerated aging tests, aging data was extracted from a liquid scintillator and lead calorimeter with immersed WLS fibers that was developed for the Fermilab COSMOS experiment (E-803) over 10 years ago. The calorimeter used double clad WLS Bicron BC-91A fibers and Bicron BC-517L liquid scintillator in a Shashlik design EM calorimeter with lead plates. The COSMOS calorimeter module was recently revived by NOνA[6], tested with cosmic rays and compared to identical measurements from a decade ago. The results shown in Figure 10.8 indicate no degradation of the fiber in this un-accelerated aging test.

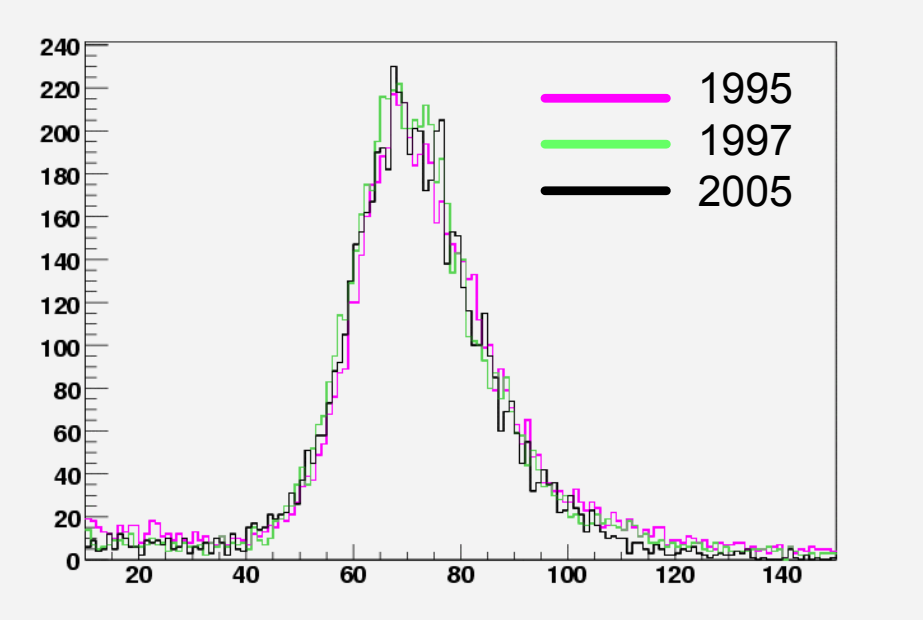

Fig. 10.8: Results from the COSMOS prototype calorimeter. The normalization uncertainty on the means of the distributions is 16%. The more robust width to mean ratio shows a 3% difference (statistically insignificant) over ten years.

A related risk is associated with the fiber loop inside the extrusion cell. The loop design introduces curvature close to the minimum bend radius of the fiber and there is a risk that the fiber could fatigue, making it more vulnerable to attack from the liquid scintillator. NOνA has tested [7] a 0.8 mm fiber coiled 10 times at a tighter bending radius than the 7 cm bend radius required in the PVC cells. The coiled fibers were immersed in a 50-50 mix of mineral oil and pseudocumene for 14 days at 42°C with no measurable degradation in light transmission.

All of the tests described above were performed on liquid scintillator with pseudocumene concentrations of at least 10%. The baseline liquid scintillator for NOνA will have a pseudocumene concentration of ~5%, reducing this risk even further.

10.7 ES&H

Polystyrene (fiber core material) burns and produces a dense black smoke. At temperatures above 300^{o}C it releases combustible gases. NOνA storage of fiber reels at the extrusion module factories will have to take these properties into account.

10.8 Value Management

One adjustable design parameter of the fiber is the concentration of the wavelength shifting dye. MINOS optimized their WLS fibers using 175 ppm of K27 dye, but the MINOS fibers had a larger diameter and were ~ 8 meters long. More K27 dye will result in greater light production in the fiber at the cost of a shorter attenuation length. R&D is required to determine the optimum dye concentration for NOνA that provides the right balance between light production and attenuation length. Dye concentration is not a cost driver so changes will have little impact on the cost of the project.

More of the coiled fibers will be subjected to accelerated aging tests to make sure S-type fiber will withstand the NOνA conditions.

Chapter 10 References

[1] Kuraray Scintillation Materials, Kuraray Co., Ltd., Methacrylic Resin Division, contact psf@kurary.co.jp. Similar data are available from St. Gobain Crystals.
[2] K.G. Young et al., Radiat. Phys. Chem. **41** 215 (1993)
[3] D. Koolbeck and K. Ruddick, a re-analysis of the ref [2] data, NOνA docdb note # 389, August 2005.
[4] P. Border et al., Nucl. Instrtum. Methods **A463**, page 194 (2001).
[5] L. Benussi et al., Nucl. Instrtum. Methods **A488**, page 503 (2001)
[6] D. Cronin-Hennesy, NOνA docdb note # 139, December 2005.
[7] Stuart Mufson and Mark Messier, private communication.

11. PVC Extrusions

11.1 Introduction

Rigid PVC extrusions are the basic building blocks of the 25 kiloton NOνA detector. Planes of PVC extrusions are bonded together to form the 15.7 m x 15.7 m x 111 m structure. The PVC extrusions serve as primary containment of the liquid scintillator. The total mass of PVC in the detector is 6.85 kilotons, so PVC is 27% of the detector mass.

As described in Chapter 3, our baseline extrusion is a 32-cell object with exterior cells of dimension 4.07 cm by 6.6 cm. The extrusions come in two flavors: one with 3 mm exterior walls and 2 mm interior webs for horizontal cells, and a thicker version with 4.5 mm exterior walls and 3 mm interior webs for the vertical cells, so the vertical interior cells sizes are slightly different from the horizontals. The PVC extrusions will be 1.3 m wide (32 cells wide), and 15.7 m long. The full NOνA detector needs about 20,000 such extrusions. The extrusion task must therefore produce 315 kilometers of 1.3 m wide material.

The rigid PVC is loaded with 15% titanium dioxide to boost the reflectivity of the material to 425 nm light emitted by liquid scintillator. Light produced in the scintillator typically bounces off the rigid PVC walls about 10 times before being captured by a wave-length shifting fiber, so a high reflectivity is needed.

11.2 The Recommended Design

11.2.1 NOνA rigid PVC Composition

The baseline composition of NOνA PVC is shown in Table 11.1. This mixture was a result of our R&D during 2004-2005 with Plastics Extrusion Technologies is called "NOνA PET-B". It is a custom blend for NOνA with minimal lubricants and minimal tin stablilizers used in the extrusion process. Since these extrusion resin mixtures are proprietary, we do not know the exact composition of the lubricants or stabilizers.

We did stipulate the brand name of uncoated rutile-type titanium dioxide in the mixture as Kerr McGee CR-834 with average particle sizes of 0.17 microns. At our request, the mixture contains no acrylic impact modifiers, no calcium carbonate fillers, and no other ingredients beyond those described in Table 11.1. The mixture was an attempt to limit the composition to the smallest number of ingredients and maximize the reflectivity of the extruded product. We have verified the titanium dioxide percentage and the absence of calcium carbonate content via chemical analyses at Argonne National Laboratory.

Component	Composition in Parts per Hundred Resin (phr)	Composition (%)
Rigid PVC Resin	100 phr	82.5 %
TiO2 (Kerr McGee CR-834)	18 phr	14.8 %
Internal and External Lubricants	~ 1 phr	0.8 %
Organo-Tin Stabilizers	~ 2.3 phr	1.9 %

Table 11.1. Composition of "NOνA PET-B" rigid PVC compound.

11.2.2 PVC Reflectivity

The reflectivity versus wavelength for the NOνA PET-B rigid PVC is shown in Figure 11.1 along with the emission spectrum of the NOνA scintillator. NOνA PET-B has a 93% reflectivity at the 430 nm peak of the scintillator emission. This reflectivity is mostly due to diffuse reflection which is proportional to the cosine of the angle normal to the surface of the PVC (Lambert's Law). So the primary intensity of reflected light is normal to the surface. Diffuse reflection comes from the titanium dioxide particles in the PVC and the light can scatter off particles that are relatively deep in the material. Titanium dioxide is the best scattering compound because of its high index of refraction (2.73), and blue light is more strongly scattered off particles in the range 0.15 – 0.20 microns [1] .

There is typically also a few percent component of specular reflection (following Snell's Law: angle of reflection = angle of incidence). The outside surface of NOνA PET-B is visibly glossy, while the inside surface has more of a matte finish. We have measured ~1 % more reflectivity from the outside surface than from the inside surface, characterizing the range of specular reflection in this PVC mixture. We need to learn more about controlling the finish of our PVC extrusions for optimal performance, but the basic performance of NOνA PET-B is adequate for the experiment.

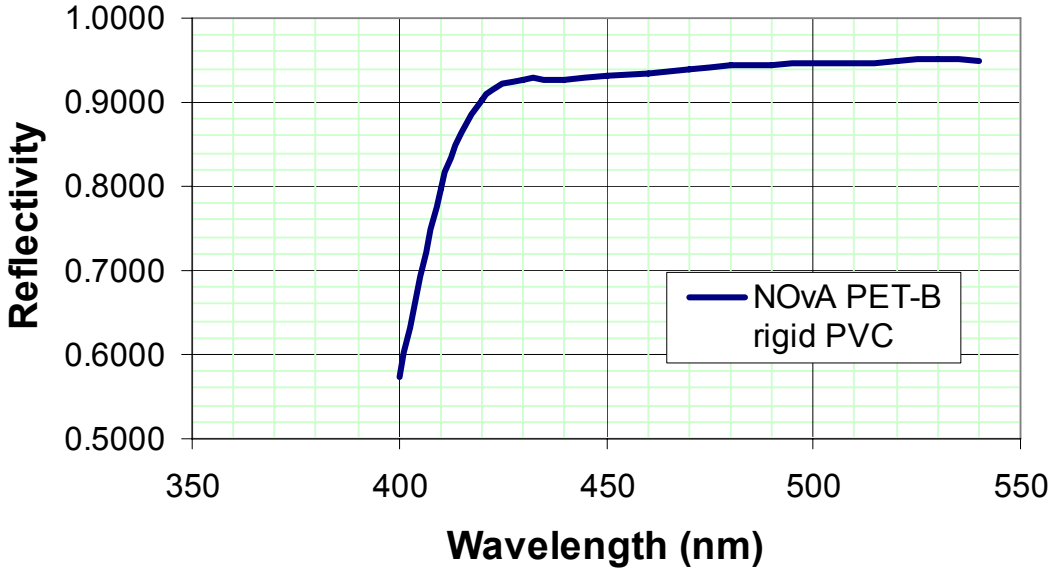

Fig. 11.1: Reflectivity of NOνA PET-B rigid PVC vs. wavelength.

Analytic calculations [2] and a Monte Carlo [3] of reflection including diffuse and specular components indicate that light captured by a wavelength shifting fiber is reflected about ten times within the NOνA cell before capture. Ten reflections is the mean of a distribution with very long tails, and ~ 10% of the collected light has > 20 reflections. This distorts the observed scintillator spectrum as shown in Figure 11.2. Since the reflections are dominantly diffuse, the light does not move very far along the 15.5 meter cell, doing a random walk with a reflected angle proportional to the cosine of the angle to the normal of the cell walls. The light path stays within about ±25 cm of the track which created the light, and the path length of the light in the scintillator before capture is then about 1 m for the typical 10 reflections. This is the relevant distance for the attenuation length of scintillator discussed in Chapter 9.

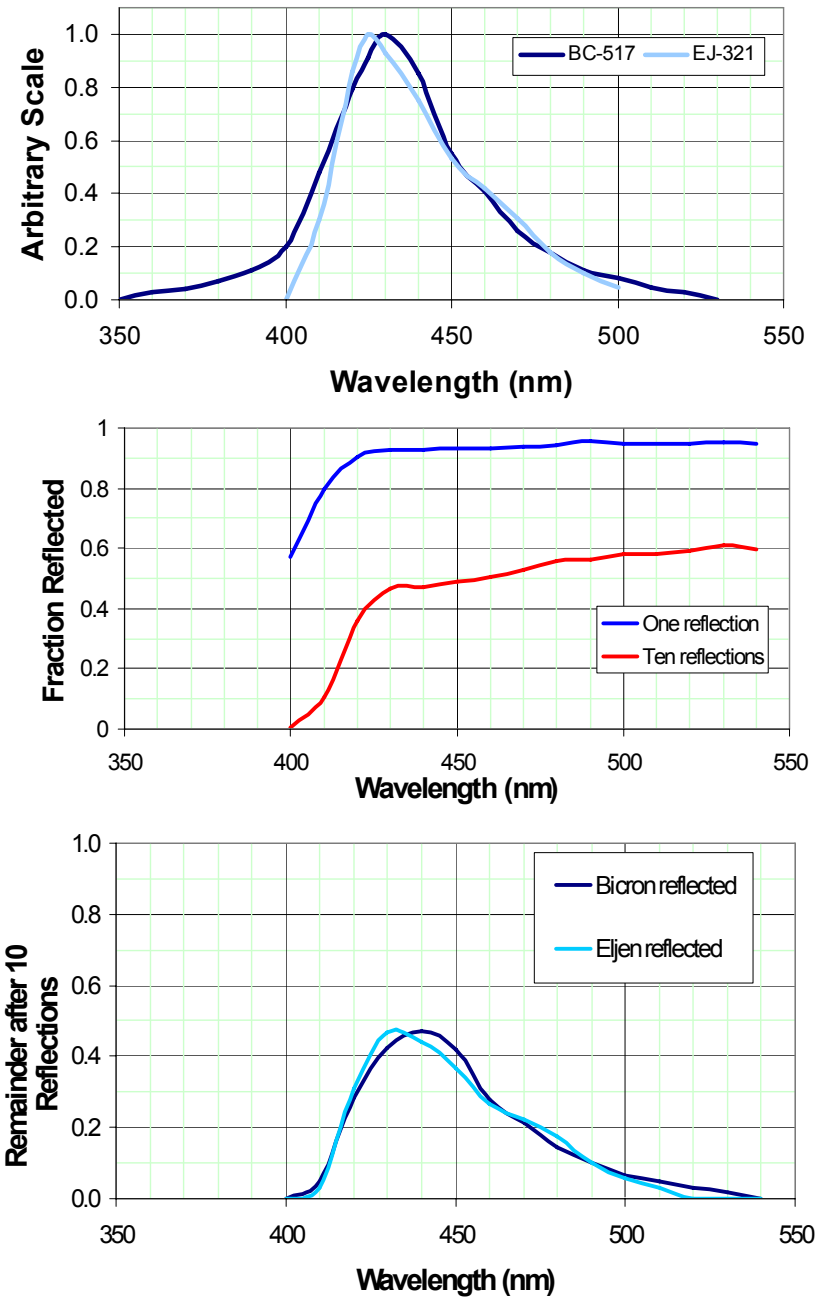

Fig. 11.2: The emission spectrum of NOvA scintillator (top), the fraction of light reflected by the PVC after one and ten reflections (middle), and the resulting observed spectrum of light entering the wavelength shifting fiber.

11.2.3 PVC & Strength of Material

Figure 11.3 shows a representative plot from ten NOvA PET-B rigid PVC tensile test samples. The modulus of elasticity value for the material is the slope of the stress/strain curve where the curve remains linear and has been measured at about 470,000 psi (3240 MPa). Like most plastics, PVC does not have a well defined elastic yield point, but a definition that uses the slope of the linear stress/strain curve offset by 0.2% indicates a yield around 4300 psi (~30 MPa).

Sometimes such plastics are characterized by the point where the stress/strain curve levels off and that value is around 5300 psi for NOνA PET-B.

PVC is plastic and the material can flow or creep over time. In thermoplastics like PVC creep is related to the Glass Transition temperature of the plastic and the temperature of its operating environment. PVC has a relatively high glass transition temperature of ~ 87°C, which is well above the NOνA operating temperature of 23°C. Problems from creep are functions of stress. This has led to a NOνA design criterion limiting design stresses to the relatively low value of 1000 psi as compared to the yield stress of 4300 psi. The choice of 1000 psi is based on information from the PVC Plastic Pipe industry [4]. The choice of 1000 psi is also clearly in the linear region of Figure 11.3.

Creep can be characterized as a reduction in the modulus of elasticity, leading to a "creep modulus" after some years. We have measured a modulus of elasticity at 470,000 psi but use 360,000 psi in all our engineering analyses of the NOνA design. Creep modulus measurements are in progress.

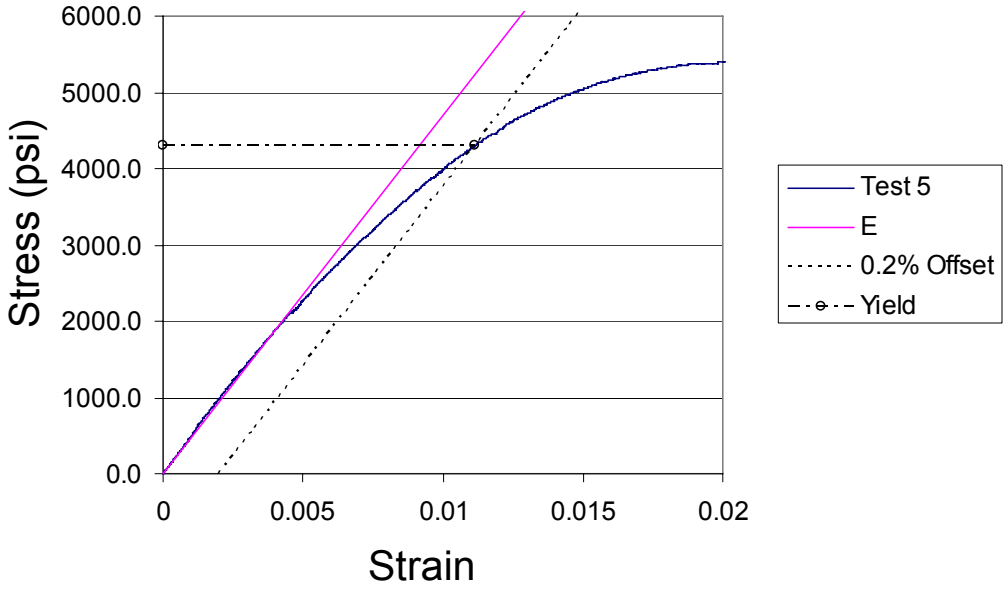

Fig. 11.3: Stress vs. Strain for a sample of the "NOνA PET-B" rigid PVC.

11.2.4 PVC Exterior Surface Quality

The assembly procedure for the NOνA detector at Ash River is discussed in Chapter 15 and requires a roughened surface for proper adhesive bonds between planes. Our investigations have shown that roughing the surface with 60-grit emery paper is adequate. We plan to get this done at the extruder vendors.

11.2.5 PVC Extrusion Shipping

Candidate extruders for the NOνA 32-cell PVC modules are all located in the Midwestern U.S. We plan to ship the extrusions to the Module Factories (see Chapter 12) by truck. The modules are sized to allow shipping inside a standard domestic 53-foot semi-trailer. We intend to stack a set of 30 extrusion modules on two special "super-pallets" (see Figure 11.4) to facilitate loading and unloading without stressing any of the PVC. Transportation of the ~20,000 modules requires 700 truckload and about 480 of the special pallets. Each truckload uses three of the special pallets, but the pallets can be used multiple times.

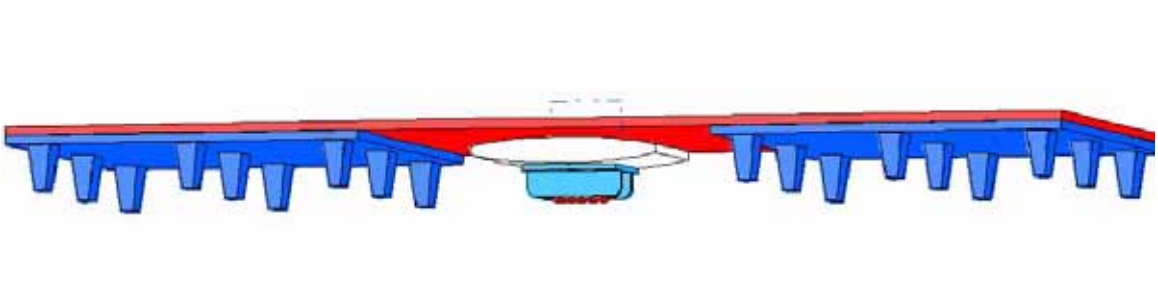

Fig. 11.4: Diagram of the special "super-pallet" for extrusion transportation. The blue objects with feet are industry standard plastic pallets. The red sheet connecting the two pallets is a plastic pallet bridge. The white pillow-shaped object is an air-jack bag that allows the load to be transferred to the roller beneath the pillow to roll the extrusion stack out of the truck. There are three of the 10 foot-long super-pallets under each stack of 30 extrusions.

11.2.4 PVC Edge Stiffeners

On vertical planes the outside extrusion modules have an outside cell which sees the full 19.2 psi pressure differential without an adjacent cell. The 4.0 cm cell span transverse to the beam holds back this pressure by design, but because the span of the cell in the beam direction is 6.0 cm , this edge of the PVC structure requires some additional support over the bottom few meters where the inside pressure is highest. Only one-sixth of the vertical extrusion modules see this particular force.

The NOνA design includes such an edge stiffener but extends it to cover the full outside edge of the outside edge verticals and the top of the horizontal plane. The stiffener would about 5 mm thick and be another extrusion of rigid PVC, but loaded with carbon black instead of titanium dioxide. This design helps to make the NOνA structure light tight (some light can enter the cells through the titanium loaded PVC extrusion walls). The Stiffener may also serve as a local cable tray and as a convenient attachment point for electronics as shown in Figure 11.5. Our plan is to attach the edge stiffeners with epoxy at the Ash River site.

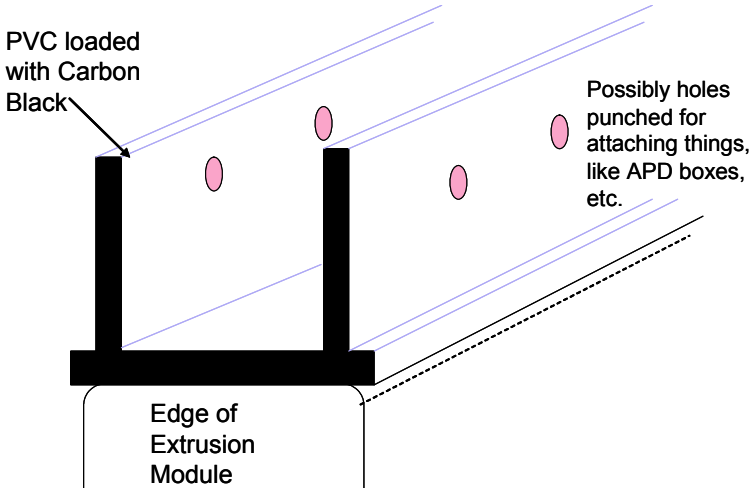

Fig. 11.5: A conceptual design of the NOνA edge stiffener.

11.3 Alternatives Considered

Other plastics and even aluminum extrusions were considered for NOνA. The properties and costs [5, 6] of some candidate materials are listed in Table 11.2. Most of the plastics could be loaded with titanium dioxide for reflectivity, but Aluminum is not reflective enough in the ultraviolet and would require an additional interior coating of titanium dioxide loaded paint. The strength of some of the plastics rules them out since NOνA needs a material with a modulus of elasticity above ~ 360,000 psi. The Glass Transition temperature (a measure of creep properties) should be well above the NOνA working temperature of 23 ^{o}C, so this criterion rules out other plastic candidates. The chemical resistance of some plastics to solvents (like pseudocumene) rules them out. Finally, Table 11.2 is organized by cost per pound and rigid PVC is the cheapest. A 25% increase in cost for 6.9 kilotons (~15 million pounds) of plastic represents a huge amount of money.

Material	**Modulus of Elasticity (psi)**	**Glass transition Temperature (^{o}C)**	**Chemical resistance to solvents**	**Cost per pound (relative to rigid PVC)**
rigid PVC (Polyvinyl Chloride)	410,000 – 450,000	87	good	1.00
Polystyrene	330,000 – 475,000	90	poor	~ 1.25
Polypropylene	190,000	-17		~ 1.32
HDPE Polyethylene	170,000	-80	excellent	~ 1.35
PET (polyethylene Terephtalate)	420,000	75	good	~ 1.40
ABS (Acrylonitrile Butadiene Styrene)	130.000 – 400,000	62		~1.52
PMMA acrylic	~ 350,000	105	poor	~ 1.72
Polycarbonate	~ 320,000	167	poor	~ 2.50
Aluminum extrusions	10,000,000	Not applicable		~ 8.00

Table 11.2: Some candidate materials for NOνA organized by price per pound. Different materials have different densities and may use a different number of pounds to realize the same design, so the price per pound is only a rough guide to the cost.

11.4 PVC Design Optimization

As discussed in Section 11.2.3, the material properties of rigid PVC strongly influence the NOνA design and we want the stress to be below 1000 psi everywhere. One such influence is the scalloped extrusion cross section shown in Figure 3.11. This design has been optimized for minimum stress within the parameters suggested to us by extrusion vendors. Figure 11.6 shows four designs considered for NOνA. A scalloped design has the smallest stress and is extrudable. The wall thicknesses of the NOνA designs are optimized for the extrusion process where the rule of thumb in the industry is that interior webs should be made of material about 25 -33% thinner than the exterior walls since the interior material is difficult to cool during extrusion. The NOνA Vertical cells have thicker walls than those in Figure 11.6, and Figure 11.7 shows that the stress in our final vertical profile is always less than 394 psi everywhere in the cell. This is well within the linear response portion of the strain-force curve in Figure 11.3 where creep effects are minimal.

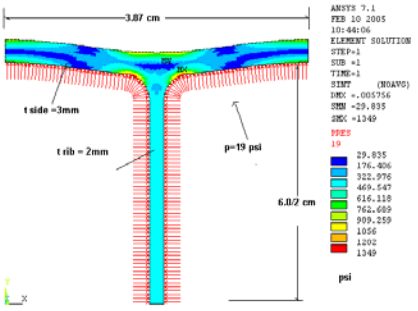

a) T shaped extrusion
1/8" radius interior corners
Maximum stress is1350 psi

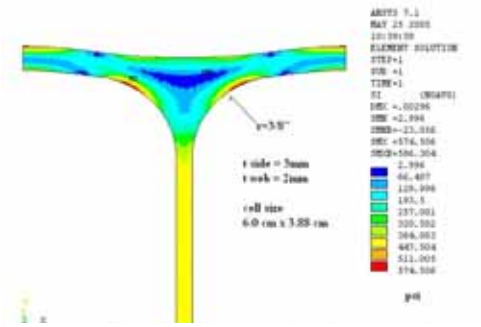

c) T shaped extrusion
with 3/8" radius interior corners
Maximum stress is 574 psi
This shape is not extrudable with
the extra material in the T

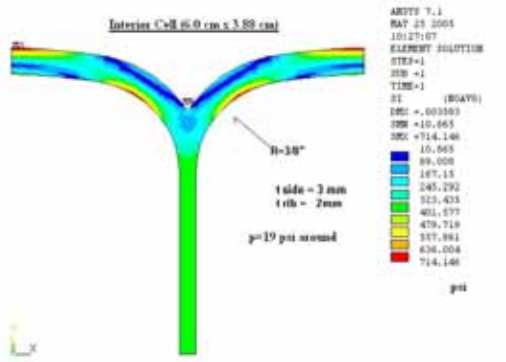

b) Scalloped extrusion
3/8" radius interior corners
Maximum stress is 714 psi

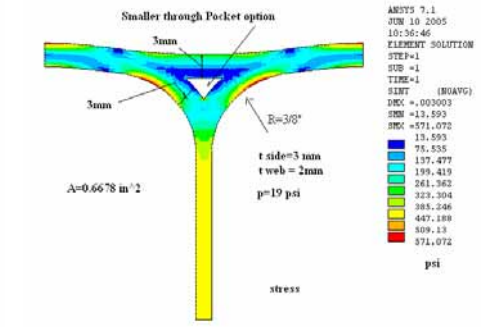

c) T shaped extrusion with hole
3/8" radius interior corners
Maximum stress is 571 psi
The hole in this shape cannot
be extruded consistently

Fig. 11.6: Four extrusion shapes considered for NOνA. Two adjacent quarter cells are shown with stress results from a finite element analysis [7]. The scalloped design (b) is the best compromise between minimal stress and manufacturability. All these analyses were for 3mm thick exterior walls and 2 mm thick interior webs.

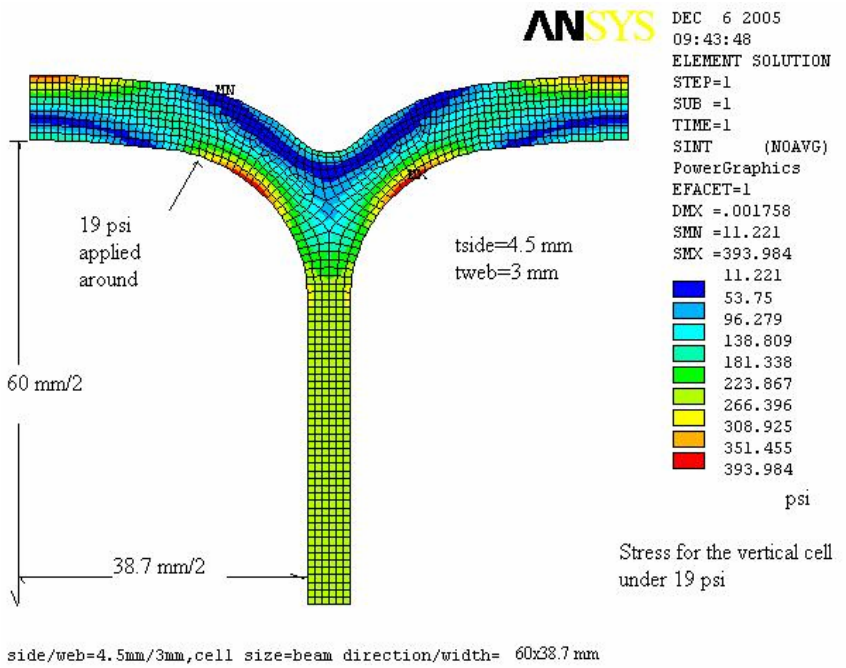

Fig. 11.7: Finite element analysis of the selected NOνA vertical cell extrusion shape. This design follows the scalloped design in Figure 11.6(b), but with 4.5 mm thick exterior walls and 3.0 mm interior webs. The maximum stress is 394 psi.

We have also optimized the fraction of titanium dioxide in our PVC mixture. Figure 11.8 shows the reflectivity for three kinds of rigid PVC with varying amounts of rutile titanium dioxide. The baseline PVC material in NOνA PET-B has the best performance.

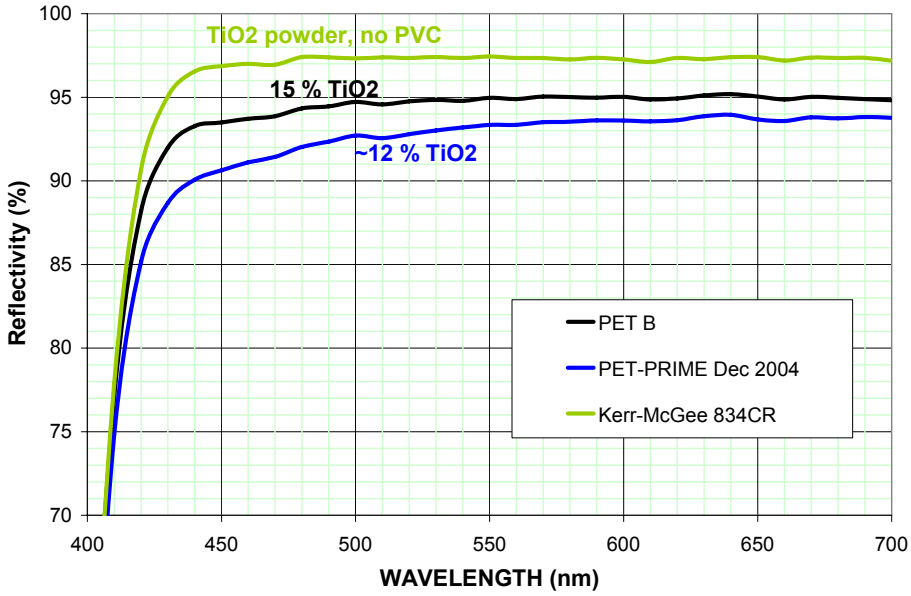

Fig. 11.8: Reflectivity curves for three NOνA prototype mixes. Mixtures with 12% and 15% titanium dioxide were tested. The reflectivity of the raw 0.17 micron titanium dioxide powder (no PVC) is also shown. The 15% mixture was measured separately from the data in Figure 11.1 and gives some indication of the repeatability of the reflectivity measurements.

11.5 Quality Assurance

Quality Assurance is a routine part of the job for extrusion manufacturers. They typically tag the parts individually and check the parts for inside / outside size tolerance, wall thickness, and bend and twist tolerances. The extrusion machine variables (temperatures, speed, vacuum, water temperature,…) are also logged so that one can correlate the conditions to the product. We will add a measurement of reflectivity to this set. Simple commercial hand-held units can measure reflectivity in the range 400 – 550 nm in a couple of minutes and can be used both inside and outside of the NOνA cell.

As a check on the mixture, we intend to analyze a sampling of the extrusions via chemical analysis at ANL to determine content. We also intend to monitor structural properties with random tests of elastic modulus and Izod impact strength

11.6 ES&H

PVC is a relatively benign material and is typically recycled in the plastics industry. In a fire the material does not typically ignite since it is self-quenching due to the chlorine. In a fire fed from other flammable sources, PVC is a hazard because its byproducts are HCl in the air and in water runoff. The Fermilab Fire Protection engineer has done preliminary tests[8] on PVC with titanium dioxide for NOνA, concluding that the PVC would not ignite even when covered with liquid scintillator.

11.7 Risks

We still need to understand the creep properties of our PVC material. Creep can be characterized as a reduction in the modulus of elasticity, leading to a "creep modulus" after some years. We need a creep modulus that will realize a stable structure throughout a nominal 20 year lifecycle of the NOνA detector. The creep modulus has not yet been measured for PET-B, but we have used a modulus of elasticity of 360,000 psi in all our engineering analyses. 360,000 psi is ~75% the measured initial value for NOνA PET-B rigid PVC in short time tensile tests.

There is some risk that the wide 32-cell extrusion will be difficult to achieve. As a measure of the challenge, we have hired an expert consultant on PVC mixtures and are advised that our 1.3 m wide module should be extrudable, but that a module of width ~ 1.45 m would be problematic for the thickness of PVC we wish to extrude. The limit comes from an inability to get complete flow inside such a large die without keeping part of the PVC mixture at too high a temperature for too long a time. Several U.S. vendors believe they can handle such an extrusion but do not have the equipment in hand to do so. The equipment startup cost is substantial, meaning it is too costly to seek 32-cell products during our R&D phase. Several backup plans are being considered and are discussed in the next section.

11.8 Value Management

Creep tests are under way to measure the properties of NOνA PET-B rigid PVC. The difficulty is in predicting a value 20 years from now based on short term tests. The standard procedure for extrapolating such information is by exploiting the time-temperature relationships for PVC. We are currently planning and performing accelerated creep and stress relaxation tests at various temperatures in an attempt to determine this value. At the same time we have long term creep tests in progress that will be used as a validation of the predictions. We have hired another expert consultant in this area to measure the properties of PET-B for us and to assist us in the development of our own tests and interpretation of our own data.

We intend to continue studies of additives to rigid PVC seeking a better performance than our baseline PET-B product. Increased reflectivity might allow cost savings in other parts of

NOνA as outlined in Chapter 5. Studies of surface gloss are indicated by our observation of different reflectivity on the inside versus outside of PET-B. Investigations into mixes with the anatase form of titanium dioxide may yield a better reflectivity (anatase reflects better below 420 nm but that enhancement is balanced by a slightly poorer reflectivity than the rutile form above 420 nm). Increased structural robustness will also be sought. Acrylic impact modifiers are typically added to rigid PVC mixtures to increase the product's impact resistance and this is one of the additives we removed in the PET-B mixture. As mentioned above, we have hired an expert consultant to advise us on appropriate PVC mixtures.

We expect to learn a lot about wide extrusions with our 16-cell prototypes now under contract. Our full 32-cell, 1.3 meter wide extrusion will be a challenge for industry. As a backup plan, we intend to investigate "tongue and groove" solutions whereby our 32-cells might be constructed out of narrower objects, say 2 x 16-cell, or 4 x 8-cell. There may be a wider competitive set of vendors for such narrower products leading to a lower price. A lower price would be offset by the labor cost to bond the objects together into 32 cells, so a complete cost accounting is required. Another parallel backup plan would be to use 16-cell modules and modify the fiber manifolds so that two modules could get connected to one APD.

Chapter 11 References

[1] See for example "Polymers, Light and the Sceince of TiO2", DuPont Technical Liabraries, 2002 (available at the SpecialChem website), or similar publications by Millenium Chemicals and other titanium dioxide suppliers.
[2] K. Ruddick, NOνA docdb note # 211, December, 2005.
[3] C. Bower, NOnA docdb note #208
[4] V. Guarino, "PVC Pipe Design Stress", NOνA docdb note #360, October 2004.
[5] The material properties are available in many places, but all the information is not available in one place. The Wikipedia free encyclopedia at http://en.wikipedia.org/wiki and references therein is a good place to start.
[6] The cost data were obtained from Plastics News, from The Plastics Web, and from Plastics Technology Online.
[7] A. Lee, NOνA docdb note # 379, June 2005.
[8] J. Priest, NOνA docdb note #358, February 2005

12. PVC Modules

12.1 Overview

The fundamental building block for the NOνA Far and Near Detectors is the PVC module. A PVC module consists of a 32-cell PVC extrusion, described in Chapter 11, a bottom closure plate, and a fiber manifold. The 32 cells each contain a looped WLS fiber, described in Chapter 10, which is looped through the fiber manifold and terminates in a fiber connector mounted on the fiber manifold. The PVC modules are 1.3 m wide and 6.6 cm deep. The PVC extrusions, comprising the active part of the PVC module, are 15.7 m or 51.5 feet long. The overall length of the module, including the manifold, closure plate and packing material must be less than 53 feet in order to fit on a truck for shipping. The PVC modules will ultimately be filled with liquid scintillator and must be leak free.

12.2 The Recommended Design

12.2.1 Bottom Closure Plate and Fiber Manifold

The bottom closure plate is a grooved RPVC block that is glued across the extrusion end, as shown in Figure 12.1. Before installing the closure plate a series of small circular holes are made in the interior webs of the PVC extrusion so that the extrusion comprises a single liquid volume. The connection of the closure plate to the extrusion must be leak-tight and the adhesive used must not deteriorate when exposed to liquid scintillator.

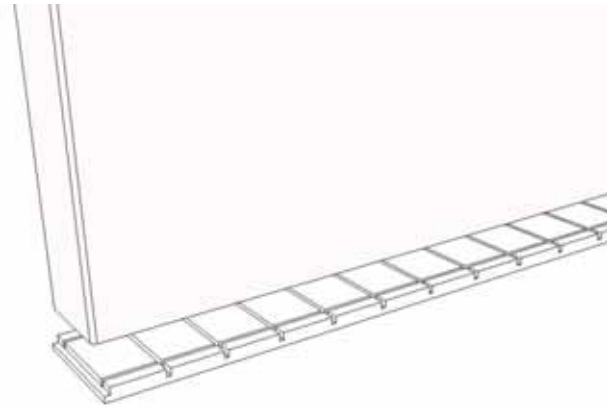

Figure 12.1 Rigid PVC bottom closure plate that seals one end of the PVC modules.

The fiber manifolds are made from injection molded plastic and are glued to the top of the PVC extrusions. The connection of the fiber manifolds to the PVC extrusions must also be leak-tight. Identical fiber manifolds are used on both the vertical and horizontal modules. Two side-by-side vertical extrusion modules with their fiber manifolds are shown in Figure 12.2. The vertical extrusion manifolds have room for thermal expansion of the liquid scintillator. The horizontal extrusions have external overflow canisters for that purpose as shown in Figure 12.3. Clips are used to position the fibers at the top of each extrusion and routing grooves align the fibers to the connector, control the fiber bend radii and facilitate assembly as shown in Figure 12.4. The manifolds provide filling and venting ports, seal the extrusions, and guide the fibers to the photodetector connector, shown in Figure 12.5, before the connector has been faced off.

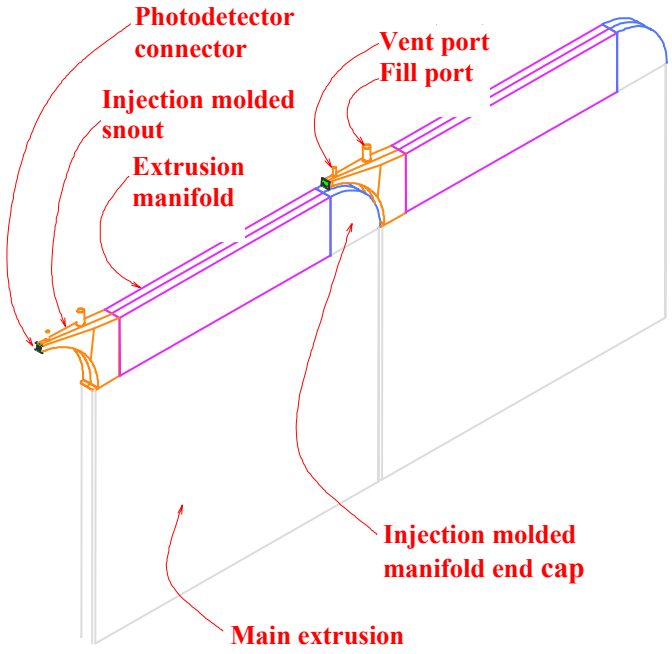

Figure 12.2 Two vertical 32-cell extrusion modules side by side.

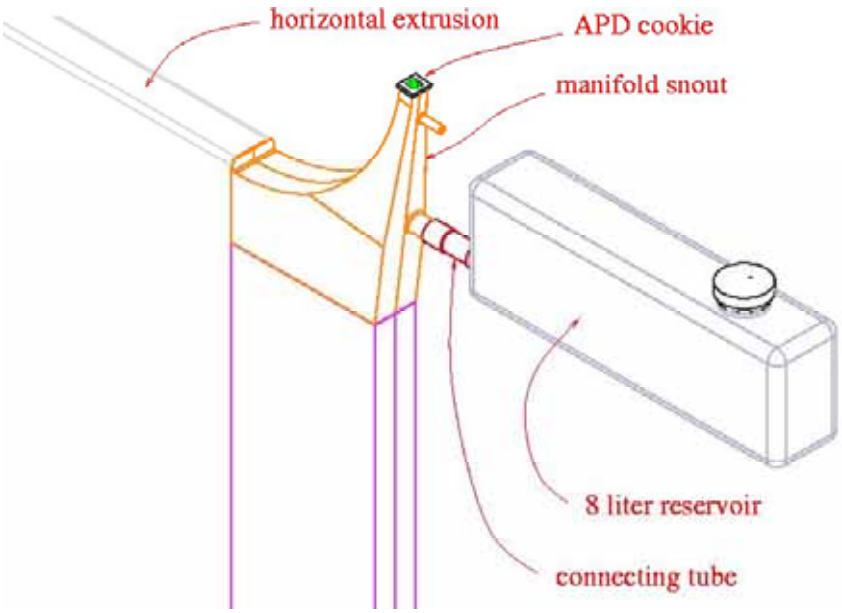

Figure 12.3 A horizontal extrusion module with its fiber manifold. Vertical extrusion manifolds have room for thermal expansion of the liquid scintillator. The horizontal extrusions have an external reservoir for that purpose.

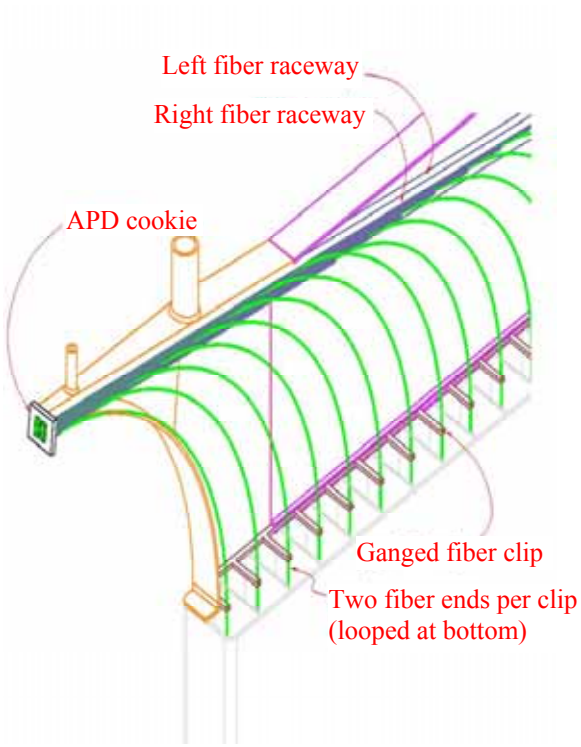

Figure 12.4 Routing of WLS fibers within a fiber manifold.

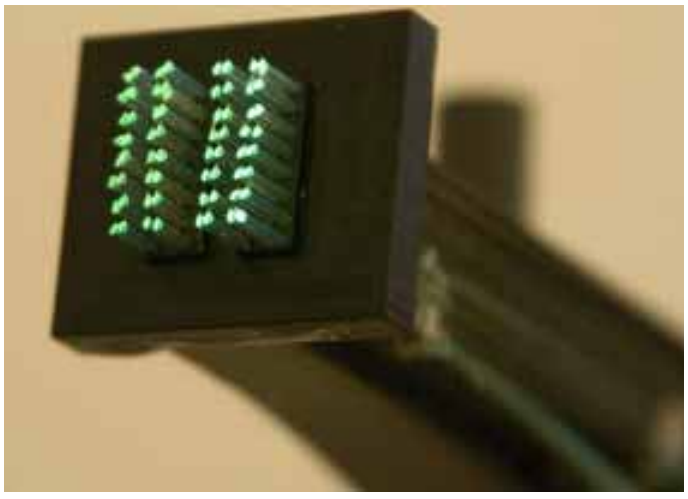

Figure 12.5 A fiber connector showing 32 pairs of fibers from an extrusion module after the fibers have been routed through the fiber manifold. Each pair of fibers corresponds to the two ends of a single looped fiber. The fiber connector is mounted on the fiber manifold and mates with a fiber connector on the APD box.

12.2.2 PVC Module Factories

PVC modules will be assembled at three module factories. PVC extrusions for modules arrive at the factories, cut to length, from the commercial extruder. The factories perform the following tasks:

1. Unload, inspect and distribute the incoming extrusions to workstations throughout the factory;
2. Install the looped WLS fiber in all cells;
3. Install end closures and manifolds;
4. Thread fibers through manifold to fiber connector;
5. Pot fibers in connectors and fly-cut faces,
6. Check fiber mapping and continuity;
7. Leak test modules;
8. Pack modules.

Many of these tasks are performed in batches to maximize efficiency and most of these processes are automated. A number of machines have to be designed to perform these tasks. These include an automatic fiber threading machine, gluing machines for attaching the endplates and manifolds, a fiber facing machine for fly cutting the optical connector after the fibers have been routed and glued in place, a light continuity and fiber mapping machine and pressure testing stations to search for leaks. The requirements for these machines are included in [1].

Each module factory will complete 12 modules per day. With a staggered startup and a ramp-up period included, this allows us to complete the module production in less than 2 ½ years. Time and motion studies combined with factory experience from MINOS have been used to estimate the effort required to accomplish this task. We will continue to refine these estimates as we obtain more experience with the handling of very large objects and as our designs for the machines listed above are finalized.

12.3 Alternatives Considered

Light output and collection at the far end of the PVC modules is a complicated process that depends on the properties of the PVC extrusions, the WLS fiber, the liquid scintillator and the photodetector. Simulations of the light paths within a NOνA cell predicted that the light level would be decreased for fibers near walls or in the corners of the cell as shown in Figure 12.6. In our default design we make no attempt to control the fiber location, though this could be done near the ends of the extrusion using plastic supports to hold the fiber away from the cell walls. Before investigating fiber position control in more detail, we attempted to confirm the simulation results and could not see any effect from fiber position in the cell. [2]. No controls will be used.

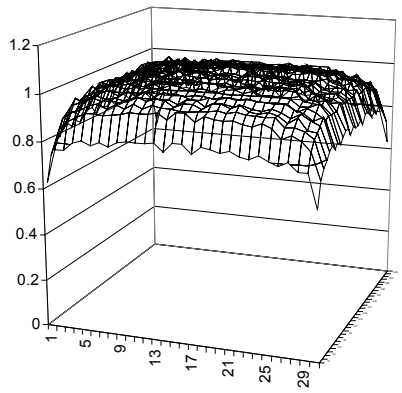

Fig. 12.6 Simulation of the relative light yield for a single un-mirrored fiber as a function of location within a scintillator cell.

12.4 Module and Factory Design Optimization

In the NOνA design there are 3 factories that begin production relatively early in the project. As a result, a large stockpile of finished extrusion modules accumulates before the Far Detector hall is completed and we begin consuming extrusion modules. The cost effectiveness of the default scheme must include shipping, handling and storage costs and must be compared to other models where there are more than 3 factories which do not start production as early and do not generate such a large backlog of finished extrusion modules. NOνA has been applying the Extend industrial production simulation tool [3] to study these issues. Extend is used to create dynamic models from building blocks, explore the processes involved, and see how they relate. The input parameters are then varied to arrive at an optimum solution. Our current factory scheme of 3 factories located in the Midwest is optimized, but the studies will continue, including different labor rates at different NOνA institutions, different warehouse rental rates near each different NOνA institution, and a more realistic shipping plan based on the pallets described in Chapter 11.

Two alternatives were considered for both the bottom closure plates and the fiber manifolds. In addition to the selected alternative for the bottom closure plate described above, we considered a more complicated injection molded design that would not have required slots to be cut in the webs of the extrusion to create a single liquid volume. The selected alternative was deemed to be more robust mechanically, an important consideration since the vertical modules rest on the bottom closure plate, and to be less expensive. A simpler and more robust design was considered for the fiber manifolds, but our fiber experience from MINOS led us to a manifold with better fiber routing and positioning capabilities built into the design.

12.5 Quality Assurance and Quality Control

Fiber quality will be tested at the Factories following procedures developed for MINOS. After fiber installation, a light flasher will be used to check fiber continuity through the loop at the bottom of the cells and to check the mapping of the 2 fibers from each cell to the APD connector. Similar QA will occur for the manifold parts.

Since the final extrusion module product has to hold the liquid scintillator without leaking, we need good assembly procedures and also plan to pressure test the finished modules. A simple bubble bottle apparatus has been developed to simplify this QA check and is shown in Figure 12.7. The modules get over pressured with air and we watch the leak rate into the module by counting bubble rates. Figure 12.8 shows how different leak rates compare using this tester.

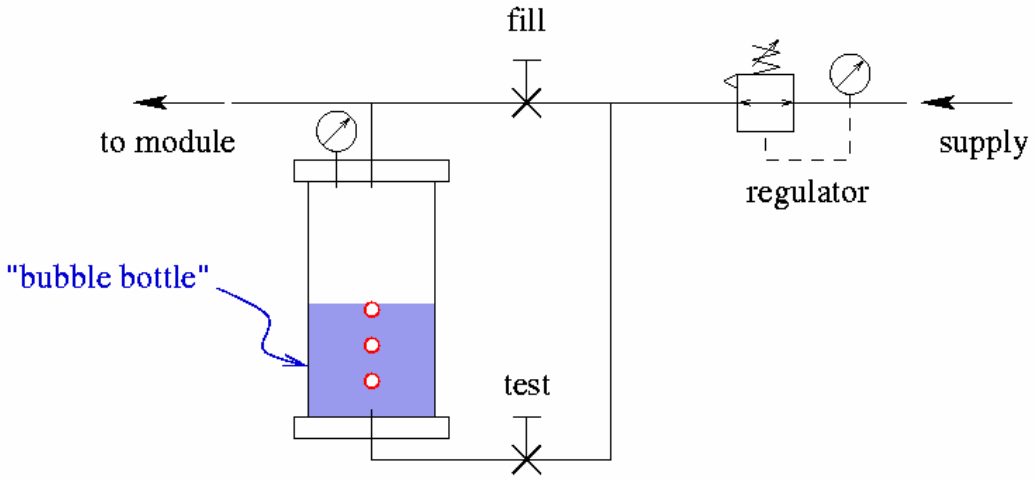

Fig. 12.7: A bubbling apparatus designed to check completed modules for leaks.

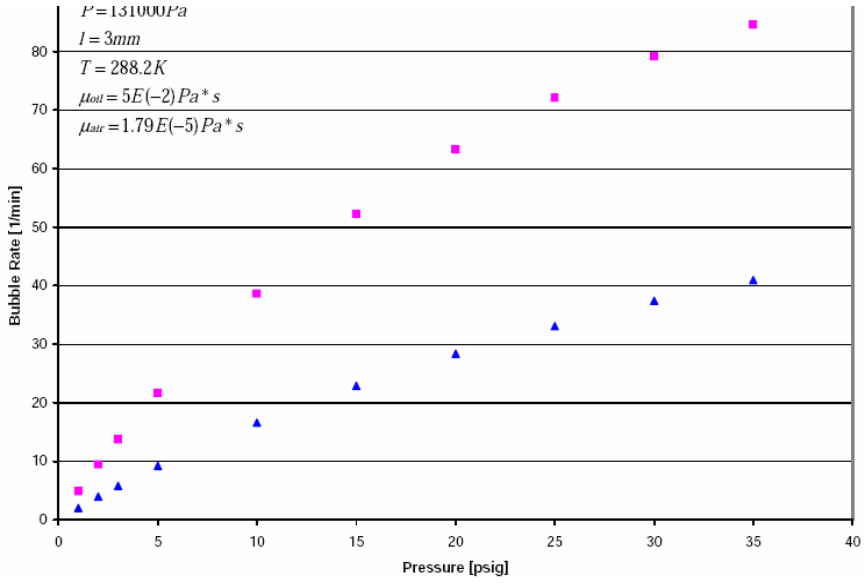

Fig. 12.8: Leak rate in bubbles per minute in the bubble bottle test apparatus. The upper curve is for a leak through a known 36 micron diameter hole in an extrusion and the lower curve is for a known 29 micron diameter hole.

As a final QA check, a sample of the completed modules will be fully instrumented with scintillator and APD readout to check the light output of the completed device in response to cosmic rays.

12.6 ES&H

Most of the activities associated with the PVC modules are standard laboratory tasks that require nothing beyond the normal safety precautions. However, the size and weight of the PVC extrusions require special precautions during handling. Explicit procedures for safely handling the PVC extrusions will be developed as part of our time and motion studies for the module factories.

A second hazard that is not typical for general laboratory settings is the pressure testing stations that are required to do leak checking of completed modules at the factories. While the operating pressures of the leak testing stations are not particularly high (1-2 Atmospheres), pressure vessels always require special safety precautions. We plan to consult with the Fermilab ES&H Group as well as the local ES&H groups at the Universities where the factories are located to determine appropriate operating conditions and procedures.

12.7 Risks

The primary risk associated with the PVC modules is a schedule slippage. The Module factories depend on timely deliveries of PVC extrusions, spools of fiber, and manifold parts, so production delays of these components could translate into delays in module production. However, as mentioned earlier, in the current plan the module factories build up a significant inventory of completed modules before they are needed for assembly, significantly mitigating this risk until later in the project when we should already have a significant fraction of the Far Detector assembled and operating.

Another risk associated with module production is the possibility of the adhesive used to attach the endplates and manifolds interacting with the liquid scintillator and weakening over

time. We are engaged in R&D to identify adhesives that do not react with liquid scintillator. This is a two-way street since any adhesive must also not degrade the scintillator in any way.

The current closure endplate design requires holes to be punched in the bottom of the extrusion webs to allow liquid scintillator to flow throughout the 32-cell extrusion during the filling process. These holes are not desirable from a mechanical perspective since they will be at a high stress point in the web. Punching such holes is now more difficult since our PVC design has led to vertical extrusions with thicker webs (3 mm) than the 2mm webs we had in the design when hole punching became our default plan. Additional labor is also required to punch the holes. We are considering modifications to this scheme.

12.8 Value Management

A different design for the bottom closure plate is shown in Figure 12.9. This design eliminates the need to punch holes in the extrusion webs by introducing common channel along the bottom of the closure. We are evaluating this design which could be realized through machining or injection molding.

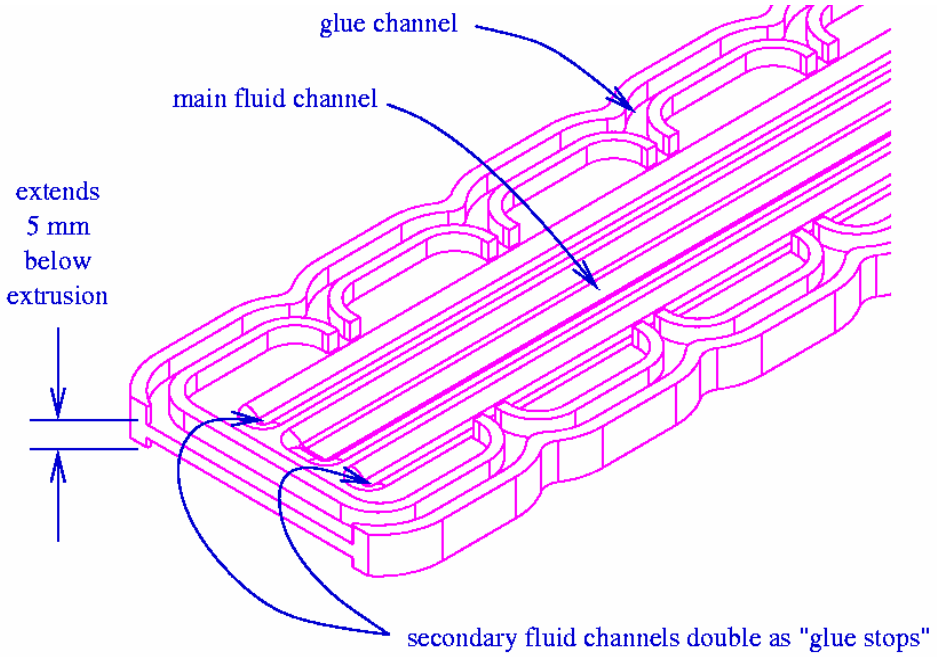

Fig. 12.9: An alternate bottom closure plate under study. The “main fluid channel” makes the 32 cells in the module into a common fluid volume.

The fiber manifolds and bottom closures are glued into place on the PVC extrusions. These seals must be leak-proof and the adhesive must not degrade when exposed to liquid scintillator. Our selected alternative for the glue is an epoxy but we continue to search for other means of sealing the extrusions. The possibility of PVC microwave brazing is being investigated. An intermediate sheet of metallic-loaded PVC would be inserted between the two PVC surfaces to absorb power from the microwave and melt the PVC, effectively brazing the parts together.

Chapter 12 References

[1] T. Chase et al, “Requirements for machines and fixtures to construct extrusion modules in the module factories,” NOvA-doc-183, November 2005.
[2] D. Cronin-Hennesy, NOvA docdb note # 139, December 2005.
[3] http://imaginethatinc.com/prods_overview.html

13. Photodetector and Electronics

13.1 Introduction

The readout of the NOνA detector has two distinct tasks: (1) read out events caused by neutrinos from the NuMI beamline at Fermilab and (2) operate between spills to collect cosmic ray events for calibration and monitoring. The readout will operate in a triggerless mode to accomplish both tasks seamlessly. A time-stamp generated from the early stages of the Main Injector cycle will be used to determine which events occur during the spill.

13.2 Avalanche Photodiodes (APDs)

The phototdetector for NOνA is an avalanche photodiode (APD). The APDs are packaged in arrays of 32 pixels and map directly onto the 32 cells of a single PVC module. Table 13.1 summarizes the key parameters for the NOνA APDs.

Manufacturer	Hamamatsu
Pixel Active Area	1.95 mm × 1.0 mm
Pixel Pitch	2.65 mm
Array Size	32 pixels
Die Size	15 × 15 mm^2
Quantum Efficiency (>525 nm)	85%
Pixel Capacitance	10 pF
Bulk Dark Current (I_B) at 25 C	10 pA
Bulk Dark Current (I_B) at -15 C	0.15 pA
Peak Sensitivity	600 nm
Operating Voltage	400 ± 50 volts
Gain at Operating Voltage	100
Operating Temperature (with Thermo-Electric Cooler)	-15°C
Expected Signal-to-Noise Ratio (Muon at Far End of Cell)	10:1
APD channels per plane	384
APD arrays per plane	12
Total number of planes	1,674
APD pixels total	642,816

Table 13.1 Avalanche Photodiode parameters.

The general structure of an APD is shown in Figure 13.1. Light is absorbed in the collection region, electron-hole pairs are generated and, under the influence of the applied electric field, electrons propagate to the p-n junction. At the junction, the electric field is sufficiently high that avalanche multiplication of the electrons occurs. The multiplication of the current is determined by the electric field at the junction and by the mean-free-path of electrons between ionizing collisions, which depends on both the accelerating field and on the temperature. This temperature dependence occurs because the probability of electron-phonon scattering increases with temperature.

One of the operational characteristics of APDs, and, in fact, all silicon devices, is the thermal generation of electron-hole pairs which mimic the signal. Since the current from the positive carriers is amplified about fifty times less than the negative carrier current at the junction, only the current from electrons generated in the photo-conversion region (I_B), or the bulk current,

needs to be considered in the noise current estimation. As it is a thermally generated cuurent, it can be reduced by lowering the operating temperature of the APD. We will operate the APDs in the NOνA detector at -15° C to keep the noise contribution from I_B small in comparison to the front-end noise. This choice is based on measurements obtained with prototype readouts.

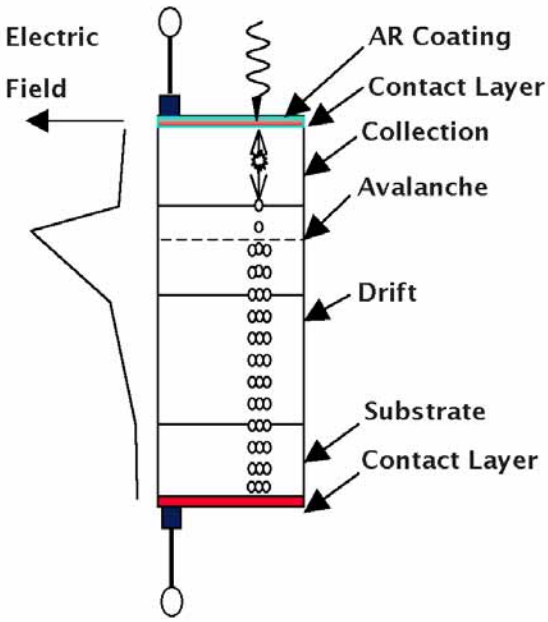

Fig. 13.1: The basic structure of a blue/green sensitive APD. Light crosses the anti-reflection coating at the surface and is absorbed in the collection region. Photoelectrons drift in the electric field to the junction where they undergo avalanche multiplication.

The amplification mechanism in the APD is itself subject to noise, characterized by the excess noise factor *F*, with such factors as device non-uniformities and the ratio of the positive to negative impact ionization coefficients contributing. This factor is well modelled and has been included in our signal to noise calculations.

APDs have two substantial advantages over other photodetectors: high quantum efficiency and low cost. The high APD quantum efficiency enables the use of very long scintillator modules, thus significantly reducing the electronics channel count, while the per channel cost is about a factor of four less than that of a multi-anode photo-multiplier tube (MAPMT). Figure 13.2 compares the quantum efficiency of a Hamamatsu APD to that of the MAPMT used in the MINOS Far Detector. In the wavelength region relevant to the output of the wavelength shifting (WLS) fibers, 500 to 550 nm, the APD quantum efficiency is 85% *vs.* 10% for the MAPMT. The quantum efficiency advantage of the APD increases with wavelength and thus the length of the fiber. This gives the APD an even greater advantage over a MAPMT for long fibers.

Hamamatsu is the only known vendor for APD pixel arrays. Hamamatsu markets a 32-pixel packaged APD with a pixel size of 1.6 mm by 1.6 mm. To maximize light output, NOνA utilizes a looped or U-shaped WLS fiber. Both ends of the looped fiber must terminate on the same APD pixel. To comfortably accommodate both fiber ends, Hamamatsu has agreed to modify the pixel size and shape. The modified APDs for NOνA will be provided in bare die form rather than in a package. Hamamatsu will bump bond the bare die to an APD carrier circuit board provided by NOνA.

The CMS experiment is using 124,000 Hamamatsu APDs, with 5 mm × 5 mm pixels, to read out their lead-tungstate calorimeter. The full order has been delivered to the experiment and

tested. The quantum efficiency for these devices is consistently measured near 85% at 550 nm as can be seen in Figure 13.3.

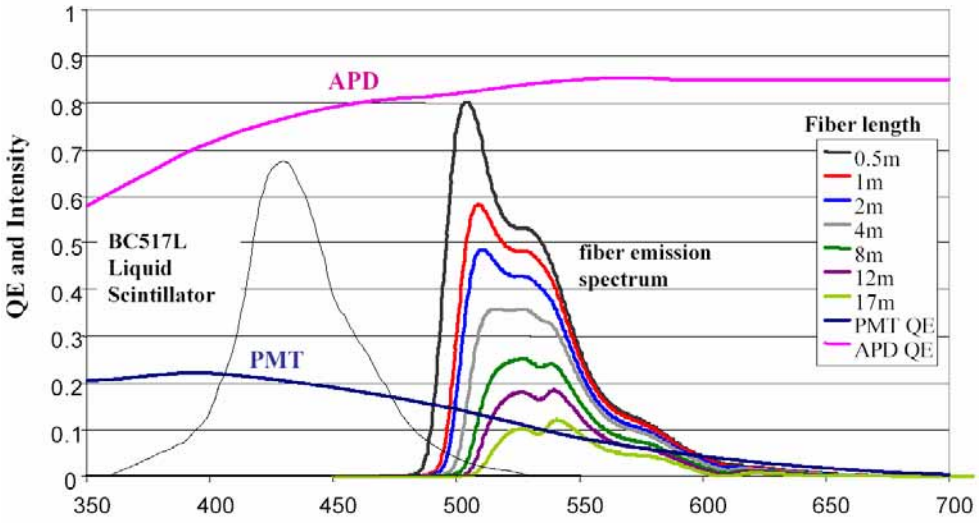

Figure 13.2 WLS fiber emission spectra measured at lengths of 0.5, 1, 2, 4, 8, 16 m, respectively illustrating the shift of the average detected wavelength as fiber length increases. Also shown are the quantum efficiencies of APDs and PMTs (bialkali photocathode) as a function of wavelength. The emmission spectrum of the liquid scincillator is also shown.

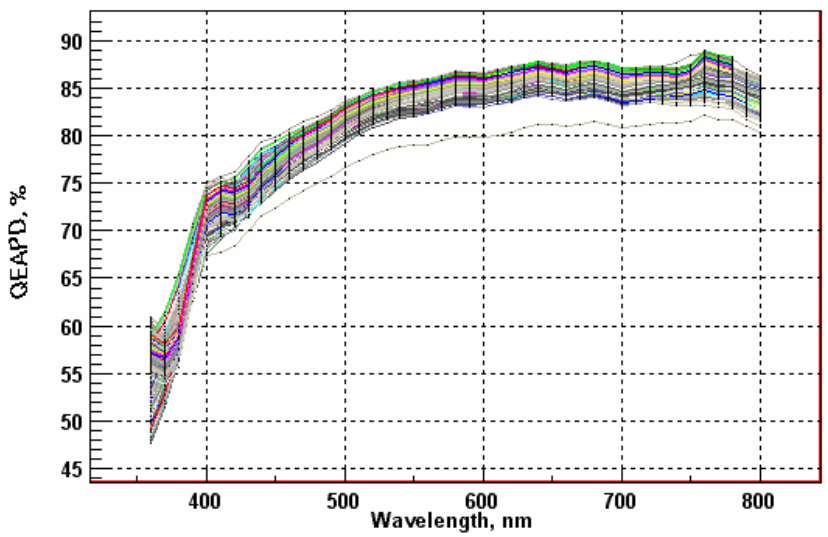

Figure 13.3 Quantum efficiency of several hundred CMS APDs.

We have purchased a number of Hamamatsu's off-the-shelf, packaged APDs for evaluation. The dark current is consistent with expectations from the CMS APD measurements and the gain is uniform from pixel to pixel on the same chip and within individual pixels. The measured pixel gain and pixel separation for one of the sample arrays are shown in Figures 13.4 and 13.5. The fall-off on the pixel edges reflects the finite spot size used to illuminate the APD pixels.

A single-stage TE cooler will cool each APD array. The TE cooler must not apply significant mechanical stress to the APD array, so we deploy a deformable, thermally conducting crush pad between the TE cooler and the APD array. The thermal power generated in the APD array itself is ~25 mW, so most of the thermal load will come from other components through the

electrical interconnects. The TE cooler will generate approximately 3W of heat for each 32 channel APD array. The APD array will be mounted on a separate APD carrier board that is environmentally isolated from the other electronic components to minimize the thermal load. The mounting will be done with flip-chip technology, so the active area of the APD will face a hole cut out of the PC board where the fibers will terminate. The flip-chip method provides an accurate means of aligning the APD to the PC board to which the fiber connector will also be aligned. The fiber connector must accurately align the fibers both longitudinally and transversely to the APD pixels.

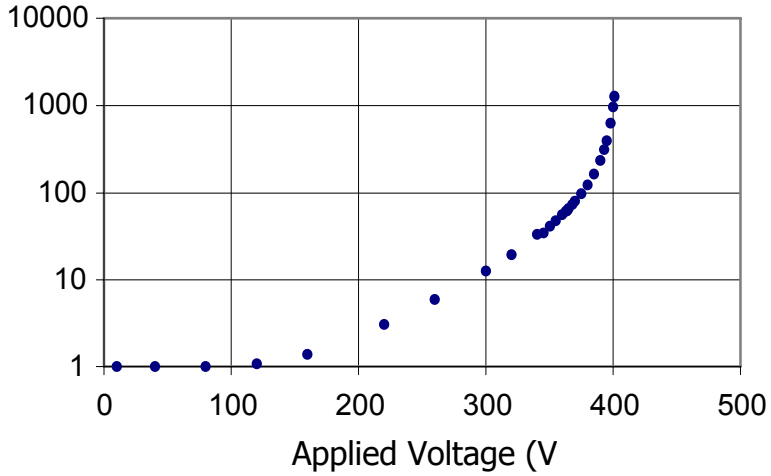

Figure 13.4 Gain *vs*. applied voltage at 25° C for Hamamatsu off-the-shelf APD arrays.

We expect a non-negligible rate of TE cooler failures and the failure rate as well as the power consumption is known to increase with temperature. Water cooling is the most reliable and effective means of removing the heat from the TE coolers. This heat will be removed from the TE cooler using a closed-loop chilled water system that provides approximately 0.04 gallons/minute of 48° F water to each TE cooler. Water will flow horizontally in order to avoid large pressure drops. Small plate-type heat exchangers will be installed down the length of the detector hall. Each heat-exchanger will be coupled to a fractional horsepower pump to supply the water to the TE coolers through ¼" insulated supply and return lines. The design of the system allows for phased commissioning of the detector.

One of the operating requirements for the APDs is that they be kept dry. Dew-point concerns associated with the low operating temperature of the TE coolers have led us to a design where the APD and TE cooler are enclosed in a dry nitrogen environment.

One of the attractive features of APDs is that once they have been calibrated, the gain can be easily determined from the applied bias voltage and the operating temperature. In the NOνA detector, we will maintain the operating bias to a precision of 0.2 Volts and control the temperature to 0.5° C and thus hold the gain stability to about 3%, consistent with the pixel-to-pixel variation. The NOνA APDs will typically operate between 350V - 450V at a standing current of approximately 50 nA per 32-channel APD array. The high voltage supplies will provide 500 V and a variable resistor will be used to set the voltage for a gain of 100. Since the current requirement is so small, there is no need for individual high voltage (HV) supplies for each 32-pixel APD array. Instead, a bulk supply can easily service many APD arrays. The front end board will filter the bulk HV and supply it to the APD array.

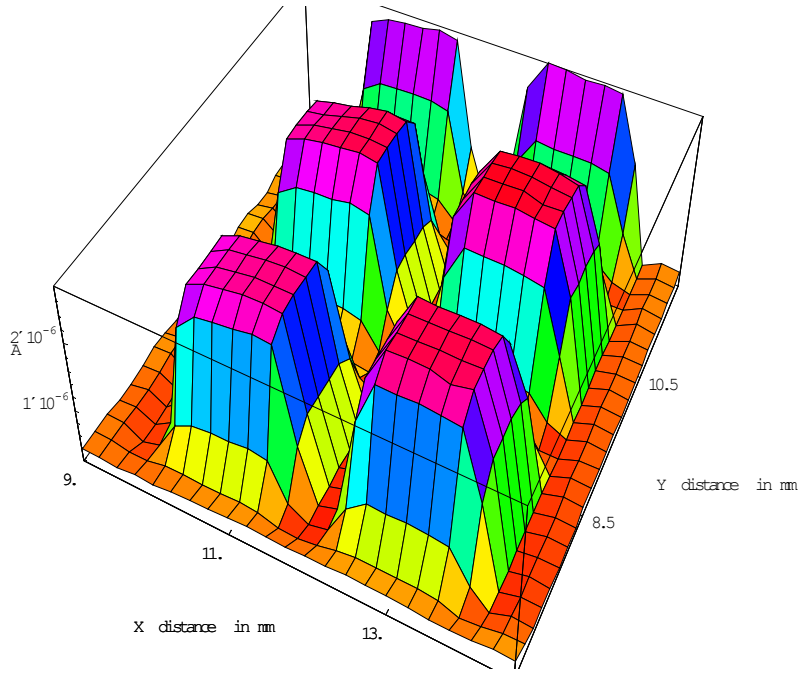

Fig. 13.5 Fine point scan across part of an off-the-shelf Hamamatsu APD array. The fall-off on the pixel edges reflects the finite spot size used to illuminate the APD pixels.

13.3 Front End Electronics

The front end electronics has the responsibility of amplifying and integrating the signals from the APD arrays, determining the amplitude of the signals and their arrival time and presenting that information to the data acquisition system (DAQ). The front-end electronics will operate in continuous digitization mode and does not require any external trigger or NUMI timing gate. Data will be time stamped and compared to a NUMI timing signal in the DAQ system to determine if the event was in or out of spill.

The front-end electronics will be deadtimeless. Signals from individual APD pixels are processed through individual amplifier and pulse-shaping stages before being multiplexed to an ADC in sets of 8 channels. The amplification, pulse-shaping and multiplexing stages are implemented in a NOνA-specific ASIC that is currently in the advanced design stage. The ADC is external to the ASIC and is a commercial component. A schematic of the layout is shown in Figure 13.6.

The front-end electronics board is connected to the APD carrier board through a short ribbon cable. In addition to the front end ASIC and ADC, the front-end board contains a connector for interfacing to the DAQ system, TE cooler controller circuitry and an FPGA for doing pedestal subtraction, zero suppression, clock regeneration, I/O functions, and general board monitoring. A schematic of the front-end board and the APD carrier board is shown in Figure 13.7.

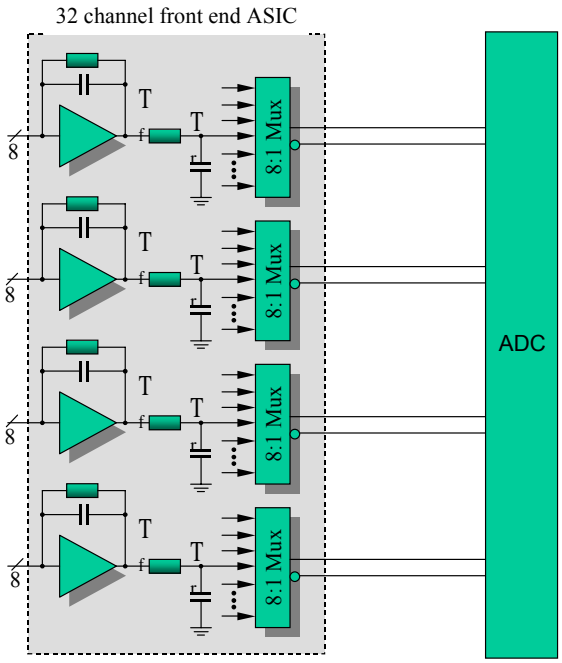

Fig. 13.6: Schematic of the Front End ASIC and external ADC for NOνA.

The computed noise level for the chip that we have designed specifically to operate with an APD with a gain of 100 and cooled to -15°C is 150 – 200 electrons. We assume that the upper end of this range will be realized for production devices. With an APD gain of 100, this 200 equivalent noise charge reduces to 2.0 photoelectrons. At -15°C we expect 2 thermally generated electrons every 1 μs. The convolution of the amplifier noise with the APD noise results in a mean of 2.5 photoelectrons of noise. This is to be compared to a worst-case average photoelectron yield at the far end of an extrusion module of ~20, spread over a very short time interval. Data from the ADC is sent to an FPGA, where multiple correlated sampling is used to remove low frequency (parallel) noise. Because of the low rate per channel in the NOνA detector, multiple sampling and more sophisticated digital signal processing is also being investigated to further reduce the noise level.

To minimize the load on the DAQ system it is important to keep the data rate from noise to an acceptable level. The noise level of the front end electronics and the imposed threshold determines the noise data rates. The simulated noise rate per 32 channel APD box as a function of threshold for 2.5 photoelectrons of noise per channel, 10 bytes of information per hit above threshold and 10^6 time slices/second is shown in Figure 13.8. The noise is assumed to be Gaussian. In order to keep the noise data rate below the rate from cosmic ray muons (with a 3 m overburden) it is necessary to impose at least a 10-photoelectron trigger. Non-Gaussian tails in the noise distribution push this requirement even higher.

The front end boards require low voltage to power the electronics and the TE cooler controller. The front end electronics boards will each require 3 W of clean power at 3 V. The TE coolers will require 3 W of lower quality power (<0.5 V of ripple) to be provided at 12 V. High quality commercial power supplies would be used to provide clean power for the electronics. Cheap commercial or home made supplies will be used for the TE coolers.

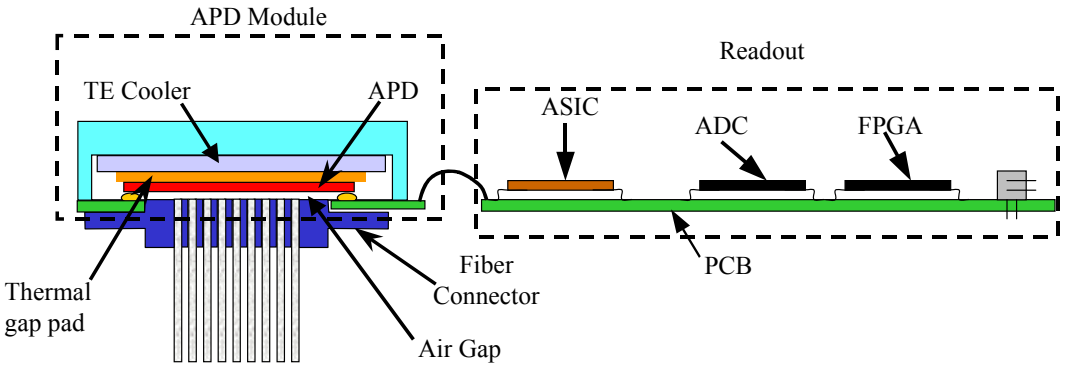

Fig. 13.7: Schematic of the APD module and the front-end electronics board showing the major components.

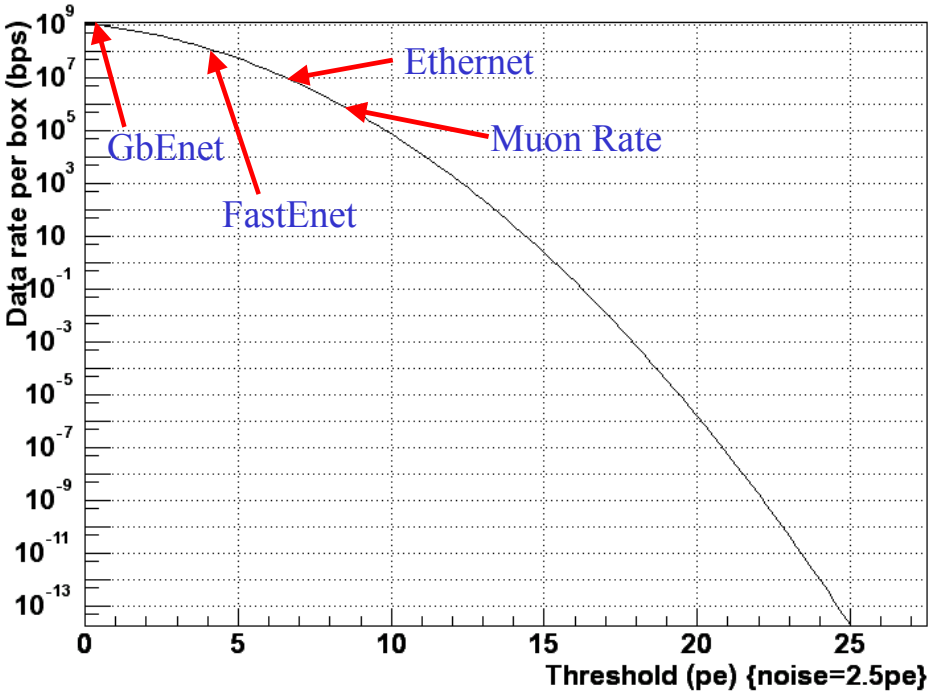

Figure 13.8 The simulated data rate at the NOνA far detector, in bits per second, as a function of the readout threshold. A Gaussian noise level per channel of 2.5 photoelectrons is assumed. The data rate due to cosmic ray muons, with a 3 m overburden, is also indicated as well as the networking technologies necessary to accommodate various rates.

The front end electronics must operate in several different modes that can be selected through the DAQ interface. These are:

- Run Mode – The Front end electronics will continuously acquire and transmit data to the DAQ system.

- Calibration mode – Data is accumulated for calibration and for determining thresholds and pedestals, noise measurements, etc.
- Test Mode – The Front end electronics must be able to simulate data and send specific test patterns to the DAQ system to check for proper operation.
- Programming mode – The front end electronics must be able to download and upload data that define its operating parameters. The front end electronics must have on-board firmware that can be reprogrammed in place via the DAQ system.

13.4 Alternatives Considered

A number of photodetector technologies exist that have been considered by NOνA as alternatives to avalanche photodiodes. These include multi anode Photomultiplier tubes (MAPMT) similar to those used by MINOS. MAPMTs were rejected for use by NOνA because of their low quantum efficiency and high cost relative to APDs. The high quantum efficiency of APDs makes it possible to use scintillator modules that are significantly longer than those used in MINOS with MAPMTs. This reduces the electronics channel count and reduces the cost of the project. In addition, the cost per channel of APDs is four times smaller that the cost per channel of MAPMTs.

Visible Light Photon Counters (VLPCs) similar to those used for the Dzero fiber tracker have also been considered. The cost of VLPCs, the operating expense of the cryogenics and the difficulty of maintaining a huge cryogenic facility at a remote site were all factors that resulted in the rejection of this alternative.

Hybrid Photodiodes (HPDs) have also been considered as an alternative to APDs. HPDs have been selected for the CMS HCAL because of their radiation tolerance and the ability to operate them in high magnetic fields. These criteria do not exist for NOνA. HPDs are significantly more expensive than the NOνA APDs and have lower quantum efficiency and have therefore been rejected.

Silicon Photomultiplier technology is very promising, but is not sufficiently advanced to be seriously considered for NOνA. The same can be said for metal resistivity semiconductor APDs.

The APDs operate between 350V – 450V and require a high voltage source. In our proposal we discussed using an Cockroft-Walton voltage divider on each board to power the APDs. This alternative has been rejected in favor of bulk HV supplies that provide power to many APDs from a single HV channel. Because the current draw for the APDs is small (~ 50 nA/APD array) an individual HV supply for each APD is not required. In addition, Cockroft-Walton voltage dividers can be a source of noise, so on-board operation would have required filtering.

In our proposal we discussed a readout architecture similar to the SVX4 with dual mode operation. On-spill, the readout would operate in high-precision mode and in low-precision mode off-spill. The ASIC needed to accommodate this readout architecture would contain a 32-channel wide, 64 deep switched capacitor array that would accumulate data during the spill and digitize the data off-spill. We have since rejected this option in favor of the continuously digitizing multiplexed readout described earlier. The switched capacitor alternative is more expensive because of the large area of silicon required for the capacitor array. The switched capacitor alternative also requires a NUMI spill gate to be distributed to every front end board. The one advantage of the switched capacitor array alternative is that digitization takes place off-spill making the low noise operation required by NOνA easier to accomplish. While we are confident that both approaches could work for NOνA, the lower cost and seamless operation both on and off-spill of the continuously digitizing multiplexed architecture make this the most attractive option.

The APD arrays must be cooled to reduce the thermal noise. As an alternative to the TE coolers, we considered the possibility of directly cooling the APDs using chilled water and cold

fingers. The engineering effort to design such a system was considered to be too large when compared with the commercial off-the-shelf TE cooler option, so these alternatives were rejected.

13.5 Optimization of the Design

The signal-to-noise ratio at the far end of the scintillator modules is an important performance characteristic for the NOνA detector. Of particular relevance for the front end electronics is the threshold level that can be set to keep the data rate due to noise to a lower level than the rate due to cosmic ray muons. This consideration, in isolation, argues to push the threshold up. However, in order to efficiently track particles through the detector it is important to have a threshold that is set at a fraction of a MIP. This is particularly important for tracking minimum ionizing particles like muons. In order to achieve good tracking efficiency it must be possible to see tracks that clip the corners of cells and do not deposit a full MIPs worth of ionization energy in the cell. This argues for a lower threshold setting.

We have optimized the gain of the APDs by studying the threshold setting required to keep the noise data rate below that of cosmic ray muons as a function of the APD gain. Noise from the front-end boards was included in this study. The results of those measurements are shown in Figure 13.9. The plot clearly demonstrates that the APD gain optimizes near a gain of 100.

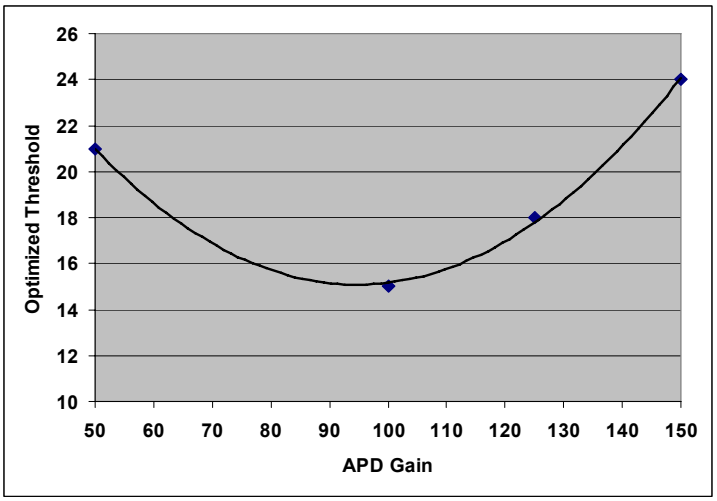

Figure 13.9 The threshold setting required to keep the noise data rate below the data rate from cosmic ray muons as a function of APD gain.

13.6 Quality Assurance

All electronics devices will be tested prior to shipping to Ash River.

13.7 ES&H

The photodetector and electronics systems do not present any special safety issues. The primary safety concern is in working with energized electrical systems. There will be no exposed low or high voltage and procedures will be in place that require systems to be de-energized when they are being worked on. Everyone involved in the work on these systems will receive basic electrical safety training.

Some varieties of TE coolers contain lead telluride. In addition, solder also contains lead, so everyone who works with the electronics will be made aware of the presence of lead and will

receive the appropriate training. Once the details of the layout, design and parts list are known, the required training will be specified in detail.

Work on the APDs or the electronics could occasionally require work to be performed at heights up to 50 feet. Procedures for working at these heights will be developed once the design of the detector hall and the details of the detector design are finalized.

13.8 Risks

There are a number of risks associated with the photodetectors and front end electronics. There is only one vendor for the APDs. This always presents a risk. However, in this case the risk is not considered large because the single vendor is Hamamatsu, a vendor well known to Fermilab procurement and the high energy physics community in general. Hamamatsu has a history of delivering on time and at a reasonable cost. This risk is considered small.

ASICs have traditionally presented schedule risks because it is often necessary to do additional foundry runs to get working parts. This risk has been reduced in recent years because of improved processes for fabricating ASICs and more advanced design and simulation tools that catch mistakes and accurately predict chip performance. In addition, significant design work on the NOνA front end ASIC has been completed at a very early stage of the project making schedule delays less likely. This risk is considered small.

The overall noise level of the APD and front end electronics poses a technical risk to the Project. NOνA currently relies on simulations and extrapolations from similar parts to estimate the expected noise level. In our simulations we currently consider only dual correlated sampling to reduce noise. Multiple sampling and digital signal processing techniques will also be employed by NOνA to reduce the noise level. Additionally, NOνA should have production parts available at an early stage with which to make real noise measurements. This risk is considered small.

13.9 Value Management

The heat from the TE coolers must be removed from the APDs and the front-end electronics. Our plan for this is to use water cooling. As part of our value management program we will compare the cost and effectiveness of air cooling to water cooling. This choice has implications not only for the electronics infrastructure but also for the design and outfitting the experimental hall.

Reducing the overall electronics noise will improve the signal-to-noise ratio and allow for lower thresholds. As mentioned earlier, we intend to study the noise reduction that can be achieved using multiple sampling and more sophisticated digital signal processing. Our current noise estimates assume only dual correlated sampling. In addition, the APD gain can be optimized. The avalanche gain amplification in the APD introduces additional noise known as excess noise, which increases with the internal APD gain. Increasing the APD gain increases S/N until at some gain the S/N ratio reaches a maximum, and any further increase in APD gain has a deleterious effect.

As part of our value management program we will study the implications of allowing the noise data rate to be somewhat higher than the rate from cosmic ray muons. This primarily has implications for the cost and design of the DAQ system.

14. Data Acquisition System

14.1 System Description

The primary task for the readout and data acquisition system (DAQ) is to concentrate the data from the large number of APD channels into a single stream that can be analyzed and archived. The DAQ also provides for an intermediate buffering location where the data can be held until it is determined that the data should be recorded or rejected. Online trigger processors will be used to analyze the data stream to correlate data with similar time stamps and to look for clusters of hits indicating an interesting event. Additional functionality for dealing with flow control, monitoring, system operations and alarms is also included.

The NOνA front end electronics operates in triggerless mode with data continuously being digitized, time-stamped, pedestal subtracted and zero-suppressed. There is no spill trigger required at the front-end. A spill signal is required to arrive within 1 or 2 seconds so that the spill time can be correlated with the time-stamped data to determine if the hits occurred in or out of spill. There is no triggering or selection of in-spill data. All hits that occur in a $\pm$ 15 μs window around the spill are recorded for further processing. This corresponds to about 1 TB of data per year.

Random data for calibration and monitoring will be collected off-spill at a rate that is approximately 100 times higher than the in-spill rate. This corresponds to about 100 TB/yr of raw data that will be subject to additional filtering before a storage decision is made. The data must be buffered for 1-2 seconds while an online farm determines if the data is useful and should be recorded.

The overall data rate is driven by cosmic ray muons that occur at a rate of approximately 210 kHz with a 3 m overburden. Monte Carlo simulations predict approximately 900 hits per cosmic ray muon, where many planes have multiple hits. This corresponds to a total hit rate of 200 MHz and a total data rate of about 2 GB/s. Table 14.1 summarizes the channel count and rates in the NOνA far detector.

14.2 System Architecture

NOνA has only one type of detector and one type of readout, making the NOνA DAQ conceptually simple compared to typical high energy physics experiments. Digitized data from the front end ADCs are input into an FPGA that applies zero suppression, timestamps and buffers the data before serialization and transmission to the DAQ. The FPGA can also provide control and monitoring of the front end electronics and APDs. The FPGA also provides for an external interface using standard Ethernet protocols and inexpensive CAT5 cabling.

The overall organization of the DAQ system is shown in Figure 14.1. Digitized data from 64 front end boards is routed through CAT5 cables to a custom Data Combiner. Six Data Combiners service each 31-plane sub-block for a total of 324. The NOνA data Combiner is based on a similar design from BTeV and is shown in Figure 14.2.

The 324 Data Combiner boards send data to a computer processor farm over Gigabit Ethernet links. The processor farm pipes data from accepted events to local storage. Data stored locally is eventually copied to Fermilab for permanent storage.

There is a Run Control Host that generates control signals for the DAQ system. The Run Control Host generates a 16 MHz clock that is distributed to the Data Combiners and then to each front end board. The absolute time, required for time stamping and correlating the data, is obtained from a GPS unit and distributed to the data combiners. The general overall scheme is shown in Figure 14.3.

Front end boxes	20,088
Front end boxes per plane	12
APD channels per box	32
Total channels	642,816
Noise rate per channel	< 75 Hz
Bytes per hit (channel ID, TDC, ADC, status)	10
Muon rate	211 kHz
Hit channels/muon	900 (multiple hits/plane)
Total hit rate	190 MHz
Average hits/channel	300
Digitizing rate	2 MHz
Bytes/hit	10
Total data rate	1.8 GB/s
Average occupancy	3×10^{-4}

Table 14.1 Channel count and rates in the NOνA far detector.

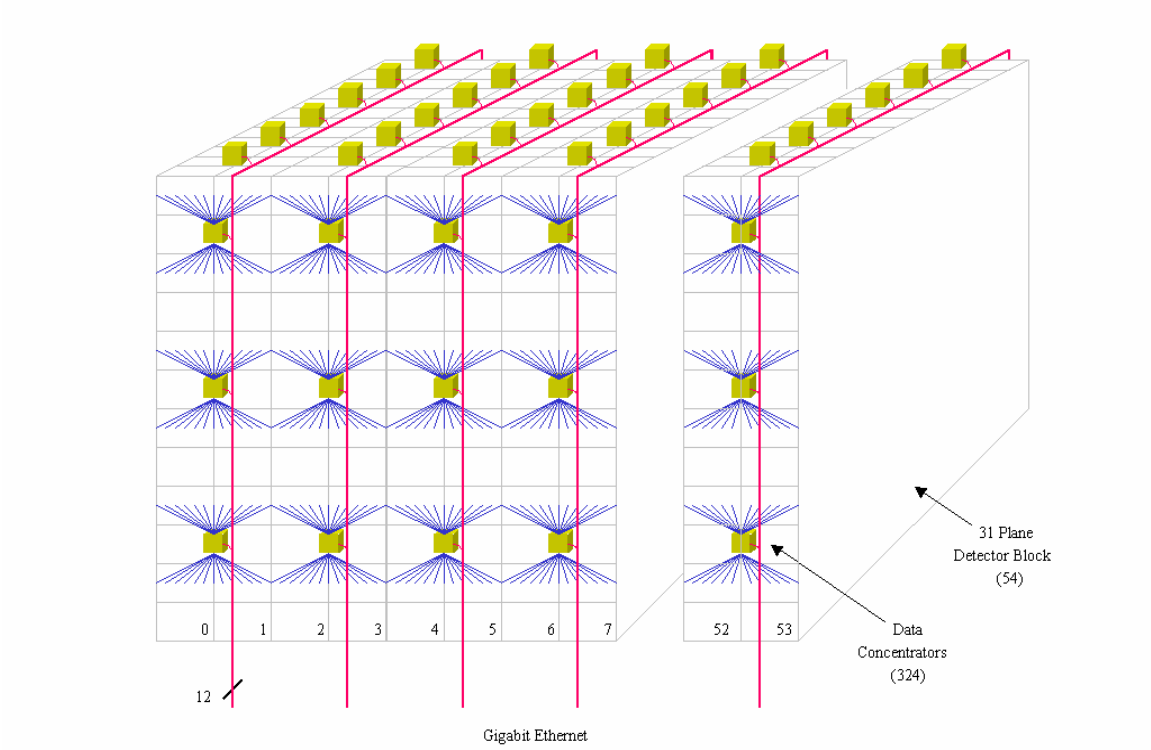

Figure 14.1 Overview of DAQ architecture showing location of Data Combiners.

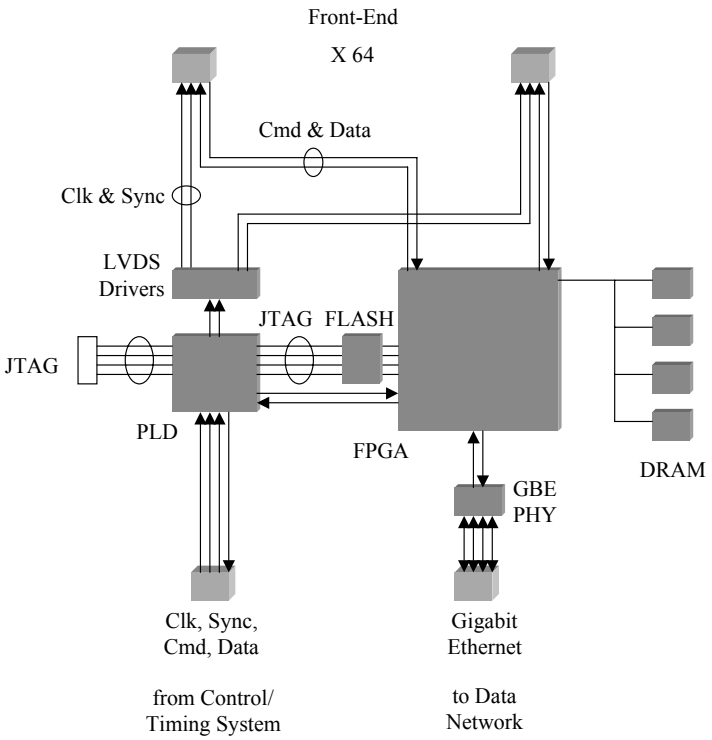

Fig. 14.2: Schematic of Data Combiner.

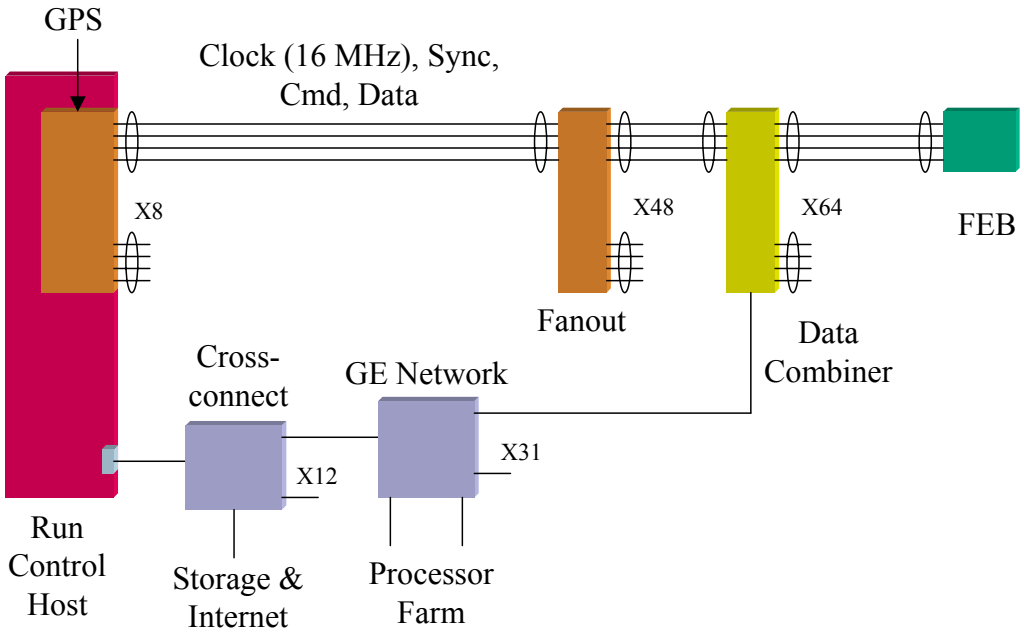

Fig. 14.3: Components of the NOvA DAQ system.

14.3 Alternatives Considered

Several schemes were considered for transmitting data from the ~20,000 front end boards to the DAQ system. The original communication scheme was to be over optical links. Optical links have higher bandwidth and no associated electrical noise or ground loops. After better understanding the real rates in the NOνA far detector we were able to move to less expensive CAT5 cables that will be more than adequate for our application.

We also considered wireless communication, but the number of wireless nodes (~20,000), the long distance over which the signals would have to be transmitted as well as line-of-sight concerns are among the reasons for rejecting this alternative.

14.4 Design Optimization

As is the case with many high energy experiments, NOνA will delay many DAQ decisions and purchases as long as possible to take advantage of the technological advances in computing and networking technology over time.

14.4.1 Supernova Detection

While not part of the scope of the NOνA project, it is possible to detect the neutrinos from supernova events in the NOνA far detector. A supernova explosion at a distance of 10 kpc will result in about 9000 neutrino interactions in the NOνA far detector. Electrons at these energies will deposit about 15 MeV of energy per cell. The majority of neutrinos from such a supernova explosion will be between 20 to 40 MeV and will result in coincident hits in adjacent cells with energy deposits greater than 0.5 MIPs.

Supernova detection requires front end electronics with low deadtime and a free running DAQ system that does not rely on a beam trigger signal from Fermilab. The NOνA front end electronics and DAQ system already meet these requirements. The search for supernova would have to be done in real time requiring the DAQ system to be able to handle the full 3 GB/s rate described in Table 14.1. The modular, parallel design of the NOνA DAQ makes this possible as well. Supernova detection would require up to 20 seconds of data buffering, an order of magnitude greater than what is necessary for the neutrino oscillation program. Additional online processing and software would also be required. While the cost of these additions is relatively small, they are not included in the NOνA base program and would have to be funded separately.

14.5 Quality Assurance

All electronics devices will be tested prior to shipping to Ash River. The DAQ readout concentrators will have a self-test diagnostic that runs on application of power

14.6 ES&H

The DAQ system does not present any special safety issues. The primary safety concern is in working with energized electrical systems. Everyone involved in the DAQ system will receive basic electrical safety training. The interface between the DAQ system and the front end electronics is made on the detector. This could occasionally require work to be performed at heights up to 55 feet. Procedures for working at these heights will be developed once the design of the detector hall and the details of the detector design are finalized.

14.7 Risks

By the standards of most high energy physics experiments at Fermilab, the DAQ system required by NOνA is relatively simple and straightforward. The only complications that arise are

the overall data rate and the fact that the DAQ system for the Far Detector must operate in Northern Minnesota making direct access more difficult.

The rates in the NOνA detector are determined by the rate of cosmic ray muons and the settings of the readout threshold relative to the noise level of the APDs and front end electronics. The thresholds must be set low enough to facilitate efficient identification of tracks in the detector but high enough to keep the number of noise hits to a reasonable level. If the detector were to produce less light than expected or if the electronics were to produce more noise than expected the data rate from noise hits would be larger than expected, perhaps straining the DAQ system. Reducing the number of channels serviced by the data combiners, increasing the number of data combiners and increasing the size of the processor farm can mitigate this risk. We expect to measure the noise rates of the APDs and front end electronics with pre-production parts in FY06 to determine if the noise levels are as expected.

14.8 Safeguards and Security

Data collected from the Far Detector will be stored locally for a short time before being transferred via the Internet to Fermilab for permanent storage. In addition, because of the remote location, Internet access to the DAQ is necessary to monitor the performance of the detector. Because of this need to be connected to the Internet, the NOνA DAQ system will have to be an environment that is secure against unauthorized access and malicious acts. Safeguards and security will be built into the DAQ system as a requirement. As this is currently a rapidly changing and timely field with the onset of grid computing, we will wait as long as possible before committing to a particular protocol.

14.9 Value Management

NOνA will delay many DAQ decisions and purchases as long as possible to take advantage of the technological advances and cost savings in computing and networking technology over time.

15. Near Detector

15.1 Introduction

NOνA proposes to construct a Near Detector on the Fermilab site at a distance of about 1 km from the NuMI target in the NuMI access tunnel upstream of the MINOS access shaft. The design of the Near Detector is constrained by two requirements. The first requirement is that the Near Detector should be as similar as possible to the Far Detector in material and segmentation. This requirement ensures that the efficiencies for signal and background events are nearly identical. Ideally, this will allow us to understand the ν_e charged current and ν neutral current beam spectra seen in the Near Detector as a measure of the expected backgrounds to $\nu_\mu \rightarrow \nu_e$ oscillation signals in the Far Detector. The second requirement is that the Near Detector must fit in the NuMI access tunnel and the pieces from which it is constructed must fit down the NuMI access shaft.

15.2 Near Detector Design

We have designed a Near Detector that uses the same technology as the NOνA Far Detector and satisfies the space constraints described earlier. The NOνA Near Detector is 2.9 m wide, 4.1 m high and 14.4 m long. The first 12.7 meters of the detector is composed of the exact same extrusion cells as in the Far Detector design. It is split into three logical parts: an upstream veto region, a fiducial event region, and a shower containment region. Figure 15.1 displays this longitudinal detector structure. The 4.63 m long shower containment length is chosen to fully contain electron showers from charged current ν_e interactions of a few GeV. The active detector sections are followed by a muon catcher composed of 1.0 meter of steel interspersed with additional planes of liquid scintillator cells. The length of the muon catcher is chosen to so that it plus the shower containment region will contain muons from charged current ν_μ interactions.

Given the modular design of the Near Detector, it can be moved relatively easily. The need to move the Near Detector to various sites in the NuMI access tunnel is a requirement that emerges from the physics measurements that must be performed to fully understand the backgrounds at the Far Detector. This is discussed in Chapter 2.

Altogether there are 196 planes of liquid scintillator cells, 95 planes with horizontal cells and 101 planes with vertical cells. The total mass of the detector is 209 tons with 126 tons totally active. The fiducial volume has a mass of 23 tons. The detector would be constructed in modular packages or segments that are each 7 or 8 planes thick. Each segment will average 4.75 tons when full of liquid and average 1.3 tons empty. The blocks reasonably fit the MINOS access shaft constraints and could be moved along the tunnel full or empty. The Near Detector parameters are summarized in Table 15.1.

15.3 Near Detector Event Rates

At a location in the MINOS access tunnel midway between the shaft and the MINOS near detector hall, the event rates in the 23 ton fiducial mass will be about 0.09 event per 10^{13} protons on the NuMI target. The rate increases about a factor of three near the MINOS near detector hall. The maximum beam from a single Main Injector (MI) pulse is expected [1] to be 6×10^{13} protons, so we would get about 0.5 events per MI spill. About two-thirds of these events would be from neutrinos with energies below 5 GeV. We would collect about 6.5 million such events in one year with 6.5×10^{20} p.o.t.

The rate of events in the whole active detector is larger. Since the total active mass is 126 tons, we would see a rate of 3.2 events per MI pulse of 6 x 10^{13} protons. Assuming a 500 ns time bin in our electronics and a 10 microsecond spill [2], that would imply 8% of our events would have two or more overlapping events in the active detector. We therefore expect to clock the Near Detector electronics at a faster speed than the Far Detector electronics.

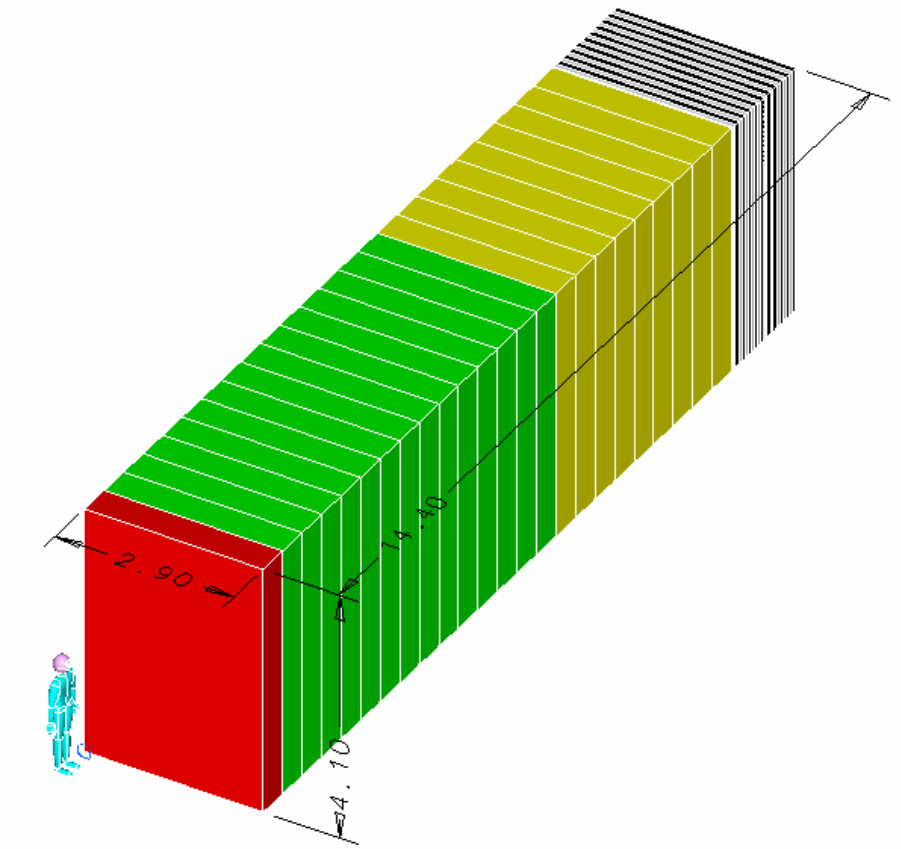

Figure 15.3 The NOνA Near Detector. The beam comes from the lower left in this diagram. Each block consists of 7 or 8 planes of extrusions, 4 vertical interleaved with 4 horizontal planes. Every 4th segment has one less horizontal plane. The upstream section is a veto region (red), the next 14 sections are the fiducial region (green), followed by a 9-section shower containment region (brown). All parts of these three sections are fully active liquid scintillator cells identical to the Far Detector and the colored areas just represent a logical assignment. Downstream of this active region is a 1.7 m muon catcher region of steel interspersed with 10 active planes of liquid scintillator (black and white).

15.4 Alternatives Considered

The design of the Near Detector is constrained by a variety of factors. The technology is constrained by the requirement that it be identical to the Far Detector. The size and shape are largely constrained by the size of the NuMI access tunnel. The modular design is required in order to get assembled pieces down the NuMI shaft and into the tunnel. Underlying this is the difficulty, expense and risk of performing any additional excavation to expand the size of the access tunnel because of the network of water control channels behind the wall and floor concrete surfaces.

The only alternatives specific to the Near Detector that have been considered relate to the speed of the readout to deal with the higher event rates. In the NOνA proposal we discussed the possibility of interspersing 6 fast-readout planes throughout the Near Detector. The fast-readout planes were to tag the presence of more than one event in a single spill. This alternative was rejected because of the added complexity of two different types of readout. The selected alternative to use Near Detector electronics that are identical to the Far Detector readout, but clocked at a faster speed that allows for faster readout of every Near Detector plane and can be executed more efficiently.

Near Detector Parameter	Parameter Value
Total mass	209 metric tons
Active detector mass	126 metric tons
Fiducial mass	23 metric tons
Extrusion cells, liquid scintillator, waveshifting fiber, APD readout	Identical to the Far Detector
Number of channels	15,584
Total Liquid Scintillator	109,960 liters, 29,048 gallons
Detector Width (m and # of cells), Height (m and # of cells), length (m)	2.9 m, 64 cells 4.1 m, 96 cells 14.4 m
Total active planes	196 planes 95 horizontal & 101 vertical
Segment pieces in the active section # planes Thickness of 7 (8) plane segment Empty weight of 7 (8) plane segment Full weight of 7 (8) plane segment	 7 or 8 planes 46.2 (52.8) cm 1203 (1340) kg 4504 (5132) kg
Veto region, # of active planes	6 planes
Fiducial region, # of active planes	110 planes
Shower Containment region, # of active planes	 70 planes
Muon catcher Steel (m/section, # of sections) # of active planes	 0.1 m, 10 sections 10 planes
Muon catcher mass Steel Scintillator planes	 81 metric tons 6.5 metric tons

Table 15.1 NOνA Near Detector Parameters.

15.5 Optimization

We have optimized the Near Detector to accommodate the unique conditions for installation down the MINOS shaft and into the MINOS access tunnel. The transverse dimensions of the detector allow it to be positioned in the access tunnel with appropriate space for passage of other equipment.

15.6 Quality Assurance

The quality assurance issues for the Near Detector are similar to the Far Detector. Special extrusion modules have to be constructed at the Module Factories as raw material for this detector. The same leak issues apply to these modules as to the ones for the Far Detector.

15.7 ES&H

The existing safety mechanisms that are in place in the NuMI access tunnel have been developed for the MINOS near detector, built from steel and solid plastic scintillator. Operation of a liquid scintillator based detector poses a different set of problems. Full secondary containment is planned for the liquid scintillator to keep it out of the NuMI sumps that get pumped to the surface. Fire safety alternatives must also be considered. The preferred fire suppression system for liquid scintillator is foam, the method chosen for the Far Detector site. The NuMI access tunnel would have to be retrofitted with a foam fire suppression system. Other alternatives include operating the Near Detector in a sealed, inert environment. This alternative raises ODH issues that would have to be addressed.

Working underground in the NuMI access tunnel presents many safety issues that are outside the experience of most experimenters. Anyone who works in the NuMI tunnel will be required to take the Fermilab Underground safety course and will be required to appropriate personal protective equipment.

15.8 Risks

Because the Near and Far Detectors are designed to be as identical as possible, there are few risks that are unique to the Near Detector. Risks that are common to both detectors will be discussed elsewhere.

The one risk unique to the Near Detector is the possibility that our plan to run the front end electronics at a higher clocking speed will not work. The speed at which the front end electronics must run is currently under study. Should it not be possible to clock the front end electronics as fast as necessary, we would revisit the possibility of interspersing a few fast readout planes throughout the Near Detector.

15.9 Value Management

One area that remains to be optimized is the clock speed of the Near Detector electronics, also described in the previous section. The current plan is to run the Near Detector electronics twice as fast as the Far Detector, sampling the charge every 250 ns. Event pileup in the Near Detector is currently being simulated to determine if this is the optimum clocking speed.

The structure surrounding the Near Detector modules will need further study as we converge on a final technical design for a mobile detector. As mentioned in Chapter 3, a discovery by MiniBooNE would add additional structural constraints for mobility, requiring the NOvA Near Detector to move up a 10.85% grade from the MINOS access shaft towards the NuMI target for some periods of data taking.

Chapter 15 References

[1] draft Fermilab Proton Plan, November 2004, see http://www.fnal.gov/directorate/program_planning/Nov2004PACPublic/PACagendaNov2004OPEN.htm

[2] The spill length is 9.78 microseconds for the case of no anti-proton operation discussed in Chapter 11. See the NuMI Technical Design Handbook, Chapter 3, “Design Parameters” at http://www-numi.fnal.gov/numwork/tdh/tdh_index.html

16. Far Detector Assembly

16.1 Assembly of planes and blocks

Completed and fully tested extrusion modules from the three extrusion module factories are delivered to the far detector hall where they are assembled into alternating horizontal and vertical planes. Each plane consists of 12 extrusion modules. Thirty-one planes of modules are glued together into a strong structure of alternating vertical and horizontal layers to form a block. There are a total of 64 such blocks, each weighing 127 metric tons. Each block begins and ends with a layer of vertical extrusions, necessary in order to support the full weight of the horizontal extrusions after they are filled.

The first block will be glued to a bookend at the far North end of the detector Hall. Subsequent blocks will be attached to the previously erected block. There will be a 1 cm expansion gap between adjacent blocks. The expansion gaps are required to allow for expansion of the extrusions when they are filled with scintillator and are described in more detail below. Expansion gaps between adjacent blocks are formed by gluing 1 cm thick by 30 cm wide by 15.7 m long PVC spacers between the blocks at the top and in the middle. The spacer block thicknesses may be adjusted to maintain a vertical detector face as the assembly progresses.

The extrusion modules will handled using vacuum lifting fixtures attached to an overhead crane. Each horizontal extrusion module weighs 274 kg and the vertical extrusion modules each weigh 405 kg. The glue will be applied to each module using an automatic glue machine running on a computer-controlled crane system. This equipment includes a system of rollers to press each module accurately into position and to spread the glue out evenly. The requirements for the NOνA structural adhesive are described in [1] and the requirements for the glue machine are described in [2].

The planes will be assembled horizontally on the same device that will be used to raise them to the vertical position and attach them to the previously erected block. The device is known as the "block raiser" and looks like a giant fork-lift with 24 tines. The block raiser is shown in the horizontal position in Figure16.1 and in the vertical position in Figure 16.2. The requirements for the block raiser can be found in [3]. The bottom end of the vertical extrusions in each block will be pushed up flush and glued to a structural base plate or pallet spanning the entire length and width of each block. The tines of the block raiser will support the pallet as the block is rotated from horizontal to vertical. Additionally, the block will be secured to the block raiser by pulling a vacuum through holes in the block raiser's surface plate.

The block raiser is stationed as close as possible to the last erected block. Elevated platforms surrounding the block raiser will be required during the plane assembly process. Once a 31-plane block has been fully assembled and is ready for installation, the block raiser moves the block along rails in the Detector Hall floor to the end of the detector. The block raiser then rotates the block from horizontal to vertical, aligns the block and sets it in place. Once in position, the block raiser will apply a uniform horizontal force of approximately 1 psi to the spacer blocks to spread the adhesive and to provide a clamping force while the adhesive cures. When the block raiser is disengaged a temporary brace, supported from the building ceiling truss, will be attached to the last installed block to provide additional support until the next block is attached.

It takes nearly one full week to build a 31-plane block, working two 8-hour shifts, 5 days per week [4]. Completed blocks will be raised on Monday morning and on Monday afternoon work will commence on assembling the next block, which should be completed by the end of the second shift on Friday. If block assembly falls behind, time can be made up on the weekend.

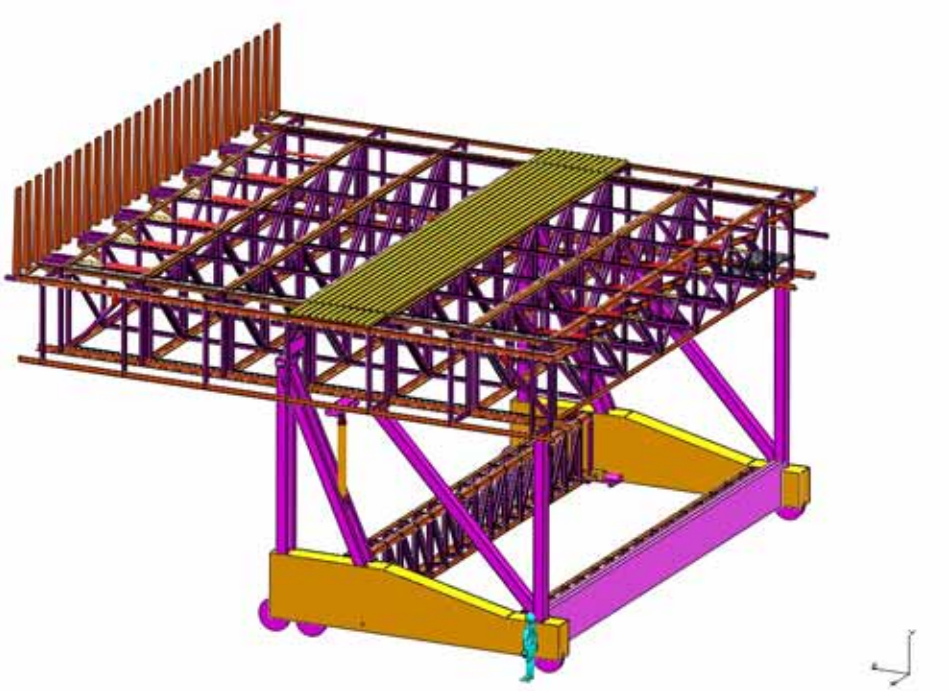

Fig. 16.1: The NOvA block raiser in its horizontal position. The block raiser is used in this position to assemble extrusion modules into alternating horizontal and vertical planes forming a 31-plane block.

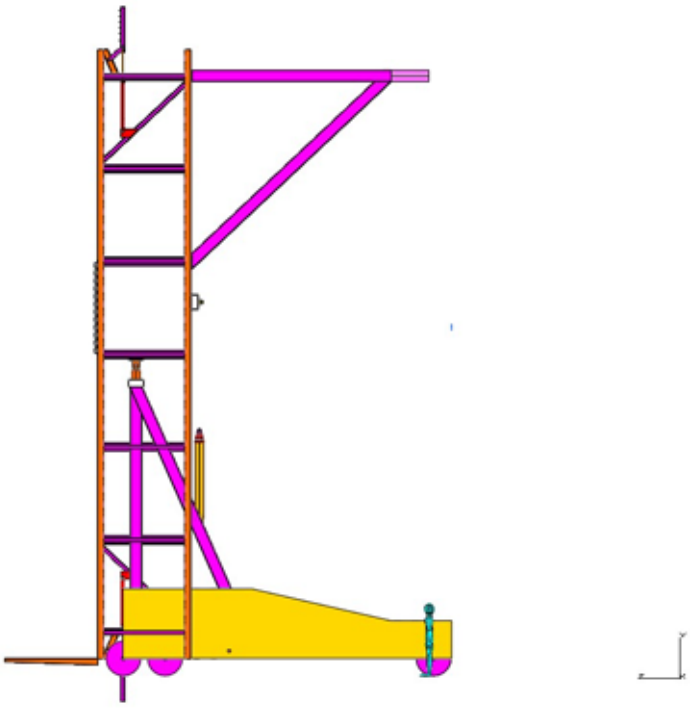

Fig. 16.2: The NOvA block raiser in its vertical position. The tines on the bottom left side of the figure support the block.

While new blocks are being assembled the erected blocks must be outfitted with front end electronics boxes and their associated infrastructure. Each extrusion module will have a front-end electronics box attached to the fiber manifold. Each front end electronics box requires chilled water, low voltage, high voltage, dry gas and a connection to the data acquisition system. These services will be distributed throughout the Far Detector Hall and will be connected to individual front end electronics boxes after the block has been erected. The vertical extrusion modules are all read out at the top of the detector. The readout for the horizontal extrusion modules alternates sides. One horizontal plane has all readouts on the left side of the detector and the next horizontal plane has its readouts on the right side of the detector. The alternating readout of the horizontal layers gives an additional handle on the horizontal track trajectory and aids in pattern recognition.

16.2 Filling the Detector With Liquid Scintillator

The detector holds 21,882 tons (about 6.8 million gallons) of liquid scintillator. To match the overall assembly time at the far site, the detector will be filled in 18 months (730 8-hour shifts), requiring a fill rate of 19 gal (72 liters) per minute. Time must be allowed for the liquid level to equalize between the 32 cells in a module. This requires the fill rate to be 3 liters/minute or less for a single module, so 24 modules (or 2 planes of the detector) must be filled simultaneously.

We will use an automated filling machine to fill 12 modules at once, metering the liquid mass output and fill rate in each module. The system will shut off the flow when the desired liquid level is reached or if any unusual situation occurs. The filling machine receives liquid scintillator from a pipeline installed along the building catwalks.

Each filling machine takes about 6.0 hours to fill 12 modules; so 3 machines can comfortably fill the entire detector in 730 shifts. While the filling machines are operating, there is time to test the quality and purity of the scintillator to be used in the next set of fills.

Pre-mixed liquid scintillator will be delivered to the detector site in standard 6341 gallon ISO tankers. We will use 93,150 gallons of scintillator mix a week, requiring 3 ISO tanks per workday. In-line quality assurance will be used at both the mixing plant and the receiving site. A one to two week buffer of ISO tankers will be maintained at the Far Detector site, allowing adequate time to verify product quality before injecting the scintillator into the distribution system.

16.3 Structural Issues

The NOvA far detector is a unique structure that is constructed entirely from alternating layers of vertical and horizontal PVC extrusion modules that are connected together only by an adhesive between layers. The surfaces of the extrusion modules that are glued together are roughed-up to improve adhesion when glued. The selected design consists of 31 planes of PVC extrusion modules (a block) being assembled and adhered together in the horizontal position on the block raiser and then lifted into the vertical position. The 31-plane blocks are stable against buckling and completely self-supporting after they are installed in the detector.

Critical to the success of this design is the strength of the PVC and the adhesive joint between extrusions. The PVC must act, not only as the main structural element of the detector, but also as a highly reflective surface to maximize the collection of light. As a result of the reflectivity requirement on the PVC, a commercial PVC mixture that is commonly available most likely will not work for the experiment. Therefore, the structural analysis on the detector has progressed without a complete knowledge of the type of PVC that would be used. Certain assumptions have been used on the acceptable level of stress that would minimize creep affects and the modulus of elasticity that should be used over the life of the experiment.

The following sections describe the considerable effort invested to understand our composite detector structure. The structure is designed to be mechanically stable for the lifetime

of the experiment and allows the completed planes of the detector to be filled with liquid scintillator and operated while the remaining planes are still being installed. The design process includes testing sample portions of the structure to validate the engineering calculations.

Rigid PVC is an inexpensive, high-strength, readily available material. It has a high glass transition temperature of 80° C and industrial extruders find it easy to work with. RPVC creeps less than plasticized PVC but more than steel. NOνA will use 8123 tons of RPVC, which represents less than one day of U.S. production capacity.

The material properties of Rigid PVC strongly impact the NOνA mechanical design. RPVC is a plastic and plastics under stress can creep to destruction. An example of a stress vs. strain curve is shown in Figure 16.3 for an RPVC sample loaded with 15% titanium dioxide. The titanium dioxide is required to maximize the reflectivity of the extrusions. The material is linearly elastic up to 2000 psi. Beyond that, the material is still elastic, but non-linear. At some point the material may become plastic and it flows without additional stress. Details regarding this plot can be found in Chapter 11. The rounded corner design for the extrusion cells, shown in Figure 16.4 has been selected specifically to minimize the stress seen in the plastic when it is fully loaded with liquid scintillator. This design maintains the stress below 750 psi everywhere in the cell and well within the linear region of the plot in Figure 16.3. Table 16.1 lists the other mechanical property requirements for the NOνA PVC. These requirements are discussed in detail in [5].

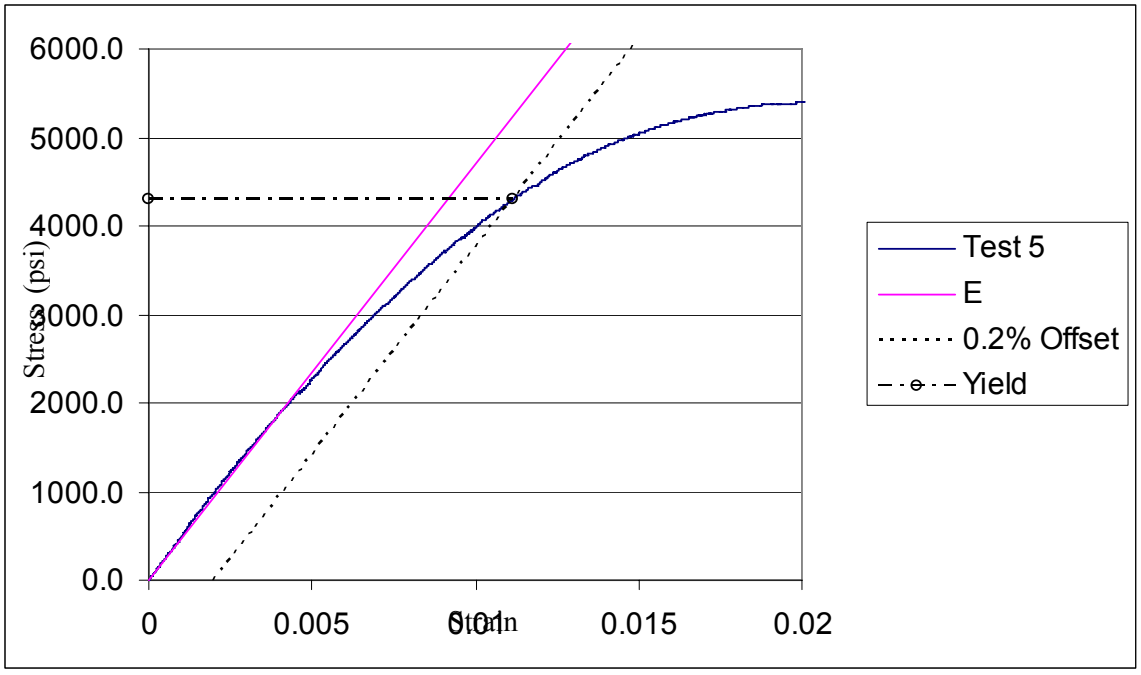

Fig. 16.3: Plot of stress (psi) versus strain for the NOνA baseline sample of rigid PVC containing 15% titanium dioxide.

Fig. 16.4: Cell cross section for the NOνA RPVC extrusions. The rounded corner design minimizes the stress in the extrusion modules when they are filled with liquid scintillator and also eliminates sharp corners where fiber light collection might be poor.

Material Property	Value	Test Method
Modulus of Elasticity	450,000 psi	ASTM D638
0.2 % Offset Yield	4000 psi	ASTM D638
Ultimate tensile Stress	5500 psi	ASTM D638
Notched Izod Impact Test	1 ft-lb/in	ASTM D256
Creep Modulus	360,000 psi after 20 years	ASTM D2990

Table 15.1: Minimum Specification for mechanical properties of the NOνA RPVC compound.

16.4 Structural Analysis

The weight of the liquid scintillator in the vertical extrusion modules is transferred to the floor by the hydraulic pressure on their base plates. Within one extrusion module, all 32 cells are hydraulically connected to allow the flow of liquid scintillator and displaced air during filling. Adjacent extrusion modules are not hydraulically connected to one another. The 15.7-m high vertical extrusion modules have a hydrostatic pressure of 19.2 psi at the bottom. The horizontal extrusion modules are only 1.3 m high and have maximum pressures of only 1.6 psi. Although the maximum hydrostatic pressure in each horizontal cell is small, the lower horizontal extrusion modules cannot support the load of the filled modules above them. For this reason the weight of the horizontal extrusions is supported by the adjacent vertical extrusions on each side. In the 31-plane block structure, horizontal extrusion modules will always be supported by vertical modules on both sides.

Each vertical extrusion will swell during filling by 2 to 5 mils near the bottom, where the hydrostatic pressure is highest, due to bowing of the outer walls and stretching of the webs. Finite element analysis (FEA) calculations show that friction will prevent the bottom plates of the vertical extrusions from sliding on the floor [6], so stresses will build up during filling. Figure 15.5 shows how this affects a stack of planes. Our FEA has determined that the local stresses that result in the RPVC will exceed our design stress if more than 80 planes are assembled in one block [6]. We therefore plan to use 31-plane blocks separated by expansion gaps to limit the buildup of hydraulic stress during filling.

The structural analysis of the NOνA detector began with an examination of individual PVC extrusions. The cell dimensions used for the NOνA PVC extrusions have been optimized for signal efficiency and background rejection using the simulation studies described in Chapter 12 of the NOνA Proposal [7]. The detector optimizes for channel count and performance with cells that have an interior cross section of 3.87 cm by 6.0 cm along the beam direction. We used FEA calculations to determine the extrusion wall thicknesses that would be required for the optimized cell geometry to provide mechanical stability of the far-detector structure at all stages of the detector construction and during filling with liquid scintillator. The effects of long-term creep in the RPVC material were also taken into account.

The selected alternative for the structure of the horizontal extrusions is to have a 3 mm thick outer wall and 2 mm thick inner webs with an interior cross section of 3.87 cm by 6.0 cm along the beam direction. For the vertical extrusions, the thickness of the material has been increased to provide additional buckling safety factor and to reduce the adhesive stresses. The vertical extrusions have been designed with 4.5 mm thick outer walls and 3 mm thick inner webs with an interior cross section of 3.76 cm by 5.7 cm along the beam direction.

Stress on the adhesive at the interface between the layers of horizontal and vertical extrusion modules is induced by several factors including the weight of the horizontal extrusions, the bending deformation of vertical extrusions due to the hydrostatic pressure and the resulting relative displacement at the interface. FEA calculations show that the maximum deflection occurs about 1 m off the floor and is about 23.3 mils along the beam direction, as shown in Figure 16.5. The maximum stress on the cell walls, shown in Figure 15.6, is calculated to be < 700 psi and occurs about 10 cm off the floor. The maximum stress on the adhesive between the horizontal and vertical extrusion modules in this configuration is 170 psi close to the floor and goes down to about 125 psi above 10" from the floor.

The FEA calculations show that the 31-plane blocks do not buckle under their own weight. Figure 16.7 shows that a 31-plane block, when free standing, has a safety factor of 5.18 against buckling. This safety factor applies to each block individually and demonstrates that a collective failure, where all blocks would buckle together, is extremely unlikely. For additional stability, successive 31-plane blocks will be connected along their top edges using the PVC spacer blocks described earlier. This further increases the buckling safety factor.

The FEA calculations indicate that there is no benefit to be seen by increasing the wall thickness of the horizontal extrusions to match the vertical extrusions. This is likely due to the fact that increasing the stiffness of the horizontal extrusions adds additional weight but does not reduce the relative displacement occurring at the interface [8].

The values that result from the FEA studies described above all represent improvements over the state of the mechanical design described in the NOνA Proposal [7]. Optimizing the geometry of the PVC extrusion to withstand the 19 psi of hydrostatic pressure within the detector is a fairly straightforward analysis. However, once these extrusions are bonded together to form a monolithic structure the challenge of the structural analysis is significantly magnified. The buckling/stress/deflection analyses of the assembled detector depend on how the adhesive bond is modeled. This makes it important to benchmark the engineering calculations with buckling, stress and deflection measurements using prototype structures assembled from NOνA PVC extrusions. This is one of the most important goals of the NOνA prototype detector program.

The PVC extrusion modules that comprise the NOνA Far Detector are held together using only adhesive, so it is important to find a strong and reliable adhesive that meets our mechanical requirements, has a pot life consistent with the needs of the mechanical assembly process and is environmentally safe for use in large quantities in an occupied, enclosed hall. Our selected adhesive is 3M 2216 epoxy. It is a two-part epoxy with shear strength of about 400 psi when used on PVC with untreated surfaces. The shear strength increases to nearly 1000 psi when the PVC surfaces are roughed-up with sandpaper. The maximum stress on the adhesive that we determine from our FEA analysis is 170 psi, so 3M 2216 epoxy gives us a good safety factor when the PVC surfaces are sanded.

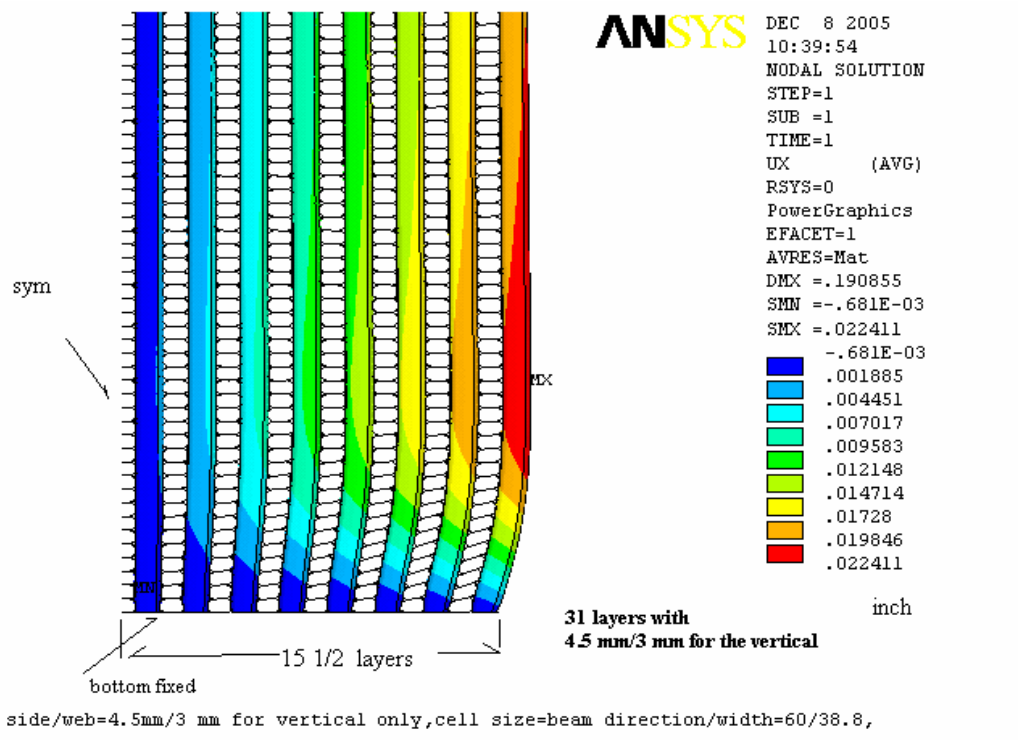

Fig. 16.5: The displacement along the beamline direction after a 31-plane block is filled with liquid scintillator. Only the bottom 3 meters of the full 15.7 meter height is shown. The displacement highly exaggerated for visual purposes. Only 15 ½ planes are shown since the analysis assumes a symmetry plane in the center of the 31-plane block. The maximum deformation, of about 23.3 mils, occurs about 1 m off the floor.

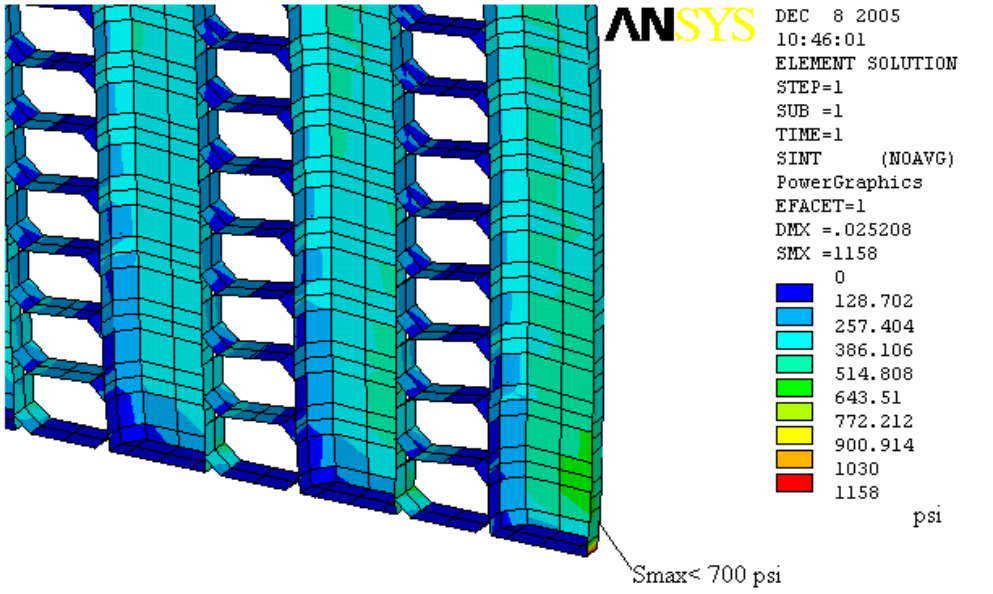

Fig. 16.6: The shear stress in the cells of a 31-plane block filled with liquid scintillator. The maximum stress is less than 700 psi and occurs about 10 cm off the floor.

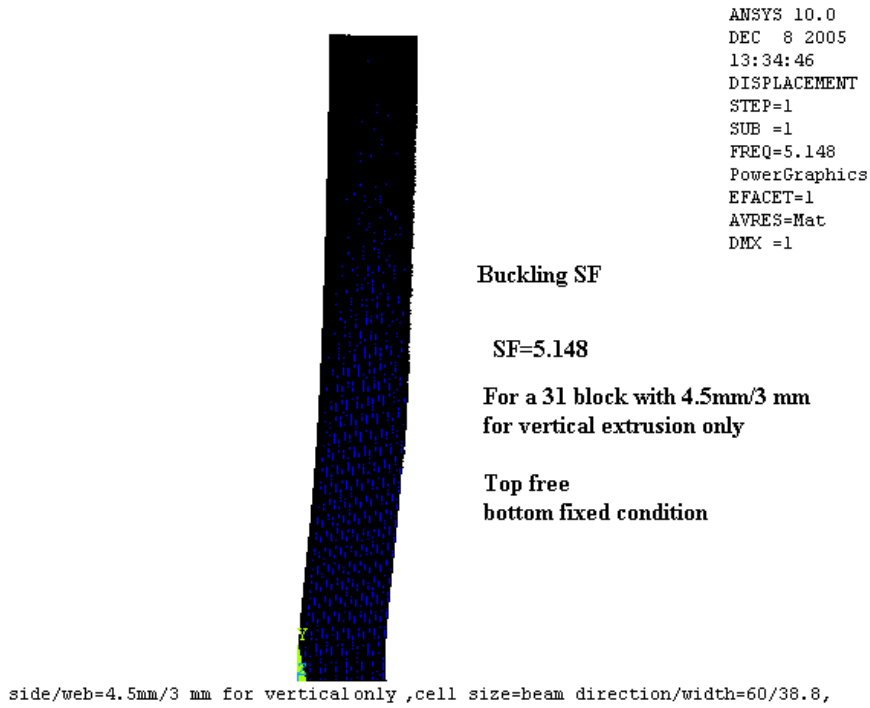

Figure 15.7: FEA calculation of the buckling stability of a 31-plane block results in a safety factor of 5.148.

16.5 Alternatives Considered

The original assembly scheme for the Far Detector, described in some detail in the NOνA Proposal [7], was to assemble sets of 8 alternating planes into sub-blocks and to use the block raiser to erect the 8-plane sub-blocks and attach them to the previously erected sub-block. Four sub-blocks formed a 32-plane block and spacer blocks connected the blocks across an expansion gap. There were a number of problems associated with this scheme. One problem was associated with erecting the second 8-plane sub-block after an expansion gap. The spacer blocks connecting the 32-plane blocks across the expansion gap cover a very small fraction of the surface area. Pushing the second 8-plane sub-block up against the first 8-plane sub-block would be difficult because the majority of the surface area of the first 8-plane sub-block is unsupported in the expansion gap. In addition, the safety factor against buckling for the 8-plane sub-blocks, while adequate, is much smaller than for an entire block. We have therefore elected to construct entire blocks in the horizontal position and then raise the entire block to the vertical position.

The original assembly scheme was to build 32-plane blocks. Constructing blocks from an even number of planes always results in a plane of horizontal modules supported by vertical modules on only one side. A single interface for supporting a horizontal plane places too much stress on the adhesive. This concern motivated the move to 31-plane blocks such that every horizontal plane is captured on both sides by a vertical plane. This results in more vertical than horizontal planes in the far detector, but there is no noticeable impact on event reconstruction.

Various block assembly schemes have been considered and discarded. The original block assembly scheme included two assembly tables and a block raiser. This was modified to a scheme with one assembly table and one block raiser. Both schemes involved the difficult task of

moving the large assembled planes from assembly table to block raiser. In addition, the assembly tables are expensive objects that were required to be mobile and consumed considerable real estate in the Far Detector Hall. The logistics for moving the block raiser and assembly table was complicated. For these reasons, assembly tables are no longer being considered. The 31-plane blocks will be fully assembled on the same device that will also lift them into place, the block raiser.

16.6 Design Optimization

As discussed in the previous sections, we have optimized the PVC extrusions, the assembly of 31-plane blocks, the adhesive used to bond the planes together, and the filling of the detector with liquid scintillator .

16.7 Quality Assurance

Quality Assurance activities for the Far Detector include the checkout of detector components as they are delivered, block assembly, block erection, scintillator filling, installation of readout hardware and commissioning of the detector.

Experts from other Level 2 tasks will develop and document procedures for verifying that delivered components, e.g., modules and readout hardware, have not been damaged in transit. They will also train assembly crewmembers to perform these tests, which will eventually become routine. WBS 2.9 engineers will develop and document procedures for testing critical commercial products, for example the block assembly adhesive, to verify that it meets specifications. In addition, they will develop and document procedures for applying and testing adhesive properties during the block assembly process itself to ensure that the expected structural properties and overall mechanical stability of the detector are achieved.

The Far Detector assembly crew will perform routine testing and maintenance of critical equipment, e.g., the block raiser, adhesive dispenser and moving equipment, to ensure that they are operating properly. The crew will develop and document operating procedures for this equipment and ensure that operators are properly trained in its use.

PVC modules are assembled and fully tested at remote module factories before the completed modules are shipped to the Far Detector Hall. The modules are inspected at the Far Detector site to ensure that they have not been damaged in transport. The leak test described in Chapter 12 will be repeated at the Far detector Hall before modules are assembled into planes to ensure that there will be no leaks. Filling the extrusion modules with liquid scintillator also falls under the responsibility of the Far Detector Assembly WBS, as does the responsibility for verifying that the modules are not leaking during filling. The crew will ensure that the liquid scintillator passes tests for attenuation length and light output before it is put into the detector, and will also maintain a database that records the origin and history of the scintillator in every module. In the unlikely event that a module is found to leak while it is being filled, the filling will immediately stop. The module will be examined and a decision will be made to repair the module in-situ or to leave the module unfilled.

Alignment fixtures built into the block raiser assembly surface will ensure the accurate positioning of extrusion modules within each block during assembly. This will ensure that the weight of each block is uniformly supported on the bottoms ends of the vertical modules and also that the block is properly aligned to its neighbors and will fit within the available space. A positioning accuracy of about 1 cm is expected to be adequate to meet both of these requirements. Transverse alignment of cells is not critical for the physics performance of the Far Detector, which is essentially a tracking calorimeter. The transverse cell size is ~4 cm, so the required accuracy is about 4 cm/$\sqrt{12}$, or again about 1 cm. Multiple scattering arguments and the transverse size of the electron showers that propagate through the detector lead to similar conclusions. The plane assembly process will work to achieve this accuracy over the full 15.7 m

length. Tooling, fixtures and procedures will be developed to achieve this goal. The same scale of accuracy is required between adjacent 31-plane blocks. The block raiser is being designed with this same requirement. Care will also be taken to ensure that the 31-plane blocks are erected square with a vertical detector face. The thickness of the spacers between 31-plane blocks can be easily adjusted to accomplish this.

Readout system cables, power distribution and water lines for cooling the Far Detector electronics will be installed by the Far Detector installation team, who will also be responsible for ensuring that they operate properly and that water lines do not leak. Detailed procedures will be written once the design for the readout system is more mature. The installation team will also be responsible for making the detector light tight and for initial checkout of module readout hardware, after being trained by WBS 2.6 engineers.

16.8 ES&H

The detector is composed of rigid PVC extrusions that require explicit handling procedures due to the extrusions properties, size and weight.

Large quantities of adhesive are used during detector assembly that could create a hazardous atmosphere inside the Far Detector Hall. The adhesive is still undergoing testing and application procedures are still being developed. Once the adhesive choice is stable and the application methods understood the means to mitigate a potential hazardous atmosphere can be developed.

Liquid scintillator of the type to be used by NOνA is commonly used in laboratory settings and can be used safely by following a few precautions. Chemically impervious gloves must be worn at all times when working with the scintillator. In addition, the workspace must be well ventilated and no open flames may be present.

16.9 Risks

The NOνA Far Detector is unique in its composition and scale, and many of the assembly tasks are beyond our direct experience. Lack of relevant experience at this size and scale presents technical, cost and schedule risks that can only be mitigated by acquiring relevant experience. We are in the process of acquiring 16 cell extrusions with the NOνA cell geometry. Many of these extrusions will be cut to our full 15.7 m length and will be used for realistic time and motion studies. Full length extrusions will be used to benchmark our extrusion module fabrication procedures and our procedures for assembling extrusion modules into planes. We will also use full length extrusions to build a full-height, partial-width, 31-plane prototype that will be raised to the vertical position. A full-height, full-width, multi-plane prototype will also be constructed to optimize block assembly procedures and to measure manpower and time requirements. These studies will help us to understand the structural and handling details with appropriately sized objects and allow us to verify requirements for the block raiser.

16.10 Value Management

Our selected adhesive alternative is 3M 2216 epoxy. While it provides the shear strength we require on sanded surfaces and meets all other NOνA requirements, it does appear to be more brittle than we would like. We are working with 3M to develop a formulation that is more ductile and we continue to look at other alternatives.

Our plans for distributing epoxy during plane assembly and block installation are still conceptual and depend on the detailed properties of the adhesive. The glue machine and gluing procedures will be optimized once we have optimized the adhesive.

The procedure for distributing liquid scintillator from the tanker trucks into the Far Detector Hall and into the extrusions requires further optimization. QA procedures for the liquid

scintillator are paramount and must be seamlessly integrated into the storage and distribution network. The designs of the automated filling machines for dispensing liquid scintillator into the extrusion modules have yet to be finalized.

Chapter 16 References

[1] T. Chase et al, "Requirements for machines and fixtures to construct extrusion modules in the module factories," NOνA-doc-183, November 2005.

[1] V. Guarino, "Requirements for the NOνA structural adhesive," NOνA-doc-145, October 2005.

[2] V. Guarino, "Requirements for the NOνA module assembly glue machine", NOνA-doc-144, October 2005.

[3] H. Jostlein and Dave Pushka, "NOνA block raiser Technical Requirements," NOνA-doc-113, October 2005.

[4] W. Miller, "Alternate Installation Schedules, 31-plane Installation for the Far Detector, Only Block Raiser," NOνA-doc-594, February 2006.

[5] A. Lee, V. Guarino, J. Grudzinski , H. Jostlein , "Summary of the Structural Analysis and Design of the NOνA Detector" NOνA-doc-495, January 24, 2006.

[6] A. Lee, "The effect of friction force for a 40-plane block - 1," NOνA-doc-367, November 2004; A. Lee, "The effect of friction force for a 40-plane block - 2," NOνA-doc-368, November 2004; A. Lee, "The effect of friction force for a 40-plane block - 3," NOνA-doc-369, December 2004.

[7] D. Ayres et al., NOνA: Proposal to Build a 30 Kiloton Off-Axis Detector to Study $\nu_\mu \rightarrow \nu_e$ Oscillations in the NuMI Beamline, March, 2005, hep-ex/0503053.

[8] A. Lee, "31 Planes with 4.5/3 mm Wall Thickness For a Vertical Extrusion Only," NOnA-doc-278, December 9, 2005.

[9] Borexino Safety Handbook, August 2002.

17. ES&H Overview

17.1 Introduction

Environment, Safety, and Health issues are discussed in Chapters 7 through 16 for each of the NOνA Level 2 subsystems. Please consult the following sections of this Conceptual Design Report for those ES&H evaluations:

Chapter 7, section 7.6
Chapter 8, section 8.6
Chapter 9, section 9.6
Chapter 10, section 10.6
Chapter 11, section 11.6
Chapter 12, section 12.6
Chapter 13, section 13.7
Chapter 14, section 14.6
Chapter 15, section 15.7, and
Chapter 16, section 16.8

In addition, Chapter 5, section 5.6 explicitly includes ES&H issues as one of four technical risk factors in the technical risk vs. cost risk analysis presented there.

The ES&H issues described in those sections are typically ones unique to the NOνA detector. While these are important, we wish to stress in this section that the more standard everyday ES&H questions are clearly in focus for this project. The draft NOνA Project Management Plan [1] has a section on Integrated Safety Management which describes how the NOνA Project ES&H policies fit within the Fermilab ES&H program.

17.2 Preliminary Hazard Assessment Documentation

The NOνA Preliminary Hazard Assessment [2] is a complete assessment of NOνA hazards. The object of the document is to detail all the hazards and not just those unique to the NOνA detector.

The Preliminary Hazard Assessment divides the project into nine separate zones: 6 zones in the Ash River building, and 3 zones at Fermilab (MINOS Surface Building, Near Detector Tunnel, and the Liquid Scintillator Blending Site). The analysis contains a 25 page spreadsheet listing all the identified hazards in each zone along with a risk-based priority model score for each hazard. Passive and active mitigation measures are listed for each hazard.

The Preliminary Hazard Assessment also considers four potential worst case accident scenarios and the mitigation strategies for each scenario.

The specific hazards present during the construction phase and the specific hazards present during the operational phase are discussed separately in detail. Operational readiness requirements are also discussed in this document.

17.3 Strategy for NEPA documentation

17.3.1 Environmental Assessment

We expect an Environmental Assessment (EA) will be required for NOνA, consisting of one part for activities at Fermilab and a second part for activities in the State of Minnesota. The elements of these two distinct activities are outlined in the next sections. A Project Information

Form has been sent by the NOνA Project Office to the Fermilab ES&H Section. The next step is for the Fermilab ES&H Section to transmit an Environmental Evaluation Notification Form (EENF) to the DOE Fermi Area Office.

17.3.2 Environmental Assessment at Fermilab

A portion of the EA must cover the NOνA work anticipated on the Fermilab site. This would include construction and operation of the NOνA Integration Near Detector Prototype in the MINOS surface building, the construction and operation of the NOνA Near Detector in the MINOS access tunnel underground at Fermilab, and the construction and operation of a scintillator blending area at Fermilab. The Project Information Form discussed above is the beginning point for this work.

17.3.3 Environmental Assessment Worksheets for the State of Minnesota

Within the State of Minnesota, environmental oversight falls to the Environmental Quality Board (EQB). The standard route for a project is for a Responsible Government Unit (RGU) within the state to forward an Environmental Assessment Worksheet (EAW) to the EQB. Such an EAW can indicate that a full Environmental Impact Statement (EIS) is required or maintain that the RGU is submitting a discretionary EAW which will not require an EIS. The Minnesota Pollution Control Agency has advised that a discretionary EAW is the logical course (see Appendix A). In either case, the EQB publishes the EAW for a public comment period, and the RGU makes a decision on the need for an EIS based on the EAW, on comments received during the 30-day period, and on responses to those comments. A guide [3] to the Minnesota EAW process is available.

Likely candidates for the RGU for NOνA are the Minnesota Department of Natural Resources, St. Louis County, the University of Minnesota, or the EQB itself. The NOνA Project has prepared draft EAWs for the Ash River [4] and Orr-Buyck [5] sites using the Minnesota environmental consulting firm Short Elliot Hendrickson Inc.

Under the Federal NEPA regulations, Federal government agencies can, and are strongly encouraged by the Council on Environmental Quality, to designate non-Federal agencies as 'Cooperating Agencies' in implementing the procedural requirements of NEPA. It is anticipated that DOE as the lead Federal Agency can designate the State of Minnesota RGU as a 'Cooperating Agency' through a request to participate in the NEPA process. The Cooperating Agency then has the authority given this designation under 40 CFR 1501.6. The DOE can then use the state EAW and proposals of the Cooperating Agency to the maximum extent possible consistent with their responsibilities as the lead agency. The Minnesota EAW Finding of Fact could be used in part to produce a Finding of No Significant Impact (FONSI) for NOνA by DOE Chicago Headquarters. This procedure was used for the MINOS experiment located in Soudan cavern in Minnesota.

Chapter 17 References

[1] See Chapter 14, “Integrated Safety Management”, in the draft NOνA Project Management Plan, NOνA docdb Note # 129.
[2] NOνA Hazard Analysis Document, NOνA docdb Note # 618 ,
[3] “EAW Guidelines”, Minnesota Environmental Quality Board, http://www.eqb.state.mn.us
[4] Ash River Environmental Assessment Worksheet, NOνA docdb Note # 205
[5] Orr-Buyck Environmental Assessment Worksheet, NOνA docdb Note # 614.

18. Quality Assurance Overview

18.1 Introduction

Quality Assurance and Quality Control issues are discussed in Chapters 7 through 16 for the Level 2 subsystems. Please consult the following sections of this Conceptual Design Report for those QA / QC evaluations:

Chapter 7, section 7.5
Chapter 8, section 8.5
Chapter 9, section 9.5
Chapter 10, section 10.5
Chapter 11, section 11.5
Chapter 12, section 12.5
Chapter 13, section 13.6
Chapter 14, section 14.5
Chapter 15, section 15.6, and
Chapter 16, section 16.7

The greatest challenge to NOνA in QA/QC lies in the parts of the detector that are assembled by the project from vendor procured components: the scintillator, the extrusion modules, and the Near and Far Detectors. These parts of the project require solid documented procedures for the work, testing of the output products relative to the specifications, training of personnel in the assembly procedures and testing procedures, and continued attention to detail by the entire project team. The raw materials used in the assembly process require a continuous effort by the project to insure that the materials meet the NOνA specifications.

In addition to design and construction of the NOνA device itself, QA is important within the project team for document control, for procurement efforts, and for budget activity and change control. The NOνA Project is committed to QA / QC as a line management function within the project. Every individual has a role to play in building a quality device for the science goals.

18.2 Quality Management Program

The NOνA Project Quality Management Program is contained in Appendix C of the draft NOνA Project Management Plan [1].

Chapter 18 References

[1] draft NOνA Project Management Plan, NOνA docdb Note # 129.

19. Risk Analysis

19.1 Introduction

Risk issues are discussed in Chapters 7 through 16 for each of the NOνA Level 2 subsystems. Please consult the following sections of this Conceptual Design Report for those risk evaluations:

Chapter 7, section 7.7
Chapter 8, section 8.7
Chapter 9, section 9.7
Chapter 10, section 10.6
Chapter 11, section 11.7
Chapter 12, section 12.7
Chapter 13, section 13.8
Chapter 14, section 14.7
Chapter 15, section 15.8, and
Chapter 16, section 16.9

In addition, Chapter 5, section 5.6 includes a detailed top down study of risks in the technical risk vs. cost risk analysis presented there.

19.2 NOνA Risk Management Plan

The NOνA Project has a draft Risk Management Plan [1]. A tenet of this plan is that each Level 2 manager should perform a risk analysis at WBS Level 3. This is in contrast to the top down risk study described in Chapter 5 of this Conceptual Design Report. We intend to complete this effort as the Conceptual Design moves towards a final Technical Design.

19.2.1 Application of the Risk Management Plan to an Actual Problem

The draft Risk Management Plan has already been implemented and used by the project in connection with the structural safety factor of the plane to plane adhesive used in the detector assembly WBS 2.9 [2]. This issue came to light in early December, 2005 and the NOνA Risk Management Board was convened to examine the problem and proposed mitigation strategies. The mitigation strategies [3] were explored in detail by the NOνA engineering staff during December 2005 and early January 2006. Several of the strategies did help mitigate the problem and one did not help. The NOνA Project Manager then charged a special independent Engineering Review Committee of experts from outside of NOνA to look at the adhesive structural problem and that review was held on January 11, 2006. The Engineering Review Close-Out [4] concluded that the mitigating efforts had led to a modified structure, an adhesive candidate, and an adhesive application strategy with an appropriate structural safety factor. The NOνA Risk Management Board was convened for a second time to consider the results of the independent Engineering Review and close out the risk [2]. Value management studies continue in an effort to find an even better candidate adhesive than the one considered by the Engineering Review in January 2006.

Chapter 19 References

[1] NOνA Risk Management Plan, NOνA docdb Note # 185.
[2] NOνA Risk #1 – Far Detector Assembly Adhesive Shear Stress, NOνA docdb Note # 500.

[3] V. Guarino et al., “Summary of Structural Analysis for Engineering Review”, NOνA docdb Note # 495, December 2005.
[4] R. Stanek, Chair, “Close-Out Report from the January 11, 2006 Engineering Review of the NOνA Conceptual Structure Design”, NOνA docdb Note # 496, January, 2006.

20. Safeguards and Security

20.1 Introduction

Safeguards and Security issues are discussed in several of the chapters for the Level 2 subsystems. Please consult the following sections of this Conceptual Design Report for Safeguards and Security evaluations:

Chapter 8, section 8.8
Chapter 14, section 14.8

During the R&D and construction of NOνA, the project ensures appropriate levels of protection via the facilities of the host institutions. In particular, the project falls under the umbrella of Fermilab, of Argonne National Laboratory, and of the Universities in the NOνA Collaboration for protection within the boundaries of those institutions. This includes protection against unauthorized access, theft, destruction of DOE assets, and other adverse impacts on the science, or on the ES&H for employees and the public via host institutions.

A vulnerability assessment by the NOνA project team has exposed several areas that will need additional attention:

1) Some of the Project's work will likely involve rented warehouse space off-campus near university collaborators and these areas will need NOνA Project Office attention. We anticipate the need for appropriate physical security of these spaces and attention to fire protection issues.
2) In addition a large fraction of the project's raw materials will be transported in dedicated transport loops, with ~ 1100 truckloads of scintillator components coming from vendors, being blended at Fermilab, and then transported in ~ 1100 truckloads to the Ash River site. Another ~ 800 truckloads of PVC extrusions move from the extruder vendors to the module factories and then ~ 800 truckloads of assembled modules move from the factories to the Ash River site. These 4000 separate truck trips will need appropriate security measures against theft and against contamination of the materials. Selection of quality transportation vendor(s) with solid security plans will be a key element of the NOνA safeguards and security plan. An aspect of this vulnerability includes the road conditions for the last 3.6 miles from the St. Louis County maintained road to the Ash River site. The project will have to maintain this road properly during winter to mitigate accidents.
3) The project is most vulnerable at the Ash River site since that site does not fall within a highly protected area like a national laboratory or a university campus. The fact that the building at Ash River is mostly underground and protected by a 3 meter thick overburden of rock will make most of the facility relatively secure. However, the south end of the building with its loading docks and exposed building walls will be more vulnerable. The NOνA Project expects to seek Fermilab help in planning for security of these areas and the project will have to work with the Cooperative Agreement institution which will be the owner and builder of the physical plant. Security here will have to extend to background checks on hired personnel, following the standard HR practices of Fermilab or the Cooperative Agreement institution.
4) Computer security will also be required at Ash River. The NOνA Project expects to follow Fermilab computing security policies [1] and procedures in this area since the data being logged will fall within the custody of Fermilab.

Chapter 20 References

[1] Director's Policy Manual, "Number 21.000 Revision 1, August 8,2000, Computing", http://www.fnal.gov/directorate/Policy_Manual.html

21. Stakeholder Input

21.1 Introduction

For the NOνA Project, the NOνA Collaboration is a primary stakeholder. The NOνA Project Management Plan outlines this relationship, but in fact the project and the collaboration are tightly knit. Interactions between the project management and the collaboration spokespersons are frequent and are in both directions. Of the more than fifty individuals comprising the project team, all are members of the collaboration. Collaboration meetings are focused around project reports by the Project Manager and Level 2 Managers. Input from the collaboration is sought in weekly meetings, at collaboration meetings, and in meetings of the elected Executive Committee of the collaboration. Attempts to engage additional members of the collaboration in project tasks are a constant quest.

The NOνA Project and NOνA Collaboration together are cognizant of the need for interactions with the other important stakeholders for this project. We have sought input from relevant stakeholders and have made a series of presentations [1] in various venues to engage these stakeholders in a dialogue. We expect to continue this effort throughout the life of the project.

Many of the presentations listed in the following sections have typically been given by Bill Miller and Marvin Marshak, both University of Minnesota collaborators on NOνA. Presentations in Minnesota and elsewhere given by non-University of Minnesota people are noted with the name of the individual making the presentation.

21.2 Local Clubs and Groups

- October 28, 2004: Presentation to the Hibbing Rotary Club- Lunch meeting with a 30 minute talk to a group of 40 people.
- October 29, 2004: Booth display at the Minnesota High School Science Teachers Fall Conference. Approximately 100 teachers stopped by our display.
- February 9, 2005: Presentation to the Ely Rotary Club-Lunch meeting with a 45 minute tallk to about 30 people.
- March 15, 2005: Presentation to the Hibbing Breakfast Rotary Club - Breakfast meeting with a 20 minute talk for approximately 40 people.
- April 5, 2005: Presentation to the Cook Lions Club - Dinner meeting with a 60 minute talk to about 40 people.
- December 7, 2005: Presentation to Northern Minnesota Engineers in Virginia, Minnesota

21.3 Local Communities

- February 5, 2004: Town meeting in Orr, Minnesota with Tom Bakk (State Representative) with a presentation to about 30-40 people.
- July 12, 2005: Presentation to about 20 people from Breitung Township in the Breitung Town Hall at Soudan.

21.4 Local Economic Development Groups in Northern Minnesota

- February 15, 2005: Meeting with “Iron Range Resources”. This is a state agency with a regional economic development focus.
- March 16, 2005: Meeting with the “East Range Community Readiness Committee” with members from the City of Babbitt, City of Hoyt Lake, City of Aurora, City of Ely, Town of

Embarrass, City of Tower, St. Louis County Arrowhead Regional Development Commission, Babbitt-Embarrass Area Development, Conservationists with Common Sense, East Range Joint Powers Board, Ely Area Development Association, Hoyt Lakes Chamber of Commerce, Iron Range Building Trades, Izaak Walton League, NE Minnesotans for Wilderness, Range Association of Municipalities and Schools.

- June 22, 2005: A second meeting with the East Range Community Readiness Committee at Hoyt Lakes attended by about 40 people.
- August 25, 2005: A third East Range Community Readiness Committee presentation.
- November 16, 2005: A fourth East Range Community Readiness Committee presentation at Aurora, Minnesota.

21.5 St. Louis County, Minnesota

- March 22, 2005: Presentation to the St. Louis County Commissioners.
- November 16, 2005: Presentation to six people in the St. Louis County Land Department.

21.6 The University of Minnesota

- April 7, 2005: Presentation to Tim Mulcahy, University of Minnesota VP of Research.
- October 14, 2005: Fermilab Director Pier Oddone traveled to Minneapolis to discuss NOνA with Tim Mulcahy, University of Minnesota VP of Research.
- December 12, 2005: Presentations by Steve Dixon (Level 2 NOνA Project Manager) and University of Minnesota NOνA collaborators to University of Minnesota Code Officials.

21.7 Minnesota State Government and Agencies

- March 15, 2005: Presentation to the Minnesota Department of Natural Resources (DNR) commissioner Gene Merriam and DNR Regional Director Courtland Nelson at Soudan.
- April 18, 2005: Visit to potential NOνA sites in the Ash River area with John Stegmeir and Ryan Hogan of the DNR along with representatives from Voyageurs National Park.
- April 19, 2005: A meeting with representatives from Minnesota DNR Parks & Recreation, Waters, Forestry, Fisheries, Trails and Waterways, Land and Minerals, and Ecological Services. Also attending was Craig Halla from Forest Capital Partners.

21.8 Voyageurs National Park

- October 24, 2003: Site visit in Ash River area with Barbara West, Park Superintendent of Voyageurs National Park and DNR representatives John Stegmier and Joe Rokala.
- April 18, 2005: Visit to potential NOνA sites in the Ash River area with Barbara West, Park Superintendent and Kate Miller, Deputy Park Superintendent (now Park Superintendent).

21.9 Fermi National Accelerator Laboratory

Interactions with Fermilab are documented on the NOνA website [3].

- June, 2002: NOνA sent a Letter of Intent for an Off-Axis Detector.
- December 2, 2003: NOνA sent a Progress Report to the Fermilab Physics Advisory Committee.
- December 2, 2003: NOνA Progress Report by Gary Feldman at the Physics Advisory Committee meeting.
- March 15, 2004: First NOνA Proposal sent to Fermilab
- April 2, 2004: Presentation by Gary Feldman of the proposal at the Fermilab Physics Advisory Committee meeting.

- June 7, 2004: Revised NOνA proposal sent to Fermilab
- June 20, 2004: Presentations by John Cooper and Gary Feldman of the revised proposal at the Fermilab Physics Advisory Committee Aspen meeting.
- March 21, 2005: Updated NOνA proposal sent to Fermilab.
- April, 2005: Presentations by Gary Feldman and John Cooper of the updated proposal at the Fermilab Physics Advisory Committee meeting.
- June 18, 2005: Presentation by John Cooper answering questions from the Fermilab Physics Advisory Committee at their Aspen meeting.
- July 18-20, 2005: Presentations by members of the NOνA Collaboration at a Preliminary Director's Review of the NOνA Experiment.
- February 28 – March 2, 2006: Presentations by the NOνA Project staff at a CD-1 Director's Review of the NOνA Experiment.

21.10 The High Energy Physics Community

Workshops on Off-Axis neutrino physics and NOνA are documented on the NOνA website [4]. Talks on NOνA at International conferences and workshops are documented on the NOνA website [5].

- May, 2002: Workshop on New Initiatives for the NuMI Neutrino Beam, Fermilab.
- January 24-26, 2003: First NuMI Off-Axis Experiment Workshop at Stanford, CA.
- April 25-27, 2003: Second NuMI Off-Axis Experiment Workshop at Argonne, IL.
- July 10-12, 2003: Third NuMI Off-Axis Experiment Workshop at Fermilab.
- September 11-13, 2003: Fourth NuMI Off-Axis Workshop at Fermilab.
- January 12, 2004: NuMI Off-Axis meeting at Cambridge, UK.
- February 7-8, 2004: Fifth NuMI Off-Axis Experiment Workshop at Fermilab.
- February, 2004: Talk by Roger Rusack at NOON, Tokyo [5].
- March, 2004: Talks by A. Marchionni and A. Weber at LaThuile, Italy [5].
- June, 2004: Talk by Mark Messier at Neutrino 04, Paris, France [5].
- June, 2004: members of NOνA participate in the American Physical Society's Multi-Divisional Neutrino Study in Snowmass, Colorado and at earlier meetings around the US. "The Neutrino Matrix" final report [6] summarizes the study.
- September, 2004: Talk by Peter Litchfield at NOW2004, Otranto, Italy [5].
- October 6-9, 2004: Members of NOνA participated in the Fermilab Proton Driver Workshop [7]. The final report [8] of the physics study for the Proton Driver was finished on September 12, 2005.
- April 7, 2005: Talk by Ron Ray at NNN05, Aussois, Savoie, France [5]
- May 29, 2005: Talk by Ron Ray at High Intensity Frontier 05, Workshop in Elba, Italy [5].
- June, 2005: Talk by Ken Heller at the Fermilab Users Meeting, Fermilab [5].
- June, 2005: Talks by Gary Feldman at the WIN05 Workshop, Delphi, Greece [5].
- June 21, 2005: Talks by Rob Plunkett and Jeff Nelson at NuFact05, Frascati, Italy [5].

21.11 The Department of Energy

Interactions with the Department of Energy are documented on the NOνA website [3].

- August 24, 2004: Briefing by Gary Feldman and John Cooper on NOνA for OHEP Associate Director Robin Stafin and staff at DOE Germantown. NOνA collaboration members Doug Michael, Stan Wojcicki, and Stephen Parke participated.
- May 16, 2005: NOνA presentation by Gary Feldman to the DOE EPP2010 panel.
- June 1, 2005: NOνA presentation by Gary Feldman to the DOE Neutrino Scientific Assessment Group (NuSAG) subpanel.

- July 27, 2005: Written answers to NuSAG questions.
- January 27, 2006: Briefing by John Cooper on the NOνA Project for OHEP Associate Director Robin Stafin at Fermilab.

21.9 Individual Briefings to State and Federal Government Officials

All of these briefings were done by Bill Miller and Marvin Marshak of the University of Minnesota.

- August 5, 2004: Presentation to Dr. Joel Parriott, Science Program Examiner, Executive Office of the President, Office of Management and Budget.
- May 6, 2005: Presentation to Minnesota Governor Tim Pawlenty and the Governor's party of 15 at Soudan, Minnesota.
- June 2, 2005: Presentation to Steve Bradach of Minnesota Senator Mark Dayton's Office.
- July 4, 2005: Presentation to Minnesota Congressman Jim Oberstar.

Chapter 21 References

[1] Bill Miller, Public NOνA Presentations, NOνA docdb Note # 188.
[2] Bill Miller, Site Visit to Ash River and Informational Meeting with the Minnesota Department of Natural Resources, NOνA docdb Note #168.
[3] Presentations to the Fermilab Physics Advisory Committee, to NuSAG, and to EPP2010 can be found at http://www-nova.fnal.gov/reports_page.html
[4] Information on past Off-Axis Workshops can be found at http://www-nova.fnal.gov/workshops/Workshops.html
[5] Talks at International Meetings by member of NOνA can be found at http://www-nova.fnal.gov/NOνA Talks and Presentations
[6] Final Report: The Neutrino Matrix, APS Multi-Divisional Study, http://www.aps.org/neutrino
[7] Fermilab Proton Driver Workshop, Fermilab Proton Driver Workshop
[8] Final Report on the physics study at the Proton Driver, M.G. Albrow et al., Physics at a Fermilab Proton Driver, final report, September 2005

22. Life Cycle Costs

22.1 Operating Costs

22.1.1 Operating Costs for NOνA at Ash River

The life cycle operating costs for NOνA can be estimated based on similar experimental operating costs observed for the MINOS and CDMS experiments in the Minnesota Soudan Mine [1]. We chose this example for its particular relevance to experimental costs of a high energy physics experiment operating remotely from Fermilab in the State of Minnesota.

We anticipate a smaller operating crew for NOνA than for Soudan since there is only one experiment at Ash River. The hoist charges and costs for Minnesota Department of Natural Resources personnel at Soudan for underground mine operations do not appear at Ash River.

The power consumption by NOνA at Ash River is estimated to be about 2.5 times that of the MINOS and CDMS experiments at Soudan. In addition the first estimate from the electrical power provider indicates the cost per kilowatt-hour at Ash River would be about twice that at Soudan.

We assume no leasing charge at Ash River (vs. a per sq. ft charge at the mine operated by the Minnesota Department of Natural Resources) since the Cooperative Agreement Institution takes full possession of the asset when NOνA is finished and should have no expectation of additional rental income.

The networking charges for a T1 communications line are assumed equal to the same costs at Soudan.

Additional operating costs come from facility maintenance needs and these costs have been estimated using elements of the Whitestone Building Maintenance and Repair Cost Reference [2]. This is a standard used at Fermilab to estimate maintenance costs for surface buildings and our facility at Ash River is much like a Fermilab detector hall. A composite cost model using weighted elements from "a warehouse + a light manufacturing plant + a small research laboratory" yields a yearly maintenance cost of ~ $ 2.50 per square foot for the ~ 50,000 square foot Ash River building. Table 22.1 summarizes these operating costs.

These NOνA operating costs are not part of the NOνA Project. It is assumed that the funds will come from the Fermilab operations budget when the detector begins operations. The NOνA schedule anticipates operations beginning with the first 5 kilotons of the detector part way through FY11, so a ramp up of operating funds should begin at that point.

NOνA Operating Costs at Ash River	
Item	**$K per year**
5 staff at site, no 24 x 7 coverage	400
Power costs	600
Space Lease charges	-
Phones & networking	50
Facility Maintenance @ $ 2.50 per square foot	125
Total	**1175**

Table 22.1: NOνA Operating Costs per year at Ash River.

22.1.2 Analysis of Operating Costs for Alternative Designs

The alternatives discussions in Chapter 4 are based on cost and performance analyses, so it is worth asking if a Life Cycle Cost analysis would change the conclusions in Chapter 4. This section examines the operating costs for the alternative designs.

The alternative sites (Chapter 4, section 4.2) in Minnesota (or Canada) would not have significantly reduced operating costs. The same on-site staff would be required for all locations. The facility maintenance costs would be equal at all sites. The power costs would be similar in all locations. Based on the power costs for MINOS in the Soudan Mine, the site at Peyla (which does not meet the scientific performance requirements) might have half the power costs, saving around $ 300 K per year.

The alternative detector structures (Chapter 4, section 4.5) would not have reduced operating costs. The "Vee" design alternative would have identical operating costs since it has the same number of electronics channels with the same power consumption as the recommended NOνA design. The Bathtub design alternative would likely have increased operating costs since to have an equivalent total mass it requires additional electronics channels where the two readout views do not overlap (see Figure 4.10). The International Shipping Container design would have increased operating costs since it has six times as many electronics channels in the vertical cells as there are in the recommended NOνA design. The power consumption of the container alternate would be ~ $ 1.2 M more per year than the recommended design.

All the alternative detector technologies (Chapter 4, section 4.4) have inferior performance or higher risk than the recommended NOνA design. The Low-Z Sampling Calorimeter alternate based on liquid scintillator comes closest to the recommended NOνA design performance but still would not meet the scientific performance requirements outlined in Chapter 2. Since the cost of this alternative was close to the cost of the recommended NOνA design, we have looked into the operating costs of this alternative. The 50 kiloton alternative sampling calorimeter design [3] has 540,000 channels of electronics compared to the recommended NOνA design with ~ 643,000 channels. Therefore to first order we could have expected this alternative design to consume ~15% less power, saving ~ $ 60,000 per year. This savings, integrated over a six year run, would have been more than offset by the increased cost of the 30% longer building required for this longer alternative.

In summary, we do not see any overwhelming advantage to alternative designs in an operating cost analysis.

22.2 Decontamination and Decommissioning Plan and Costs

22.2.1 Decommissioning of a Previous Experiment

The Integration Prototype Near Detector for NOνA requires ~ 31,000 gallons of scintillator. Two-thirds of this will be blended at Fermilab as part of the R&D for NOνA and serve as a test bed for the blending operation. The remaining third will be blended from ~ 4,000 gallons of St. Gobain Bicron BC-517L scintillator extracted from the NuTeV detector at Fermilab and in storage at Fermilab since 1999. NOνA plans to blend this 10% pseudocumene scintillator with mineral oil to produce 8,000 – 10,000 gallons of 4% or 5% pseudocumene scintillator for the Integration Prototype. We have tested a small quantity of this blend and find it has adequate light output for the NOνA prototype.

22.2.2 Decontamination and Decommissioning of NOνA

A conceptual decontamination and decommissioning plan [4] has been developed for NOνA. The basic plan is to remove the NOνA Detector from the Ash River building and return the empty building to the Cooperative Agreement Institution. The detector components could be

retained for use by future experiments or recycled as scrap. It is worth noting that retaining the detector components (for example, retaining the 5.7 million gallons of liquid scintillator) would require a building exactly the size of the NOνA Far Detector building. The remainder of this section assumes removal and recycling as the base plan.

The electronics and data acquisition equipment would be removed and recycled at an estimated $ 0.05 per pound.

The liquid scintillator would be removed but this requires some effort. The horizontal extrusion modules are easily emptied since the maximum pressure is only 1.5 psi and within the delta pressure range of an exterior pumping operation. The vertical extrusion modules are more difficult since the pressure at the bottom of the modules is 19.2 psi and removal cannot be accomplished with an exterior pump. Instead we imagine inserting a small diameter pump into the top of the extrusion and lowering to the bottom of the cell. Pumps with diameters of 4.2 cm exist and can lift liquids 19 meters [5]. This tiny interior pump then operates like a pump at the bottom of a deep water well and removes the scintillator. Phone conversations with used oil recyclers indicate that the 5.7 million gallons could realize $0.75 per gallon (~ $ 4 M total, less transportation to the recycler) towards the decontamination and decommissioning effort. This particular nearby recycler can only accept ~12,000 gallons per day, so the scintillator removal would take about 3 years with a crew of 2 or 3 people.

Once drained of scintillator, the PVC can be broken down into manageable sections. This is a big job requiring care to accomplish safely and would perhaps take about a year with a crew of at least 5 people. This demolition effort is about 1/3 the effort that we estimate is required to assemble the PVC. It is doubtful that the PVC can be recycled, since PVC recyclers are not interested in re-melting a product with an admixture of epoxy. The 8 kilotons of PVC may have to be disposed of as refuse waste at a cost of ~ $ 27 per ton (~ $ 200 K total).

22.2.3 Analysis of Decommissioning Costs for Alternative Designs

The alternatives discussions in Chapter 4 are based on cost and performance analyses, so it is worth asking if a Decontamination and Decommissioning (D&D) Cost analysis would change the conclusions in Chapter 4. This section examines the D&D costs for the alternative designs.

The alternative sites (Chapter 4, section 4.2) in Minnesota (or Canada) would not have reduced D&D costs. The D&D plan outlined in Section 22.2.2 for the selected NOνA design would still have to be exercised. Some sites might have a slight advantage or disadvantage to Ash River for the transportation costs of the recycled scintillator or waste refuse PVC.

The alternative detector structures (Chapter 4, section 4.5) would not have reduced D&D costs. The “Vee” design alternative would have identical D&D costs since it has the same structure and is the exact same size. The Bathtub design alternative would probably have an small advantage since removing the scintillator can take place at a few points instead of individually from each extrusion module as in the selected NOνA design. The Bathtub design still has the problem of epoxy on the PVC. The International Shipping Container design would have cheaper D&D costs since there is no epoxy in that design and the PVC could be recycled, avoiding the $ 200 K in waste refuse fees and gaining ~ $ 0.15 per pound (~$ 2.3 M, less transportation costs) in recycling income. The shipping containers themselves would be ~ 2 kilotons of steel and that steel could be recycled [6] for perhaps $ 360 per ton realizing ~ $800 K in income.

All the alternative detector technologies (Chapter 4, section 4.4) have inferior performance or higher risk than the recommended NOνA design. The Low-Z Sampling Calorimeter alternate based on liquid scintillator comes closest to the recommended NOνA design performance but still would not meet the scientific performance requirements outlined in Chapter 2. Since the cost of this alternative was slightly cheaper than the cost of the recommended NOνA design, we have looked into the D&D costs of this alternative. The 50 kiloton alternative sampling calorimeter

design [1] would contain less scintillator (~2.1 million gallons vs. 5.7 million gallons) and therefore realize a lower recycling income by some $ 2.5 M. The 50 kiloton alternative sampling calorimeter design has less PVC with no epoxy. This would be an advantage, since the PVC could be recycled for ~ $ 600 K of income. The 50 kiloton alternative sampling calorimeter contains 42 kilotons of wood particle board, and this is probably a D&D disadvantage since the wood was designed to be screwed together and would require care to disassemble for any resale. In addition, we anticipated that the wood would have been painted with intumescent fire retardant paint as a fire protection measure, and this would have limited any resale value. Burning particle board is not a particularly good option since the wood particles are held together with a urethane epoxy and the combustion fumes are an ES&H risk.

In summary, the alternative technologies hold no D&D cost advantage. The alternative structure with liquid scintillator in shipping containers would gain ground in cost on the selected NOνA design, closing the gap from being ~ 10% more expensive to being only about 7% more expensive. This decrease would be more than offset by the increased container operating costs discussed in section 22.1.2.

Our conclusion is that the estimated Life Cycle cost differences do not change our alternatives analysis.

Chapter 22 References

[1] R. Rameika, Fermilab Neutrino Department Head, private communication.
[2] Lufkin, Miller, and Turner , The Whitestone Building Maintenance and Repair Cost Reference 2005-2006, , Tenth Edition, Whitestone Research, August 2005.
[3] I. Ambats et al., March 15, 2004 NOνA Proposal, see the first entry for 2004 at http://www-nova.fnal.gov/reports_page.html
[4] K. Schuh, Preliminary NOνA Decontamination and Decommissioning Plan, NOνA docdb Note # 737.
[5] An example of a 4.2 cm diameter pump can be found at http://www.comet-pumpen.de/Produkte/pumpen/tauchpumpen2005.html, click on GEO-DUPLO-PLUS
[6] See Grede Foundries, Inc. [Scrap Steel Price History] as a typical source for scrap steel prices in the United States.

23. Cost, Schedule, and Scope Range

23.1 Project Deliverables, Test and Acceptance Criteria

23.1.1 The Far Detector Building at Ash River

The first project deliverable is an accessible experimental hall at the Ash River site. The test and acceptance criteria for the site access road and building are beneficial occupancy and completion of the final punch list of deficiencies.

23.1.2 The NOνA Far Detector

A 25 kiloton NOνA Far Detector is the second project deliverable. The NOνA Far Detector test and acceptance criteria are that a neutrino charged current event be seen within the NuMI spill gate in each 5 kiloton segment of the detector.

23.1.3 The NOνA Near Detector

A 212 ton Near Detector in the Fermilab NuMI tunnel is the third project deliverable. The NOνA Near Detector test and acceptance criterion is observation of a neutrino charged current event within the NuMI spill gate in the Near Detector fiducial volume.

23.2 Cost Range

The Total Estimated Cost (TEC) range is $ 185 M - $ 244 M. The Total Project Cost (TPC) range including R&D is $ 197 M - $ 256 M. The estimates are in Actual Year $ (AY$). The difference between TPC and TEC is R&D funding during FY2006-FY2008. The TEC includes Preliminary Engineering Design funding and Cooperative Agreement funding needed for the Far Detector experimental hall and access road.

The cost ranges assume a fifty month construction schedule for the project during FY2008 – FY2012. The best estimate for the TPC with this schedule is $ 247 M. This best estimate is near the top end of the range because it conservatively includes a contingency with a risk-based analysis for the future price of crude oil. The contingency estimate uses the 95% confidence level upper value of crude oil price projections from the Department of Energy's Energy Information Administration (EIA) combined in a Monte Carlo risk analysis using the historical prices of crude oil as input. The price of crude oil impacts the price of scintillator and PVC. The contingency also conservatively includes large estimates on assembly labor for tasks that have only conceptual time and motion studies at this time.

At the low end of the TPC range, the contingency estimates are relaxed. In the case of crude oil they are relaxed to the 95% confidence level lower value from EIA. For assembly labor the cost + contingency is relaxed to the estimate resulting from the detailed (but conceptual) minute by minute, task by task time and motion studies. These labor estimates are based on similar time and task estimates from the MINOS detector which built plastic and steel objects at half the scale of NOνA (8 meters instead of 16 meter) in a 5 kiloton device. That is, the time and motion studies are "informed" though still conceptual. The low end of the TPC range also includes estimated potential in-kind contributions from collaborators outside the U.S.

23.2.1 R&D Funding Requirements

R&D funds in the amount of $ 12 M are requested during FY2006 -2008. R&D funds in FY2006 are used to specify the package required for a design-build bid process on the Ash River building and site access road. The remaining R&D funds enable completion of an Integration

Prototype Near Detector in calendar 2007. The Integration Prototype focuses the project team on the final NOνA design choices and the resulting detector can then be used to collect test neutrino data in the NuMI beam while sitting in the existing MINOS Surface Building at Fermilab. This is discussed in Chapter 3, Section 3.4.9.

23.2.2 Cooperative Agreement Requirements

Cooperative Agreement funding is required for the Far Detector experimental hall and access road. A cooperative agreement institution will be selected by DOE via a bid process.

23.2.3 PED Funding Requirements

FY2007 PED funds in the amount of $ 10.3 M are requested to enable selection of a design-build firm for the Ash River Far Detector Building and site access roads. The design-build vendor selection occurs at the beginning of FY2007 Q2.

23.3 Scope Range

The 25 kiloton NOνA detector TPC cost estimate is near the high end of the TPC range in Section 23.2 since the project contingency estimate conservatively includes a risk-based analysis for the future price of crude oil and conservatively includes large contingencies on assembly labor for tasks that have only conceptual time and motion studies.

A Scope Range for the NOνA project has been derived assuming the detector is built to a fixed cost equal to the 25 kiloton detector TPC, but with less conservative contingencies. The unused contingency value can be translated into additional detector mass. The analysis indicates that a detector mass in the range of 25 – 34 kilotons could be built in various scenarios. The base project described in this Conceptual Design Report includes a building large enough for a 30 kiloton detector, so a 34 kiloton scenario would require an up-front decision to build enough space for 34 kilotons. The cost of such a building extension is about $ 3 M.

23.4 Schedule Range

The 25 kiloton NOνA TEC and TPC estimates are based on a 50 month construction schedule, starting at the beginning of FY2008 and continuing through FY2012 Q1. The schedule assumes major procurements for PVC extrusions, wavelength shifting fiber, and the Far Detector experimental hall will be placed as soon as the construction funds are allocated. The schedule also assumes PED funds are available for a design-build package on the Far Detector hall as requested in FY2007.

The base schedule estimate of 50 months includes a schedule float throughout the project of approximately 5 months between completion of the Ash River experimental hall and start of the detector assembly in the building. Delivery of detector components has approximately 12 months of float throughout the project leading to completion of the detector assembly at Ash River.

The Scope Range discussed in Section 23.3 impacts the Schedule Range. If 34 kilotons of detector were built, the schedule length would increase from 50 months to ~58 months. Part of the increase would be due to slower detector construction at the end of the project as the last part of the assembly task shoehorned the last detector modules into an experimental hall just big enough for 34 kilotons. In addition the schedule float in delivery of detector components would be reduced to only ~4 months. The float between beneficial occupancy of the longer building and start of assembly would also be reduced. This is a more aggressive schedule than for the 25 kiloton base estimate.

We conclude that the Schedule Range for the NOνA project is approximately 45 – 58 months.

Appendix A. WBS Dictionary for R&D

A.1 R&D WBS Dictionary at Levels 2 and 3

This section defines the WBS tasks for a NOνA R&D Project through Level 3. WBS 1.0 is for the research and development of the NOνA Near and Far Detectors and the Far Detector Hall. NOνA design and construction is covered in WBS 2.0 and that dictionary is in Chapter 6

WBS 1.1 Site and Building

This Level 2 element covers the design, planning and value management for the far detector hall as well as the site evaluation and environmental assessment.

WBS 1.1.1 Site Conditions Investigation:
This WBS element includes the investigations required to provide a comprehensive understanding of the site conditions necessary to specify design/build bid package.

WBS 1.1.2 CDR Document Revisions:
This WBS element continues the document development of the conceptual design and includes integration of building systems and materials and development of precise drawings and specifications.

WBS 1.1.3 Site Logistics:
This WBS element consists of an investigation of the site support activities that will be necessary during the construction phase of the project.

WBS 1.1.4 Management R&D Phase:
This WBS element includes the management required for planning, controlling and reporting efforts for WBS 1.1. This includes the identification and execution of value management task as well as appropriate external reviews.

WBS 1.2 Liquid Scintillator R&D

This level 2 summary element covers the development and documentation of requirements for the liquid scintillator required for both the near and far detectors. This includes various studies, simulations and measurements required to define these requirements.

WBS 1.2.1 Requirements:
This WBS element provides for development of a document detailing the experimental requirements for the liquid scintillator.

WBS 1.2.2 Scintillator Composition Studies:
This WBS element provides for scintillator composition studies. These include various light yield studies, simulations and measurements of attenuation length.

WBS 1.2.3 Accelerated Aging Studies:
This WBS task provides for accelerated aging studies and effects of various components used in the detector.

WBS 1.2.4 Scintillator Production Method Studies:
This WBS element provides for development of the plan for the scintillator production at Fermilab.

WBS 1.2.5 Development of QC Methods:
This WBS element includes the tasks required to develop methods, procedures and plans for reliable and accurate QC testing procedures for the liquid scintillator components.

WBS 1.2.6 Scintillator Transportation Studies:
This WBS element includes the tasks required to develop methods, procedures and plans for delivering the liquid scintillator components to the Fermilab blending facility.

WBS 1.2.7 Vendor Investigations:
This WBS element includes the tasks required to develop, assess, and verify the ability of vendors to produce and QC liquid scintillator to meet our specs.

WBS 1.2.8 Integration Prototype Detector Scintillator Production:
This WBS element includes the tasks necessary to blend liquid scintillator at Fermilab for the integration prototype near detector.

WBS 1.2.9 Production Scintillator Specifications:
This WBS element provides for development of the technical specifications documents for production quantities of liquid scintillator.

WBS 1.2.10 Management R&D Phase:
This WBS includes the tasks required to support and manage WBS 1.2 activities including subproject activities and management for the liquid scintillator R&D phase.

WBS 1.3 Wavelength Shifting Fiber R&D

This level 2 summary element covers the development and documentation of the requirements for procurement, QA and shipping of the wavelength shifting fiber.

WBS 1.3.1 Requirements:
This WBS element provides for development of a document detailing the experimental requirements for the wavelength shifting fiber.

WBS 1.3.2 Vendor Investigations:
This WBS element includes the tasks required to develop, assess, and verify the ability of vendors to produce and QC wavelength shifting fiber to meet our specifications.

WBS 1.3.3 WLS Fiber Optimization Studies:
This WBS task provides for studies of wavelength shifting fiber to optimize the performance for our specific application.

WBS 1.3.4 Development of QA Methods:
This WBS element provides for development of the methods and procedures for QA testing of the wavelength shifting fiber.

WBS 1.3.5 Integration Prototype Detector Fiber Production:
This WBS element provides for delivery and QA of fiber for the integration prototype near detector.

WBS 1.3.6 Production WLS Fiber Specification:
This WBS element includes the tasks required to produce the technical specification documents for procurement of production quantities of wavelength shifting fiber.

WBS 1.3.7 Management R&D Phase:
This WBS includes the tasks required to support and manage WBS 1.3 activities including subproject activities and management for the wavelength shifting fiber R&D phase.

WBS 1.4 PVC Extrusions R&D

This level 2 summary element includes studies of various PVC materials and their properties as well as the development and documentation of QA and shipping plans for the PVC extrusions.

WBS 1.4.1 Physical Properties Determination and Test Method Development:
This WBS element includes measuring the optical and mechanical properties of various PVC compounds and extrusions to compare with the NOvA specifications.

WBS 1.4.2 Raw Materials:
This WBS element includes selection of the PVC blend for prototype extrusion production.

WBS 1.4.3 Extrusions:
This WBS element identifies venders capable of producing extrusions to meet the NOvA specifications and produces extrusions for the Integration Prototype Near Detector. The task will also develop methods for assuring the quality of extruded products.

WBS 1.4.4 Shipping & Handling:
This WBS element includes tasks to develop a shipping and handling plan for delivery of extrusions.

WBS 1.4.5 Quality Assurance Hardware Modifications:
This WBS element provides for the modification of prototype QA hardware to be used for QA of preproduction extrusions.

WBS 1.4.6 Management R&D Phase:
This WBS element includes the tasks required to support and manage WBS 1.4 activities for the PVC extrusion R&D phase.

WBS 1.5 PVC Modules R&D

This level 2 summary element provides for development and documentation of the procedures for assembly of the PVC modules and the design of the fiber manifolds and endseals. Development of QA and shipping plans is also included.

WBS 1.5.1 Requirements:
This WBS element provides for development of requirements documents for module assembly, manifolds and end seals. QA requirements for the completed modules are also included.

WBS 1.5.2 End Seal R&D:
This WBS element includes the design and development of the manifolds and end seals as well as specification of QA procedures.

WBS 1.5.3 Photo Detector Interface R&D:
This WBS element includes the design and development of the photodetector interface as well specification of QA procedures.

WBS 1.5.4 Module Factory R&D:
This WBS element includes the development of assembly methods for the PVC modules as well as the design of machines, tooling and moving fixtures.

WBS 1.5.5 Quality Assurance and Quality Control Methods Development:
This WBS task provides for the development of a QA plan for PVC module production. Construction of the required testing equipment is also included.

WBS 1.5.6 Module Shipping and Storage R&D:
This WBS element provides for the development of a plan for shipping and handling of extrusion modules to the Detector sites and for managing the equipment necessary for shipping and handling.

WBS 1.5.7 Integration Prototype Detector Modules:
This WBS element provides for production of the PVC modules for the integration near detector prototype.

WBS 1.5.8 Initial Production Module Specifications:
This WBS element provides for the design and development of the initial production module specifications.

WBS 1.5.9 Initial Factory Tooling Specifications:
This WBS element provides for the design and development of the initial factory tooling specifications.

WBS 1.5.10 Management R&D Phase:
This WBS element includes the tasks required to support and manage WBS 1.5 management activities for the for PVC module subproject during the R&D phase.

WBS 1.6 Electronics R&D

This level 2 summary element includes the design, development and testing of the front end electronics and infrastructure.

WBS 1.6.1 APD Modules:
This WBS element includes development and procurement of prototype APD chips, APD carrier boards, TE coolers, optical connectors and the associated hardware that comprise the APD modules. Development of specifications for fiber alignment, power consumption, cooling and QA are also included. APD modules for the Integration Prototype Near Detector are included here.

WBS 1.6.2 Front End Board:
This WBS element includes design of the front-end boards as well as the development of testing and installation procedures. Front-end boards for the Integration Prototype Near Detector are included here.

WBS 1.6.3 Readout Infrastructure:
This WBS element includes the design and specification of the infrastructure required to support the operation of the readout electronics including low voltage, high voltage, cooling and power distribution. Infrastructure required for the Integration Prototype Near Detector is included here.

WBS 1.6.4 Management R&D Phase:
This WBS element includes the tasks required to support and manage WBS 1.6 management activities for the Electronics subproject during R&D phase.

WBS 1.7 DAQ System R&D

This level 2 summary element includes the development of specifications and design of the hardware and software necessary to acquire and record data to archival storage and to control and monitor both the Near and Far Detectors.

WBS 1.7.1 DAQ Software:
This WBS element includes the development of specifications and the design of the DAQ software. An initial system for the Integration Prototype Near Detector is included here.

WBS 1.7.2 DAQ Hardware:
This WBS element includes the development of specifications and the design of hardware for receiving signals from the FEBs, buffering and

archival of data and distribution of clock/timing signals. Hardware required for the Integration Prototype Near Detector is included here.

WBS 1.7.3 Integration:
This WBS element includes the development of specifications and requirements for integration of the DAQ hardware and software.

WBS 1.7.4 Slow Control Systems:
This WBS element includes the development of specifications and requirements for the slow control system. An initial system for the Integration Prototype Near Detector is included.

WBS 1.7.5 Management R&D:
This WBS element includes the tasks required to support and manage WBS 1.7 management activities for the DAQ System R&D phase.

WBS 1.8 Detector Assembly R&D

This level 2 summary includes R&D work to validate and optimize the mechanical designs and installation procedures for the NOvA Near and Far Detectors. This includes structural engineering calculations of the fully and partially assembled detectors, the mechanical design and prototyping of detector assembly mechanical systems and tooling, and the construction and testing of prototypes of both Near and Far Detectors. This task will select and document the baseline designs that will be used as the basis for the NOvA CDR and TDR.

WBS 1.8.1 Plane Assembly Adhesives R&D:
This WBS element includes the tasks required to choose an adhesive that is suitable for bonding the extrusion modules together for the Far and Near detector.

WBS 1.8.2 Structural Design and Validation:
This WBS element includes the tasks required to develop and optimize the structural design of the far detector.

WBS 1.8.3 Liquid Scintillator Filling and Handling R&D:
This WBS element includes the tasks required to develop techniques and semi-automatic equipment for filling the Integration Prototype, Near and Far and detector.

WBS 1.8.4 Near Detector Assembly R&D:
This WBS element includes the tasks required to develop the procedures, equipment and assembly plan for the near detector. The task also includes the design of an assembly facility and associated procedures and equipment for assembling extrusion modules. Finally, this task will design the steel-plate muon-catcher segment of the near detector, along with associated support structures and assembly equipment.

WBS 1.8.5 Integration Prototype Near Detector:
This WBS element includes the tasks required to design, fabricate and install the Integration prototype Near Detector.

WBS 1.8.6 Far Detector Assembly Engineering:
This WBS element includes the tasks required to specify and design the equipment needed to assemble and install the far detector.

WBS 1.8.7 Far Detector Installation Procedures:
This WBS element includes the tasks required to develop the far detector installation procedures, schedules and labor requirements.

WBS 1.8.8 Far Detector Prototypes:
This WBS element includes the tasks required to test and optimize the procedures and equipment designs developed under other WBS 1.8 far detector tasks. This task will lead to the final optimization of the designs of assembly tooling and materials handling equipment.

WBS 1.8.9 Management R&D Phase:
This WBS element includes the tasks required to support and manage WBS 1.8 management activities for the Detector Assembly R&D phase.

WBS 1.9 Project Management R&D

This Level 2 summary element consists of reviews, reports, site visits, local supervision, running technical board meetings, standards preparation, tracking and analysis, schedule preparation tracking and analysis and change control. It also includes procurement of relevant software and computers, the cost of running the project office and the salaries of non-scientists working on the project.

Appendix B. Minnesota Pollution Control Agency Statement on NOνA Scintillator

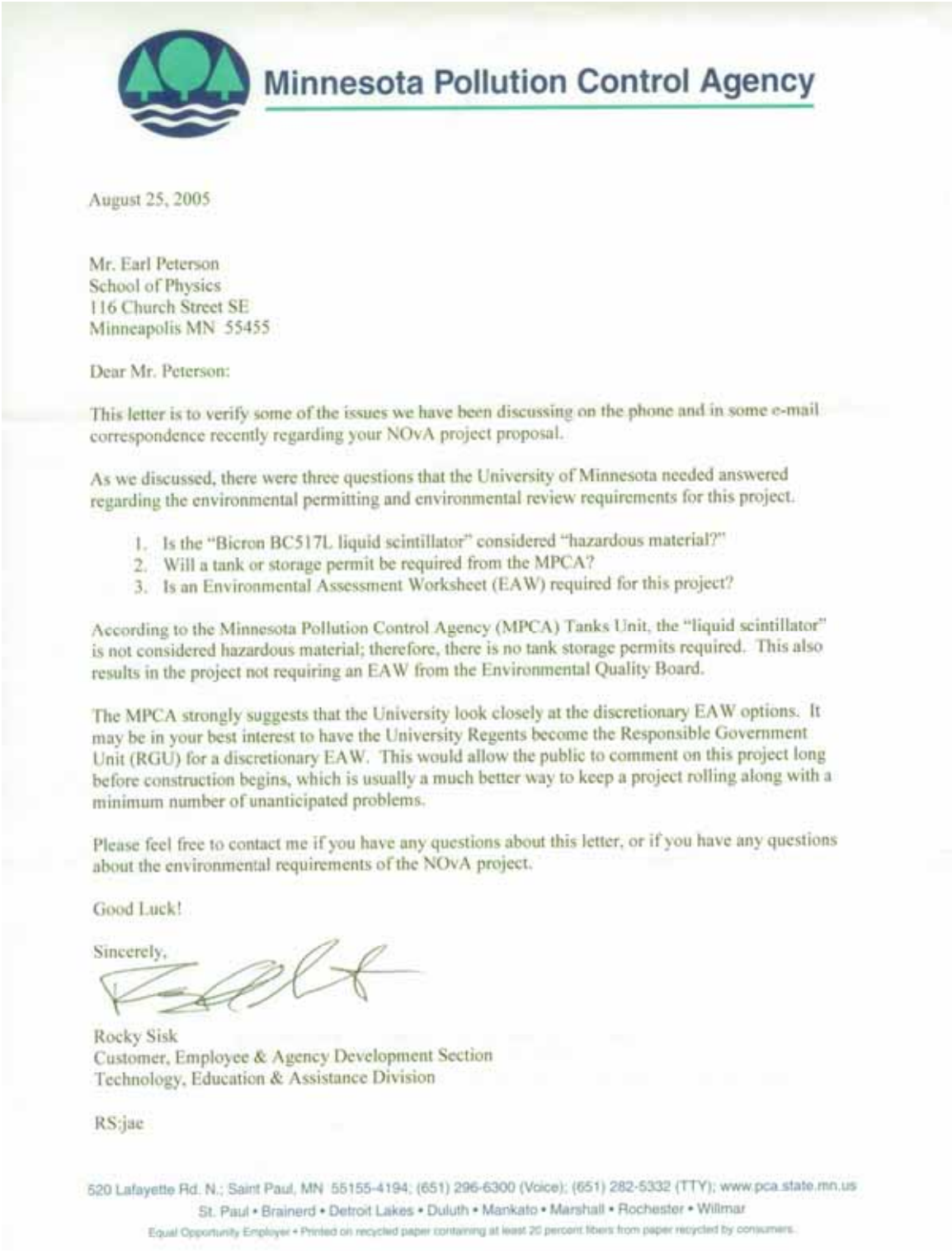

Minnesota Pollution Control Agency

August 25, 2005

Mr. Earl Peterson
School of Physics
116 Church Street SE
Minneapolis MN 55455

Dear Mr. Peterson:

This letter is to verify some of the issues we have been discussing on the phone and in some e-mail correspondence recently regarding your NOvA project proposal.

As we discussed, there were three questions that the University of Minnesota needed answered regarding the environmental permitting and environmental review requirements for this project.

1. Is the "Bicron BC517L liquid scintillator" considered "hazardous material?"
2. Will a tank or storage permit be required from the MPCA?
3. Is an Environmental Assessment Worksheet (EAW) required for this project?

According to the Minnesota Pollution Control Agency (MPCA) Tanks Unit, the "liquid scintillator" is not considered hazardous material; therefore, there is no tank storage permits required. This also results in the project not requiring an EAW from the Environmental Quality Board.

The MPCA strongly suggests that the University look closely at the discretionary EAW options. It may be in your best interest to have the University Regents become the Responsible Government Unit (RGU) for a discretionary EAW. This would allow the public to comment on this project long before construction begins, which is usually a much better way to keep a project rolling along with a minimum number of unanticipated problems.

Please feel free to contact me if you have any questions about this letter, or if you have any questions about the environmental requirements of the NOvA project.

Good Luck!

Sincerely,

Rocky Sisk
Customer, Employee & Agency Development Section
Technology, Education & Assistance Division

RS:jae

520 Lafayette Rd. N.; Saint Paul, MN 55155-4194; (651) 296-6300 (Voice); (651) 282-5332 (TTY); www.pca.state.mn.us
St. Paul • Brainerd • Detroit Lakes • Duluth • Mankato • Marshall • Rochester • Willmar
Equal Opportunity Employer • Printed on recycled paper containing at least 20 percent fibers from paper recycled by consumers.